

Dissertation zur Erlangung des Doktorgrades
der Fakultät für Chemie und Pharmazie
der Ludwig-Maximilians-Universität München

**NH₄F-Assisted High-Pressure Synthesis of
Novel Nitrides and Atomic-Resolution
Chemical Mapping by STEM**

Lucien André Eisenburger

aus

Düsseldorf, Deutschland

2022

Erklärung

Diese Dissertation wurde im Sinne von § 7 der Promotionsordnung vom 28. November 2011 von Herrn Prof. Dr. Wolfgang Schnick betreut.

Eidesstattliche Versicherung

Diese Dissertation wurde eigenständig und ohne unerlaubte Hilfe erarbeitet.

München, den 26.05.2022

.....
Lucien André Eisenburger

Dissertation eingereicht am:

12.04.2022

1. Gutachter:

Prof. Dr. Wolfgang Schnick

2. Gutachter:

Prof. Dr. Oliver Oeckler

Mündliche Prüfung am:

24.05.2022

Für alle, die mich zu dem gemacht haben, der ich heute bin.

„Es wird ja fleißig gearbeitet und viel mikroskopiert, aber es müßte mal wieder einer einen
gescheiterten Gedanken haben.“

Rudolf Ludwig Carl Virchow (*1821–†1902), Physician

Danksagung

Ich möchte Herrn Prof. Dr. Wolfgang Schnick herzlichst für die Betreuung meiner Dissertation danken. Trotz zahlreicher Ratschläge und freudiger Diskussionen bekam ich nie das Gefühl der Bevormundung. Ganz im Gegenteil wurde ich selbst von aussichtslos erscheinenden Syntheseunterfangen nicht abgehalten und einige dieser Ergebnisse haben es auch in diese Arbeit geschafft.

Herrn Prof. Dr. Oliver Oeckler möchte ich danken für die schier unzähligen Gespräche, das Brainstorming über Zoom, dafür mein Mentor im Bereich Kristallographie gewesen zu sein und natürlich das Koreferat meiner Arbeit. Ohne das alles wäre die Arbeit so nicht zu Stande gekommen.

Weiterer Dank gilt Herrn Prof. Dr. Johrendt, Herrn Prof. Dr. Müller-Caspary, Herrn Prof. Dr. Böttcher und Herrn PD Dr. Hoch für die Teilnahme an der Prüfungskommission meiner Dissertation.

Ganz besonderer Dank gilt Herrn Dr. Markus Döblinger und Herrn Dr. Steffen Schmidt für die Einarbeitung in die Welt der Elektronenmikroskopie und für die freundschaftliche Arbeitsatmosphäre!

Allen internen wie externen Kollaborationspartnern möchte ich herzlichst danken. Auch wenn es bei weitem nicht alle Manuskripte in diese Arbeit geschafft haben, so haben wir doch viel erreicht!

Mein Dank gilt Frau Olga Lorenz für sämtliche Hilfe bei administrativen Dingen aller Art. Frau Catrin Löhnert möchte ich danken, denn die Kaffeemaschine war eins der wichtigsten Geräte für meine Dissertation und deren Instandhaltung absolut unerlässlich!

Danke an Herrn Wolfgang Wünschheim für die Betreuung der IT und Herrn Dr. Dieter Rau für die Wahrung der Arbeitssicherheit.

Besonderer Dank gilt meinen ehemaligen Laborkollegen Dr. Christian Maak, Dr. Philipp Strobel, Dr. Christine Pösl, Dr. Robin Niklaus, Dr. Lukas Neudert, Sophia Wandelt, Eugenia Elzer und Monika Pointner. Die Laborabende und gemeinsamen Aktivitäten werden mir gerne in Erinnerung bleiben! Herrn Dr. Lukas Neudert sei auch gedankt, dass er mir zu meiner Bachelorarbeit die Elektronenmikroskopie nähergebracht hat.

Danke auch an Frau Jennifer Steinadler! Auch, wenn wir es beide nicht für möglich gehalten haben, dass wir miteinander auskommen werden, aber du bist tatsächlich in den wenigen Monaten zu einer meiner Lieblingskolleginnen geworden. Ich hoffe, dass zukünftige KollegInnen meinen Tag zumindest annähernd so bereichern können.

Mein Dank gilt natürlich auch allen anderen Mitgliedern der Arbeitskreise Schnick, Johrendt, Lotsch und Hoch für das produktive und angenehme Arbeitsumfeld.

Vielen Dank an Monika Pointer, Alexander Schmidts, Benjamin Glaser und Julian Aicher, deren Praktika meine Arbeit auf vielseitige Weisen bereichert haben. Monika Pointner bin ich über alle Maße dankbar für die Freundschaft, die sich aus dem ehemaligen Betreuungsverhältnis entwickelt hat. Danke, dass du stets eine Stütze warst und danke für das „mutual understanding“ angesichts unserer „besonderen“ Arbeitssituation.

Danke an Tobias Giftthaler für die breite Palette an Gesprächsthemen, sowohl Wissenschaftliches als auch Privates, und deine unglaublich reflektierte Sicht auf die verschiedensten Dinge.

Dem AK Oeckler sei gedankt für zahlreiche Übernachtungsmöglichkeiten in Leipzig und die vorbildliche Aufnahme. Besonders möchte ich Herrn Dr. Benndorf, Herrn Dr. Nentwig, Frau Fraunhofer, Herrn Günther und Herrn Jakob erwähnen.

Ganz besonderen Dank möchte ich hier meinen Freunden im Westerwald und in München aussprechen, allen voran Michael Kasperski und Dr. Valentin Weippert. Danke, dass ihr immer für mich da wart. Hätte ich Brüder, dann würde ich mir wünschen, dass sie mindestens so großartig sind wie ihr.

Meiner Mutter Angelika danke ich für die bedingungslose Unterstützung, Liebe und den unendlichen Glauben an mich und meine Fähigkeiten.

Mein größter Dank gilt jedoch denen, die stets an mich geglaubt haben, aber das Ende dieser Arbeit nicht mehr erleben können: Meine Großmutter Ingeborg und mein Vater Dietmar. Ohne euch wäre ich nicht so weit gekommen.

Was ich im Endeffekt ausdrücken möchte: Danke euch allen! Die Auflistung ist auf gar keinen Fall vollständig, aber ihr seid alle der Grund dafür, dass ich mit Fug und Recht behaupten kann, dass ich mein bisheriges Leben genau so noch einmal führen würde.

Lucien Eisenburger

Table of contents

1	<i>Introduction</i>	1
1.1	Nitride Materials	1
1.2	Syntheses of Nitridosilicates and -phosphates	2
1.3	Modern Methods of Structure Elucidation	4
1.4	Scope of this Thesis	5
1.5	References	7
2	<i>A Layered Tin Bismuth Selenide with Three Different Building Blocks that Account for an Extremely Large Lattice Parameter of 283 Å</i>	13
2.1	Introduction with Results and Discussion	13
2.2	References	22
3	<i>High-Pressure High-Temperature Synthesis of Mixed Nitridosilicatephosphates and Luminescence of $\text{AESiP}_3\text{N}_7\text{:Eu}^{2+}$ ($\text{AE} = \text{Sr}, \text{Ba}$)</i>	28
3.1	Introduction with Results and Discussion	28
3.2	References	37
4	<i>Nitridic Analogs of Micas $\text{AESi}_3\text{P}_4\text{N}_{10}(\text{NH})_2$ ($\text{AE} = \text{Mg}, \text{Mg}_{0.94}\text{Ca}_{0.06}, \text{Ca}, \text{Sr}$)</i>	41
4.1	Introduction with Results and Discussion	41
4.2	References	49
5	<i>High-Pressure Synthesis of $\text{Sc}_5\text{P}_{12}\text{N}_{23}\text{O}_3$ and $\text{Ti}_5\text{P}_{12}\text{N}_{24}\text{O}_2$ by Activation of Binary Nitrides ScN and TiN with NH_4F</i>	54
5.1	Introduction with Results and Discussion	54
5.2	References	62
6	<i>Discovery of Two Polymorphs of TiP_4N_8 Synthesized from Binary Nitrides</i>	67
6.1	Introduction with Results and Discussion	67
6.2	References	76
7	<i>Discussion and Outlook</i>	81

7.1	Novel Nitrides	81
7.2	STEM in Materials Science	83
7.3	Final Remarks	84
7.4	References	86
8	Summary	89
8.1	General Aspects	89
8.2	A Layered Tin Bismuth Selenide with Three Different Building Blocks that Account for an Extremely Large Lattice Parameter of 283 Å	90
8.3	High-Pressure High-Temperature Synthesis of Mixed Nitridosilicatephosphates and Luminescence of $AE\text{SiP}_3\text{N}_7\text{:Eu}^{2+}$ ($AE = \text{Sr}, \text{Ba}$)	90
8.4	Nitridic Analogs of Micas $AE\text{Si}_3\text{P}_4\text{N}_{10}(\text{NH})_2$ ($AE = \text{Mg}, \text{Mg}_{0.94}\text{Ca}_{0.06}, \text{Ca}, \text{Sr}$)	91
8.5	High-Pressure Synthesis of $\text{Sc}_5\text{P}_{12}\text{N}_{23}\text{O}_3$ and $\text{Ti}_5\text{P}_{12}\text{N}_{24}\text{O}_2$ by Activation of Binary Nitrides ScN and TiN with NH_4F	91
8.6	Discovery of Two Polymorphs of TiP_4N_8 Synthesized from Binary Nitrides	92
A	Supporting Information for Chapter 2	95
	Experimental Procedures	95
	Results and Discussion	100
	References	116
B	Supporting Information for Chapter 3	119
	Experimental Procedures	119
	Results and Discussion	123
	References	137
C	Supporting Information for Chapter 4	140
	Experimental Procedures	140
	Results and Discussion	144
	References	164

<i>D</i>	<i>Supporting Information for Chapter 5</i>	167
	Experimental Procedures	167
	Results and Discussion	171
	References	183
<i>E</i>	<i>Supporting Information for Chapter 6</i>	185
	Experimental Procedures	185
	Results and Discussion	189
	References	212
<i>F</i>	<i>Miscellaneous</i>	215
F.1	List of Publications within this Thesis	215
F.2	Full List of Publications	217
F.3	Conference Contributions	220
F.4	Deposited Crystal Structures	222
<i>G</i>	<i>Curriculum Vitae</i>	224

1 Introduction

1.1 Nitride Materials

The ongoing increase in population demands new technologies to bring into line the finiteness of resources and the claim to, at least, maintain overall wealth. The role of fundamental science, in this case, is the discovery of new materials suited to future technologies. The compound class of nitrides attracted interest as their versatility spans many fields of applications. Silicon nitride Si_3N_4 is used in the valves of high-performance combustion engines, in ball bearings, as an abrasive material, and as a passivating layer in integrated circuits.^[1-4] This range of applications is enabled by the covalent character and therefore strong Si–N bond with a molar bond energy of $335 \text{ kJ}\cdot\text{mol}^{-1}$ ^[5] as well as a high degree of condensation (κ^*) of the underlying tetrahedral network which combines to a material of high hardness with thermal as well as chemical stability. If we increase the complexity by introducing at least a third element we obtain a compound class called nitridosilicates. Noteworthy representatives of nitridosilicates are the compounds $AE_2\text{Si}_5\text{N}_8$ ($AE = \text{Ca}, \text{Sr}, \text{Ba}$) which, upon doping with Eu^{2+} and irradiation with blue light, emit orange light.^[6] Based on the phosphor-converted InGaN LED this led to the mass production of the first warm white pc-LED (phosphor-converted light-emitting diode) marketed to a wide consumer base. The aforementioned properties like chemical and thermal stability are similarly beneficial even for these more elaborate applications.

Another binary main group nitride, P_3N_5 , although having a higher degree of condensation lacks thermal stability. P_3N_5 readily decomposes at 850°C ^[7] under ambient pressure which can be attributed to the weaker P–N bond with a molar bond energy of $290 \text{ kJ}\cdot\text{mol}^{-1}$ ^[5] if compared to the previously mentioned Si–N bond. Despite the differences, there are likewise multinary compounds called nitridophosphates.

The last binary group of nitrides relevant for this thesis are the interstitial transition metal nitrides, for example, TiN and ScN. These compounds show remarkable thermal stability and in the case of TiN also mechanical stability hence its use as a coating material for drill heads and also bicycle chains.^[8] For a comprehensive overview of some applications of nitride-based materials see Figure 1.1.

* κ is defined as the ratio of the number of tetrahedra centers and the number of coordinating atoms. For example, $\text{Sr}_2\text{Si}_5\text{N}_8$ has a κ of $5/8$.

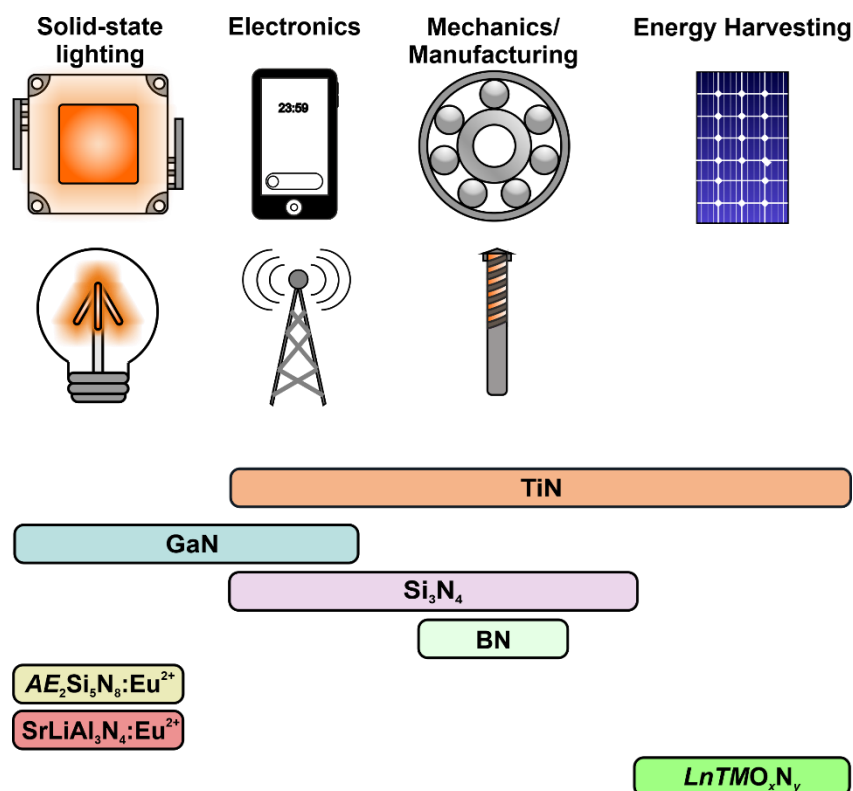


Figure 1.1. Applications of some nitridic materials ranging from solid-state lighting to manufacturing.

1.2 Syntheses of Nitridosilicates and -phosphates

The synthesis of Si_3N_4 is either performed from the elements or by the imide-decomposition process by the pyrolysis of $\text{Si}(\text{NH})_2$.^[9,10] The synthesis of nitridosilicates is likewise readily performed by conventional solid-state methods such as the heating of the starting materials in a tube- or either radio-frequency furnaces delivering the activation energy needed to surpass the stability of Si_3N_4 .^[6,11–14] The metal-bearing starting materials, according to literature, range from nitrides, hydrides, amides to even the elemental form.^[15] The limits of this intuitive approach however are reached when transition metals shall be incorporated. As mentioned in literature the transition metals are prone to reduction while the nitride-ion is in turn oxidized.^[16,36] A problem expected to become more severe as the oxidation state of the metal is increased. Bielec et. al. synthesized the compound $\text{Fe}_2\text{Si}_5\text{N}_8$ from $\text{Ca}_2\text{Si}_5\text{N}_8$ and FeCl_2 in an ion-exchange type of reaction.^[16] It is suggested that Ca^{2+} migrates through channels in the nitridic network, upon heating, to form CaCl_2 while cation sites are refilled by Fe^{2+} . Bielec et al. not only managed aliovalent substitution, in the case of $\text{Sc}_{0.2}\text{Ca}_{1.7}\text{Si}_5\text{N}_8$ but also avoided the use of refractory ScN by their ion-exchange approach.^[17] However, a drawback of this approach is its dependence on the preformed network if only topotactical reactions are

considered as “ion-exchange” reactions. Wendl et al. demonstrated post-synthetic modifications, via metathesis, altering the underlying nitridic network during the reaction.^[18] The synthesis of P_3N_5 is performed at 850 °C from P_4S_{10} in flowing ammonia, which yields an amorphous bulk sample as described by Stock and Grüneberg as early as 1907.^[19] Suitable samples for powder X-ray diffraction structure elucidation from synchrotron radiation were achieved by Horstmann et al. only after the pyrolysis of $[P(NH_2)_4]I$ in 1997.^[20] Further research yielded compounds like the nitridic sodalites $Zn_8[P_{12}N_{24}]X_2$ ($X = O, S, Se, Te$), and quasi-binary HPN_2 from syntheses in tube furnaces but the success story of nitridophosphates was yet to come.^[21–25] With the advent of multianvil Walker-type large volume presses the thermal decomposition of P_3N_5 could be prevented according to Le Chateliers’ principle supported by the use of group 1 or 2 azides which upon heating decompose under the evolution of N_2 .^[26] This enabled systematic screening for nitridophosphates but the obstacle of missing single-crystals for X-ray diffraction remained. After Marchuk et al. employed NH_4Cl as a mineralizer, the high-pressure high-temperature (HP/HT) approach yielded the desired quality and size of single crystals, reliably.^[27] The ability to obtain accurate and precise structural data of nitridophosphates also coincided with a beginning interest in potential luminescent materials among nitridophosphates.^[28–31] Despite tremendous efforts, expanding the structural and compositional variety of nitridophosphates beyond the group 1 and 2 elements to transition metal (*TM*) or rare-earth metals (*RE*) was not feasible. In analogy to nitridosilicate syntheses, the *TM*- or *RE* nitrides were believed to be too unreactive and the reduction of the metal or P and the oxidation of the nitride ion seemed to impede the discovery of new compounds. In addition, the investigated *TMs* tend to form stable phosphides like FeP. Kloß et al. developed the HP/HT solid-state metathesis that employs a metal halide and $LiPN_2$ resulting in a nitridophosphate and the lithium halide which is the driving force of the reaction. Following this approach, the compound class of *RE* nitridophosphates was made accessible and a few representatives of *TM* nitridophosphates were synthesized.^[32–38] Surprisingly, the syntheses of compounds of group 4 elements resulted exclusively in oxonitridophosphates. Most of the presented syntheses aimed at negatively charged networks that needed metal cations for balancing charges. Vogel et al. delivered access to neutral main group nitrides BP_3N_6 and SiP_2N_4NH . This was achieved by employing the binary nitrides BN or Si_3N_4 respectively, $(PNCI_2)_3$ and NH_4N_3 which led to the development of quantitative amounts of HCl in contrast to Marchuk’s mineralizer

approach.^[39,40] $\text{SiP}_2\text{N}_4\text{NH}$ constitutes the second nitride of Si and P after Baldus et al. discovered SiPN_3 both having syntheses from molecular precursors in common.^[41]

A unified synthetic approach that allows for the reaction of P_3N_5 with refractory nitrides like Si_3N_4 and *TMN*, the first objective of this thesis, was still missing. We employed NH_4F as a mineralizer either exploiting the fluorophilicity of Si or the industrially known processes of nitride etching with HF. The syntheses were performed at 8 GPa of pressure and 1400–1700 °C hindering the decomposition of P_3N_5 while delivering thermal energy for the reaction of either Si_3N_4 or the *TMN*.

1.3 Modern Methods of Structure Elucidation

Explaining the properties of a new material is linked to the knowledge of its crystal structure. Challenges arise if routine structure elucidation by SCXRD (single crystal X-ray diffraction) fails due to microcrystallinity and/or real structure phenomena. Structure elucidation from PXRD (powder X-ray diffraction) has been the most common method in the case of microcrystalline samples as shown for $\alpha\text{-P}_3\text{N}_5$. However, the loss of information from SCXRD to PXRD leads to a loss in the precision of atomic site parameters. In addition, the presence of side phases, especially unknown ones, can severely complicate structure elucidation. Fahrnbauer et al. reported the collection of single-crystal X-ray diffraction data sets from microcrystallites, which have been precharacterized using a transmission electron microscope (TEM) and been subjected to subsequent diffraction experiments carried out employing microfocused synchrotron radiation.^[40] This approach enabled the structure elucidation of e. g. $\text{Pb}_2\text{Si}_5\text{N}_8$. The claim of an unusually short Pb-Pb distance of 3.190(1) Å, compared to Pb metal with 3.49 Å, was supported by accurate diffraction data.^[41] Other examples of this approach include the crystal structures of $\text{U}_{0.5x}\text{Sr}_{2-0.75x}\text{Si}_5\text{N}_8$ with $x \approx 1.05$, $\text{Lu}_4\text{Ba}_2[\text{Si}_{12}\text{O}_2\text{N}_{16}\text{C}_3]:\text{Eu}^{2+}$, $\text{BaP}_8\text{N}_{14}$, or $\text{La}_{21}\text{P}_{40}\text{O}_{46}\text{N}_{57}$.^[17,31,38,44]

The imaging mode of high-resolution TEM aided in clarifying ambiguous results from SCXRD as shown for $\text{CaMg}_2\text{P}_6\text{O}_3\text{N}_{10}$.^[29] SCXRD analysis led to a Ca position with a rather oblate displacement ellipsoid coordinated octahedrally by six N atoms. The interpretation of a randomly displaced Ca position in the octahedron was supported by HRTEM images compared to simulations based on SCXRD data. Aside from nitrides, this approach was also used for the chalcogenide $\text{Pb}_5\text{Sb}_4\text{S}_{11}$ to distinguish a disordered and an ordered polymorph

based on simulations.^[45] This already shows the drawback of HRTEM as images are not readily interpretable and contrast maxima do not necessarily coincide with atomic positions. The advent of aberration-corrected scanning TEM (STEM) with a high-angle annular dark-field (HAADF) detector enabled an imaging mode with a direct correlation of contrast maxima and atomic positions with sub-Angstrom resolution. The dependence of image contrast from $\sim Z^2$ enabled the distinction between ordered and disordered structure models for $\text{Ca}_{1-x}\text{Li}_x\text{Al}_{1-x}\text{Ge}_{1+x}\text{N}_3$ ($x \approx 0.2$) and in the case of $\text{Ce}_4\text{Li}_3\text{P}_{18}\text{N}_{35}$, the slight displacement of Ce atoms could be identified as the cause for superstructure reflections.^[46,47] Considering that contrast scaling depends on $\sim Z^2$ the limitations of this method become apparent if the atomic numbers of two elements become increasingly similar or are far apart. The interpretation of images can be complicated by insufficient dynamic range of the detector in both cases. A combination of atomic resolution STEM-HAADF and energy dispersive X-ray spectroscopy (EDX) yields a 3D dataset with image contrast in two dimensions and pixel-wise EDX spectra as the third. As shown for SrTiO_3 and predominantly perovskite-related compounds this method finally delivers images that are comparable to those from structure visualization software.^[48,49] The emphasis on oxides in the literature can be most likely attributed to the potential beam damage caused by this method, especially as X-ray collection is less efficient for elements with $Z < 30$ thus either demanding longer acquisition times or increased beam currents and therefore aggravating the issue of beam damage even more.^[50]

1.4 Scope of this Thesis

Despite the tremendous efforts in synthesizing novel nitrides that have been achieved by high-pressure high-temperature chemistry, the reaction between multiple refractory nitrides had not been successful. In the two cases where double nitrides of Si and P were formed, SiPN_3 and $\text{SiP}_2\text{N}_4\text{NH}$, there was a need for molecular precursors, $\text{SiPN}(\text{NH})(\text{NH}_2)_4$ or $(\text{PNCl}_2)_3$ respectively.^[41,39] To overcome these limitations and employ the nitrides P_3N_5 and Si_3N_4 , the previously reported mineralizer-assisted approaches were developed further by employing NH_4F as mineralizing agent.^[27–29] This led to the compound classes of alkaline earth nitridosilicatephosphates and silicon imidonitridophosphates. The elemental combination Si and P is troublesome concerning X-ray diffraction as the atomic scattering factors of Si and P are similar. STEM-EDX with atomic resolution enables reliable statements on the distribution

of elements like Si and P in nitridic networks. The refractory interstitial transition metal nitrides were used as starting materials to evaluate the limits of the NH_4F -assisted approach. This yielded (oxo)nitridophosphates with band gaps in the visible part of the electromagnetic spectrum.

In summary, this thesis addresses two needs of materials sciences. The first is developing a systematic access to novel compounds and materials: The NH_4F -assisted HP/HT syntheses for mixed nitridic nitridosilicatephosphates and silicon imidonitridophosphates. Both classes of compounds may include promising phosphors for solid-state-lighting and are discussed in Chapters 3 and 4. Following this approach, the transition metal (oxo)nitridophosphates $\text{Sc}_5\text{P}_{12}\text{N}_{23}\text{O}_3$, $\text{Ti}^{\text{III}}_4\text{Ti}^{\text{IV}}\text{P}_{12}\text{N}_{24}\text{O}_2$, and $\text{Ti}^{\text{IV}}\text{P}_4\text{N}_8$ were synthesized from the highly stable binary nitrides ScN and TiN as presented in Chapters 5 and 6. Accordingly, refractory nitrides have finally been included in the staple of starting materials and semiconductor-like band gaps in (oxo)nitridophosphates have been obtained. The second demand addressed is the accurate structural investigation of occupational and positional disorder. Aberration-corrected STEM was performed on all compounds including $\text{Sn}_{2.8(4)}\text{Bi}_{20.2(4)}\text{Se}_{27}$ to elucidate real structure effects and order/disorder effects which will be discussed beginning from chapter 2.

1.5 References

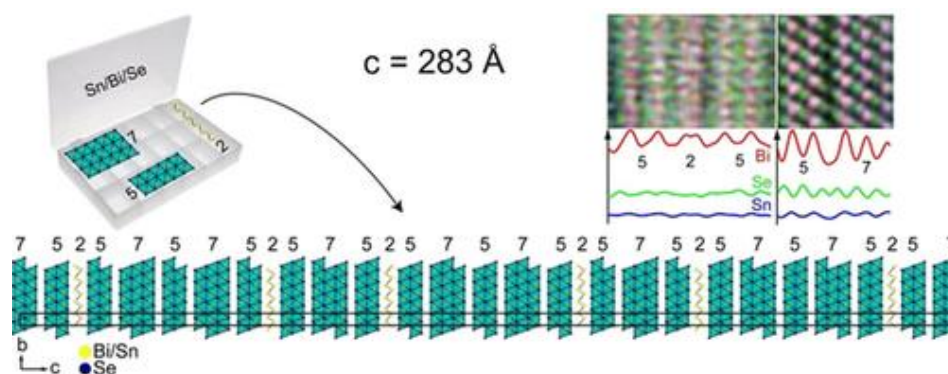
- [1] J. G. Sun, J. M. Zhang, M. J. Andrews, J. S. Trethewey, N. S. L. Phillips, J. A. Jensen, *Int. J. Appl. Ceram. Technol.* **2008**, *5*, 164–180.
- [2] M. Jiang, R. Komanduri, *Wear* **1998**, *215*, 267–278.
- [3] X. Zhang, P. Chen, J. Zhang, S. Li, H. Zhou, *Int. J. Adv. Manuf. Technol.* **2021**, *115*, 3139–3148.
- [4] D. M. Knotter, T. J. J. (Dee) Denteneer, *J. Electrochem. Soc.* **2001**, *148*, F43.
- [5] A. F. Holleman, N. Wiberg, in *Lehrbuch Der Anorganischen Chemie*, De Gruyter, Berlin, **2016**, p. 154.
- [6] M. Zeuner, S. Pagano, W. Schnick, *Angew. Chem. Int. Ed.* **2011**, *50*, 7754–7775; *Angew. Chem.* **2011**, *123*, 7898–7920.
- [7] S. Horstmann, E. Irran, W. Schnick, *Angew. Chem. Int. Ed.* **1997**, *36*, 1873–1875; *Angew. Chem.* **1997**, *109*, 1938–1940.
- [8] E. Santecchia, A. M. S. Hamouda, F. Musharavati, E. Zalnezhad, M. Cabibbo, S. Spigarelli, *Ceram. Int.* **2015**, *41*, 10349–10379.
- [9] T. N. Tiegs, F. C. Montgomery, J. L. Schroeder, D. L. Barker, P. A. Menchhofer, in *Proc. 21st Annu. Conf. Compos. Adv. Ceram. Mater. Struct. Ceram. Eng. Sci. Proc.*, Oak Ridge, TN, **2008**, pp. 437–447.
- [10] P. E. D. Morgan, *Research on Densification, Character and Properties of Dense Silicon Nitride*; Franklin Institute, Philadelphia, **1974**, TR AD 778 373.
- [11] M. Seibald, T. Rosenthal, O. Oeckler, W. Schnick, *Crit. Rev. Solid State Mater. Sci.* **2014**, *39*, 215–229.
- [12] M. Seibald, T. Rosenthal, O. Oeckler, C. Maak, A. Tücks, P. J. Schmidt, D. Wiechert, W. Schnick, *Chem. Mater.* **2013**, *25*, 1852–1857.
- [13] M. Seibald, O. Oeckler, V. R. Celinski, P. J. Schmidt, A. Tücks, W. Schnick, *Solid State Sci.* **2011**, *13*, 1769–1778.
- [14] M. Seibald, T. Rosenthal, O. Oeckler, F. Fahrenbauer, A. Tücks, P. J. Schmidt, W. Schnick,

- Chem. Eur. J.* **2012**, *18*, 13446–13452.
- [15] H. Yamane, H. Morito, *Inorg. Chem.* **2013**, *52*, 5559–5563.
- [16] P. Bielec, O. Janka, T. Block, R. Pöttgen, W. Schnick, *Angew. Chem. Int. Ed.* **2018**, *57*, 2409–2412; *Angew. Chem.* **2018**, *130*, 2433–2436.
- [17] P. Bielec, L. Eisenburger, H. L. Deubner, D. Günther, F. Kraus, O. Oeckler, W. Schnick, *Angew. Chem. Int. Ed.* **2019**, *58*, 840–843; *Angew. Chem.* **2019**, *131*, 850–853.
- [18] S. Wendl, L. Seidl, P. Schüler, W. Schnick, *Angew. Chem. Int. Ed.* **2020**, *59*, 23579–23582; *Angew. Chem.* **2020**, *132*, 23785–23788
- [19] A. Stock, H. Grüneberg, *Ber. Dtsch. Chem. Ges.* **1907**, *40*, 2573–2578.
- [20] S. Horstmann, E. Irran, W. Schnick, *Angew. Chem. Int. Ed. Engl.* **1997**, *36*, 1873–1875; *Angew. Chem.* **1997**, *109*, 1938–1940.
- [21] J. Weitkamp, S. Ernst, F. Cubero, F. Wester, W. Schnick, *Adv. Mater.* **1997**, *9*, 247–248.
- [22] F. Wester, W. Schnick, *Z. Anorg. Allg. Chem.* **1996**, *622*, 1281–1286.
- [23] W. Schnick, J. Lücke, *Angew. Chem. Int. Ed. Engl.* **1992**, *31*, 213–215; *Angew. Chem.* **1992**, *104*, 208–209.
- [24] F. Karau, O. Oeckler, F. Schäfers, R. Niewa, W. Schnick, *Z. Anorg. Allg. Chem.* **2007**, *633*, 1333–1338.
- [25] W. Schnick, J. Lücke, *Z. Anorg. Allg. Chem.* **1992**, *610*, 121–126.
- [26] S. D. Kloß, W. Schnick, *Angew. Chem. Int. Ed.* **2019**, *58*, 7933–7944; *Angew. Chem.* **2019**, *131*, 8015–8027.
- [27] A. Marchuk, F. J. Pucher, F. W. Karau, W. Schnick, *Angew. Chem. Int. Ed.* **2014**, *53*, 2469–2472; *Angew. Chem.* **2014**, *126*, 2501–2504.
- [28] A. Marchuk, V. R. Celinski, J. Schmedt auf der Günne, W. Schnick, *Chem. Eur. J.* **2015**, *21*, 5836–5842.
- [29] A. Marchuk, L. Neudert, O. Oeckler, W. Schnick, *Eur. J. Inorg. Chem.* **2014**, *2014*, 3427–3434.

- [30] A. Marchuk, W. Schnick, *Angew. Chem. Int. Ed.* **2015**, *54*, 2383–2387; *Angew. Chem.* **2015**, *127*, 2413–2417.
- [31] S. Wendl, L. Eisenburger, P. Strobel, D. Günther, J. P. Wright, P. J. Schmidt, O. Oeckler, W. Schnick, *Chem. Eur. J.* **2020**, *26*, 7292–7298.
- [32] S. D. Kloß, W. Schnick, *Angew. Chem. Int. Ed.* **2015**, *54*, 11250–11253; *Angew. Chem.* **2015**, *127*, 11402–11405
- [33] S. D. Kloß, N. Weidmann, R. Niklaus, W. Schnick, *Inorg. Chem.* **2016**, *55*, 9400–9409.
- [34] S. D. Kloß, N. Weidmann, W. Schnick, *Eur. J. Inorg. Chem.* **2017**, *2017*, 1930–1937.
- [35] S. D. Kloß, A. Weis, S. Wandelt, W. Schnick, *Inorg. Chem.* **2018**, *57*, 4164–4170.
- [36] S. D. Kloß, S. Wandelt, A. Weis, W. Schnick, *Angew. Chem. Int. Ed.* **2018**, *57*, 3192–3195
Angew. Chem. **2018**, *130*, 3246–3249.
- [37] S. D. Kloß, O. Janka, T. Block, R. Pöttgen, R. Glaum, W. Schnick, *Angew. Chem. Int. Ed.* **2019**, *58*, 4685–4689; *Angew. Chem.* **2019**, *131*, 4733–4737.
- [38] M. Nentwig, S. D. Kloß, L. Neudert, L. Eisenburger, W. Schnick, O. Oeckler, *Chem. Eur. J.* **2019**, *25*, 14382–14387.
- [39] S. Vogel, A. T. Buda, W. Schnick, *Angew. Chem. Int. Ed.* **2019**, *58*, 3398–3401; *Angew. Chem.* **2019**, *131*, 3436–3439.
- [40] S. Vogel, A. T. Buda, W. Schnick, *Angew. Chem. Int. Ed.* **2018**, *57*, 13202–13205; *Angew. Chem.* **2018**, *130*, 13386–13389.
- [41] H. P. Baldus, W. Schnick, J. Lücke, U. Wannagat, G. Bogedain, *Chem. Mater.* **1993**, *5*, 845–850.
- [42] F. Fahrnbauer, T. Rosenthal, T. Schmutzler, G. Wagner, G. B. M. Vaughan, J. P. Wright, O. Oeckler, *Angew. Chem. Int. Ed.* **2015**, *54*, 10020–10023; *Angew. Chem.* **2015**, *127*, 10158–10161.
- [43] P. Bielec, R. Nelson, R. P. Stoffel, L. Eisenburger, D. Günther, A. K. Henß, J. P. Wright, O. Oeckler, R. Dronskowski, W. Schnick, *Angew. Chem. Int. Ed.* **2019**, *58*, 1432–1436; *Angew. Chem.* **2019**, *131*, 1446–1450.
- [44] C. Maak, L. Eisenburger, J. P. Wright, M. Nentwig, P. J. Schmidt, O. Oeckler, W. Schnick,

- Inorg. Chem.* **2018**, *57*, 13840–13846.
- [45] P. Schultz, F. Nietschke, G. Wagner, C. Eikemeier, L. Eisenburger, O. Oeckler, *Z. Anorg. Allg. Chem.* **2017**, *643*, 1531–1542.
- [46] J. Häusler, L. Eisenburger, O. Oeckler, W. Schnick, *Eur. J. Inorg. Chem.* **2018**, *2018*, 759–764.
- [47] S. D. Kloß, L. Neudert, M. Döblinger, M. Nentwig, O. Oeckler, W. Schnick, *J. Am. Chem. Soc.* **2017**, *139*, 12724–12735.
- [48] D. A. Muller, L. F. Kourkoutis, M. Murfitt, J. H. Song, H. Y. Hwang, J. Silcox, N. Dellby, O. L. Krivanek, in *Microsc. Microanal.*, American Association For The Advancement Of Science, **2008**, pp. 132–133.
- [49] R. Egoavil, S. Hühn, M. Jungbauer, N. Gauquelin, A. Béché, G. Van Tendeloo, J. Verbeeck, V. Moshnyaga, *Nanoscale* **2015**, *7*, 9835–9843.
- [50] D. Attwood, *Soft X-Rays and Extreme Ultraviolet Radiation*, Cambridge University Press, **1999**.

DOI: 10.1002/chem.202000663



2.1 Introduction with Results and Discussion

Owing to their pronounced compositional and structural diversity, chalcogenides represent one of the most intriguing classes of compounds in solid-state chemistry and physics.^[1] Besides Bi₂Se₃, which is one of the most well-known topological insulators,^[2] recent studies of for example, Bi₂Te₃,^[3] MnBi₂Te₄,^[4] and SnBi₂Te₄.^[5] revealed their potential as topologically

non-trivial materials. In addition, layered chalcogenides like BiSe,^[6] SnSe,^[7] and Bi-doped SnSe,^[8] have attracted much attention in the field of thermoelectrics. Such chalcogenides also constitute a fascinating field of fundamental research. For example, single-crystal data of Ge₄Se₃Te revealed unexpected Ge–Ge bonds, which have been confirmed by STEM (scanning transmission electron microscopy) and theoretical calculations.^[9] Modular stacking can lead to new inorganic-organic hybrid materials, for example, by inserting polymer chains in tin selenides.^[10]

Layered chalcogenides often form homologous series of compounds, where variations of the slab thicknesses between van der Waals gaps characterize a plethora of new phases.^[11] This can lead to compounds with large lattice parameters, which can be expected to be beneficial for thermoelectric properties as phonon scattering on the nanometer scale decreases thermal conductivity.^[12] Compounds in the binary M/X systems with $M = \text{Sb, Bi}$ and $X = \text{Se, Te}$ form trigonal layered structures built up from M_2 double layers (symbolized by “2”)—comparable to those in the element structures of Sb and Bi—and tetradymite-like M_2X_3 quintuple blocks symbolized by “5”. Complex stacking results in large lattice parameters, for example, $c = 103 \text{ \AA}$ for Bi₈Te₉, which features a 2555|2555|2555 sequence.^[13] So far, no single-crystal X-ray data have been reported for such layered chalcogenides with long-periodic stacking sequences that exhibit lattice parameters larger than these 103 Å. Electron diffraction data and high-resolution transmission electron microscopy (HRTEM) of quenched samples, however, showed the presence of a rhombohedral bismuth telluride Bi_{2+δ}Te₃ with a 138R-type stacking sequence ($\delta \approx 0.11\text{--}0.75$, $c \approx 275 \text{ \AA}$) of 55525552552|55525552552|55525552552.^[14] In ternary systems such as $Tt\text{Te}(\text{Bi}_2\text{Te}_3)_n$ ($Tt = \text{Ge, Sn, Pb}$), the structural chemistry is extended by building blocks with septuple (“7”) $Tt\text{Bi}_2\text{Te}_4$ slabs in addition to quintuple (“5”) Bi₂Te₃ slabs.^[15] The structure with the longest periodicity has been found in a 159R-type germanium bismuth telluride that exhibits a 557575757|557575757|557575757 stacking sequence with $c \approx 318 \text{ \AA}$ as deduced from electron diffraction patterns.^[16] However, crystal structure refinements have not been reported for such extreme cases.

With respect to inorganic compounds, unit-cell dimensions of more than 100 Å are very unusual in general. They have been reported for a few binary compounds like the well-known polytypes of SiC,^[17] ZnS,^[18] CdI₂,^[19] and PbI₂.^[20] Varying sequences and orientations of the same structural entities result in polytypes with huge lattice parameters of up to 990 Å in

SiC.^[21] Such crystallographic phenomena have usually been observed only in small domains by electron microscopy; and the structures were assigned by plausibility or trial and error methods in case diffraction data were available. Only very few actual structure refinements based on single-crystal data of structure models with very large lattice parameters do exist. In this respect, even lattice parameters of around 57 Å as recently observed for cesium rare-earth silicates $\text{Cs}_3\text{RESi}_6\text{O}_{15}$ ($RE = \text{Dy-Lu, Y, In}$) have been reported as being unusually large,^[22] although for example, for the mineral turtmannite with $c = 204$ Å, a full structure refinement has been carried out.^[23] Hexaferrites are also prone to form anisotropic structures with large translation periods along the stacking direction of Ba-rich and Fe-rich slabs, which can be arranged with varying sequences that exhibit translation periods of up to 1577 Å for $\text{Ba}_{70}\text{Zn}_{66}\text{Fe}_{444}\text{O}_{802}$.^[24] While this extraordinary layer stacking has only been identified by electron microscopy, Rosseinsky et al. fully refined the crystal structure of Ba/Fe/Zn oxide hexaferrite polytypes, for example, $\text{Ba}_{10}\text{Fe}_{72}\text{Zn}_8\text{O}_{126}$ with $c = 488$ Å, from single-crystal synchrotron data.^[25] Hexaferrites can be identified by the $00l$ reflections in electron diffraction patterns and described by a unified (3+1)D superspace model.^[26] Similar descriptions have been reported for perovskite-like compounds.^[27] Lidin et al. developed a similar superspace formalism for the system Bi/Se described above.^[28] Such superspace descriptions are well known from modulated structures, but the (3+1)D description of long-periodic layered structures does not mean that a somehow simpler structure is modified by wave-like displacements or occupation modulations. In fact, the hypothetical basic structure would consist of just one or a few atoms. Therefore, the superspace formalism focuses, on the one hand, on a unified description of a series of compounds. On the other hand, it gives access to elegant structure refinements in cases where the reflections of extremely large unit cells are too closely spaced to be integrated from area-detector data based on a 3D periodic indexing.

In the pseudobinary system $(\text{SnSe})_x\text{Bi}_2\text{Se}_3$, compounds with very diverse structures are formed.^[29] Besides cubic $\text{Sn}_4\text{Bi}_2\text{Se}_7$ ($x = 4$) with defect NaCl-type structure, and layered SnBi_4Se_7 ($x = 0.5$) with defect GeSb_2Te_4 -type structure, at least four compounds ($0.8 \leq x \leq 3$) with structures derived from lillianite ($\text{Pb}_3\text{Bi}_2\text{S}_6$)^[30] have been discovered. Here we report the single-crystal structure of a new compound in the system Sn/Bi/Se, which features an extraordinarily long lattice parameter of $c = 282.6$ Å in a $150R$ stacking sequence.

A complex layered phase with the chemical composition $\text{Sn}_{2.8(4)}\text{Bi}_{20.2(4)}\text{Se}_{27}$ was formed during the decomposition of samples of SnBi_4Se_7 with defect GeSb_2Te_4 -type structure.^[29] The fact that this decomposition occurred during repeated slow heating indicates that the new phase is most likely thermodynamically stable at temperatures below $\approx 500^\circ\text{C}$. The heterogeneous product was examined by scanning electron microscopy (SEM) and energy-dispersive X-ray spectroscopy (EDX), which revealed regions of different contrast and composition (Figure A1 and Table A1, “A” denotes Figures and Tables in the Supporting Information). In addition to a minority phase, which according to EDX corresponds to $\text{Sn}_{11.49}\text{Bi}_{12.39}\text{Se}_{30}$,^[29] and a main phase of $\text{Sn}_{0.85}\text{Bi}_{2.15}\text{Se}_4$,^[29] the title compound has been identified as a main component that is slightly Sn-depleted compared to the nominal composition SnBi_4Se_7 .

A single crystal (Figure A2) of this unknown phase has been characterized by transmission electron microscopy (TEM) and EDX (Table A2). Using a fluorescence detector, this crystallite has been centered in a microfocused synchrotron beam at the European Synchrotron Radiation Facility (ESRF) and single-crystal diffraction data were recorded.^[31] The crystallite exhibits a complex diffraction pattern. Initial attempts to determine the crystal structure from the single-crystal data by “routine data processing” resulted in a structure close to that of BiSe .^[32] However, the fact that 60 % of all reflections remained unindexed indicated that this was a wrong model. Taking into account the precise positions of the reflections leads to a unit cell with $c = 282.6(6) \text{ \AA}$; however, reasonable data cannot be extracted as many very weak reflections lie very close to strong ones that impede intensity integration. This problem can be overcome by formally describing the diffraction pattern based on the (3+1) dimensional superspace group $R\bar{3}m(00\gamma)00$. This involves a formal basic cell of $a = 4.1819(4)$ and $c = 5.6528(5) \text{ \AA}$, which contains just one atom, with a commensurate modulation vector $q = 87/50 = 1.74$. This way, all reflections in the reciprocal lattice can be indexed (Figure A3–A5). Following the concept outlined by Lidin et al.,^[28] the structure solution and refinement were based on modulation parameters of the single atom site at the origin of the small unit cell of the basic structure (for details on the refinement see the Supporting Information). Initially assuming one Bi and one Se atom on this site, both fully occupied, the additional dimension in (3+1)D superspace can be used to modulate the occupancy using discontinuous functions. Crenel functions were used to describe the occupancy modulation by defining intervals in the additional dimension x_4 where the corresponding atom exists. The refinement of the crenel function width Δ defines the overall chemical composition.

corresponds to Bi/Sn atom columns and darker contrast to Se atom columns. Se atoms are displayed as gray circles and Bi/Sn as white circles.

Figure 2.3 shows a 525 stacking sequence with a double layer in the center (a–d) and a 57 stacking sequence with a van der Waals gap between the two blocks (e–h). Intensities in STEM images and their projection perpendicular [001] further confirm the atom distribution along the sequence (Figure A10). Selected-area electron diffraction (SAED) patterns and Fourier transforms of STEM images along [210] match the diffraction pattern calculated from the 3D model derived from the (3+1)D structure refinement (Figure 2.4) and thus additionally confirm the lattice parameter of 286.6(6) Å. A further SAED pattern along [100] with the corresponding simulation is shown in Figure A11.

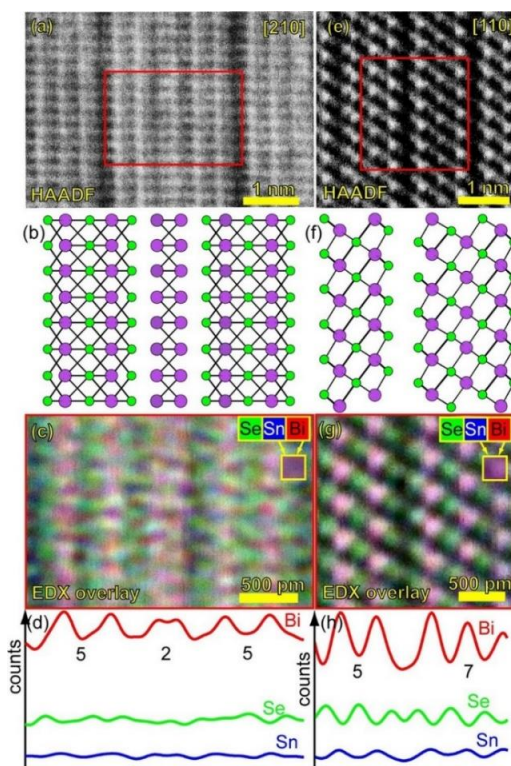


Figure 2.3. STEM-HAADF images along zone axes [210] (a) and [110] (e), brighter contrast corresponds to Bi/Sn atom columns and darker contrast to Se atom columns; (c, g) EDX maps of the indicated (red box) section of the STEM-HAADF images with (b, f) corresponding structure projections and (d, h) integrated EDX signal projected perpendicular to the layers (projection along [210] or [110], that is, parallel to the layers, Se signals and atoms are highlighted in green and Bi/Sn signals and atoms in red and blue), showing mixed occupancy on all cation positions as indicated by the violet color. (b), (c) and (d) show a 525 stacking sequence with a double layer in the center; (f), (g) and (h) depict a 57 stacking sequence with a van der Waals gap between the two blocks. (a, c) were recorded using 200 kV, (e, g) using 300 kV accelerating voltage.

Occasionally, stacking faults and different stacking sequences have locally been observed during extensive electron microscopy studies (Figure A12). Yet, the presented structure is by far the predominant stacking sequence.

In conclusion, repeated annealing afforded $\text{Sn}_{2.8(4)}\text{Bi}_{20.2(4)}\text{Se}_{27}$, a new compound in the system Sn/Bi/Se with an extraordinarily long-periodic 150R stacking sequence 7525757525|7525757525|7525757525, resulting in a lattice parameter of $c = 282.6(6)$ Å. The structure is built up from three different types of slabs, which significantly expands the plethora of known structure models for layered chalcogenides. In $\text{Sn}_{2.8(4)}\text{Bi}_{20.2(4)}\text{Se}_{27}$, the structural features of binary pnictogen-rich chalcogenides, that is, double and quintuple layers and those of ternary tetradymite-like chalcogenides, that is, quintuple and septuple layers, are combined and lead to the unusual long-range ordering. It remains, however, an open and very intriguing question, why such structures form and why they are seemingly thermodynamically stable. The large unit cell and the mixed occupancies impede theoretical calculations as alternative models with different arrangements of the same building blocks will show only tiny differences in the strength of van der Waals interactions between the slabs. For example, in the related compound $\text{Ge}_2\text{Sb}_2\text{Te}_5$, which features much smaller translation periods, activation energies for transitions between ordered and disordered models, which differ by ca. 1 eV in energy, have been calculated to be as low as 0.005 eV.^[35] The structure model was obtained by means of X-ray diffraction using a microfocused synchrotron beam and confirmed by STEM-HAADF measurements with atomic resolution and EDX mappings. The synergism of these methods enables unprecedented accuracy of structure determinations of microcrystalline compounds and promotes the discovery of numerous new related layered compounds with mixed site occupancies. These may exhibit intriguing physical properties such as thermoelectricity or non-trivial topological behavior.

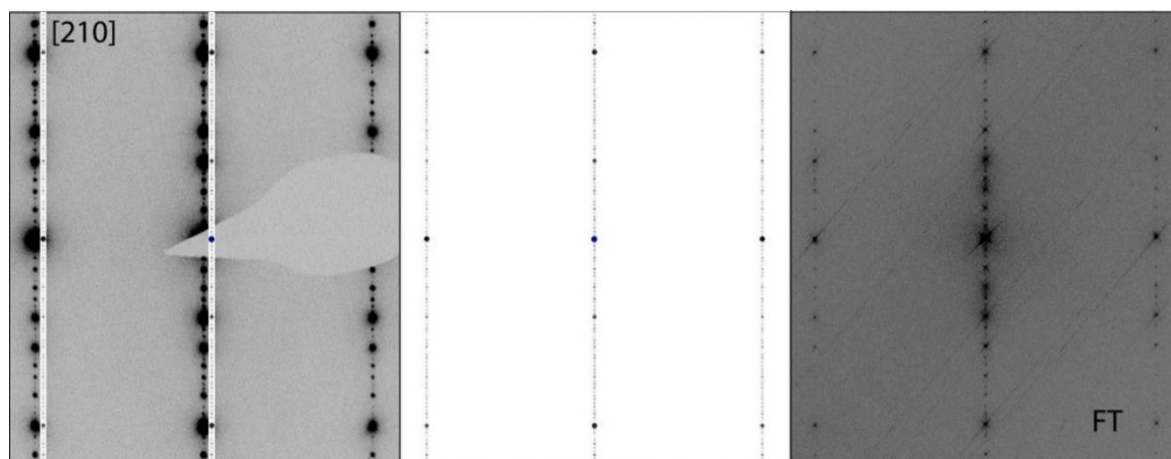


Figure 2.4. Comparison of an experimental SAED pattern (top, zone axis [210]) (left), a Fourier transform of the STEM-HAADF image displayed in Figure 2.2 (right) with a simulated SAED pattern (middle, based on the structure model from single crystal data); for better comparability, cutouts of the simulation are repeated as insets in the experimental pattern

Experimental Section

$\text{Sn}_{2.8(4)}\text{Bi}_{20.2(4)}\text{Se}_{27}$ was formed during the decomposition of a quenched sample of SnBi_4Te_7 ^[29] upon repeated heating. For TEM measurements, the powdered sample was drop-cast on a copper grid coated with a holey carbon film. This grid was fixed on a glass capillary for single crystal data collection at the European Synchrotron Radiation Facility (ESRF). For STEM measurements, polycrystalline pieces were embedded in epoxy resin and mechanically cut and thinned to a thickness of $\approx 20 \mu\text{m}$ in the center using a dimple grinder. Electron transparency was achieved by polishing a hole in the center of the disc by Ar-ion milling (Figure A13). Further details are given in the Supporting Information.

Acknowledgements

We gratefully acknowledge beamtime at the ESRF (project CH-4612) and support by V. Dyadkin (ESRF), P. Schultz and S. Schwarzmüller (both Leipzig University) during data collection. We further thank Prof. Dr. Wolfgang Schnick (LMU Munich) for generous support and valuable comments and Dr. Markus Döblinger for taking care of the TEM and helpful discussions. The Deutsche Forschungsgemeinschaft is acknowledged for financial support (project OE530/3-2). Open access funding enabled and organized by Projekt DEAL.

2.2 References

- [1] M. G. Kanatzidis, *Inorg. Chem.* **2017**, *56*, 3158–3173.
- [2] a) T. Zhang, Y. Jiang, Z. Song, H. Huang, Y. He, Z. Fang, H. Weng, C. Fang, *Nature* **2019**, *566*, 475–479; b) D. Kong, Y. Cui, *Nat. Chem.* **2011**, *3*, 845–849.
- [3] Y. L. Chen, J. G. Analytis, J.-H. Chu, Z. K. Liu, S.-K. Mo, X. L. Qi, H. J. Zhang, D. H. Lu, X. Dai, Z. Fang, S. C. Zhang, R. Z. Fisher, Z. Hussain, Z.-X. Shen, *Science* **2009**, *325*, 178–181.
- [4] a) A. Zeugner, F. Nietschke, A. U. B. Wolter, S. Gaß, R. C. Vidal, T. R. F. Peixoto, D. Pohl, C. Damm, A. Lubk, R. Hentrich, S. K. Moser, C. Fornari, C. H. Min, S. Schatz, K. Kißner, M. 3nzelmann, M. Kaiser, F. Scaravaggi, B. Rellinghaus, K. Nielsch, C. Heß, B. Bechner, F. Reinert, H. Bentmann, O. Oeckler, T. Doert, M. Ruck, A. Isaeva, *Chem. Mater.* **2019**, *31*, 2795–2806; b) M. M. Otrokov, I. I. Klimovskikh, H. Bentmann, A. Zeugner, Z. S. Aliev, S. Gaß, A. U. B. Wolter, A. V. Koroleva, D. Estyunin, A. M. Shikin, M. Blanco Rey, M. Hoffmann, A. Y. Vyazovskaya, S. V. Ereemeev, Y. M. Koroteev, I. R. Amiraslanov, M. B. Babanly, N. T. Mamedov, N. A. Abdullayev, V. N. Zverev, B. Bechner, E. F. Schwier, S. Kumar, A. Kimura, L. Petaccia, G. Di Santo, R. C. Vidal, S. Schatz, K. Kiner, C.-H. Min, S. K. Moser, T. R. F. Peixoto, F. Reinert, A. Ernst, P. M. Echenique, A. Isaeva, E. V. Chulkov, **2018**, arxiv.org/abs/1809.07389.
- [5] R. Vilaplana, J. A. Sans, F. J. Manjón, A. Andrada-Chacón, J. Sánchez-Benítez, C. Popescu, O. Gomis, A. L. J. Pereira, B. García-Domene, P. Rodríguez-Hernández, A. Muñoz, D. Daisenberger, O. Oeckler, *J. Alloys Compd.* **2016**, *685*, 962–970.
- [6] M. Samanta, K. Pal, P. Pal, U. V. Waghmare, K. Biswas, *J. Am. Chem. Soc.* **2018**, *140*, 5866–5872.
- [7] L.-D. Zhao, S.-H. Lo, Y. Zhang, H. Sun, G. Tan, C. Uher, C. Wolverton, V. P. Dravid, M. G. Kanatzidis, *Nature* **2014**, *508*, 373–377.
- [8] A. T. Duong, V. Q. Nguyen, G. Duvjir, V. T. Duong, S. Kwon, J. Y. Song, J. K. Lee, J. E. Lee, S. D. Park, T. Min, J. Lee, J. Kim, S. Cho, *Nat. Commun.* **2016**, *7*, 13713.
- [9] M. Kepers, P. M. Konze, S. Maintz, S. Steinberg, A. M. Mio, O. Cojocaru-Mirédin, M. Zhu, M. Meller, M. Luysberg, J. Mayer, M. Wuttig, R. Dronskowski, *Angew. Chem. Int. Ed.* **2017**, *56*, 10204–10208; *Angew. Chem.* **2017**, *129*, 10338–10342.

- [10] W.-W. Xiong, J. Miao, K. Ye, Y. Wang, B. Liu, Q. Zhang, *Angew. Chem. Int. Ed.* **2015**, *54*, 546–550; *Angew. Chem.* **2015**, *127*, 556–560.
- [11] M. G. Kanatzidis, *Acc. Chem. Res.* **2005**, *38*, 359–368.
- [12] J. R. Sootsman, D. Y. Chung, M. G. Kanatzidis, *Angew. Chem. Int. Ed.* **2009**, *48*, 8616–8639; *Angew. Chem.* **2009**, *121*, 8768–8792.
- [13] Y. Feutelais, B. Legendre, N. Rodier, V. Agafonov, *Mater. Res. Bull.* **1993**, *28*, 591–596.
- [14] N. Frangis, S. Kuypers, C. Manolikas, G. Van Tendeloo, J. Van Landuyt, S. Amelinckx, *J. Solid State Chem.* **1990**, *84*, 314–334; note that Amelinckx et al. do not differentiate between possible Te-Bi-Te-Bi-Te-Bi-Bi and a Te-Bi-Te-Bi-Te-Bi-Te sequences and denote both as septuple (7) layers, whereas the nomenclature in this article would call Te-Bi-Te-Bi-Te-Bi-Bi a 52 sequence.
- [15] a) L. E. Shelimova, O. G. Karpinskii, V. S. Zemskov, P. P. Konstantinov, *Inorg. Mater.* **2000**, *36*, 235–242; b) O. G. Karpinskii, L. E. Shelimova, M. A. Kretova, E. S. Avilov, V. S. Zemskov, *Inorg. Mater.* **2003**, *39*, 240 – 246; c) O. G. Karpinskii, L. E. Shelimova, E. S. Avilov, M. A. Kretova, V. S. Zemskov, *Inorg. Mater.* **2002**, *38*, 17–24; d) L. E. Shelimova, O. G. Karpinskii, P. P. Konstantinov, E. S. Avilov, M. A. Kretova, V. S. Zemskov, *Inorg. Mater.* **2004**, *40*, 451–460.
- [16] N. Frangis, S. Kuypers, C. Manolikas, J. Van Landuyt, S. Amelinckx, *Solid State Commun.* **1989**, *69*, 817–819.
- [17] R. S. Rai, P. Korgul, G. Singh, *Acta Crystallogr. Sect. B* **1984**, *40*, 132–138.
- [18] a) I. Kiflawi, S. Mardix, *Acta Crystallogr. Sect. B* **1969**, *25*, 2415–2417; b) V. Medizadeh, S. Mardix, *Acta Crystallogr. Sect. C* **1986**, *42*, 518–519.
- [19] a) B. Pałosz, S. Gierlotka, *Acta Crystallogr. Sect. C* **1983**, *39*, 521–528; b) B. Pałosz, S. Gierlotka, *Acta Crystallogr. Sect. C* **1984**, *40*, 1117–1119.
- [20] B. Pałosz, S. Gierlotka, B. Wiktorowska, D. Dziag, *Acta Crystallogr. Sect. C* **1985**, *41*, 1407–1409.
- [21] A. F. Wells, *Structural Inorganic Chemistry*, Oxford University Press, New York, **1984**.
- [22] R. Terry, D. Vinton, C. D. McMillen, J. W. Kolis, *Angew. Chem. Int. Ed.* **2018**, *57*, 2077–2080; *Angew. Chem.* **2018**, *130*, 2099–2102.

- [23] J. Brugger, T. Armbruster, N. Meisser, C. Hejny, B. Grobety, *Am. Mineral.* **2001**, *86*, 1494–1505.
- [24] a) J. A. Kohn, D. W. Eckart, C. F. Cook, Jr., *Science* **1971**, *172*, 519–525; b) L. A. Kohn, D. W. Eckart, *J. Appl. Phys.* **1965**, *36*, 1171–1172.
- [25] C. Delacotte, G. F. S. Whitehead, M. J. Pitcher, C. M. Robertson, P. M. Sharp, M. S. Dyer, J. Alaria, J. B. Claridge, G. R. Darling, D. R. Allan, G. Winter, M. J. Rosseinsky, *IUCrJ* **2018**, *5*, 681–698.
- [26] I. Orlov, L. Palatinus, A. Arakcheeva, G. Chapuis, *Acta Crystallogr. Sect. B* **2007**, *63*, 703–712.
- [27] L. Elcoro, J. M. Perez-Mato, R. L. Withers, *Acta Crystallogr. Sect. B* **2001**, *57*, 471–484.
- [28] H. Lind, S. Lidin, *Solid State Sci.* **2003**, *5*, 47–57.
- [29] F. Heinke, P. Urban, A. Werwein, C. Fraunhofer, T. Rosenthal, S. Schwarzmüller, D. Souchay, F. Fahrenbauer, V. Dyadkin, G. Wagner, O. Oeckler, *Inorg. Chem.* **2018**, *57*, 4427–4440.
- [30] J. Takagi, Y. Tak8uchi, *Acta Crystallogr. Sect. B* **1972**, *28*, 649–651.
- [31] a) G. B. M. Vaughan, J. P. Wright, A. Bytchkov, C. Curfs, C. Gundlach, M. Orlova, L. Erra, H. Gleyzolle, T. Buslaps, A. Götz, G. Suchet, S. Petitdemange, M. Rossat, L. Margulies, W. Ludwig, A. Snigirev, I. Snigireva, S. Schmidt, H. O. Sørensen, E. M. Lauridsen, U. L. Olsen, J. Oddershede, H. F. Poulsen, *Proc. 31st Risø Int. Symp. Mater. Sci.* **2010**, *521*, 457–476; b) F. Fahrenbauer, T. Rosenthal, T. Schmutzler, G. Wagner, G. B. M. Vaughan, J. P. Wright, O. Oeckler, *Angew. Chem. Int. Ed.* **2015**, *54*, 10020 – 10023; *Angew. Chem.* **2015**, *127*, 10158–10161; c) P. Bielec, R. Nelson, R. P. Stoffel, L. Eisenburger, D. Genther, A.-K. Henß, J. P. Wright, O. Oeckler, R. Dronskowski, W. Schnick, *Angew. Chem. Int. Ed.* **2019**, *58*, 1432 – 1436; *Angew. Chem.* **2019**, *131*, 1446–1450.
- [32] M. M. Stasova, *J. Struct. Chem.* **1967**, *8*, 584 – 589.
- [33] Superspace group $R\bar{3}m(00g)00$, $a = 4.1819(4)$, $c = 5.6528(5)$ Å, $V = 85.61(1)$ Å³, $Z = 3$, $\rho_{\text{diff}} = 7.7857$ g•cm⁻³, $R1$ (all data) = 0.0451, $R1$ [$I > 2\sigma(I)$] = 0.0446, wR (all) = 0.0699, wR [$I > 2\sigma(I)$] = 0.0678, $R_{\text{int}} = 0.0310$, $R_{\sigma} = 0.054$, 12 parameters for 6375 reflections (411 independent). 3D model: space group $R\bar{3}m$, $a = 4.1819(4)$, $c = 282.64(6)$ Å. Further details of the crystal structure investigations are given in the Supporting

Information. Deposition number 1949450 contains the supplementary crystallographic data for this paper. These data are provided free of charge by the joint Cambridge Crystallographic Data Centre and Fachinformationszentrum Karlsruhe Access Structures service.

- [34] C. Pérez Vicente, J. L. Tirado, K. Adouby, J. C. Jumas, A. Abba Touré, G. Kra, *Inorg. Chem.* **1999**, 38, 2131 – 2135.
- [35] S. He, L. Zhu, J. Zhou, Z. Sun, *Inorg. Chem.* **2017**, 56, 11990 – 11997.

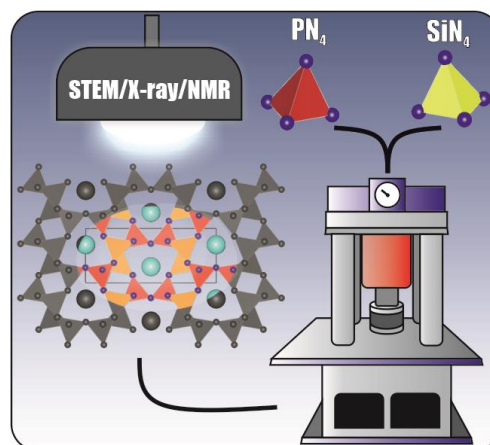
3 High-Pressure High-Temperature Synthesis of Mixed Nitridosilicatephosphates and Luminescence of $AE\text{SiP}_3\text{N}_7:\text{Eu}^{2+}$ ($AE = \text{Sr}, \text{Ba}$)

Lucien Eisenburger, Oliver Oeckler and Wolfgang Schnick

Chem. Eur. J. **2021**, 27, 4461.

DOI: 10.1002/chem.202005495

Abstract: Tetrahedra-based nitrides with network structures have emerged as versatile materials with a broad spectrum of properties and applications. Both nitridosilicates and nitridophosphates are well-known examples of such nitrides that upon doping with Eu^{2+} exhibit intriguing luminescence properties, which makes them attractive for applications. Nitridosilicates and nitridophosphates show manifold



structural variability; however, no mixed nitridosilicatephosphates except SiPN_3 and $\text{SiP}_2\text{N}_4\text{NH}$ have been described so far. The compounds $AE\text{SiP}_3\text{N}_7$ ($AE = \text{Sr}, \text{Ba}$) were synthesized by a high-pressure high-temperature approach using the multianvil technique (8 GPa, 1400–1700 °C) starting from the respective alkaline earth azides and the binary nitrides P_3N_5 and Si_3N_4 . The latter were activated by NH_4F , probably acting as a mineralizing agent. SrSiP_3N_7 and BaSiP_3N_7 were obtained as single crystals. They crystallized in the barylite-10 ($M = \text{Sr}$) and barylite-20 structure types ($M = \text{Ba}$), respectively, with P and Si being occupationally disordered. Cation disorder was further supported by solid-state NMR spectroscopy and energy-dispersive X-ray spectroscopy (EDX) mapping of BaSiP_3N_7 with atomic resolution. Upon doping with Eu^{2+} , both compounds showed blue emission under UV excitation.

3.1 Introduction with Results and Discussion

Emerging environmental consciousness has pushed the development of solid-state lighting solutions forward. The invention of efficient InGaN-based blue LEDs (light-emitting diodes) enabled the development of pc-LEDs (phosphor-converted) with remarkable properties in terms of color temperature, color rendition, and efficacy. Significant improvements in the aforementioned properties were possible due to nitride compounds such as $M_2\text{Si}_5\text{N}_8:\text{Eu}^{2+}$ ($M = \text{Sr}, \text{Ba}$), $M\text{Si}_2\text{O}_2\text{N}_2:\text{Eu}^{2+}$ ($M = \text{Ca}, \text{Sr}, \text{Ba}$), $\text{SrLiAl}_3\text{N}_4:\text{Eu}^{2+}$, and $\text{MAlSiN}_3:\text{Eu}^{2+}$.^[1–4]

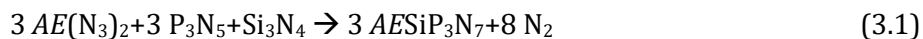
Materials properties concerning solid-state lighting can be tuned by dopant concentration to a limited extent, affecting Stokes shifts in emission spectra, or by a variation of the size of coordination polyhedra by substitution such as introducing Sr on Ba sites. Completely shifted emission properties, however, can only be achieved by a fundamental alteration of the host lattice.^[5, 6]

The main goal of this work was to expand the compositional and structural diversity of tetrahedra-based luminescent materials. Thus, discovery of the title compounds SrSiP_3N_7 and BaSiP_3N_7 opens up the novel compound class of mixed nitridosilicatephosphates, which can now be further explored as innovative host lattices. While nitridosilicates have been investigated thoroughly and nitridophosphates show similar promising structures and properties, only two compounds that contain both SiN_x ($x = 4, 6$) and PN_4 units have been reported so far, that is, SiPN_3 and $\text{SiP}_2\text{N}_4\text{NH}$.^[7–9] The crystal structure of SiPN_3 corresponds to a defect wurtzite-type arrangement with mixed occupation of Si and P at the tetrahedral sites. The crystal structure of $\text{SiP}_2\text{N}_4\text{NH}$ is related to sillimanite-type Al_2SiO_5 . It is built up from edge-sharing SiN_6 octahedra interconnected by all-side vertex-sharing PN_4 tetrahedra. A possible explanation for the challenges concerning syntheses that are involved in the preparation of mixed nitridosilicatephosphates could be the chemical inertness of Si_3N_4 , while P_3N_5 already decomposes at temperatures above 850 °C if no external pressure is applied. As shown in previous publications, according to Le Chatelier's principle, the decomposition of P_3N_5 under the formation of N_2 is suppressed by external pressure.^[10]

NH_4Cl has been successfully employed as a mineralizer facilitating crystal growth of nitridophosphates. HCl formed in situ most likely leads to reversible P–N bond formation and cleavage.^[11, 12] After nitridosilicatephosphates proved to be not accessible with the help of NH_4Cl , changing the mineralizing agent to NH_4F afforded the title compounds $AE\text{SiP}_3\text{N}_7$ ($AE = \text{Sr}, \text{Ba}$). This may be explained by the fact that HF cannot only reversibly cleave and form P–N bonds, but also Si–N bonds. The surface of Si_3N_4 features SiNH_2 groups that can be attacked by F in a nucleophilic substitution.^[13]

The nitridosilicatephosphates $AE\text{SiP}_3\text{N}_7$ ($AE = \text{Sr}, \text{Ba}$) were synthesized by high-pressure high-temperature (HP/HT) reactions at 8 GPa and 1400 °C (Ba) and 1700 °C (Sr), respectively, using a modified Walker-type multianvil apparatus.^[14] The synthesis of SrSiP_3N_7 at temperatures below 1700 °C resulted in samples with significant amounts of unknown side phases. Reactions followed the so-called azide route using P_3N_5 , Si_3N_4 , and the respective

metal azide as starting materials with additional NH_4F (≈ 5 wt %) as a mineralizing agent [Eq. (3.1)]. To investigate luminescence properties, samples with the addition of approximately 1 mol % of EuF_3 (concerning AE^{2+}) to the starting mixture were prepared.



The title compounds were obtained as colorless powders (Eu^{2+} -doped samples of SrSiP_3N_7 show a yellow tint) and showed no sensitivity to air or moisture. More detailed information on the HP/HT synthesis is given in the Supporting Information.

The crystal structures were elucidated by single-crystal X-ray diffraction (SCXRD) using direct methods and least-squares refinement. SrSiP_3N_7 crystallizes in space group $Pmn2_1$ (no. 31) with $Z = 2$. BaSiP_3N_7 crystallizes in space group $Pnma$ (no. 62) with $Z = 4$; details are given in Tables 1 and B2–7. In addition, Rietveld refinements indicate the presence of BaSiP_3N_7 crystallizing in space group $Pmn2_1$ (no. 31) with $Z = 2$ as a side phase. Both compounds are isotypic to the two polymorphs of barylite $\text{BaBe}_2\text{Si}_2\text{O}_7$. SrSiP_3N_7 corresponds to the barylite-10 polymorph, whereas BaSiP_3N_7 features the structure of barylite-20. The structures of barylite-10 and barylite-20 represent the maximum degree of order (MDO) polytypes of their polytype family. Both structures consist of a network of all-vertex-sharing PN_4 and $(\text{Si}_{0.5}\text{P}_{0.5})\text{N}_4$ tetrahedra and elongated square pyramid (J_8) $AE\text{N}_9$ ($AE = \text{Sr}, \text{Ba}$) polyhedra (Figure B1).^[15]

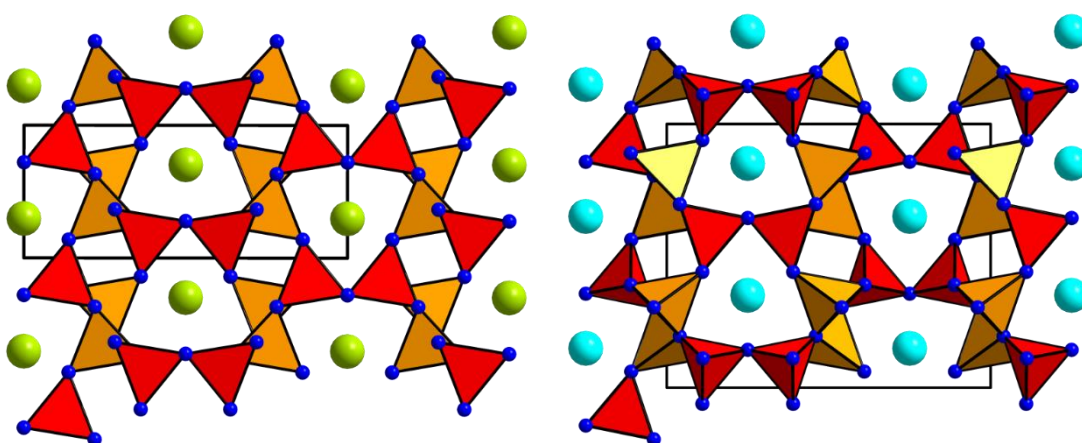


Figure 3.1. Crystal structures of SrSiP_3N_7 (left) and BaSiP_3N_7 (right) both along $[001]$. For SrSiP_3N_7 PN_4 tetrahedra (red) and $(\text{Si}_{0.5}\text{P}_{0.5})\text{N}_4$ (orange) all vertices point in the same direction (behind the plane of projection). For BaSiP_3N_7 the orientation of tetrahedra vertices alternate.

The main difference between the two polymorphs concerns the arrangement of tetrahedra. While in SrSiP_3N_7 all tetrahedra vertices point in the same direction, those in BaSiP_3N_7 alternate, which results in a doubled unit cell with $2b$ (SrSiP_3N_7) = a (BaSiP_3N_7) (Figure 3.1). Although tetrahedra orientation differs in both compounds, the environment of AE atoms is strikingly similar. The tetrahedra connection patterns show that both compounds consist of *dreier*, *vierer*, and *sechser* rings that, apart from slight distortions, are arranged and distributed in the same manner (Figure 3.2), leading to the same topology point symbol $\{3^2.4^3.5.6^4\}\{3^4.4^5.5^4.6^2\}$.^[16] Both compounds exhibit one tetrahedrally coordinated site shared by Si and P, while the other site is solely occupied by P. CSD 2050660 and 2050661 contain supplementary crystallographic data for this paper. These data can be obtained free of charge from FIZ Karlsruhe via www.ccdc.cam.ac.uk/structures. In the case of SrSiP_3N_7 , potential ordering of Si and P was considered by symmetry reduction and refinement of the structure against SCXRD data in the subgroups $P2_1$, Pn , and Pm of space group $Pmn2_1$. However, no indications of complete ordering were found. In all structure models, the volumes of the resulting four symmetrically independent tetrahedra were compared as (P,Si)–N bond lengths were not sufficiently meaningful for discrimination.^[17] This investigation led to two different kinds of tetrahedra.

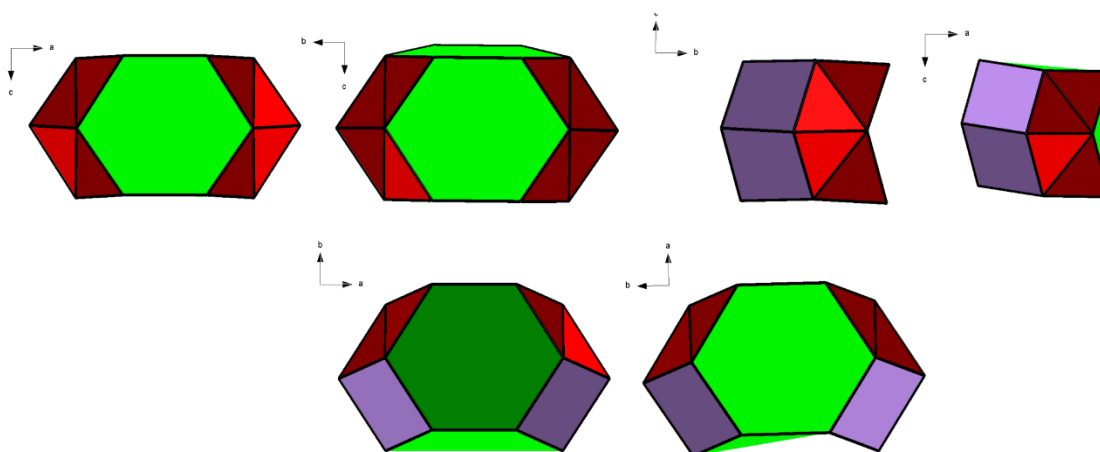


Figure 3.2. Tetrahedra connection patterns of SrSiP_3N_7 (left) and BaSiP_3N_7 (right). Patterns of both compounds show *dreier* (red), *vierer* (lilac), and *sechser* rings (green).

Structure models in subgroups $P2_1$, Pn , and Pm reveal two tetrahedra exhibiting a volume of $2.21\text{--}2.24 \text{ \AA}^3$ that coincides with the volume of PN_4 tetrahedra from known nitridophosphates in literature and corresponds to one site in the final structure model in $Pmn2_1$. The other two

tetrahedra have a volume of 2.37–2.40 Å³, which lies between the volumes of PN_4 (2.13–2.28 Å³) and SiN_4 tetrahedra (2.52–2.76 Å³) (Tables B10 and 11).^[8, 9, 26–28, 18–25] BVS (bond valence sum) calculations performed on all structure models revealed two tetrahedral sites fully occupied by P and two tetrahedral sites occupied by Si and P in a 1:1 ratio (Tables B13–15).^[29] In the case of BaSiP_3N_7 , the ordering of tetrahedra was considered by symmetry reduction and refinement of the structure against SCXRD data in subgroups $Pna2_1$, $P2_1ma$, and $P2_1/c$ of space group $Pnma$. Only subgroups retaining the extinction condition of the a glide planes present in $Pnma$ were taken into account because electron diffraction parallel to $[001]$ showed no violation of the extinction conditions. Additional electron diffraction patterns parallel to $[100]$ showed no violation of the extinction conditions of the n glide, too, further supporting the structure model in space group $Pnma$ (a comparison of experimental diffraction patterns with simulated ones based on the structure model in space group $Pnma$ is given in Figure B5).

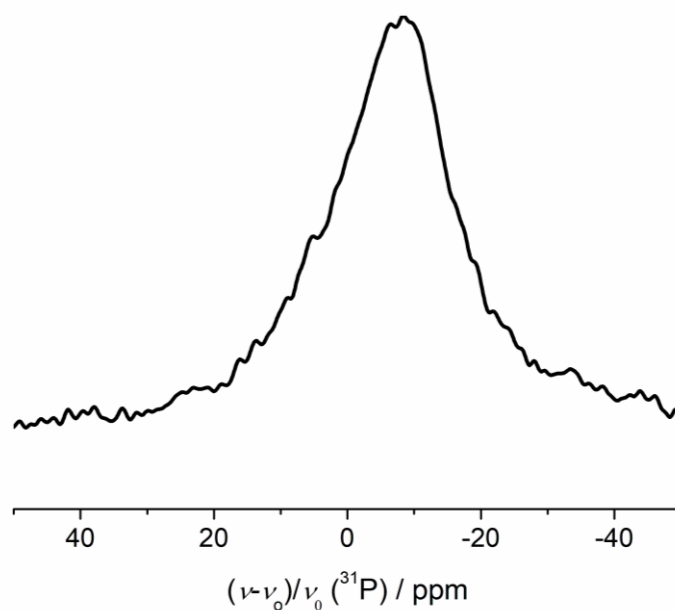


Figure 3.3. ^{31}P NMR spectrum showing one broad signal for BaSiP_3N_7 instead of two signals for the different crystallographic sites most likely due to the occupational disorder

Table 3.1: Crystallographic data of the single-crystal structure refinements of $AE\text{SiP}_3\text{N}_7$ ($AE = \text{Sr}, \text{Ba}$).

Standard deviations are given in parentheses.

formula	SrSiP_3N_7	BaSiP_3N_7
molar mass / $\text{g}\cdot\text{mol}^{-1}$	306.69	356.41
crystal system	orthorhombic	orthorhombic
space group	$Pmn2_1$ (no. 31)	$Pnma$ (no. 62)
lattice parameters / \AA	$a = 11.979(2)$	$a = 9.9048(3)$
	$b = 4.9040(10)$	$b = 12.1858(3)$
	$c = 4.6870(9)$	$c = 4.73580(10)$
cell volume / \AA^3	275.34(10)	571.60(3)
formula units/ unit cell	2	4
density / $\text{g}\cdot\text{cm}^3$	3.699	4.142
μ / mm^{-1}	10.807	7.927
temperature / K	296(2)	297(2)
absorption correction	semiempirical	
radiation	Mo- K_α ($\lambda = 0.71073 \text{ \AA}$)	
F(000)	292	656
θ range / $^\circ$	$3.4 \leq \theta \leq 44.09$	$3.34 \leq \theta \leq 38.44$
total no. of reflections	9890	10523
Independent reflections [$I \geq 2\sigma(I)$ / all]	1253/ 1379	959/ 1128
R_σ, R_{int}	0.0393, 0.0952	0.0234, 0.0481
refined parameters	60	58
Goodness of fit	1.100	1.044
R -values [$I \geq 2\sigma(I)$]	$R_1 = 0.0293$	$R_1 = 0.0261$
	$wR_2 = 0.0731$	$wR_2 = 0.0576$
R -values (all data)	$R_1 = 0.0343$	$R_1 = 0.0340$
	$wR_2 = 0.0750$	$wR_2 = 0.0599$
$\Delta\rho_{\text{max}}, \Delta\rho_{\text{min}}$ / $\text{e}\cdot\text{\AA}^{-3}$	2.18, -1.49	0.81, -1.53

The comparison of resulting tetrahedral volumes showed the same features as for SrSiP_3N_7 (Table B12). BVS calculations performed for the different structure models again suggested two sites completely occupied by P and two sites shared by Si and P (Tables B16–18). The simple approach of comparing tetrahedra volume as a tool for assigning Si and P, which lack scattering contrast, to the respective sites was indeed confirmed by scanning transmission electron microscope energy-dispersive X-ray spectroscopy (STEM-EDX) mapping with atomic resolution

for BaSiP_3N_7 . These data support the model in space group $Pnma$, showing two sites with mixed Si/P occupation (Figure 3.4, enlarged version see Figure B6). This result is also corroborated by ^{31}P solid-state magic angle spinning (MAS)-NMR spectra, which show a broad signal [full width at half-maximum (fwhm) = 19.7 ppm] that is consistent with a disordered model (Figure 3.3, Figure B4).

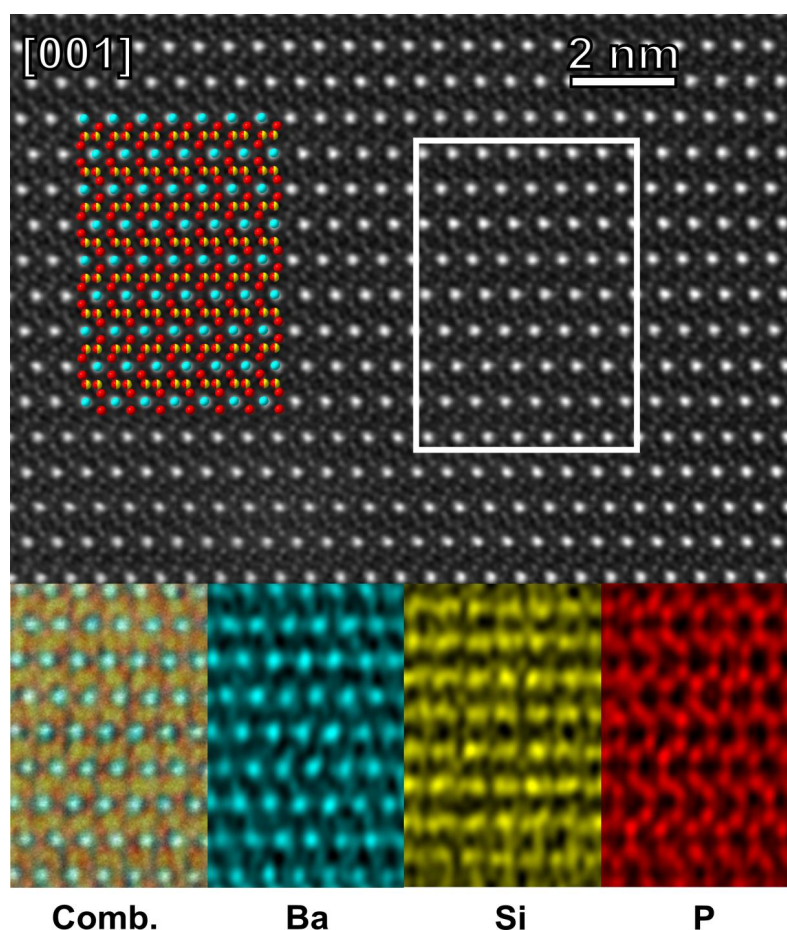


Figure 3.4. Atomic resolution STEM EDX of BaSiP_3N_7 along $[001]$. STEM HAADF image (top) with structure overlay (Ba cyan, P red, Si yellow). The inset shows the corresponding area for EDX maps (bottom) with a combined color map, Ba map (cyan), Si map (yellow), and P map (red).

Line broadening in the NMR spectrum is probably due to disorder in the second coordination sphere of P atoms. In contrast, ordered nitrides like BP_3N_6 or $\text{Li}_{12}\text{P}_3\text{N}_9$ show very narrow signals in their ^{31}P NMR spectra.^[8, 30]

In both structures, the connectivity of the tetrahedra via their vertices can explain the presence of different tetrahedral volumes. The smaller tetrahedra have three vertices occupied by twofold bridging nitrogen atoms $\text{N}^{[2]}$ and one vertex occupied by a threefold bridging nitrogen atom $\text{N}^{[3]}$. The larger tetrahedra, in contrast, feature two vertices occupied

by $\text{N}^{[2]}$ and two vertices occupied by $\text{N}^{[3]}$. Chemical analysis by EDX agrees with the sum formulas. Due to ambiguous O contents (as indicated by EDX measurements) either surface hydrolysis or slight compositional variations cannot completely be ruled out so that a phase width according to $AE\text{Si}_{1+x}\text{P}_{3-x}\text{N}_{7-x}\text{O}_x$ ($AE = \text{Sr}, \text{Ba}$) with $x < 1$ could also be considered (Table B8) even though some analyses show no O.

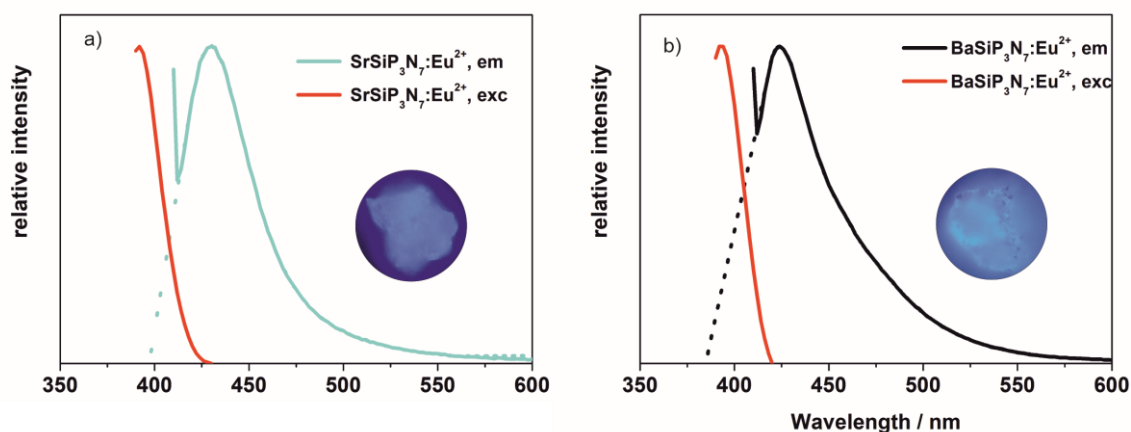


Figure 3.5. Emission spectra of a) $\text{SrSiP}_3\text{N}_7:\text{Eu}^{2+}$ (blue) and b) $\text{BaSiP}_3\text{N}_7:\text{Eu}^{2+}$ (black), measured data in solid lines and extrapolation in dotted lines, respective excitation spectra (red) (insets: micrographs of luminescent particles).

Upon doping with Eu^{2+} , both compounds emit blue light under UV excitation. Luminescence spectra show emission maxima of $\lambda_{\text{max}} = 430$ nm for $\text{SrSiP}_3\text{N}_7:\text{Eu}^{2+}$ and $\lambda_{\text{max}} = 424$ nm for $\text{BaSiP}_3\text{N}_7:\text{Eu}^{2+}$ upon excitation with $\lambda_{\text{exc}} = 400$ nm. The emission curves were extrapolated to give an estimate of the fwhm, which amount to 45 nm (2404 cm^{-1}) for $\text{SrSiP}_3\text{N}_7:\text{Eu}^{2+}$ and 53 nm (2731 cm^{-1}) for $\text{BaSiP}_3\text{N}_7:\text{Eu}^{2+}$ (Figure 3.5). The corresponding Stokes shifts are 38 nm (2254 cm^{-1}) for $\text{SrSiP}_3\text{N}_7:\text{Eu}^{2+}$ and 32 nm (1925 cm^{-1}) for $\text{BaSiP}_3\text{N}_7:\text{Eu}^{2+}$. The presence of a single narrow emission band for both phosphors can be explained by the emission properties of Eu^{2+} and the presence of a single crystallographic site for the alkaline earth ions suitable for doping with Eu^{2+} with $AE\text{-N}$ distances ranging from $2.696(3)\text{--}3.270(3) \text{ \AA}$ (SrSiP_3N_7) to $2.872(3)\text{--}3.230(3) \text{ \AA}$ (BaSiP_3N_7). The similarity of emission properties in terms of fwhm are most likely to be explained by the $\text{P-Si}_{0.5}\text{P}_{0.5}$ „cages“ around the AE position, which are very similar. Thus, only minute deviations are caused by different AE cation sizes even though both structures differ with respect to their space groups, unit cell volumes, and tetrahedra orientations.

Conclusions

High-pressure high-temperature synthesis with the addition of NH_4F is a suitable approach to the synthesis of mixed nitridosilicatephosphates. The compounds $AE\text{SiP}_3\text{N}_7$ ($AE = \text{Sr}, \text{Ba}$) adopt the structure types of the two polymorphs of the mineral barylite. This structure type has not been observed for nitride compounds so far. Although silicon and phosphorus exhibit little contrast in X-ray diffraction, the comparison of polyhedra volumes led to structure models with an occupationally disordered site that also persists if potential ordering is considered by symmetry reduction. The disordered model for BaSiP_3N_7 is further supported by solid-state NMR spectroscopy. Scanning transmission electron microscopy energy-dispersive X-ray spectroscopy (STEM-EDX) mapping with atomic resolution enables to directly observe said disorder, which is additionally in accordance with systematic absences observed in electron diffraction patterns. Therefore, nitridosilicatephosphates have the potential to significantly diversify the structural chemistry of nitrides. Their suitability as host lattices for rare-earth activator ions seems especially intriguing considering the emission properties of other compounds with multiple tetrahedra centers like $\text{CaAlSiN}_3\text{:Eu}^{2+}$, $\text{Sr}[\text{Li}_2\text{Al}_2\text{O}_2\text{N}_2]\text{:Eu}^{2+}$, or $\text{Sr}[\text{LiAl}_3\text{N}_4]\text{:Eu}^{2+}$.^[2, 31, 32]

Acknowledgements

Financial support by the Deutsche Forschungsgemeinschaft DFG (projects SCHN 377/18-1 and OE 513/6-1) is gratefully acknowledged. We thank Dr. Peter Mayer for single-crystal data collection, Dr. Thomas Bräuniger, Christian Minke, and Dr. Otto Zeman for NMR measurements, Lisa Gamperl (all at Department of Chemistry at LMU Munich) for SEM investigations and Dr. Philipp Strobel (Lumileds Phosphor Center Aachen) for luminescence measurements and helpful discussions.

3.2 References

- [1] M. Zeuner, S. Pagano, W. Schnick, *Angew. Chem. Int. Ed.* **2011**, *50*, 7754–7775; *Angew. Chem.* **2011**, *123*, 7898–7920.
- [2] P. Pust, P. J. Schmidt, W. Schnick, *Nat. Mater.* **2015**, *14*, 454–458.
- [3] K. Uheda, N. Hirosaki, Y. Yamamoto, A. Naito, T. Nakajima, H. Yamamoto, *Electrochem. Solid-State Lett.* **2006**, *9*, H22.
- [4] L. Wang, R. J. Xie, T. Suehiro, T. Takeda, N. Hirosaki, *Chem. Rev.* **2018**, *118*, 1951–2009.
- [5] Y. Q. Li, A. C. A. Delsing, G. De With, H. T. Hintzen, *Chem. Mater.* **2005**, *17*, 3242–3248.
- [6] F. Wang, W. Wang, L. Zhang, J. Zheng, Y. Jin, J. Zhang, *RSC Adv.* **2017**, *7*, 27422–27430.
- [7] H. P. Baldus, W. Schnick, J. Lücke, U. Wannagat, G. Bogedain, *Chem. Mater.* **1993**, *5*, 845–850.
- [8] S. Vogel, A. T. Buda, W. Schnick, *Angew. Chem. Int. Ed.* **2018**, *57*, 13202–13205; *Angew. Chem.* **2018**, *130*, 13386–13389.
- [9] S. Wendl, L. Eisenburger, P. Strobel, D. Günther, J. P. Wright, P. J. Schmidt, O. Oeckler, W. Schnick, *Chem. A Eur. J.* **2020**, *26*, 7292–7298.
- [10] S. D. Kloß, W. Schnick, *Angew. Chem. Int. Ed.* **2019**, *58*, 7933–7944; *Angew. Chem.* **2019**, *131*, 8015–8027.
- [11] A. Marchuk, F. J. Pucher, F. W. Karau, W. Schnick, *Angew. Chem. Int. Ed.* **2014**, *53*, 2469–2472; *Angew. Chem.* **2014**, *126*, 2501–2504.
- [12] D. Baumann, W. Schnick, *Inorg. Chem.* **2014**, *53*, 7977–7982.
- [13] D. Martin Knotter, T. J. J. (Dee) Denteneer, *J. Electrochem. Soc.* **2001**, *148*, F43.
- [14] H. Huppertz, *Z. Kristallogr.* **2004**, *219*, 330–338.
- [15] S. Merlino, C. Biagioni, E. Bonaccorsi, N. V. Chukanov, I. V. Pekov, S. V. Krivovichev, V. N. Yakovenchuk, T. Armbruster, *Mineral. Mag.* **2015**, *79*, 145–155.
- [16] V. A. Blatov, A. P. Shevchenko, D. M. Proserpio, *Cryst. Growth Des.* **2014**, *14*, 3576–3586.
- [17] K. Momma, F. Izumi, *J. Appl. Crystallogr.* **2011**, *44*, 1272–1276.

- [18] T. Schlieper, W. Milius, W. Schnick, *Z. Anorg. Allg. Chem.* **1995**, 621, 1380–1384.
- [19] H. Yamane, T. Nagura, T. Miyazaki, *Acta Crystallogr. Sect. E* **2014**, 70, i23–i24.
- [20] C. Schmolke, D. Bichler, D. Johrendt, W. Schnick, *Solid State Sci.* **2009**, 11, 389–394.
- [21] G. Pilet, H. A. Höpfe, W. Schnick, S. Esmailzadeh, *Solid State Sci.* **2005**, 7, 391–396.
- [22] M. Woike, W. Jeitschko, *Inorg. Chem.* **1995**, 34, 5105–5108.
- [23] J. David, Y. Laurent, J.-P. Charlot, J. Lang, *Bull. Soc. Fr. Mineral. Cristallogr.* **1973**, 96, 21–24.
- [24] F. W. Karau, W. Schnick, *J. Solid State Chem.* **2005**, 178, 135–141.
- [25] S. D. Kloß, N. Weidmann, R. Niklaus, W. Schnick, *Inorg. Chem.* **2016**, 55, 9400–9409.
- [26] K. Landskron, W. Schnick, *J. Solid State Chem.* **2001**, 156, 390–393.
- [27] R. Marchand, P. L’Haridon, Y. Laurent, *J. Solid State Chem.* **1982**, 43, 126–130.
- [28] K. Landskron, E. Irran, W. Schnick, *Chem. Eur. J.* **1999**, 5, 2548–2553.
- [29] N. E. Brese, M. O’Keeffe, *Acta Crystallogr. Sect. B* **1991**, 47, 192–197.
- [30] E. Bertschler, R. Niklaus, W. Schnick, *Chem. Eur. J.* **2017**, 23, 9592–9599.
- [31] X. Piao, K. I. Machida, T. Horikawa, H. Hanzawa, Y. Shimomura, N. Kijima, *Chem. Mater.* **2007**, 19, 4592–4599.
- [32] G. J. Hoerder, M. Seibald, D. Baumann, T. Schröder, S. Peschke, P. C. Schmid, T. Tyborski, P. Pust, I. Stoll, M. Bergler, C. Patzig, S. Reißaus, M. Krause, L. Berthold, T. Höche, D. Johrendt, H. Huppertz, *Nat. Commun.* **2019**, 10, 1–9.

4 Nitridic Analogs of Micas $AE\text{Si}_3\text{P}_4\text{N}_{10}(\text{NH})_2$ ($AE = \text{Mg}, \text{Mg}_{0.94}\text{Ca}_{0.06}, \text{Ca}, \text{Sr}$)

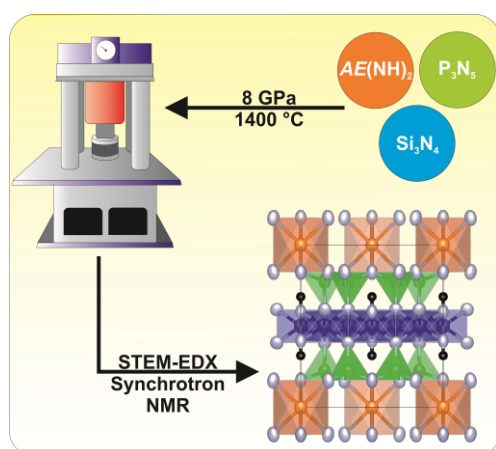
Lucien Eisenburger, Philipp Strobel, Peter J. Schmidt, Thomas Bräuniger, Jonathan Wright, Eleanor Lawrence Bright, Carlotta Giacobbe, Oliver Oeckler and Wolfgang Schnick

Angew. Chem. Int. Ed. **2022**, 61, e202114902.

Angew. Chem. **2022**, 134, e202114902.

DOI: 10.1002/anie.202114902

DOI: 10.1002/ange.202114902



Abstract: We present the first nitridic analogs of micas, namely $AE\text{Si}_3\text{P}_4\text{N}_{10}(\text{NH})_2$ ($AE = \text{Mg}, \text{Mg}_{0.94}\text{Ca}_{0.06}, \text{Ca}, \text{Sr}$), which were synthesized under high-pressure high-temperature conditions at 1400 °C and 8 GPa from the refractory nitrides P_3N_5 and Si_3N_4 , the respective alkaline earth amides, implementing NH_4F as a mineralizer. The crystal structure was elucidated by single-crystal

diffraction with microfocused synchrotron radiation, energy-dispersive X-ray spectroscopic (EDX) mapping with atomic resolution, powder X-ray diffraction, and solid-state NMR. The structures consist of typical tetrahedra–octahedra–tetrahedra (T–O–T) layers with P occupying T and Si occupying O layers, realizing the rare motif of sixfold coordinated silicon atoms in nitrides. The presence of H, as an imide group forming the $\text{SiN}_4(\text{NH})_2$ octahedra, is confirmed by SCXRD, MAS-NMR, and IR spectroscopy. Eu^{2+} -doped samples show tunable narrow-band emission from deep blue to cyan (451–492 nm).

4.1 Introduction with Results and Discussion

Silicates offer a broad range of structural diversity ranging from discrete SiO_4 tetrahedra to ribbons, sheets and frameworks. These structural motifs are unmatched in their diversity as compared to other tetrahedral anions like phosphates, sulfates or vanadates. Such structural diversity accompanied by chemical stability and their mechanical properties allows silicates to be employed in several applications, e.g. dielectrics, construction materials, fire retardants,

and as host compounds for activator ions in luminescent materials.^[1-3] The plethora of structural motifs is enabled by the feasibility of SiO_4 tetrahedra to condense in a manifold of patterns. Whereas oxygen atoms rarely interconnect more than two tetrahedra, in silicate-related structures, nitrogen atoms may even bridge up to four tetrahedra, which for example form star-shaped units and even edge-sharing tetrahedra have been observed. This has led to a multitude of compounds with very diverse structures. The manifold of structures has also been observed when tetrahedra centers were exchanged for P in so-called nitridophosphates. Many of these compounds exhibit promising properties for application in phosphor-converted LEDs.^[4, 5] Structural diversification can be furthermore enhanced by mixed networks in terms of oxo- and nitridosilicates alike as displayed by aluminosilicates and their related nitridoaluminosilicates.

Syntheses of nitridosilicates and -phosphates are typically performed at high temperatures ($>1000\text{ }^\circ\text{C}$) and, especially for nitridophosphates often under high pressures ($>4\text{ GPa}$).^[6] With the recent discovery of $\text{SiP}_2\text{N}_4\text{NH}$, a significant step was taken to accommodate the high-pressure motif of SiN_6 octahedra.^[7-9] Sixfold coordinated Si atoms are also very rare in oxidic compounds where examples include rutile-type stishovite, a high-pressure polymorph of SiO_2 , or $\text{K}_2\text{Si}[\text{Si}_3\text{O}_9]$.^[10, 11] Despite the aforementioned structural diversity, the observation of mineral-analogous nitridosilicates and -phosphates is uncommon if the charge of the counterion is to be preserved. This is simply explained by the high anionic charge of the nitride networks. The incorporation of Si and P allows mitigating the high anionic charge thus enabling the syntheses of mineral analogous compounds like $AE\text{SiP}_3\text{N}_7$ ($AE = \text{Sr}, \text{Ba}$), which crystallize isotypic to the mineral barylite ($\text{BaBe}_2\text{Si}_2\text{O}_7$).^[12] Synthetic challenges targeting nitridosilicate phosphates arise from the decomposition of P_3N_5 at temperatures above $850\text{ }^\circ\text{C}$ and the relative chemical inertness of Si_3N_4 . This problem has been overcome by high partial pressures of HCl ($\text{SiP}_2\text{N}_4\text{NH}$) or employing small amounts of NH_4F ($AE\text{SiP}_3\text{N}_7$ ($AE = \text{Sr}, \text{Ba}$)) as mineralizing agents and applying high external pressures of 8 GPa at $1100\text{--}1700\text{ }^\circ\text{C}$ realized by a multianvil press.^[7, 12] As shown previously, NH_4F seems to be able to reversibly cleave the bonds in refractory nitrides allowing straightforward synthesis of nitridic compounds.^[12, 13] NH_4F however cannot be found in the reaction products as side reactions with the BN crucible material seem possible.

Following the NH_4F mineralizer-assisted approach we have now found a simple way to access mica-like layered silicon imidonitridophosphates[†] $AE\text{Si}_3\text{P}_4\text{N}_{10}(\text{NH})_2$ ($AE = \text{Mg}, \text{Mg}_{0.94}\text{Ca}_{0.06}, \text{Ca}, \text{Sr}$) at high-pressure/high-temperature conditions (details are described in Ref. 14) from the respective AE -amide, P_3N_5 , and Si_3N_4 with NH_4F as a mineralizer according to Equation (4.1). To further investigate luminescence properties, Eu^{2+} -doped samples have been synthesized by addition of ≈ 1 mole% of EuF_3 (with respect to AE) to the starting mixtures.



The reactions yielded the title compounds as colorless, microcrystalline powders, which are stable towards air and moisture. Samples of $AE\text{Si}_3\text{P}_4\text{N}_{10}(\text{NH})_2$ ($AE = \text{Mg}_{0.94}\text{Ca}_{0.06}, \text{Ca}, \text{Sr}$) doped with Eu^{2+} are yellow. More details on the synthesis are given in the Supporting Information. The crystal structure of $\text{CaSi}_3\text{P}_4\text{N}_{10}(\text{NH})_2$, was elucidated by single-crystal diffraction (SCXRD) with microfocused synchrotron radiation ($C2/m$ (no. 12), $a = 4.91790(10)$, $b = 8.5159(2)$, $c = 9.8267(2)$ Å, $\beta = 99.476(3)^\circ$, $Z = 2$, $R_1 = 0.0805$). For this purpose, pre-characterized crystallites on TEM-grids (Figure C1) were used at beamline ID11 of the ESRF (Grenoble, France).^[15–17] Data from two twinned crystallites were merged to increase completeness. Structure elucidation from single-crystal X-ray diffraction (SCXRD) enabled Rietveld refinements, also for the compounds with $AE = \text{Mg}, \text{Mg}_{0.94}\text{Ca}_{0.06}$, and Sr . The silicon imidonitridophosphates $AE\text{Si}_3\text{P}_4\text{N}_{10}(\text{NH})_2$ are isotypic to e.g. clintonite, a brittle mica with composition $\text{Ca}(\text{Mg}, \text{Al})_3(\text{Al}_3\text{Si})\text{O}_{10}(\text{OH})_2$.^[18] Single-crystal diffraction patterns of $\text{CaSi}_3\text{P}_4\text{N}_{10}(\text{NH})_2$ show diffuse streaks and signs of twinning, which are typical for mica-type materials.^[19, 20] Twinning by rotation of 120° around $[310]$ for both crystals was taken into account and the position of H was determined from difference Fourier maps. The N–H bond length was restrained at 0.89 Å.^[21]

Elemental compositions of the title compounds were confirmed by X-ray spectroscopy (EDX) (Table C6) and phase compositions of respective samples were analyzed by Rietveld refinements (Figures C2–S5, Tables C7–S11). The structures of $AE\text{Si}_3\text{P}_4\text{N}_{10}(\text{NH})_2$ ($AE = \text{Mg}, \text{Mg}_{0.9}\text{Ca}_{0.1}, \text{Ca}, \text{Sr}$) consist of layers of $AE\text{N}_6$ octahedra, PN_4 tetrahedra and $\text{SiN}_4(\text{NH})_2$ octahedra following the general scheme of tetrahedra–octahedra–tetrahedra (T – O – T) arrangement for mica-like structures (Figure 4.1).^[22, 23]

[†] According to IUPAC nomenclature the compounds are called silicon imidonitridophosphate in this reprint.

Interatomic distances P–N range from 1.614(6) to 1.702(5) Å with the latter corresponding to a surprisingly long P–N bond that is comparable to those in compounds like $\text{Sr}_3\text{P}_3\text{N}_7$ (1.683(11) Å), Mg_2PN_3 (1.693(5) Å) and $\beta\text{-HP}_4\text{N}_7$ (1.697(2) Å).^[21, 24, 25] Bond lengths Si–N range between 1.837(8) and 1.923(7) Å; similar to those reported for the high-pressure compounds $\gamma\text{-Si}_3\text{N}_4$ (1.8626(1) Å) or $\text{SiP}_2\text{N}_4\text{NH}$ (1.8031(9)–2.0146(10) Å).^[7–9]

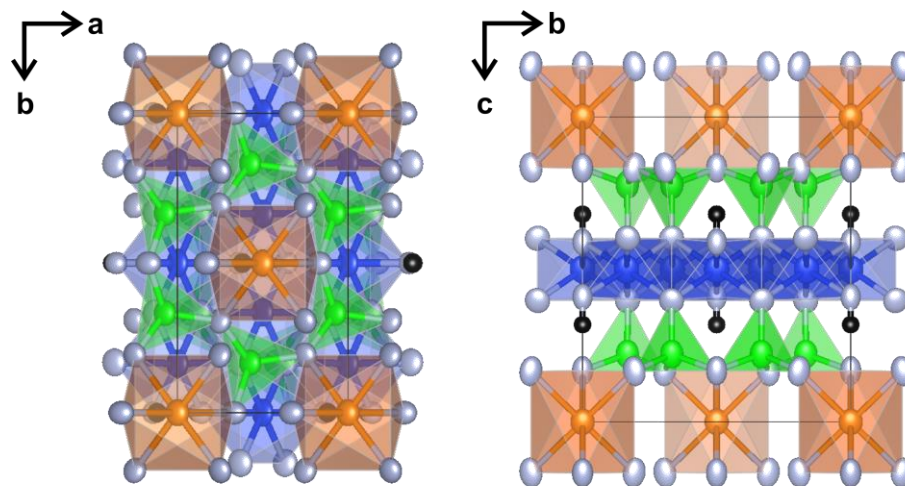


Figure 4.1: Structure of $\text{CaSi}_3\text{P}_4\text{N}_{10}(\text{NH})_2$ with coordination polyhedra of Ca displayed in orange, P green, Si blue, N gray and H black. Displacement ellipsoids are displayed with 99% probability (except for H).

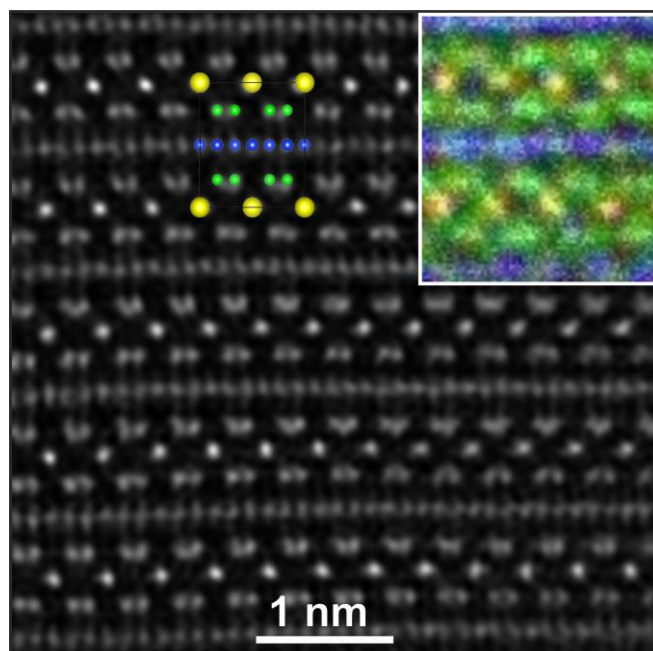


Figure 4.2: STEM HAADF image of $\text{CaSi}_3\text{P}_4\text{N}_{10}(\text{NH})_2$ along [100] with structure projection (top middle) and EDX map top right. Ca yellow, P green and Si blue. H and N were omitted for clarity. Further experimental details are given in the Supporting Information.

The title compounds incorporate the alkaline earth metals Mg, Ca and Sr, which results in the lattice parameter c varying by ≈ 0.8 Å. Synthesis aiming at $\text{BaSi}_3\text{P}_4\text{N}_{10}(\text{NH})_2$, however, yielded BaSiP_3N_7 . Possibly, Ba cannot be accommodated, which can be explained by the limited space along $[100]$ and $[010]$ compared with micas with high Ba-content like kinoshitalite $(\text{BaMg}_3[\text{Al}_2\text{Si}_2\text{O}_{10}](\text{OH})_2)$.^[26]

As the correct assignment of atom types to crystallographic positions is impeded by the similar X-ray scattering form factors of Si and P, STEM-EDX mappings with atomic resolution were performed (Figure 4.2). The overlay of STEM-EDX maps with an HAADF image shows the ordering of Si and P and led to the conclusion that the title compounds consist of PN_4 tetrahedra and $\text{SiN}_4(\text{NH})_2$ octahedra.

IR spectra (Figure C17) show absorption bands for each of the title compounds at 3313–3334 cm^{-1} , indicating the presence of N–H stretching vibrations.^[27] The positions of the corresponding H atom were localized from single-crystal diffraction data and confirmed by solid-state NMR as imide groups adjacent to Si, forming $\text{SiN}_4(\text{NH})_2$ octahedra.

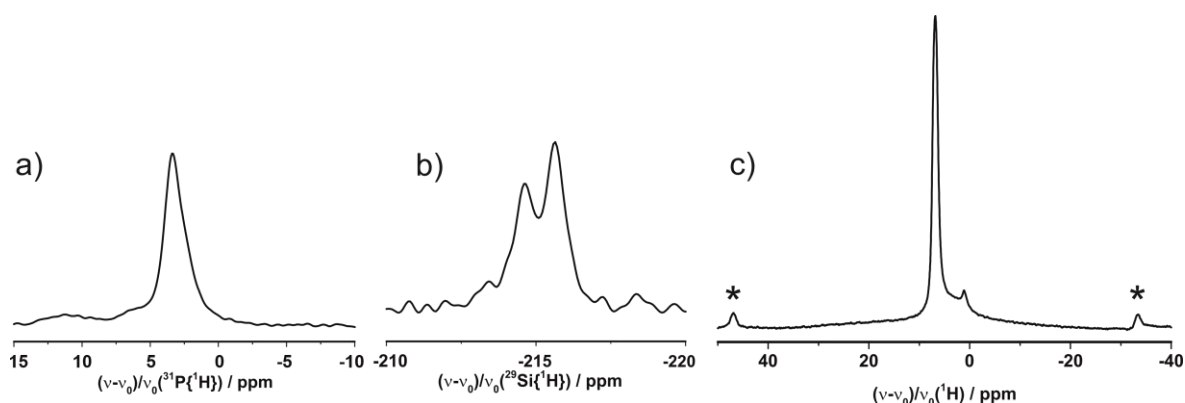


Figure 4.3: Solid-state NMR spectra of $\text{CaSi}_3\text{P}_4\text{N}_{10}(\text{NH})_2$ at 20 kHz MAS speed. One signal in the $^{31}\text{P}\{^1\text{H}\}$ (a) and two signals in the $^{29}\text{Si}\{^1\text{H}\}$ (b) spectra agree with the structure model. ^1H NMR reveals one intense signal of the imide group of $\text{CaSi}_3\text{P}_4\text{N}_{10}(\text{NH})_2$ while the weaker one belongs to $\text{MgSi}_3\text{P}_4\text{N}_{10}(\text{NH})_2$. Rotation sidebands are marked with asterisks. Full spectra are provided in the Supporting Information.

All signals in ^1H , ^{31}P , cross-polarized (CP) $^1\text{H} \rightarrow ^{31}\text{P}$ and $^1\text{H} \rightarrow ^{29}\text{Si}$ (indicated by the notation $\{^1\text{H}\}$) $^{31}\text{P}\{^1\text{H}\}$ and $^{29}\text{Si}\{^1\text{H}\}$ MAS NMR spectra of $\text{CaSi}_3\text{P}_4\text{N}_{10}(\text{NH})_2$ shown in Figure 4.3 are consistent with the structure model. Additional weak peaks are attributed to the side phase $\text{MgSi}_3\text{P}_4\text{N}_{10}(\text{NH})_2$, which forms by reaction with MgO spacer disks used in the multianvil assembly. The sharp ^{31}P signal at 3.5 ppm corresponds to the single Wyckoff site and agrees

with NMR data for P in $\text{SiP}_2\text{N}_4\text{NH}$. The persistence of this signal in the $^{31}\text{P}\{^1\text{H}\}$ measurements indicate the vicinity of H to the P site. $^{29}\text{Si}\{^1\text{H}\}$ spectra show two signals with an estimated integral ratio of 1 : 2 centered at 214.6 and 215.6 ppm, respectively. Although the use of integrated intensities is problematic for CP spectra, it is warranted here in good approximation as the average distances of the ^{29}Si to the four neighboring protons in the structure are similar, see Table C13. The two ^{29}Si resonances can accordingly be attributed to the Wyckoff sites 2*d* and 4*h* occupied by sixfold coordinated Si, comparable to $\gamma\text{-Si}_3\text{N}_4$ and $\text{SiP}_2\text{N}_4\text{NH}$ with resonances at -225 and -205 ppm, respectively.^[7, 28] Again, the presence of both signals in cross-polarization experiments indicates the vicinity of H to both Si sites. ^1H NMR shows a strong signal at 6.8 ppm, consistent with H localized above the $\text{SiN}_4(\text{NH})_2$ layers and centered in the void formed by the PN_4 *sechser* rings. BVS calculations (Table C14) are in agreement with the structure model.^[29]

The thermal behavior of $\text{CaSi}_3\text{P}_4\text{N}_{10}(\text{NH})_2$ was analyzed by temperature-dependent powder X-ray diffraction (PXRD), revealing thermal stability up to 900 °C with exceptionally low thermal expansion of the unit cell volume (Figure C10–S12).

The direct optical band gaps of the undoped title compounds derived from Tauc plots amount to 4.6, 4.2 and 3.9 eV for $AE = \text{Mg}, \text{Ca}, \text{Sr}$, respectively, with decreasing band gap towards heavier homologs (Figure C18).^[30, 31] The large band gaps are beneficial concerning luminescence of Eu^{2+} -doped samples. The only reported luminescent imidonitride so far is $\text{BaP}_6\text{N}_{10}\text{NH}:\text{Eu}^{2+}$ with $\lambda_{\text{max}} = 451$ nm and a FWHM of 52 nm (2423 cm^{-1}).^[32] $\text{SrSi}_3\text{P}_4\text{N}_{10}(\text{NH})_2:\text{Eu}^{2+}$ and $\text{CaSi}_3\text{P}_4\text{N}_{10}(\text{NH})_2:\text{Eu}^{2+}$ show narrow emission bands upon excitation with UV light at $\lambda_{\text{max}} = 451$ nm and 478 nm with FWHMs of 26 nm (1300 cm^{-1}) and 30 nm (1298 cm^{-1}), respectively (Figure 4.4).

$\text{MgSi}_3\text{P}_4\text{N}_{10}(\text{NH})_2$ showed no luminescence since the smaller size of the coordination polyhedron impedes Eu^{2+} incorporation. However, intrigued by the natural solid solution series of micas like the phlogopite–aspidolite series $(\text{K}(\text{Mg})_3\text{AlSi}_3\text{O}_{10}(\text{F},\text{OH})_2\text{-NaMg}_3\text{AlSi}_3\text{O}_{10}(\text{OH})_2)$,^[33] we have synthesized the compound $\text{Mg}_{1-x}\text{Ca}_x\text{Si}_3\text{P}_4\text{N}_{10}(\text{NH})_2:\text{Eu}^{2+}$ ($x \approx 0.06$). Since the Ca content in this compound is below 0.5 at%, the Ca content was estimated by extrapolation of unit cell volumes between the end members $\text{MgSi}_3\text{P}_4\text{N}_{10}(\text{NH})_2$ and $\text{CaSi}_3\text{P}_4\text{N}_{10}(\text{NH})_2$. This compound showed the most red-shifted, narrow emission of the series at $\lambda_{\text{max}} = 492$ nm with an FWHM of 35 nm (1444 cm^{-1}).

Low-temperature emission spectra were recorded at 6 K (Figure C19), revealing the zero-phonon-line and giving insights into the vibrational modes of the layered crystal structure with an estimated phonon frequency of ca. 430 cm^{-1} . The rather high phonon-frequency may explain the strong thermal quenching (Figure C20).

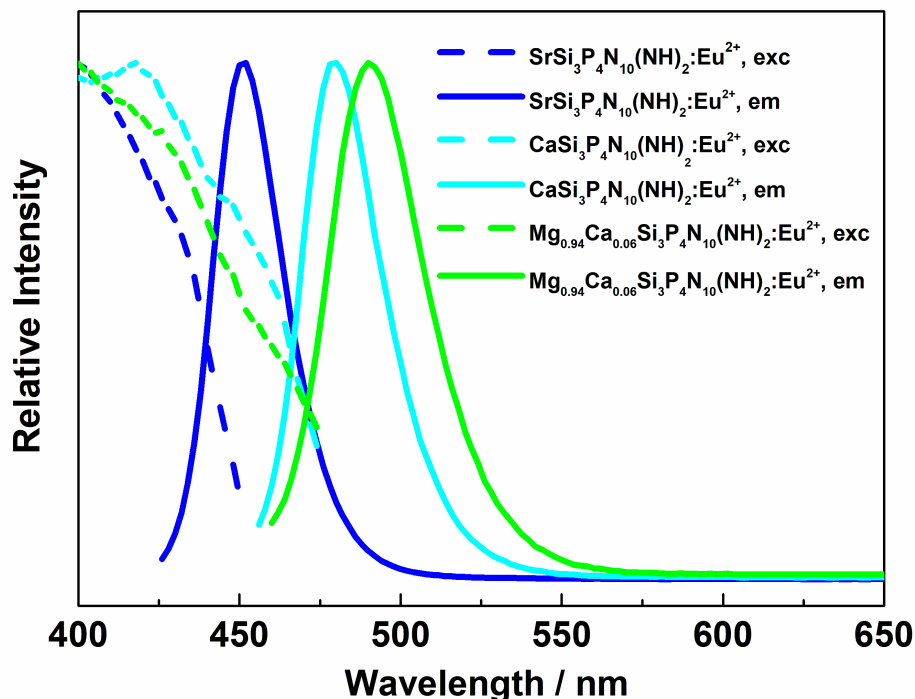


Figure 4.4: Emission spectra of $AE\text{Si}_3\text{P}_4\text{N}_{10}(\text{NH})_2$ ($AE = \text{Mg}_{0.94}\text{Ca}_{0.06}, \text{Ca}, \text{Sr}$) in solid lines. Emission maxima and fwhms are: $\text{Mg}_{0.94}\text{Ca}_{0.06}$ 492 nm, 35 nm (1444 cm^{-1}), Ca 478 nm, 30 nm (1298 cm^{-1}) and Sr 451 nm, 26 nm (1300 cm^{-1}). Corresponding excitation spectra in dashed lines.

Summarizing, based on the approach of employing NH_4F as a mineralizing agent, we were able to synthesize the first nitridic analogous mica through HP/HT syntheses. Structure determination was performed by a combination of diffraction of microfocused synchrotron radiation on twinned crystallites, STEM-EDX and solid-state NMR. Eu^{2+} -doped samples showed narrow band emission from blue (451 nm) to cyan (492 nm). These findings represent the possibility of mimicking one of the most abundant and important aluminum silicates offering new scope for structural diversity and materials properties of nitrides. We expect that nitridic micas can act as model compounds to investigate the influence of aliovalent substitution of the cations and the influence of mixed anionic frameworks on physical properties such as luminescence and dielectric constants, e.g., by exchange of the

imide group against OH groups or fluoride as this compositional range is already observed in natural micas.

Acknowledgements

Financial support by the Deutsche Forschungsgemeinschaft (DFG, SCHN 377/18-1, OE 513/6-1) is gratefully acknowledged. We thank Christian Minke for the acquisition of NMR data, SEM and EDX investigations. Furthermore, we are thankful for beamtime at the ESRF for the acquisition of microfocused single-crystal diffraction data (project CH-5663).

4.2 References

- [1] O. Kazmina, E. Lebedeva, N. Mitina, A. Kuzmenko, *J. Coat. Technol. Res.* **2018**, *15*, 543–554.
- [2] C. G. Low, Q. Zhang, *Small* **2012**, *8*, 2178–2183.
- [3] M. Zhao, H. Liao, M. S. Molokeev, Y. Zhou, Q. Zhang, Q. Liu, Z. Xia, *Light: Sci. Appl.* **2019**, *8*, 38.
- [4] L. Wang, R. J. Xie, T. Suehiro, T. Takeda, N. Hirotsaki, *Chem. Rev.* **2018**, *118*, 1951–2009.
- [5] M. Zeuner, S. Pagano, W. Schnick, *Angew. Chem. Int. Ed.* **2011**, *50*, 7754–7775; *Angew. Chem.* **2011**, *123*, 7898–7920.
- [6] S. D. Klotz, W. Schnick, *Angew. Chem. Int. Ed.* **2019**, *58*, 7933–7944; *Angew. Chem.* **2019**, *131*, 8015–8027.
- [7] S. Vogel, A. T. Buda, W. Schnick, *Angew. Chem. Int. Ed.* **2019**, *58*, 3398–3401; *Angew. Chem.* **2019**, *131*, 3436–3439.
- [8] A. Zerr, G. Miehe, G. Serghiou, M. Schwarz, E. Kroke, R. Riedel, H. Fieß, P. Kroll, R. Boehler, *Nature* **1999**, *400*, 340–342.
- [9] M. Schwarz, G. Miehe, A. Zerr, E. Kroke, B. T. Poe, H. Fuess, R. Riedel, *Adv. Mater.* **2000**, *12*, 883–887.
- [10] W. Sinclair, A. E. Ringwood, *Nature* **1978**, *272*, 714–715.
- [11] N. Kinomura, S. Kume, M. Koizumi, *Mineral. Mag.* **1975**, *40*, 401–404.
- [12] L. Eisenburger, O. Oeckler, W. Schnick, *Chem. Eur. J.* **2021**, *27*, 4461–4465.
- [13] L. Eisenburger, V. Weippert, O. Oeckler, W. Schnick, *Chem. Eur. J.* **2021**, *27*, 14184–14188.
- [14] H. Huppertz, *Z. Kristallogr.* **2004**, *219*, 330–338.
- [15] J. Wright, C. Giacobbe, M. Majkut, *Curr. Opin. Solid State Mater. Sci.* **2020**, *24*, 100818.

- [16] F. Fahrnbauer, T. Rosenthal, T. Schmutzler, G. Wagner, G. B. M. Vaughan, J. P. Wright, O. Oeckler, *Angew. Chem. Int. Ed.* **2015**, 54, 10020–10023; *Angew. Chem.* **2015**, 127, 10158–10161.
- [17] Deposition Number 2096670 contains the supplementary crystallographic data for this paper. These data are provided free of charge by the joint Cambridge Crystallographic Data Centre and Fachinformationszentrum Karlsruhe Access Structures service www.ccdc.cam.ac.uk/structures. Further details on the structure determination are given in the Supporting Information.
- [18] E. H. Kisi, J. A. A. Crossley, S. Myhra, M. W. Barsoum, *J. Phys. Chem. Solids* **1998**, 59, 1437–1443.
- [19] M. Nespolo, G. Ferraris, H. Takeda, *Acta Crystallogr. Sect. A* **2000**, 56, 132–148.
- [20] H. Kalo, W. Milius, M. Bräu, J. Breu, *J. Solid State Chem.* **2013**, 198, 57–64.
- [21] M. Mallmann, C. Maak, R. Niklaus, W. Schnick, *Chem. Eur. J.* **2018**, 24, 13963–13970.
- [22] R. M. Hezen, C. W. Bunn, *Am. Mineral.* **1973**, 58, 889–900.
- [23] E. W. Radoslovich, *Acta Crystallogr.* **1960**, 13, 919–932.
- [24] M. Mallmann, S. Wendl, P. Strobel, P. J. Schmidt, W. Schnick, *Chem. Eur. J.* **2020**, 26, 6257–6263.
- [25] D. Baumann, W. Schnick, *Inorg. Chem.* **2014**, 53, 7977–7982.
- [26] E. Gnos, T. Armbruster, *Am. Mineral.* **2000**, 85, 242–250.
- [27] K. Nakamoto, *Infrared and Raman Spectra of Inorganic and Coordination Compounds*, Wiley, Hoboken, **2009**, p. 388.
- [28] T. Sekine, M. Tansho, M. Kanzaki, *Appl. Phys. Lett.* **2001**, 78, 3050–3051.
- [29] N. E. Brese, M. O’Keeffe, *Acta Crystallogr. Sect. B* **1991**, 47, 192–197.
- [30] J. Tauc, R. Grigorovici, A. Vancu, *Phys. Status Solidi* **1966**, 15, 627–637.
- [31] E. A. Davis, N. F. Mott, *Philos. Mag.* **1970**, 22, 903–922.

- [32] S. Wendl, L. Eisenburger, M. Zipkat, D. Günther, J. P. Wright, P. J. Schmidt, O. Oeckler, W. Schnick, *Chem. Eur. J.* **2020**, 26, 5010–5016.
- [33] G. Tischendorf, H.-J. Förster, B. Gottesmann, M. Rieder, *Mineral. Mag.* **2007**, 71, 285–320.

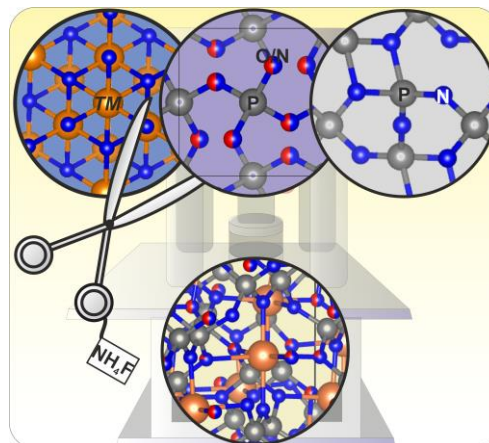
5 High-Pressure Synthesis of $\text{Sc}_5\text{P}_{12}\text{N}_{23}\text{O}_3$ and $\text{Ti}_5\text{P}_{12}\text{N}_{24}\text{O}_2$ by Activation of Binary Nitrides ScN and TiN with NH_4F

Lucien Eisenburger, Valentin Weippert, Oliver Oeckler and Wolfgang Schnick

Chem. Eur. J. **2021**, 27, 14184.

DOI: 10.1002/chem.202101858

Abstract: Multinary transition metal nitrides and oxonitrides are a versatile and intriguing class of compounds. However, they have been investigated far less than pure oxides. The compounds $\text{Sc}_5\text{P}_{12}\text{N}_{23}\text{O}_3$ and $\text{Ti}_5\text{P}_{12}\text{N}_{24}\text{O}_2$ have now been synthesized from the binary nitrides ScN and TiN, respectively, by following a high-pressure high-temperature approach at 8 GPa and 1400 °C. NH_4F acts as a mineralizing agent that



supports product formation and crystallization. The starting materials ScN and TiN are seemingly an uncommon choice because of their chemical inertness but, nevertheless, react under these conditions. $\text{Sc}_5\text{P}_{12}\text{N}_{23}\text{O}_3$ and $\text{Ti}_5\text{P}_{12}\text{N}_{24}\text{O}_2$ crystallize isotypically with $\text{Ti}_5\text{B}_{12}\text{O}_{26}$, consisting of solely vertex-sharing $\text{P}(\text{O}/\text{N})_4$ tetrahedra forming two independent interpenetrating diamond-like nets that host $\text{TM}(\text{O}/\text{N})_6$ ($\text{TM} = \text{Sc}, \text{Ti}$) octahedra. $\text{Ti}_5\text{P}_{12}\text{N}_{24}\text{O}_2$ is a mixed-valence compound and shows ordering of Ti^{3+} and Ti^{4+} ions.

5.1 Introduction with Results and Discussion

A plethora of nitridophosphates was discovered in the last decades. However, only few examples containing transition metals have been described so far which is rather intriguing bearing the ongoing research on transition metal phosphates and their applications in mind.^[1–5] Oxonitridophosphates like $M^{\text{I}}M^{\text{III}}\text{P}_3\text{O}_9\text{N}$ ($M^{\text{I}} = \text{Na}, \text{K}$, $M^{\text{III}} = \text{Al}, \text{Ga}, \text{Cr}, \text{Fe}, \text{Mn}$) were the first compounds paving the way for transition metal (oxo)nitridophosphates.^[6,7] By using high-pressure conditions accessible by Walker-type multianvil presses, compounds like MnP_2N_4 , CdP_2N_4 and Zn_2PN_3 were synthesized. The metal-containing starting materials were either the *TM* azides (Cd), metal powders (Cd, Mn), or binary nitride (Zn).^[8–11] Despite these achievements, no systematic access to this class of compounds was reported as illustrated by

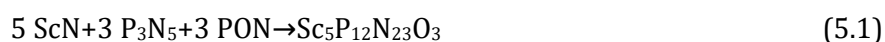
the different starting materials. Common chemicals such as azides and nitrides are either too sensitive and detonate on impact or are too inert, respectively. The first systematic approach to a variety of *TM* compounds is represented by metathesis reactions under high-pressure high-temperature conditions as shown for MP_8N_{14} ($M = \text{Fe, Co, Ni}$), $M_{1-x}PO_{3+4x}N_{1-4x}$ ($x \approx 0.05$), $M_{0.75}PO_4$ ($M = \text{Zr, Hf}$) and $Hf_{9-x}P_{24}N_{52-4x}O_{4x}$ ($x \approx 1.84$).^[12–15]

High-pressure metathesis with the formation of lithium halides from $LiPN_2$ and *TM* halides, however, features inherent drawbacks. Like many HP/HT syntheses, this approach typically yields microcrystalline powders which impede precise structure elucidation by conventional single-crystal X-ray diffraction. The addition of Li can also pose a problem if the latter is incorporated unintentionally, especially in presence of heavy metal atoms. This combination is rather problematic in terms of structure determination by X-ray methods as it is hard to distinguish between heavy metal vacancies or occupational disorder of the heavy metal and Li.

To facilitate crystal growth of nitridophosphates in high-pressure high-temperature reactions, the addition of small amounts of NH_4Cl to the mixture of starting materials as mineralizer proved to be successful. NH_4Cl most likely aids in reaction and crystal growth by reversible P–N bond cleavage and formation.^[16] As shown for group 1, 2 and 13 elements, this kind of activation seems sufficient to provide access to a number of different structures and compounds.^[17–19] As previously shown for $AESiP_3N_7$ ($AE = \text{Sr, Ba}$), the capability of NH_4Cl is limited as some starting materials such as Si_3N_4 are less reactive and the decomposition, as well as activation temperatures of the starting materials, may differ significantly; for example, thermal decomposition of P_3N_5 may compete with the activation of Si_3N_4 .^[20] The question arose if previous findings on the stability of transition metal nitrides remain valid if the mineralizing agent is changed. The starting materials ScN and TiN were chosen because of their refractory character and notorious inertness. For example, TiN is used as a wear- and heat-resistant coating for drill heads.^[21] Etching of TiN films is heavily investigated in semiconductor fabrication. Solutions for etching consisting of a source of hydrogen fluoride and an oxidizing agent have proven to be successful in reducing TiN film thickness. The oxidizing agent in these cases is needed to oxidize Ti^{3+} to Ti^{4+} which forms volatile TiF_4 , in contrast to non-volatile TiF_3 .^[22] As the volatility of the fluoride is not an issue in HP/HT syntheses, and we assumed a similar behavior for ScN, we explored the capability of NH_4F as

a safe and convenient HF source in reactions yielding the transition-metal oxonitridophosphates Sc₅P₁₂N₂₃O₃ and Ti₅P₁₂N₂₄O₂.

Both compounds were synthesized at 1400 °C and 8 GPa by using a modified Walker-type multianvil apparatus.^[23] Reactions followed the so-called nitride-route using P₃N₅ and TMN (*TM* = Sc, Ti) with additional NH₄F as a mineralizing agent [Eqs. (5.1) and (5.2)]. PON or TiO₂ were added as oxygen sources. The synthesis of Ti₅P₁₂N₂₄O₂, however, was performed with only 0.8 equivalents of TiO₂ as stoichiometric amounts lead to microcrystalline samples and split reflections in the PXRD possibly due to excess oxygen from surface hydrolysis of the BN crucible.



Both reactions yielded moisture- and air-resistant crystalline powders with gray and black color for Sc₅P₁₂N₂₃O₃ and Ti₅P₁₂N₂₄O₂, respectively. More detailed information on the synthesis is given in the Supporting Information.

Structure elucidation was performed by single-crystal X-ray diffraction (SCXRD). Deposition Numbers 2084626 (for Sc₅P₁₂N₂₃O₃) and 2084627 (for Ti₅P₁₂N₂₄O₂) contain the supplementary crystallographic data for this paper. These data are provided free of charge by the joint Cambridge Crystallographic Data Centre and Fachinformationszentrum Karlsruhe.

Both compounds are isotypic and crystallize in space group *I*4₁/*acd* (no. 142) with *Z* = 8 (Table 5.1). Additional Rietveld refinements indicate that the title compounds are the main constituents of the obtained samples (Figures D2 and D3, Table D9). Both compounds are isotypic to Ti₅B₁₂O₂₆.^[24] The transition metals are coordinated octahedrally by O/N. The TM1(O/N)₆ octahedra share one common edge and form pairs in contrast to the TM2(O/N)₆ octahedra, which are not condensed (Figure 5.1).

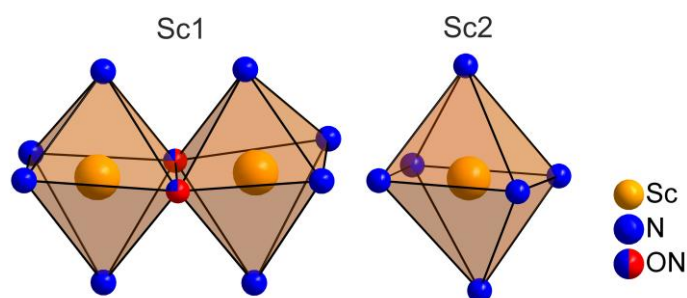


Figure 5.1. Edge-sharing ScO_{0.75}N_{5.25} and isolated ScN₆ octahedra.

Table 5.1. Crystallographic data for the single-crystal structure refinements of Sc₅P₁₂N₂₃O₃ and Ti₅P₁₂N₂₄O₂. Standard deviations are given in parentheses.

formula	Sc ₅ P ₁₂ N ₂₃ O ₃	Ti ₅ P ₁₂ N ₂₄ O ₂
molar mass / g·mol ⁻¹	966.67	979.38
crystal system	tetragonal	
space group	<i>I</i> 4 ₁ / <i>acd</i> (no. 142)	
lattice parameters / Å	<i>a</i> = 12.3598(2) <i>c</i> = 24.0151(4)	<i>a</i> = 12.1214(2) <i>c</i> = 23.8458(5)
cell volume / Å ³	3668.66(13)	3503.62(14)
formula units/ unit cell	8	
density / g·cm ³	3.500	3.713
μ / mm ⁻¹	2.893	3.369
temperature / K	296(2)	298(2)
absorption correction	semiempirical	
radiation	Mo-K α (λ = 0.71073 Å)	
F(000)	3760	3792
θ range / °	3.3 – 36.3	2.9 – 33.1
total no. of reflections	66300	52537
Indep. reflections [$I \geq 2\sigma(I)$ / all]	1971 / 2226	1567 / 1676
R_{σ} , R_{int}	0.0158, 0.0616	0.0108, 0.0353
refined parameters	100	99
Goodness of fit	1.187	1.432
R-values [$I \geq 2\sigma(I)$]	R_1 = 0.0210 wR_2 = 0.0474	R_1 = 0.0222 wR_2 = 0.0680
R-values (all data)	R_1 = 0.0264 wR_2 = 0.0489	R_1 = 0.0240 wR_2 = 0.0690
$\Delta\rho_{\text{max}}$, $\Delta\rho_{\text{min}}$ / e·Å ⁻³	0.552 / -0.715	0.921 / -1.636

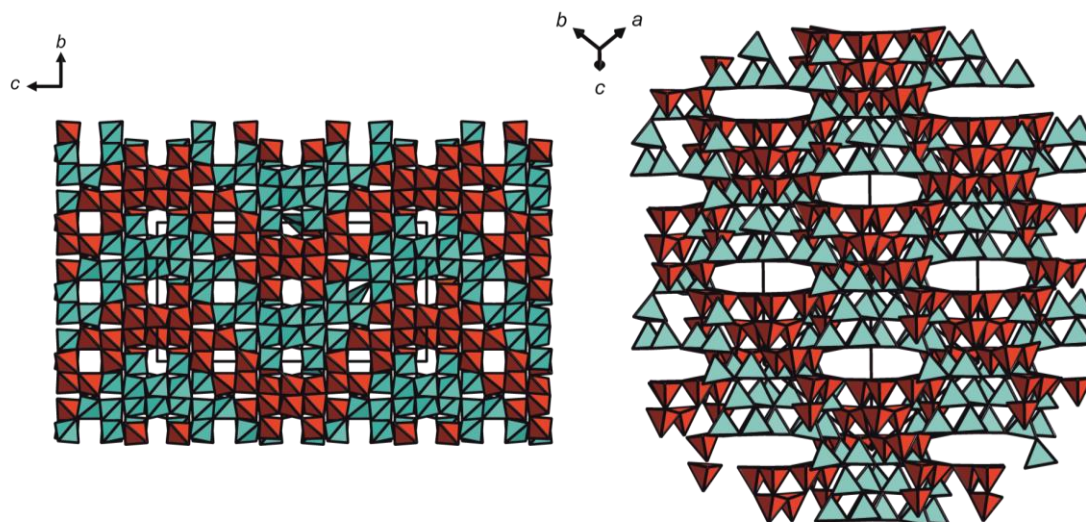


Figure 5.2 Structure projections viewed from [100] (left) and [111] (right). The different diamond-like nets of tetrahedra are colored in red or blue, respectively. *TM* atoms are omitted for clarity.

The $\text{P}(\text{O}/\text{N})_4$ network consists of edge-sharing tetrahedra forming truncated, hollow supertetrahedra which in turn form two separate interpenetrating networks (Figure 5.2). As differentiation between O and N is not unambiguous from X-ray data, and ordering of O and N is not possible in terms of charge neutrality, mixed occupied sites were assigned by considering a combination of bond lengths, bond valence sums and charge neutrality. Following this combination, the position O5/N5 and N2 in $\text{Sc}_5\text{P}_{12}\text{N}_{23}\text{O}_3$ both showed potential mixed occupation according to BVS but position O5/N5 was considered more likely because of the short P–O/N bond lengths of 1.5722(9) Å and N2 forming unusually large Sc–N distances explained in the following. In $\text{Ti}_5\text{P}_{12}\text{N}_{24}\text{O}_2$ assigning mixed occupied positions led to positions O2/N2, O5/N5 and O6/N6 fully consistent with BVS calculations as only these positions showed deviations from the ideal value of 3 for N. Distances *TM*–O/N are between 2.1421(9)–2.4424(9) Å for Sc–O/N and 2.0435(11)–2.2911(11) Å for Ti–O/N (Tables D6 and D7). Both compounds exhibit rather large interatomic distances concerning the *TM*2 position. In the equatorial plane of the *TM*2(O/N)₆ octahedron, the distances Sc2–N2 (2.4424(9) Å) deviate quite significantly from those in ScN (2.25 Å).^[25] The Ti2 position exhibits distances Ti–(O_{0.15}N_{0.85}) of 2.2911(11) Å which are also larger than expected with respect to TiN or rutile-type TiO₂, where they are 2.13 and 1.81–2.06 Å, respectively.^[26,27] The long interatomic distances result in a “rattling” effect which is reflected by low BVS values for these positions

and their rather large and prolate displacements ellipsoids (Figure D1). The BVS values are 2.42 for Sc2 and 2.64 for Ti2 instead of the expected values of 3 for Sc and 4 for Ti2.

The chemical compositions of Sc₅P₁₂N₂₃O₃ and Ti₅P₁₂N₂₄O₂ are supported by energy-dispersive X-ray spectroscopy (Table D8) and FTIR spectra indicate the absence of N–H groups (Figure D4). Scanning transmission electron microscope high-angle annular dark-field (STEM-HAADF) images correspond well to structure projections (Figure 5.3).

In order to confirm the presence of both Ti³⁺ and Ti⁴⁺ in Ti₅P₁₂N₂₄O₂, UV-Vis absorption spectra and magnetic measurements were performed. UV-Vis spectra show a broad absorption band centered at 420 nm, which corresponds well with the presence of Ti³⁺ (Figure D6).^[28] Figure 5.4 shows the magnetic susceptibility with a linear paramagnetic behavior for temperatures >200 K. The fit indicates an effective paramagnetic moment of $\mu_{\text{eff}} = 1.7(1) \mu_{\text{B}}$ for each Ti cation on Wyckoff position 32 *g* assuming Ti⁴⁺ on Wyckoff position 8*b*. This is in agreement with the theoretical spin-only value for Ti³⁺ with $\mu_{\text{eff}} = 1.73 \mu_{\text{B}}$.^[29] Below 200 K, the curve deviates from Curie–Weiss behavior with a continuously increasing magnetic moment. Magnetization isotherms at 300 K with purely paramagnetic behavior and with a small saturation effect at 2 K towards higher fields are shown in the bottom part of Figure 5.4.

In analogy to Ti₅B₁₂O₂₆, we could assign crystallographic sites for Ti³⁺ and Ti⁴⁺ according to the presence of both valence states.^[24] Although the similarity of the ordering of Ti³⁺ and Ti⁴⁺ is quite remarkable given the fact that the composition of the tetrahedral network is completely altered.

The optical bandgap of Ti₅P₁₂N₂₄O₂ was approximated by converting reflectance spectra to the Kubelka-Munk function and calculating a Tauc plot under the assumption of a direct bandgap. Linear regression between 2.1 and 3.1 eV was used to determine the inflection point yielding a bandgap of about 1.6 eV.^[30,31] In the same way, the optical bandgap of Sc₅P₁₂N₂₃O₃ was estimated by linear regression between 4.0 and 4.5 eV and determined as a direct bandgap of 3.8 eV (Figure D7).

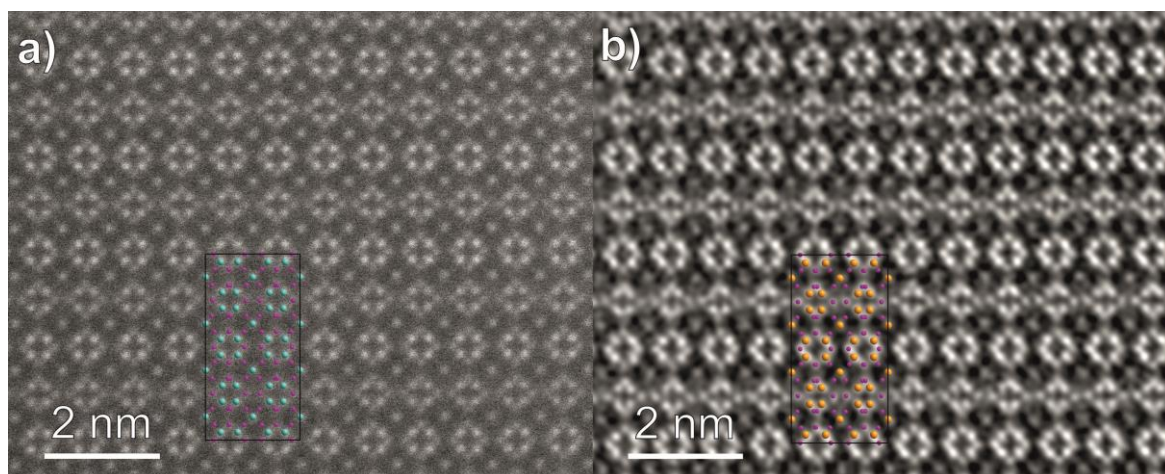


Figure 5.3. STEM-HAADF images of $\text{Ti}_5\text{P}_{12}\text{N}_{24}\text{O}_2$ (a) and $\text{Sc}_5\text{P}_{12}\text{N}_{23}\text{O}_3$ (b) with structure projections as overlays (Ti blue, Sc orange, P violet, O/N omitted for clarity)

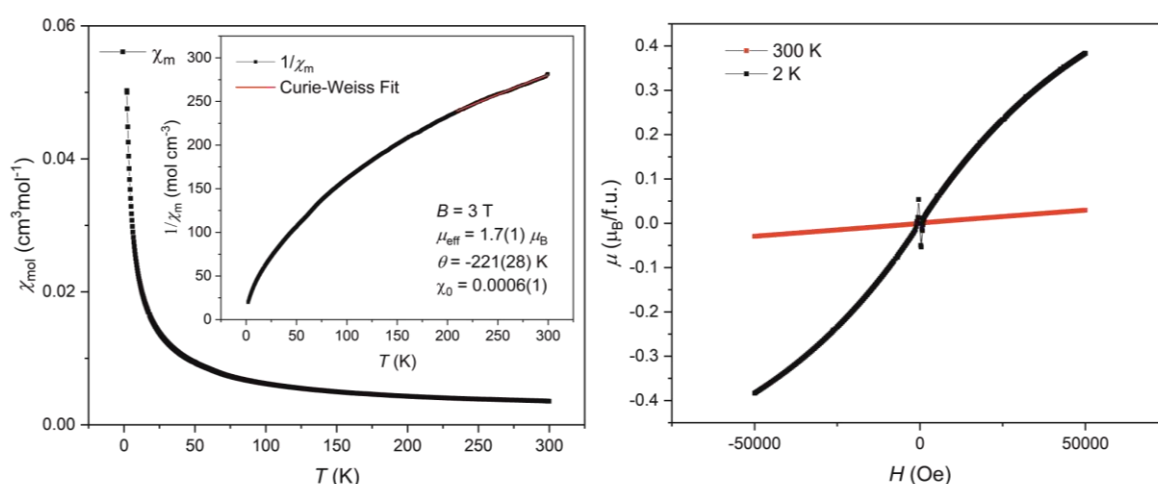


Figure 5.4. Magnetic susceptibility of $\text{Ti}_5\text{P}_{12}\text{N}_{24}\text{O}_2$ and inverse magnetic susceptibility (inset) with an extended Curie-Weiss fit (red) (left) and Magnetic isotherm (right) of $\text{Ti}_5\text{P}_{12}\text{N}_{24}\text{O}_2$ at 300 (red) and 2 K (black) (bottom). At low field strengths, it reveals a small superconducting impurity of most likely TiN ($T_c = 5.6$ K).^[5]

Conclusion

The oxonitridophosphates $\text{Ti}_5\text{P}_{12}\text{N}_{24}\text{O}_2$ and $\text{Sc}_5\text{P}_{12}\text{N}_{23}\text{O}_3$ have been synthesized with NH_4F as a mineralizing agent by high-pressure high-temperature synthesis. The use of NH_4F as a mineralizing agent seems promising to access a variety of yet unknown compounds. The mechanistic reasons for the apparent superiority of NH_4F in contrast to NH_4Cl , still need to be investigated and will certainly be interesting. The presence of Ti^{3+} and Ti^{4+} in $\text{Ti}_5\text{P}_{12}\text{N}_{24}\text{O}_2$ was

derived from crystal-chemical considerations and confirmed by magnetic measurements as well as UV-Vis spectroscopy.

The easy accessibility of *TM* oxonitridophosphates from binary nitrides constitutes a significant progress in the exploration of multinary nitride network structures. This, in turn, is now offering a new scope of properties for nitridophosphates like magnetic properties for spintronic applications as diluted magnetic semiconductors, for example, by substoichiometric doping with *TM*.^[33] The incorporation of *TM* in nitridophosphates also allows the metal cations to be mixed-valent, as shown for Ti₅P₁₂N₂₄O₂, which could also be formulated as Ti^{III}₄Ti^{IV}P₅N₂₄O₂ for clarification. This leads to significantly smaller bandgaps compared to group 1 or group 2 nitridophosphates, which, so far, result in ultrawide-bandgap semiconductors. Research on Ti₅P₁₂N₂₄O₂ regarding solar power harvesting and photocatalysis seems intriguing judging by its bandgap of 1.6 eV and the fact that TiO₂ and TiN are both intensively investigated in those fields.^[34–37]

The next obstacle to overcome are syntheses of oxygen-free *TM* nitrides, by employing NH₄F and the binary *TM* nitrides. Thus, delivering straightforward access to a group of multinary nitrides which are, despite their projected potential applications, scarcely investigated.

Acknowledgements

Financial support by the Deutsche Forschungsgemeinschaft (DFG, SCHN 377/18-1, OE 513/6-1) is gratefully acknowledged. We thank Dr. Peter Mayer for single-crystal data collection, Dr. Steffen Schmidt and Lisa Gamperl for SEM investigations and Prof. Dr. Dirk Johrendt for his support and enabling us to perform magnetic measurements.

5.2 References

- [1] H. S. Ahn, T. D. Tilley, *Adv. Funct. Mater.* **2013**, *23*, 227–233.
- [2] B. Lung-Hao Hu, F. Y. Wu, C. Te Lin, A. N. Khlobystov, L. J. Li, *Nat. Commun.* **2013**, *4*, 1–7.
- [3] X. Shen, Q. Zhou, M. Han, X. Qi, B. Li, Q. Zhang, J. Zhao, C. Yang, H. Liu, Y.-S. Hu, *Nat. Commun.* **2021**, *12*, 2848.
- [4] S. Y. Chung, J. T. Bloking, Y. M. Chiang, *Nat. Mater.* **2002**, *1*, 123–128.
- [5] B. Kang, G. Ceder, *Nature* **2009**, *458*, 190–193.
- [6] S. D. Klotz, W. Schnick, *Angew. Chem Int. Ed.* **2019**, *58*, 7933–7944; *Angew. Chem.* **2019**, *131*, 9158–9161.
- [7] W. Feldmann, *Z. Chem.* **1987**, *27*, 182–183.
- [8] S. J. Sedlmaier, M. Eberspächer, W. Schnick, *Z. Anorg. Allg. Chem.* **2011**, *637*, 362–367.
- [9] F. Karau, O. Oeckler, F. Schäfers, R. Niewa, W. Schnick, *Z. Anorg. Allg. Chem.* **2007**, *633*, 1333–1338.
- [10] F. J. Pucher, F. Hummel, W. Schnick, *Eur. J. Inorg. Chem.* **2015**, *2015*, 1886–1891.
- [11] F. J. Pucher, F. W. Karau, J. Schmedt auf der Günne, W. Schnick, *Eur. J. Inorg. Chem.* **2016**, *2016*, 1497–1502.
- [12] S. D. Klotz, A. Weis, S. Wandelt, W. Schnick, *Inorg. Chem.* **2018**, *57*, 4164–4170.
- [13] S. D. Klotz, S. Wandelt, A. Weis, W. Schnick, *Angew. Chem. Int. Ed.* **2018**, *57*, 3192–3195; *Angew. Chem.* **2018**, *130*, 3246–3249.
- [14] S. D. Klotz, O. Janka, T. Block, R. Pöttgen, R. Glaum, W. Schnick, *Angew. Chem. Int. Ed.* **2019**, *58*, 4685–4689; *Angew. Chem.* **2019**, *131*, 4733–4737.
- [15] S. D. Klotz, N. Weidmann, W. Schnick, *Eur. J. Inorg. Chem.* **2017**, *2017*, 1930–1937.
- [16] D. Baumann, W. Schnick, *Inorg. Chem.* **2014**, *53*, 7977–7982.
- [17] S. Wendl, L. Eisenburger, P. Strobel, D. Günther, J. P. Wright, P. J. Schmidt, O. Oeckler,

- W. Schnick, *Chem. Eur. J.* **2020**, *26*, 7292–7298.
- [18] A. Marchuk, V. R. Celinski, J. Schmed auf der Gönne, W. Schnick, *Chem. Eur. J.* **2015**, *21*, 5836–5842.
- [19] L. Neudert, F. Heinke, T. Bräuniger, F. J. Pucher, G. B. Vaughan, O. Oeckler, W. Schnick, *Chem. Commun.* **2017**, *53*, 2709–2712.
- [20] L. Eisenburger, O. Oeckler, W. Schnick, *Chem. Eur. J.* **2021**, *27*, 4461–4465.
- [21] E. Santecchia, A. M. S. Hamouda, F. Musharavati, E. Zalnezhad, M. Cabibbo, S. Spigarelli, *Ceram. Int.* **2015**, *41*, 10349–10379.
- [22] Y. Lee, S. M. George, *Chem. Mater.* **2017**, *29*, 8202–8210.
- [23] H. Huppertz, *Z. Kristallogr.* **2004**, *219*, 330–338.
- [24] A. Haberer, H. Huppertz, *J. Solid State Chem.* **2009**, *182*, 484–490.
- [25] B. Hájek, V. Brožek, P. H. Duvigneaud, *J. Less-Common Met.* **1973**, *33*, 385–386.
- [26] M. N. Khan, K. Shahzad, J. Bashir, *J. Phys. D: Appl. Phys.* **2008**, *41*, 085409.
- [27] S. Inamura, K. Nobugai, F. Kanamaru, *J. Solid State Chem.* **1987**, *68*, 124–127.
- [28] X. Meng, B. Huang, X. Ma, Z. Wang, Z. Zheng, J. Wang, X. Qin, X. Zhang, Y. Dai, *CrystEngComm* **2014**, *16*, 6538–6541.
- [29] H. Lueken, in *Magnetochemie*, Vieweg+Teubner Verlag, Wiesbaden, **1999**.
- [30] J. Tauc, R. Grigorovici, A. Vancu, *Phys. Status Solidi* **1966**, *15*, 627–637.
- [31] E. A. Davis, N. F. Mott, *Philos. Mag.* **1970**, *22*, 903–922.
- [32] W. Spengler, R. Kaiser, A. N. Christensen, G. Müller-Vogt, *Phys. Rev. B* **1978**, *17*, 1095–1101.
- [33] M. H. Kane, S. Gupta, I. T. Ferguson, in *Rare Earth Transit. Met. Doping Semicond. Mater. Synth. Magn. Prop. Room Temp. Spintron.*, Elsevier Inc., **2016**, pp. 315–370.
- [34] Y. Bai, I. Mora-Seró, F. De Angelis, J. Bisquert, P. Wang, *Chem. Rev.* **2014**, *114*, 10095–10130.

- [35] H. Chen, C. E. Nanayakkara, V. H. Grassian, *Chem. Rev.* **2012**, *112*, 5919–5948.
- [36] B. Yoo, K. J. Kim, Y. H. Kim, K. Kim, M. J. Ko, W. M. Kim, N. G. Park, *J. Mater. Chem.* **2011**, *21*, 3077–3084.
- [37] S. Ishii, S. L. Shinde, W. Jevasuwan, N. Fukata, T. Nagao, *ACS Photonics* **2016**, *3*, 1552–1557.

6 Discovery of Two Polymorphs of TiP_4N_8 Synthesized from Binary Nitrides

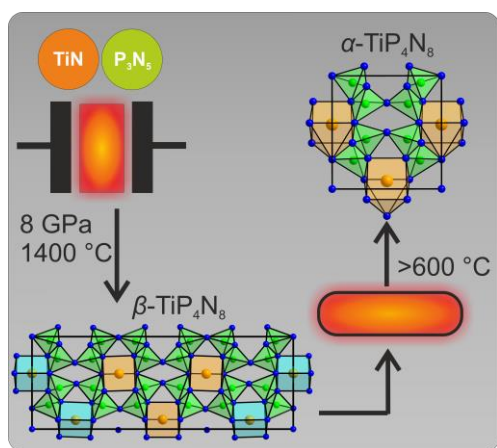
Lucien Eisenburger, Valentin Weippert, Carsten Paulmann, Dirk Johrendt, Oliver Oeckler and Wolfgang Schnick

Angew. Chem. Int. Ed. **2022**, e202202014.

Angew. Chem. **2022**, e202202014.

DOI: 10.1002/anie.202202014

DOI: 10.1002/ange.202202014



Abstract: TiP_4N_8 was obtained from the binary nitrides TiN and P_3N_5 upon addition of NH_4F as a mineralizer at 8 GPa and 1400 °C. An intricate interplay of disorder and polymorphism was elucidated by in situ temperature-dependent single-crystal X-ray diffraction, STEM-HAADF, and the investigation of annealed samples. This revealed two polymorphs, that consist of dense networks of PN_4

tetrahedra (degree of condensation $\kappa = 0.5$) and either augmented triangular TiN_7 prisms or triangular TiN_6 prisms for α - and β - TiP_4N_8 , respectively. The structures of TiP_4N_8 exhibit body-centered tetragonal (bct) framework topology. DFT calculations confirm the measured bandgaps of α - and β - TiP_4N_8 (1.6–1.8 eV) and predict the thermochemistry of the polymorphs in agreement with the experiments.

6.1 Introduction with Results and Discussion

A variety of group 1 and 2 nitridophosphates has been characterized over the last decades with silicate-related structural motifs like discrete tetrahedra, layers, or frameworks.^[1] An explanation for this abundance of group 1 and 2 nitridophosphates is, that P_3N_5 , at ambient pressure, readily decomposes above 850 °C under the evolution of N_2 .^[2] To suppress this degradation, high-pressure high-temperature (HP/HT) synthesis emerged as a viable pathway, following Le Chatelier's principle. The use of stable azides of alkali and alkaline

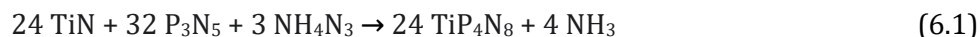
earth elements proved to be crucial for syntheses. The amount of N_2 from the decomposition of these azides further prevents the decomposition of P_3N_5 .

The incorporation of transition metals (*TM*) in nitridic tetrahedral framework structures constitutes a less explored field of research compared to compounds containing group 1 and 2 elements. *TM* bearing compounds are especially interesting given the opportunity to find stable nitrides with suitable band gaps for semiconductor applications like photovoltaics or photocatalysis.^[3-5] Although many ternary nitrides with outstanding properties have been predicted by theorists, the synthetic limits still restrict experimental confirmation of these claims.^[6,7] Only on a few occasions, the azide-route could be transferred to the synthesis of transition metal nitridophosphates as the respective *TM* azides are either nonexistent or pose serious safety issues due to being explosive.^[8] The nitride route, employing the transition metal nitride, was dismissed on many occasions as numerous *TM* nitrides such as ScN , TiN and VN are refractory and unreactive. The requirement to prevent the oxidation of the nitride ion and reduction of P or the transition metal constitutes a problem that becomes more severe when the oxidation state of the transition metal increases. Two versatile approaches to gain access to ternary transition metal nitrides have recently been described ^[1,9,10] and expanded the compositional range of nitridosilicates and -phosphates beyond the well-investigated group 1 and 2 compounds. The cation-exchange approach relies on preformed nitridic networks. For instance, $\text{Ca}_2\text{Si}_5\text{N}_8$ reacts with a FeCl_2 melt to yield $\text{Fe}_2\text{Si}_5\text{N}_8$ and CaCl_2 .^[11] Solid-state metathesis of nitridophosphates employs a metal halide and LiPN_2 with the formation of lithium halide as a driving force.^[12] Both pathways circumvent the formation of stable transition metal phosphides. However, the cation-exchange approach is often limited to the respective nitridic network used in this top-down approach. Solid-state metathesis can be hindered by substantial amounts of Li present. The incorporation of Li beside a heavy transition metal can pose serious problems in terms of structure elucidation.

In our previous studies on the NH_4F mediated HP/HT synthesis, NH_4F has shown its ability to overcome the differing reactivities of Si_3N_4 and P_3N_5 resulting in mixed nitridic networks like the recently described nitridic barylite- (AESiP_3N_7 $AE = \text{Sr}, \text{Ba}$) as well as mica-type compounds ($\text{AESi}_3\text{P}_4\text{N}_{10}(\text{NH})_2$ $AE = \text{Mg}, \text{Mg}_{0.94}\text{Ca}_{0.06}, \text{Ca}, \text{Sr}$).^[9,13] In a similar fashion we employed P_3N_5 and TiN as starting materials although TiN is used as a heat and chemically resistant coating material^[14] and despite the tendency of group 4 cations to necessitate the

incorporation of oxygen in oxonitridophosphates.^[14,15] One may also question if N_2 is a sufficiently strong oxidizing agent at conditions achievable with a multianvil press. Diamond-anvil cell (DAC) experiments resulting in the Ti^{IV} -compounds Ti_3N_4 and TiN_2 from TiN and N_2 had been conducted at 73–75 GPa and 2400 K.^[16,17] The oxidizing behavior of nitrogen at elevated pressure could originate from a weakening of the triple bond in N_2 as signaled by the existence of polymeric N exhibiting the crystal structure of black phosphorus or non-molecular N polymorphs.^[18–20]

Two polymorphs of the first Ti^{IV} nitridophosphate were discovered by HP/HT synthesis employing P_3N_5 and TiN as starting materials with the addition of NH_4F as a mineralizing agent and NH_4N_3 as nitrogen source (eq. 6.1) at 8 GPa and 1400 °C and subsequent annealing at 700°C in fused silica ampoules.



The HP/HT conditions were achieved by employing a modified Walker-type multianvil press.^[21–23] The underlying reason for the success of NH_4F seems to be the reversible element-nitrogen bond cleavage for refractory nitrides that may result in unstable molecular intermediates. In the case of TiN , HF is industrially exploited to convert TiN to the respective Ti fluorides in etching processes.^[24] There is no NH_4F with the reaction products, as side reactions with BN, the crucible material, probably occur. HP/HT synthesis yielded $\beta\text{-TiP}_4\text{N}_8$ ($Pmn2_1$, $a = 22.9196(5)$, $b = 4.58800(10)$, $c = 8.0970(2)$ Å, $Z = 6$, $R_1 = 0.0221$) as amber crystals (Table 6.1, E2, E6–8).^[25] Ti atoms are coordinated sixfold in TiN_6 triangular prisms with bond lengths $d_{\text{Ti-N}}$ ranging from 2.086(3)–2.241(2) Å. The network of PN_4 tetrahedra features all-side vertex-sharing tetrahedra with bond lengths $d_{\text{P-N}}$ 1.5998(15)–1.6608(16) Å. The topology of the tetrahedral network can be described as *bct* topology with point symbol 4.6⁵ as determined by TOPOS, exhibiting *vierer*, *sechser*, and *achter* rings, according to the nomenclature introduced by Liebau, and a degree of condensation $\kappa = 0.5$ (Figure E1–E2).^[26–28]

Table 6.1: Selected crystallographic information for α - and β - TiP_4N_8 from SCXRD data.

Formula	α - TiP_4N_8	β - TiP_4N_8
molar mass ($\text{g}\cdot\text{mol}^{-1}$)	283.86	
crystal system	orthorhombic	
space group	$Pmn2_1$ (no. 31)	
lattice parameters (\AA)	$a = 7.6065(2)$	$a = 22.9196(5)$
	$b = 4.63320(10)$	$b = 4.58800(10)$
	$c = 7.8601(3)$	$c = 8.0970(2)$
cell volume (\AA^3)	277.009(14)	851.44(3)
formula units/ unit cell	2	6
density ($\text{g}\cdot\text{cm}^{-3}$)	3.403	3.322

Structure elucidation of β - TiP_4N_8 by SCXRD led to occupational disorder on Ti sites, an issue that was encountered on datasets of several crystals. STEM-HAADF investigations showed different cation-site occupations for different crystallites ranging from nearly ordered to severely disordered (Figure 6.1, Table E2, E9–11). *In situ* HTSCXRD investigations showed that Ti disorder was eliminated by heating to 600 °C, which became apparent after accounting for limited short-range order by using separate scale factors for reflections with $h = 3n$ and $h \neq 3n$ (Table E2, E12–14).

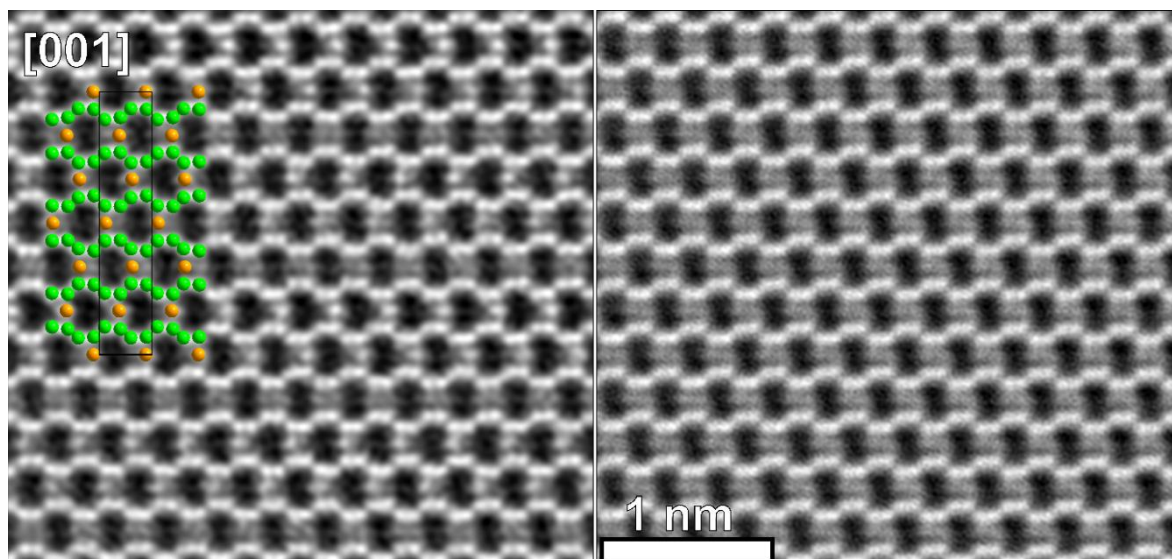


Figure 6.1: STEM HAADF images of β - TiP_4N_8 before heat treatment along [001]. Almost ordered crystallite on the left and severely disordered on the right. Structure projection of β - TiP_4N_8 with Ti orange, P green, N omitted for clarity.

Cation ordering was also shown *ex situ* with samples annealed in silica ampoules at 600 °C. Bond lengths $d_{\text{Ti-N}}$ and $d_{\text{P-N}}$ are 2.097(4)–2.268(3) Å and 1.605(3)–1.645(3) Å, respectively, at 600 °C and change, as well as bonding angles, only slightly compared to ambient temperatures indicating the rigidity of the network. However, products annealed at 700 °C showed a drastic decrease in crystallite sizes and a change of color (Figure E3).

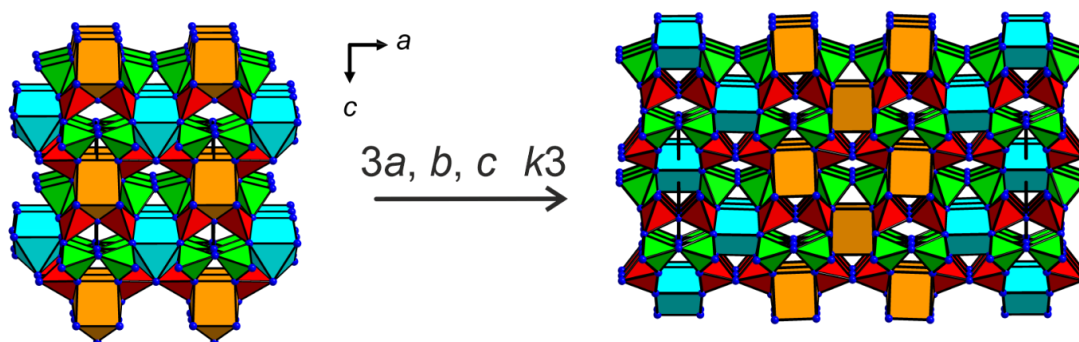


Figure 6.2: Structure projections of $\alpha\text{-TiP}_4\text{N}_8$ (left) and $\beta\text{-TiP}_4\text{N}_8$ (right) along $\sim[010]$. PN_4 tetrahedra in green and red and TiN_x polyhedra in orange and blue, respectively. Different coloring of polyhedra shows different orientations.

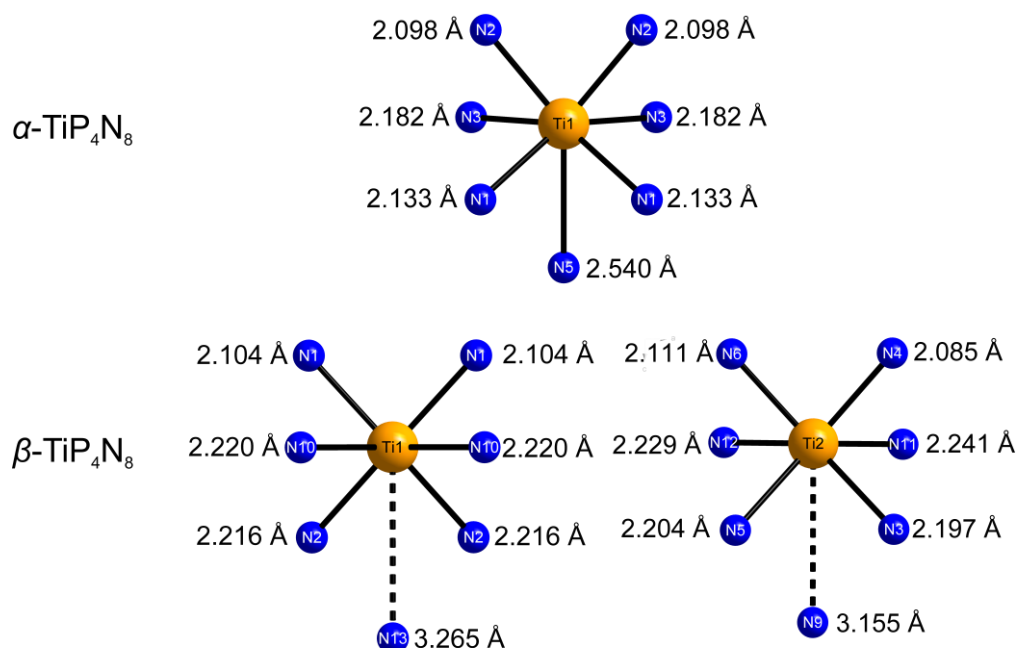


Figure 6.3: TiN_7 polyhedron in $\alpha\text{-TiP}_4\text{N}_8$ (top) and both TiN_6 triangular prisms in $\beta\text{-TiP}_4\text{N}_8$ (bottom): Ti-N bond lengths given next to the corresponding N atom. Dashed Ti-N bonds in $\beta\text{-TiP}_4\text{N}_8$ correspond to the capping atom in $\alpha\text{-TiP}_4\text{N}_8$.

Ruby-red crystals of $\alpha\text{-TiP}_4\text{N}_8$ ($Pmn2_1$, $a = 7.6065(2)$, $b = 4.63320(10)$, $c = 7.8601(3)$ Å, $Z = 2$, $R_1 = 0.0256$) were isolated from a sample that was annealed at 700 °C. The structure elucidated by SCXRD (Table E2, E3-5)^[25] is related to that of $\beta\text{-TiP}_4\text{N}_8$ by a cell transformation of $3a, b, c$ (Table 6.1, Figure 6.2 and E4). This also became evident from lattice parameters and reciprocal lattice sections. The structure of $\alpha\text{-TiP}_4\text{N}_8$ strongly resembles that of pseudo-orthorhombic svyatoslavite ($\text{CaAl}_2\text{Si}_2\text{O}_8$, space group $P2_1$).^[29,30] As compared to $\beta\text{-TiP}_4\text{N}_8$, $\alpha\text{-TiP}_4\text{N}_8$ features no superstructure reflections and a smaller unit cell volume. The orientation of the TiN_x polyhedra is different (Figure 6.2). Ti is coordinated sevenfold to form TiN_7 augmented triangular prisms enabled by a deformation of the *achter* rings. This leads to a shorter Ti–N distance of 2.540(4) Å (compared to 3.264(4) Å in $\beta\text{-TiP}_4\text{N}_8$). The bond lengths in $\alpha\text{-TiP}_4\text{N}_8$ are $d_{\text{Ti-N}}$ 2.098(2)–2.540(4) Å and $d_{\text{P-N}}$ 1.5758(15)–1.644(2) Å (Figure 3). All observed interatomic distances $d_{\text{P-N}}$ agree well with those in comparable compounds.^[31,32] To the best of our knowledge, there is no SCXRD data of a purely nitridic compound featuring Ti^{IV} on a cation site in literature to compare the bonding distances $d_{\text{Ti-N}}$ of TiP_4N_8 to. Compositional analyses of bulk samples, performed by Rietveld refinements, show TiP_4N_8 as the main constituent of all investigated samples. Minor impurities result from black P, resulting from decomposed P_3N_5 , and *h*-BN, which is used as the crucible material (Figure E5–6, Table E16). Energy-dispersive X-ray spectroscopy confirms the composition of Ti:P:N of 1:4:8 supporting the oxidation state of +IV for Ti (Table E15). IR spectroscopy showed no N–H valence modes (Figure E10). BVS calculations of the polymorphs show almost expected values for the bond-valence sums of the individual atom sites for $\alpha\text{-TiP}_4\text{N}_8$. For $\beta\text{-TiP}_4\text{N}_8$, the lower coordination numbers lead to smaller values for Ti as well as the affected N sites in contrast to the P sites which again show almost regular values (Table E17-18). HTPXRD shows thermal stability up to at least 950 °C in Ar atmosphere (Figure E7). HTPXRD with two subsequent heating cycles showed no structural change once $\beta\text{-TiP}_4\text{N}_8$ is converted to $\alpha\text{-TiP}_4\text{N}_8$ (Figure E8)

DFT calculations of the electronic properties identify both TiP_4N_8 polymorphs as semiconductors with indirect bandgaps of 1.35–1.96 eV (α) and 1.21–1.73 eV (β), depending on the exchange-correlation functional used. Figure E12 shows exemplary band structure and

density of state plots. Experimental values from reflectance spectra (Figure E11)^[33] lead to indirect bandgaps of 1.8 and 1.6 eV, respectively, in agreement with the calculated values.

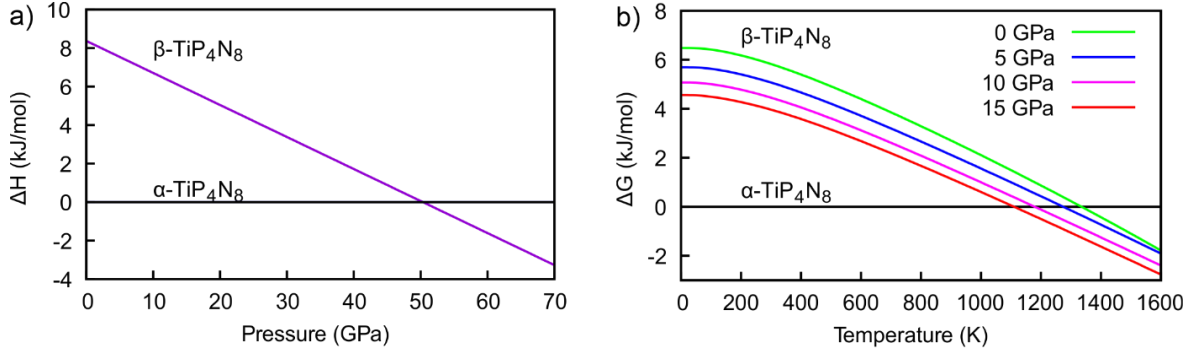


Figure 6.4: (a) Enthalpy difference ΔH between β - and $\alpha\text{-TiP}_4\text{N}_8$ with increasing pressure. (b) Temperature dependence of the Gibbs free energy difference ΔG at different pressures.

Given the synthesis of $\beta\text{-TiP}_4\text{N}_8$ under HP/HT conditions and subsequent conversion to $\beta\text{-TiP}_4\text{N}_8$ by annealing, it seems obvious that $\beta\text{-TiP}_4\text{N}_8$ is a metastable high-pressure modification. Calculations of the pressure-dependent enthalpy-difference ΔH indicate that $\beta\text{-TiP}_4\text{N}_8$ is only about 8 kJ/mol less stable than $\alpha\text{-TiP}_4\text{N}_8$. However, the pressure dependence of ΔH is very small and the β -modification is predicted to form only at pressures around 50 GPa (Figure 6.4a), much higher than the synthesis pressure of 8 GPa. To resolve this discrepancy, we have calculated the pressure and temperature dependence of the free energy $G(T,p)$ using the quasi-elastic approximation (QHA) method.^[34,35] For that purpose, the phonon contributions to the free energy F_{ph} at different volumes were calculated, and combined with the electronic energy $U(V)$ to obtain the Gibbs free energy using the expression^[36]:

$$G(T,p) = \min_V [U(V) + F_{\text{ph}}(T,V) + pV] \quad (2)$$

Figure 6.4b shows the temperature dependence of the Gibbs free energy at different pressures, which reveals that $\beta\text{-TiP}_4\text{N}_8$ is stable above about 1300 K even at zero pressure and that the transition shifts to lower temperatures with increasing pressure. This matches the experimental results much better and predicts that $\beta\text{-TiP}_4\text{N}_8$ is a quenched high-temperature rather than a high-pressure phase. Finally, we calculated the energy barrier between the polymorphs using the climbing nudged elastic band (Cl-NEB) method.^[37]

Figure 6.5 shows the NEB energy profile and a cutout of the structure at the transition state. Titanium has four short (2.01–2.03 Å) and four long (2.75–2.87 Å) Ti–N contacts. The position is almost symmetric between the two distant nitrogen atoms (3.12–3.37 Å), one of which becomes the capping atom of the TiN_7 polyhedron in $\alpha\text{-TiP}_4\text{N}_8$ (Figure 3).

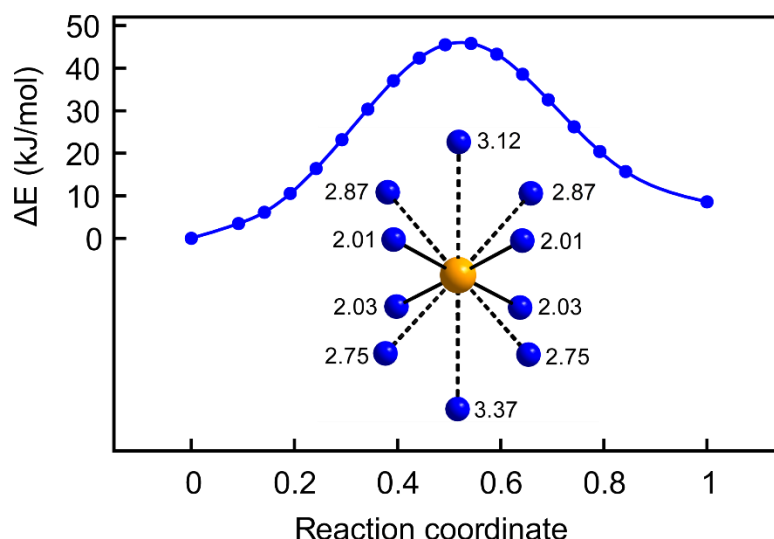


Figure 6.5: Energy barrier of the $\alpha\text{-TiP}_4\text{N}_8$ to $\beta\text{-TiP}_4\text{N}_8$ transition and the coordination of titanium at the transition state with $d_{\text{Ti-N}}$ (in Å) adjacent to N atoms.

Summing up, TiP_4N_8 was synthesized by HT/HP synthesis with NH_4F as a mineralizing agent. A combination of STEM-HAADF, *in situ* HTSCXRD investigations and annealing experiments revealed two polymorphs of TiP_4N_8 . The occupational disorder of Ti almost vanished at 600 °C resulting in $\beta\text{-TiP}_4\text{N}_8$. Further heating leads to a transformation to $\alpha\text{-TiP}_4\text{N}_8$. DFT calculations including temperature-dependent phonon contributions indicate that $\beta\text{-TiP}_4\text{N}_8$ is a metastable high-temperature polymorph. The presented synthesis of the first Ti^{IV} -nitridophosphate from binary nitrides marks a starting point to straightforward syntheses of a multitude of ternary transition metal nitrides. Given the band gaps of α - and $\beta\text{-TiP}_4\text{N}_8$ both compounds absorb light in the visible part of the spectrum. Band gaps are comparable to those of CdTe, 1.513 eV, and GaAs, 1.423 eV.^[38,39] It is most likely that the NH_4F -assisted approach can be adapted for other *TM* nitrides as well, diversifying the compositional range and variability of crystal structures in nitrides, significantly. The present results indicate that the oxidative potential of N in the pressure and temperature range of a multianvil press is sufficient to prevent the formation of *TM* phosphides from reactions of the binary nitrides.

Acknowledgements

Financial support by the Deutsche Forschungsgemeinschaft DFG (projects SCHN 377/7, SCHN 377/18-1 and OE 513/6-1) as well as under Germany's Excellence Strategy – EXC 2089/1 – 390776260 is gratefully acknowledged. We thank Dr. Peter Mayer for single-crystal data collection and Lisa Gamperl for SEM investigations. We are also indebted to Daniel Günther, Tobias Lindemann and Lennart Staab for the collection of HTSCXRD data. Parts (project I-20191265) of this research were carried out at PETRA III at DESY, a member of the Helmholtz Association. We would like to thank Martin Tolkiehn for his assistance in using beamline P24. The authors gratefully acknowledge the computational and data resources provided by the Leibniz Supercomputing Centre (www.lrz.de).

6.2 References

- [1] S. D. Kloß, W. Schnick, *Angew. Chem. Int. Ed.* **2019**, *58*, 7933–7944; *Angew. Chem.* **2019**, *131*, 8015–8027.
- [2] S. Horstmann, E. Irran, W. Schnick, *Angew. Chem. Int. Ed. Engl.* **1997**, *36*, 1873–1875; *Angew. Chem.* **1997**, *109*, 1938–1940.
- [3] I. Dincer, C. Zamfirescu, *Sustain. Hydrog. Prod.*, **2016**, pp. 309–391.
- [4] A. Fuertes, *J. Mater. Chem.* **2012**, *22*, 3293–3299.
- [5] R. S. Ningthoujam, N. S. Gajbhiye, *Prog. Mater. Sci.* **2015**, *70*, 50–154.
- [6] A. L. Greenaway, C. L. Melamed, M. B. Tellekamp, R. Woods-Robinson, E. S. Toberer, J. R. Neilson, A. C. Tamboli, *Annu. Rev. Mater. Res.* **2021**, *51*, 591–618.
- [7] W. Sun, C. J. Bartel, E. Arca, S. R. Bauers, B. Matthews, B. Orvañanos, B. R. Chen, M. F. Toney, L. T. Schelhas, W. Tumas, J. Tate, A. Zakutayev, S. Lany, A. M. Holder, G. Ceder, *Nat. Mater.* **2019**, *18*, 732–739.
- [8] F. J. Pucher, F. W. Karau, J. Schmedt auf der Günne, W. Schnick, *Eur. J. Inorg. Chem.* **2016**, *2016*, 1497–1502.
- [9] L. Eisenburger, O. Oeckler, W. Schnick, *Chem. Eur. J.* **2021**, *27*, 4461–4465.
- [10] L. Eisenburger, V. Weippert, O. Oeckler, W. Schnick, *Chem. Eur. J.* **2021**, *27*, 14184–14188.
- [11] P. Bielec, O. Janka, T. Block, R. Pöttgen, W. Schnick, *Angew. Chem. Int. Ed.* **2018**, *57*, 2409–2412; *Angew. Chem.* **2018**, *130*, 2433–2436.
- [12] S. D. Kloß, O. Janka, T. Block, R. Pöttgen, R. Glaum, W. Schnick, *Angew. Chem. Int. Ed.* **2019**, *58*, 4685–4689; *Angew. Chem.* **2019**, *131*, 4733–4737.
- [13] L. Eisenburger, P. Strobel, P. J. Schmidt, T. Bräuniger, J. Wright, E. L. Bright, C. Giacobbe, O. Oeckler, W. Schnick, *Angew. Chem. Int. Ed.* **2022**, *61*, e202114902; *Angew. Chem.* **2022**, *134*, e202114902.
- [14] E. Santecchia, A. M. S. Hamouda, F. Musharavati, E. Zalnezhad, M. Cabibbo, S. Spigarelli, *Ceram. Int.* **2015**, *41*, 10349–10379.

- [15] S. D. Kloss, S. Wandelt, A. Weis, W. Schnick, *Angew. Chem. Int. Ed.* **2018**, *57*, 3192–3195; *Angew. Chem.* **2018**, *130*, 3246–3249.
- [16] V. S. Bhadram, D. Y. Kim, T. A. Strobel, *Chem. Mater.* **2016**, *28*, 1616–1620.
- [17] V. S. Bhadram, H. Liu, E. Xu, T. Li, V. B. Prakapenka, R. Hrubik, S. Lany, T. A. Strobel, *Phys. Rev. Mater.* **2018**, *2*, DOI 10.1103/PhysRevMaterials.2.011602.
- [18] A. F. Goncharov, E. Gregoryanz, H. K. Mao, Z. Liu, R. J. Hemley, *Phys. Rev. Lett.* **2000**, *85*, 1262.
- [19] D. Laniel, B. Winkler, T. Fedotenko, A. Pakhomova, S. Chariton, V. Milman, V. Prakapenka, L. Dubrovinsky, N. Dubrovinskaia, *Phys. Rev. Lett.* **2020**, *124*, 216001.
- [20] C. Ji, A. A. Adeleke, L. Yang, B. Wan, H. Gou, Y. Yao, B. Li, Y. Meng, J. S. Smith, V. B. Prakapenka, W. Liu, G. Shen, W. L. Mao, H. K. Mao, *Sci. Adv.* **2020**, *6*, 9206–9209.
- [21] D. Walker, *Am. Mineral.* **1991**, *76*, 1092–1100.
- [22] D. Walker, M. A. Carpenter, C. M. Hitch, *Am. Mineral.* **1990**, *75*, 1020–1028.
- [23] H. Huppertz, *Z. Kristallogr.* **2004**, *219*, 330–338.
- [24] Y. Lee, S. M. George, *Chem. Mater.* **2017**, *29*, 8202–8210.
- [25] CSD 2121161-2121164 contain supplementary crystallographic data for this paper. These data can be obtained free of charge from FIZ Karlsruhe via www.ccdc.cam.ac.uk/structures. Further details on the structure determination are given in the Supporting Information.
- [26] W. A. Dollase, C. R. Ross, *Am. Mineral.* **1993**, *78*, 627–632.
- [27] V. A. Blatov, A. P. Shevchenko, D. M. Proserpio, *Cryst. Growth Des.* **2014**, *14*, 3576–3586.
- [28] F. Liebau, *Structural Chemistry of Silicates*, Springer Berlin Heidelberg, **1985**.
- [29] S. V. Krivovichev, E. P. Shcherbakova, T. P. Nishanbaev, *Can. Mineral.* **2012**, *50*, 585–592.
- [30] Y. Takéuchi, N. Haga, J. Ito, *Z. Kristallogr. - New Cryst. Struct.* **1973**, *137*, 380–398.
- [31] S. Wendl, L. Eisenburger, P. Strobel, D. Günther, J. P. Wright, P. J. Schmidt, O. Oeckler,

- W. Schnick, *Chem. Eur. J.* **2020**, *26*, 7292–7298.
- [32] S. Vogel, A. T. Buda, W. Schnick, *Angew. Chem. Int. Ed.* **2018**, *57*, 13202–13205; *Angew. Chem.* **2018**, *130*, 13386–13389.
- [33] J. Tauc, R. Grigorovici, A. Vancu, *Phys. status solidi* **1966**, *15*, 627–637.
- [34] M. T. Dove, *Introduction to Lattice Dynamics*, Cambridge University Press, **1993**.
- [35] R. P. Stoffel, C. Wessel, M. W. Lumey, R. Dronskowski, *Angew. Chem. Int. Ed.* **2010**, *49*, 5242–5266; *Angew. Chem.* **2010**, *122*, 5370–5395.
- [36] A. Togo, I. Tanaka, *Scr. Mater.* **2015**, *108*, 1–5.
- [37] K. J. Caspersen, E. A. Carter, *Proc. Natl. Acad. Sci. U. S. A.* **2005**, *102*, 6738–6743.
- [38] G. Fonthal, L. Tirado-Mejía, J. I. Marín-Hurtado, H. Ariza-Calderón, J. G. Mendoza-Alvarez, *J. Phys. Chem. Solids* **2000**, *61*, 579–583.
- [39] J. S. Blakemore, *J. Appl. Phys.* **1982**, *53*, R123.

7 Discussion and Outlook

7.1 Novel Nitrides

A multitude of synthetic pathways has been developed before this thesis to tackle synthesis-related obstacles in the high-pressure synthesis of nitridophosphates. The advent of the azide route marked systematic access to group 1 and 2 nitridophosphates. The use of NH_4Cl as a mineralizer reliably yielded single crystals suitable for in-house diffractometers.^[1-3] The high-pressure solid-state metathesis where *RE* or *TM* halides and LiPN_2 form the respective *RE*- or *TM*-nitridophosphate and the Li halide was the first systematic access to these nitridophosphates.^[4-8] Although this method proved successful, quantitative amounts of Li are present in the starting materials, which may lead to undesired incorporation of Li. Mixed nitridic networks have become accessible through the acid-assisted approach by molecular $(\text{PNCl}_2)_3$.^[9,10] This method, however, involves the release of large amounts of HCl, which enables reactions with the BN crucible and did yet not deliver non-neutral network compounds.

In this context, NH_4F mediated HP/HT synthesis can be viewed as the synergism of all the aforementioned. Similar to NH_4Cl , NH_4F yielded single crystals suitable for laboratory diffractometers as shown by AESiP_3N_7 ($AE = \text{Sr}, \text{Ba}$), $\text{Sc}_5\text{P}_{12}\text{N}_{23}\text{O}_3$, $\text{Ti}_5\text{P}_{12}\text{N}_{24}\text{O}_2$, and α - and β - TiP_4N_8 .

The syntheses of nitridosilicatephosphates AESiP_3N_7 ($AE = \text{Sr}, \text{Ba}$) and silicon imidonitridophosphates $\text{AESi}_3\text{P}_4\text{N}_{10}(\text{NH})_2$ ($AE = \text{Mg}, \text{Mg}_{0.94}\text{Ca}_{0.06}, \text{Ca}, \text{Sr}$) with NH_4F as a mineralizer yielded anionic mixed nitridic networks. In contrast to the acid-assisted route, no excessive amounts of HF are needed and inertness of the BN crucible seems to be maintained. A possible reaction pathway is given in Figure 7.1. The surface amide groups of a hypothetical A_xN_z are attacked by HF from NH_4F decomposition resulting in NH_3 as a leaving group upon the formation of the A-F bond. In the next step, the amide group of a hypothetical B_yN_z attacks at the A atom, and HF acts as a leaving group thus NH_4F is regained. After multiple steps, the crystallization enthalpy could act as a driving force of the overall formation of the nitride

$A_xB_yN_z$. This is in accordance with investigations of the etching processes of Si_3N_4 in aqueous HF solutions.^[11]

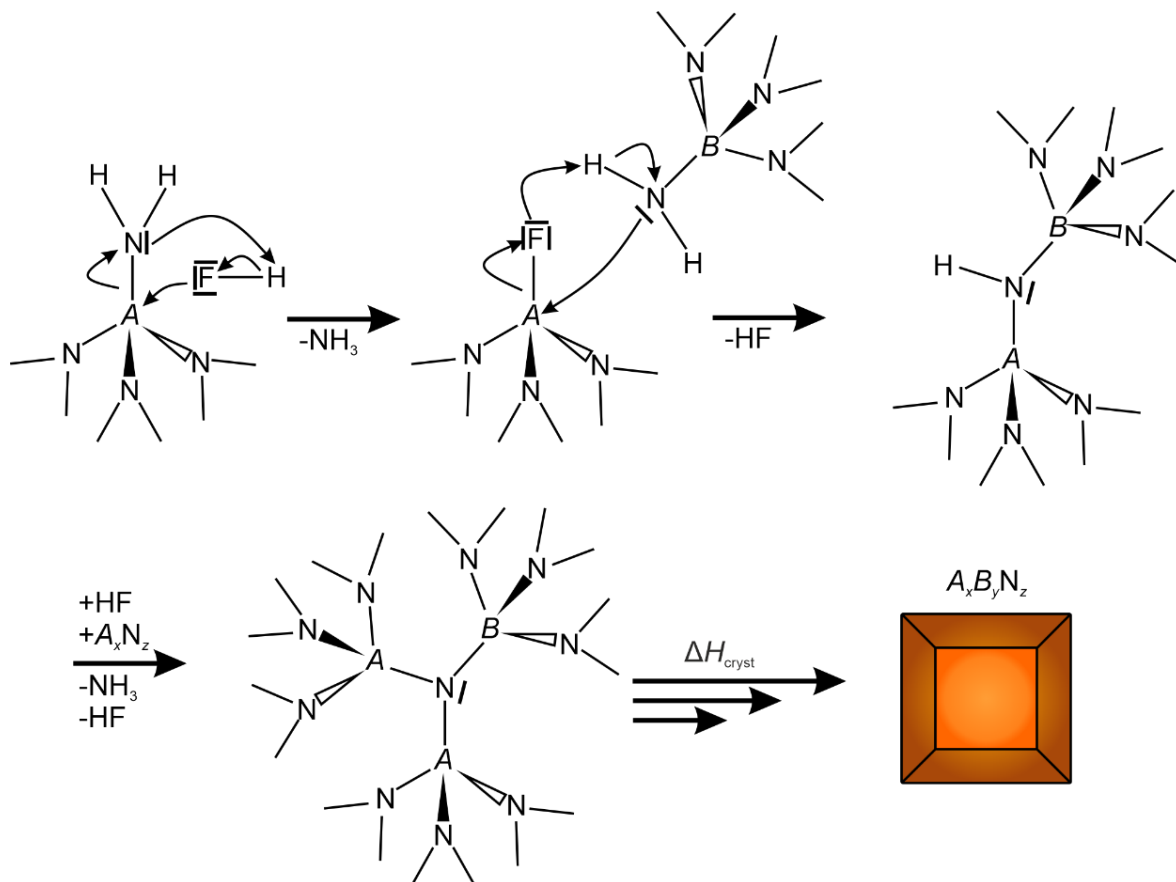


Figure 7.1. Possible reaction pathway of hypothetical nitrides A_xN_z and B_yN_z to $A_xB_yN_z$ via the NH_4F mediated HP/HT synthesis.

The preparation of $Sc_5P_{12}N_{23}O_3$, $Ti_5P_{12}N_{24}O_2$, and α - and β - TiP_4N_8 shows the benefits of NH_4F over solid-state metathesis. The interstitial *TM* nitrides were believed to be too unreactive as starting materials. Yet, NH_4F as a mineralizer can activate these compounds. This comes without the drawback of the quantitative use of Li in the starting materials. The formation of the first ternary compound of Ti, P, and N, $Ti^{IV}P_4N_8$, also shows that N is a sufficient oxidizing agent for the oxidization of transition metals at the reaction conditions realized by multianvil presses.

Based on the findings of this thesis it is likely that these results can also be projected to other rare earth and transition metal nitrides. This enables systematic access to open shell nitridophosphates incorporating Co, Ni, Fe, Sm, or Mn. If these elements are only used in dopant quantities this could lead to a possible application of nitridophosphates as dilute

magnetic semiconductors.^[12] With band gaps in the visible part of the spectrum, photocatalysis comes to mind as a viable research interest for *TM* nitridophosphates.^[13–15]

Expanding the compositional range even further, syntheses of nitridophosphates containing group 1 or 2 elements and *TM* or *RE* seem feasible from NH_4F as a mineralizer. In analogy to compounds like $\text{La}_{3-x}\text{Ca}_{1.5x}\text{Si}_6\text{N}_{11}:\text{Eu}^{2+}$ ($x \approx 0.77$)^[16] nitridophosphates similar in composition could lead to unprecedented host lattices and therefore desired emission properties.

It is reasonable to assume that the activation of refractory nitrides could also be extended to other nitrides, e. g. Be_3N_2 , AlN or Ge_3N_4 . This would lead to a broad spectrum of novel mixed networks like nitridoalumophosphates with yet unknown structure types and potentially intriguing properties. Not limited to nitridophosphates, the activation of interstitial and refractory nitrides could also lead to the discovery of some proposed nitridic perovskites with interesting electronic properties.

7.2 STEM in Materials Science

Modern aberration-corrected (scanning) transmission electron microscopy enabled the reliable results of crystal structure determinations presented in this thesis. For $\text{Sn}_{2.8(4)}\text{Bi}_{20.2(4)}\text{Se}_{27}$ the preparation of oriented cross-section samples for atomic-resolution STEM-EDX clarified the distribution of Bi and Sn in combination with the results from structure determination from synchrotron diffraction. Both experiments show disorder of Bi and Sn on all corresponding Wyckoff sites. This is especially remarkable given a lattice parameter of $282.64(6)$ Å which results in 12 Wyckoff sites occupied by Sn/Bi. As the detection efficiency of EDX detectors favors heavy elements and as reports on chemical mapping of Si and P with atomic resolution could not be found in literature, the application of this technique became intriguing for nitridosilicatephosphates and silicon imidonitridophosphates. Considering that both compounds were yielded as powders, the time efficiency of this approach was not limited by the preparation of cross-sections but highly dependent on preferred orientations encountered in $\text{CaSi}_3\text{P}_4\text{N}_{10}(\text{NH})_2$. Nonetheless, STEM-EDX mappings could be performed on a crystallite with dimensions of a few hundred nanometers.

The presence of superstructure reflections and their origin could be confirmed by atomic-resolution STEM-HAADF and electron diffraction in the case of $\beta\text{-TiP}_4\text{N}_8\text{F}$. In addition, STEM-

HAADF showed the presence of imperfect long-range ordering seen as Ti split position. This led to the acquisition of HTSCXRD data and subsequently the discovery of α -TiP₄N₈.

The results of this thesis showcase the feasibility, necessity, and information gained by electron microscopy for explorative material sciences. Positional and occupational order/disorder could be readily elucidated by STEM-HAADF and/or STEM-EDX with atomic resolution.

A prospect here is the parallel acquisition of EELS and EDX spectra with atomic resolution which would expand the distinguishable elements to even lighter elements e. g. N, O, F. This will lead to yet unachieved confidence in atom-type assignment in structure determination of (oxo)nitrides.

The advent of iDPC (integrated differential phase contrast) enables the visualization of the projected electronic potential of the sample.^[17] This eliminates the drawback of STEM-HAADF namely the dependency of the image contrast of $\sim Z^2$ which leads to an underrepresentation of light elements in the image contrast. With iDPC, image contrast is nearly dependent on Z and therefore direct imaging of light elements like Li with simultaneous presence of heavy elements is feasible. In combination with another emerging field, *in situ* STEM, this could lead to unprecedented insights into the charging and discharging of Li-Ion batteries.

Still unachieved but long sought after is the combination of STEM-HAADF tomography with atomic resolution spectroscopy. This would result in a 3D model of the investigated nanocrystallite with information on the element type of each atom. In addition to 3D electron crystallography methods like ADT (automated electron diffraction tomography)^[18] or RED (rotation electron diffraction)^[19], this could surpass structure elucidation from PXRD data in terms of accuracy and efficiency if the (S)TEM routines become user-friendly.

7.3 Final Remarks

A synthetic approach to novel nitrides was found within this thesis that delivered simple and effective access to mixed nitridic networks and transition metal nitride semiconductors. Crystallographic characterizations by atomic-resolution STEM and single-crystal synchrotron diffraction became only possible with techniques that were not available two decades ago.

The structural diversity achievable by mixed networks is undoubtedly immense and, in nature, illustrated by the diversification enabled by going from oxosilicates to oxoalumosilicates. The synthetic pathway presented in this thesis may certainly provide

access to further possible host materials for activator ions containing SiN_x and PN_y polyhedra simultaneously. Since the synthetic part of this thesis tackled the issue of differing reactivities of nitrides, it is to be expected that the NH_4F mediated synthesis can be applied to other network-forming refractory nitrides such as Be_3N_2 and AlN .

Although nitridophosphates gained interest as possible components for solid-state lighting, most of these compounds have band gaps at an insulator level. With the preparation of transition metal compounds, the possible range of applications grew by semiconductor applications like photocatalysis and photovoltaic as comparable band gaps to compounds like CdTe were achieved by combining the non-toxic elements Ti, P, and N. Experimental results on transition metal compounds may soon confirm theoretical chemists' claims on the stability and performance of predicted ternary nitrides.^[20,21]

The electron microscopy presented emphasizes the need for advanced structural characterization in materials science already at the level of explorative and fundamental research. This will be of future interest and need in the emerging field of energy conversion.

7.4 References

- [1] A. Marchuk, F. J. Pucher, F. W. Karau, W. Schnick, *Angew. Chem. Int. Ed.* **2014**, *53*, 2469–2472; *Angew. Chem.* **2014**, *126*, 2501–2504.
- [2] A. Marchuk, V. R. Celinski, J. Schmedt auf der Gönne, W. Schnick, *Chem. Eur. J.* **2015**, *21*, 5836–5842.
- [3] A. Marchuk, L. Neudert, O. Oeckler, W. Schnick, *Eur. J. Inorg. Chem.* **2014**, *2014*, 3427–3434.
- [4] S. D. Kloß, S. Wandelt, A. Weis, W. Schnick, *Angew. Chem. Int. Ed.* **2018**, *57*, 3192–3195; *Angew. Chem.* **2018**, *130*, 3246–3249.
- [5] S. D. Kloß, O. Janka, T. Block, R. Pöttgen, R. Glaum, W. Schnick, *Angew. Chem. Int. Ed.* **2019**, *58*, 4685–4689; *Angew. Chem.* **2019**, *131*, 4733–4737.
- [6] S. D. Kloß, W. Schnick, *Angew. Chem. Int. Ed.* **2015**, *54*, 11250–11253; *Angew. Chem.* **2015**, *127*, 11402–11405.
- [7] S. D. Kloß, N. Weidmann, R. Niklaus, W. Schnick, *Inorg. Chem.* **2016**, *55*, 9400–9409.
- [8] S. D. Kloß, N. Weidmann, W. Schnick, *Eur. J. Inorg. Chem.* **2017**, *2017*, 1930–1937.
- [9] S. Vogel, A. T. Buda, W. Schnick, *Angew. Chem. Int. Ed.* **2018**, *57*, 13202–13205; *Angew. Chem.* **2018**, *130*, 13386–13389.
- [10] S. Vogel, A. T. Buda, W. Schnick, *Angew. Chem. Int. Ed.* **2019**, *58*, 3398–3401; *Angew. Chem.* **2019**, *131*, 3436–3439.
- [11] D. Martin Knotter, T. J. J. (Dee) Denteneer, *J. Electrochem. Soc.* **2001**, *148*, F43.
- [12] M. H. Kane, S. Gupta, I. T. Ferguson, in *Rare Earth Transit. Met. Doping Semicond. Mater. Synth. Magn. Prop. Room Temp. Spintron.*, Elsevier Inc., **2016**, pp. 315–370.
- [13] A. Fuertes, *Mater. Horizons* **2015**, *2*, 453–461.
- [14] I. Dincer, C. Zamfirescu, in *Sustain. Hydrog. Prod.*, Elsevier, **2016**, pp. 309–391.
- [15] X. Meng, W. Qi, W. Kuang, S. Adimi, H. Guo, T. Thomas, S. Liu, Z. Wang, M. Yang, *J. Mater. Chem. A* **2020**, *8*, 15774–15781.

- [16] C. Maak, D. Durach, C. Martiny, P. J. Schmidt, W. Schnick, *Chem. Mater.* **2018**, *30*, 3552–3558.
- [17] E. Yücelen, I. Lazić, E. G. T. Bosch, *Sci. Rep.* **2018**, *8*, 1–10.
- [18] U. Kolb, T. Gorelik, C. Kübel, M. T. Otten, D. Hubert, *Ultramicroscopy* **2007**, *107*, 507–513.
- [19] D. Zhang, P. Oleynikov, S. Hovmoller, X. Zou, *Z. Kristallogr.* **2010**, *225*, 94–102.
- [20] W. Sun, C. J. Bartel, E. Arca, S. R. Bauers, B. Matthews, B. Orvañanos, B. R. Chen, M. F. Toney, L. T. Schelhas, W. Tumas, J. Tate, A. Zakutayev, S. Lany, A. M. Holder, G. Ceder, *Nat. Mater.* **2019**, *18*, 732–739.
- [21] A. L. Greenaway, C. L. Melamed, M. B. Tellekamp, R. Woods-Robinson, E. S. Toberer, J. R. Neilson, A. C. Tamboli, *Annu. Rev. Mater. Res.* **2021**, *51*, 591–618.

8 Summary

8.1 General Aspects

The results of this thesis illustrate the synergy of explorative solid-state chemistry and atomic resolution STEM in the preparation and structure elucidation of novel nitrides and other compounds. For instance, the structure elucidation of $\text{Sn}_{2.8(4)}\text{Bi}_{20.2(4)}\text{Se}_{27}$ from microfocused synchrotron radiation was complemented by atomic-resolution STEM-HAADF and -EDX mappings. The synergistic approach revealed a complicated stacking sequence resulting in a lattice parameter of $282.64(6) \text{ \AA}$ and Sn/Bi occupational disorder on 12 Wyckoff sites.

Before this work, only two compounds featured SiN_x and PN_y polyhedra simultaneously: SiPN_3 and $\text{SiP}_2\text{N}_4\text{NH}$.^[1,2] By applying NH_4F in high-pressure high-temperature (HP/HT) synthesis, the first nitridosilicatephosphates AESiP_3N_7 ($\text{AE} = \text{Sr}, \text{Ba}$) were synthesized from the alkaline-earth azides, Si_3N_4 and P_3N_5 .^[3] The compounds proved suitable as host lattices for activator ions as shown by their luminescence spectra upon Eu^{2+} doping. The occupational disorder of Si and P on one Wyckoff site in the simultaneous presence of one Wyckoff site solely occupied by P was investigated by the geometrical considerations of polyhedra volumes and STEM-EDX mapping with atomic resolution.

With the alkaline-earth azides exchanged for the alkaline-earth amides, the new approach resulted in the first nitridic mica-like compounds $\text{AESi}_3\text{P}_4\text{N}_{10}(\text{NH})_2$ ($\text{AE} = \text{Mg}, \text{Mg}_{0.94}\text{Ca}_{0.06}, \text{Ca}, \text{Sr}$).^[4] These compounds feature the high-pressure motif of sixfold coordinated Si beside PN_4 tetrahedra as shown by STEM-EDX mappings with atomic resolution in combination with microfocused synchrotron SCXRD experiments. Therefore, the NH_4F -assisted approach also proved successful in synthesizing imide group-containing compounds.

The preparation of transition metal-containing nitrides with NH_4F as a mineralizer constitutes another central aspect of this thesis. The oxonitridophosphates $\text{Sc}_5\text{P}_{12}\text{N}_{23}\text{O}_3$ and $\text{Ti}_5\text{P}_{12}\text{N}_{24}\text{O}_2$ were synthesized from the refractory nitrides ScN or TiN , and P_3N_5 upon the addition of PON or TiO_2 , respectively, as a solid oxygen source.^[5] The mixed-anion compounds also show mixed-valence for $\text{Ti}_5\text{P}_{12}\text{N}_{24}\text{O}_2$ with the ordering of Ti^{3+} and Ti^{4+} ions.

The polymorphs of TiP_4N_8 showcase the analytical demand ranging from *ex situ* SCXRD, *in situ* HTSCXRD, HPXRD, atomic resolution STEM-HAADF to DFT calculations following the simple reaction of TiN with P_3N_5 , NH_4N_3 , and NH_4F . Additionally, the NH_4F mediated HP syntheses

presented themselves as a reasonable approach to new ternary transition metal nitride semiconductors.

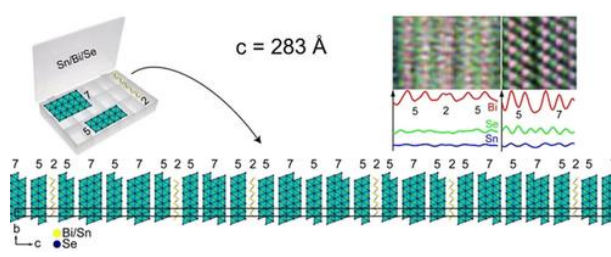
8.2 A Layered Tin Bismuth Selenide with Three Different Building Blocks that Account for an Extremely Large Lattice Parameter of 283 Å

published in: M. Nentwig, L. Eisenburger, F. Heinke, D. Souchay, O. Oeckler

Chem. Eur. J. **2020**, *26*, 10676.

DOI: 10.1002/chem.202000663

The crystal structure of 150R- $\text{Sn}_{2.8(4)}\text{Bi}_{20.2(4)}\text{Se}_{27}$ was elucidated by microfocused synchrotron diffraction. Crystal structure refinements yielded an unusually large unit cell in space group



$R\bar{3}m$ with $a = 4.1819(4)$ Å and $c = 282.64(6)$ Å. All 12 Sn/Bi Wyckoff sites are occupationally disordered according to SCXRD. A cross-section sample from bulk $\text{Sn}_{2.8(4)}\text{Bi}_{20.2(4)}\text{Se}_{27}$ was analyzed by atomic-resolution STEM-HAADF and STEM-EDX mapping.

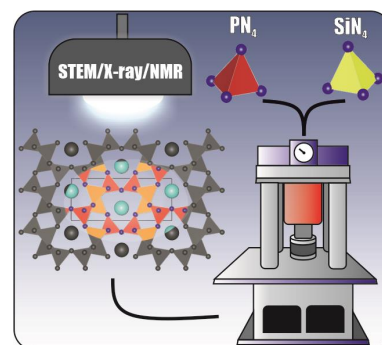
8.3 High-Pressure High-Temperature Synthesis of Mixed Nitridosilicatephosphates and Luminescence of $\text{AESiP}_3\text{N}_7:\text{Eu}^{2+}$ ($\text{AE} = \text{Sr}, \text{Ba}$)

published in: L. Eisenburger, O. Oeckler, W. Schnick

Chem. Eur. J. **2021**, *27*, 4461.

DOI: 10.1002/chem.202005495

The first nitridosilicatephosphates were synthesized by high-pressure high-temperature synthesis employing a Walker-type multianvil press and NH_4F as a mineralizer at 8 GPa and 1400–1700 °C. The crystal structures of SrSiP_3N_7 and BaSiP_3N_7 were elucidated by single-crystal X-ray diffraction and atomic resolution STEM-EDX mappings. This revealed a disordered $\text{Si}_{0.5}\text{P}_{0.5}$ and a fully ordered P site. Additional characterization



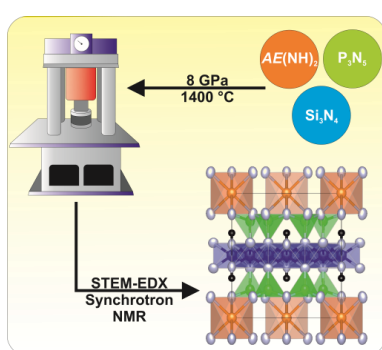
was performed by FTIR, SEM, MAS-NMR, and luminescence spectroscopy on Eu^{2+} doped samples.

8.4 Nitridic Analogs of Micas $\text{AESi}_3\text{P}_4\text{N}_{10}(\text{NH})_2$ ($\text{AE} = \text{Mg}, \text{Mg}_{0.94}\text{Ca}_{0.06}, \text{Ca}, \text{Sr}$)

published in: L. Eisenburger, P. Strobel, P. J. Schmidt, T. Bräuniger, J. Wright, E. L. Bright, C. Giacobbe, O. Oeckler, W. Schnick, *Angew. Chemie Int. Ed.* **2022**, 61, e202114902.

Angew. Chemie **2022**, 134, e202114902.

DOI: 10.1002/anie.202114902



High-pressure high-temperature synthesis employing NH_4F led to the first nitridic analogs of micas. The compounds $\text{AESi}_3\text{P}_4\text{N}_{10}(\text{NH})_2$ ($\text{AE} = \text{Mg}, \text{Mg}_{0.94}\text{Ca}_{0.06}, \text{Ca}, \text{Sr}$) crystallize isotypic to the mineral clintonite. The crystal structure was elucidated on microcrystalline samples of $\text{CaSi}_3\text{P}_4\text{N}_{20}(\text{NH})_2$ from microfocused synchrotron radiation experiments and STEM-EDX mappings with atomic resolution revealing PN_4

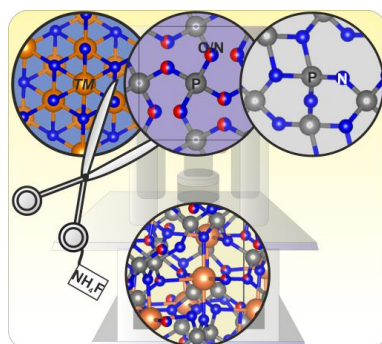
tetrahedra and $\text{SiN}_4(\text{NH})_2$ octahedra layers. The presence and location of the imide group, $-\text{NH}$, were furthermore confirmed by FTIR and MAS-NMR spectroscopy. Eu^{2+} doped samples showed narrow-band emission with maxima ranging from 451 to 492 nm.

8.5 High-Pressure Synthesis of $\text{Sc}_5\text{P}_{12}\text{N}_{23}\text{O}_3$ and $\text{Ti}_5\text{P}_{12}\text{N}_{24}\text{O}_2$ by Activation of Binary Nitrides ScN and TiN with NH_4F

published in: L. Eisenburger, V. Weippert, O. Oeckler, W. Schnick,

Chem. Eur. J. **2021**, 27, 14184.

DOI: 10.1002/chem.202101858



The compounds $\text{Sc}_5\text{P}_{12}\text{N}_{23}\text{O}_3$ and $\text{Ti}_5\text{P}_{12}\text{N}_{24}\text{O}_2$ were synthesized by the NH_4F mediated high-pressure high-temperature approach from the binary nitrides and PON or TiO_2 , respectively, acting as an O source. Both compounds are isotypic to $\text{Ti}_5\text{B}_{12}\text{O}_{26}$ as elucidated by single-crystal X-ray diffraction. Magnetic measurements revealed the ordering of Ti^{3+} and Ti^{4+} ions on Wyckoff positions 32g and 8b

respectively. The optical band gaps were determined as direct band gaps of 1.6 eV for $\text{Ti}_5\text{P}_{12}\text{N}_{24}\text{O}_2$ and 3.8 eV for $\text{Sc}_5\text{P}_{12}\text{N}_{23}\text{O}_3$.

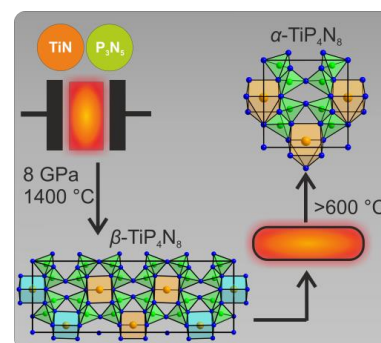
8.6 Discovery of Two Polymorphs of TiP_4N_8 Synthesized from Binary Nitrides

published in: L. Eisenburger, Valentin Weippert, Carsten Paulmann, Dirk Johrendt, Oliver Oeckler, W. Schnick, *Angew. Chem. Int. Ed.* **2022**, DOI 10.1002/anie.202202014.
Angew. Chemie **2022**, DOI 10.1002/ange.202202014.

DOI: 10.1002/anie.202202014.

The first Ti^{IV} nitridophosphate was synthesized via the NH_4F -assisted high-pressure high-temperature route from the binary nitrides. The combination of STEM-HAADF, in situ single-crystal X-ray diffraction, and annealing of samples, revealed the crystal structures of two polymorphs. While the crystal structure of $\alpha\text{-TiP}_4\text{N}_8$ strongly resembles that of orthorhombic svyatoslavite ($\text{CaAl}_2\text{Si}_2\text{O}_8$) the crystal structure

of $\beta\text{-TiP}_4\text{N}_8$ is a threefold superstructure along h thereof. $\alpha\text{-TiP}_4\text{N}_8$ and $\beta\text{-TiP}_4\text{N}_8$ feature indirect band gaps in the visible part of the spectrum as shown by DFT calculations of 1.78 and 1.5 eV, respectively. DFT calculations also revealed that $\beta\text{-TiP}_4\text{N}_8$ is a metastable polymorph and the observed phase transition is monotropic.



Appendix

A Supporting Information for Chapter 2

Experimental Procedures

Synthesis. $(\text{SnSe})_{0.5}\text{Bi}_2\text{Se}_3 = \text{SnBi}_4\text{Se}_7$ was synthesized from a stoichiometric mixture of the elements Sn (99.999%, Koch chemicals or Aluterv-FKI), Bi (99.999%, Aldrich or Alfa Aesar), and Se (99.999%, ChemPur). The mixture (total weight ~ 3 g) was fused in a sealed silica glass ampule (length ~ 10 cm, diameter 15 mm) under dry Ar atmosphere and melted at 900 °C for two days, followed by quenching at air. After annealing the sample at 500 °C for one week, it was quenched in water. The resulting product with a nominal composition of $\text{Sn}_{0.571}\text{Bi}_{2.286}\text{Se}_4$ was heated three times up to 500 °C. The heterogeneous product was examined by scanning electron microscopy (SEM) and energy-dispersive X-ray spectroscopy (EDX) as described below, which revealed regions of different contrast and composition (Fig. S1 and Table S1). Next to a minority phase, which can be identified as $\text{Sn}_{11.49}\text{Bi}_{12.39}\text{Se}_{30}$ (phase 1)^[1] by EDX, and one main phase of $\text{Sn}_{0.85}\text{Bi}_{2.15}\text{Se}_4$ (phase 2),^[1] there is a slightly Sn-depleted (compared to the nominal composition SnBi_4Se_7) phase (phase 3), which constitutes the title compound of this contribution.

Conventional transmission electron microscopy. Selected-area electron diffraction (SAED), high resolution transmission electron microscopy (HRTEM) and further EDX measurements (Table S2) were executed on a Philips CM-200 STEM transmission electron microscope (LaB₆ cathode, 200 kV, super-twin lens, point resolution 0.23 nm) equipped with RTEM 136-5 EDX detector (EDAX, Genesis software).^[2] A double-tilt low-background sample holder (Gatan) was used. For these TEM measurements, i.e. the selection of crystallites for synchrotron measurements, the powdered sample was suspended in ethanol and deposited on a copper grid coated with a holey carbon film. Evaluation of SAED data was done using the *analySIS* software.^[3] For HRTEM and SAED simulations, jEMS was used.^[4] Micrographs and diffraction patterns were evaluated using Digital Micrograph.^[5]

Sample preparation for scanning transmission electron microscopy. Polycrystalline pieces of the sample were embedded in Gatan G1 epoxy resin (Gatan, USA) between two

silicon wafers, which were subsequently glued into a brass tube (inner diameter 2.4 mm, wall thickness 0.3 mm) with the same epoxy resin. Discs of $\sim 500\text{ }\mu\text{m}$ thickness were cut from this assembly using a diamond wire saw (well GmbH, Germany). The discs were mechanically thinned to a thickness of ca. $80\text{ }\mu\text{m}$ with a disc grinder (Gatan, USA) using SiC abrasive paper with particle sizes of $40\text{ }\mu\text{m}$ and subsequently $10\text{ }\mu\text{m}$ (Gatan, USA). The sample was further thinned from both sides to a thickness of $\sim 20\text{ }\mu\text{m}$ in the center using a dimple grinder (Gatan 656 dimple grinder, Gatan, USA) and diamond paste ($5\text{ }\mu\text{m}$ and $1\text{ }\mu\text{m}$, Kemet International LTD, Kent, UK). Electron transparency was achieved by Ar-ion milling using a precision ion polishing system (PIPS, Gatan, USA) at incidence angles of 6° and a voltage of 4 keV. After a hole in the center of the disc was visible, the sample was polished at 0.9, 0.6 and 0.3 keV for five minutes each. An image of the prepared sample is shown in Figure A13.

Scanning transmission electron microscopy. The sample was mounted on a double-tilt holder and transferred into a C_s DCOR probe-corrected Titan Themis 300 (FEI, USA) instrument equipped with X-FEG, post-column filter (Enfinium ER-799, Gatan, USA), US1000XP/FT camera system (Gatan, Germany) and a windowless, 4-quadrant Super-X EDX detector. TEM images were recorded using a $4k \times 4k$ FEI Ceta CMOS camera. The microscope was operated at 300 kV or 200 kV accelerating voltage for SAED and STEM-HAADF (16.6 mrad convergence angle, $50\text{ }\mu\text{m}$ aperture, 63 mrad detector inner half angle for 100 mm camera length). TEM data were evaluated with Digital Micrograph [5] for image analysis, ProcessDiffraction7 [6] for geometric calculations concerning SAED patterns, JEMS [4] for SAED simulations and the software suite Velox v2.8 (Thermo Fisher Scientific, USA) for recording and evaluating EDX maps. These were acquired over 120×138 pixels with $20\text{ }\mu\text{s}$ dwell time each. The resulting maps consist of 953 (300 keV) / 140 (200 keV) individual frames. Drift corrections were applied. EDX signals were integrated as a projection on a line of 135 pixels (2.441 nm) in length, using an integration width of 100 pixels for 300 keV (Fig. 3c). For 200 keV, they were projected on a line of 285 pixels (2.297 nm) in length, using an integration width of 140 pixels (Fig. 3f). The element maps were filtered using a radial Wiener filter (highest frequency 20.0 software-specific units and edge smoothing 30.0 units for 300 keV; highest frequency 13.0 units and edge smoothing 30.0 units for 200 keV).

Single-crystal X-ray diffraction. Single-crystal data of a crystallite on a copper finder grid (Fig. S2), which was fixed on a glass capillary, were collected at beamline ID11 of the European Synchrotron Radiation Facility (ESRF, Grenoble) using microfocused synchrotron radiation. The crystal was centered in a beam of ca. $1.5 \times 3 \mu\text{m}^2$ with the help of fluorescence scans using the Bi- K_α emission lines, which were recorded and processed using a SiriusD Silicon Drift Detector with a XIA Mercury pulse processor (Ketek, Germany). Diffraction data were recorded with a Frelon4k CCD detector.^[7] Integration and semiempirical absorption correction were performed with CrysAlisPro.^[8] A correction for incomplete absorption of high-energy radiation in the phosphor of the CCD detector was applied.^[9] Structure solution and refinement as well as the calculation of Fourier maps and simulation of diffraction patterns were performed with JANA2006 (version 08/10/2018).^[10] For the tentative refinement of the structure model in 3D, the program SHELX ^[11] was used. Crystal structures were visualized with Diamond.^[12] Further details of the crystal structure investigations may be obtained from the Fachinformationszentrum Karlsruhe, 76344 Eggenstein-Leopoldshafen, Germany (fax: +49-7247-808-666; e-mail: crys-data@fiz-karlsruhe.de), on quoting the depository number 1949450.

Sample characterization by SEM, TEM and EDX

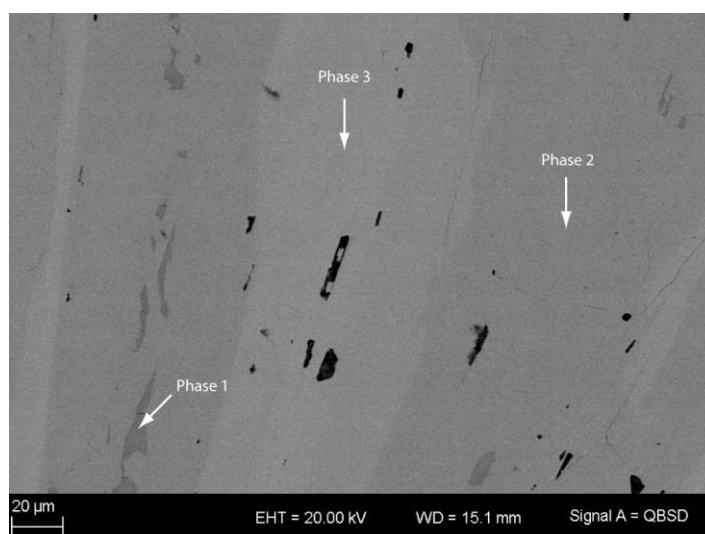


Figure A1. SEM-BSE image of a thermally treated sample (3 times cycled between RT and 500 °C) with the nominal composition SnBi_4Se_7 . The image shows the presence of two majority phases (phase 2 and phase 3) and one minority phase (phase 1) after thermal treatment during the thermoelectric measurements. The compositions of the different phases are displayed in Table S1. Phase 2 ($\text{Sn}_{0.85}\text{Bi}_{2.15}\text{Se}_4$) has been investigated in detail by F. Heinke et al.^[1]

Table A1. SEM-EDX analyses (average of six point measurements for phase 1 and of four point measurements each for phases 2 and 3) for the sample with the nominal composition SnBi_4Se_7 after thermal treatment (3 times cycled up to 500 °C).^[1]

Element	Nominal composition SnBi_4Se_7	Phase 1 (minority phase)	Calculated for $\text{Sn}_{11.49}\text{Bi}_{12.39}\text{Se}_{30}$ ref. [1]	Phase 2 (majority phase)	Calculated for $\text{Sn}_{0.85}\text{Bi}_{2.15}\text{Se}_4$ ref. [1]	Phase 3 (majority phase)	Calculated for $\text{Sn}_{2.8}\text{Bi}_{20.2}\text{Se}_{27}$ (this work)
Sn / at-%	8.3%	21.9(6)	22.0%	9.6(5)	12.2%	5.6(5)	5.6%
Bi / at-%	33.3%	24.3(4)	22.3%	35.9(3)	30.7%	39.9(4)	40.4%
Se / at-%	58.3%	53.8(9)	55.7%	54.5(10)	57.1%	54.6(10)	54.0 %

Table A2. EDX analysis (average of three point measurements) of the single crystal used for synchrotron data collection (Fig. S2). Note that these EDX results may be rather imprecise as the position of the crystal on the TEM grid was not ideal for recording EDX spectra.

Element	Single crystal	Calculated for SnBi_4Se_7	Calculated for $\text{Sn}_{2.8(4)}\text{Bi}_{20.2(4)}\text{Se}_{27}$
Sn / at-%	6.9(6)	8.3%	5.6%
Bi / at-%	35.1(5)	33.3%	40.4%
Se / at-%	58.0(3)	58.3%	54%

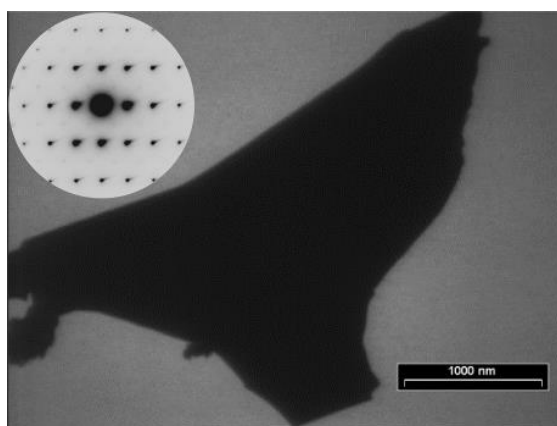


Figure A2. Transmission electron micrograph (Philips CM-200) and a SAED pattern of the crystallite used for synchrotron data collection.

Results and Discussion

General remarks. An initial attempt to determine the crystal structure solution from the single-crystal data by “routine data processing” resulted in the space group $P\bar{3}m1$ with $a = 4.0955(2) \text{ \AA}$ $c = 22.172(2) \text{ \AA}$, which is close to the metrics of BiSe.^[13] However, ca. 60% of all reflections remained unindexed. Close inspection of the diffraction pattern (cf. following figures) suggested that the diffraction pattern is best described using a (3+1)D superspace approach. A small trigonal unit cell with $a = 4.1819(4) \text{ \AA}$ and $c = 5.6528(4)$ describes the strong main reflections. The other reflections are indexed with a q -vector along $[001]^*$ with $q = 1.74 = 87/50$, taking into account satellite reflections up to the 8th order. This (3+1)D commensurate modulation explains all reflections on the reciprocal lattice sections (Fig. S3 – S5). Due to the presence of no systematic absences for the satellite reflections, the superspace group $R\bar{3}m(00\gamma)00$ was chosen instead of the other possibility - i.e. $R\bar{3}m(00\gamma)0s$ - corresponding to the 3D space group $R\bar{3}m$. Structure solution by charge flipping ^[14] confirmed the assumed superspace group $R\bar{3}m(00\gamma)00$ with a single atom site (0 0 0). This (3+1)- dimensional model with a small trigonal unit cell and a q -vector along $[001]^*$ is consistent with the superspace formalism developed for layered bismuth selenides.^[15] This straightforward description unifies all these compounds in a single structure model whose modulation vector actually determines which variant is present. This approach can be used for both commensurate and incommensurately modulated structures.

Diffraction patterns

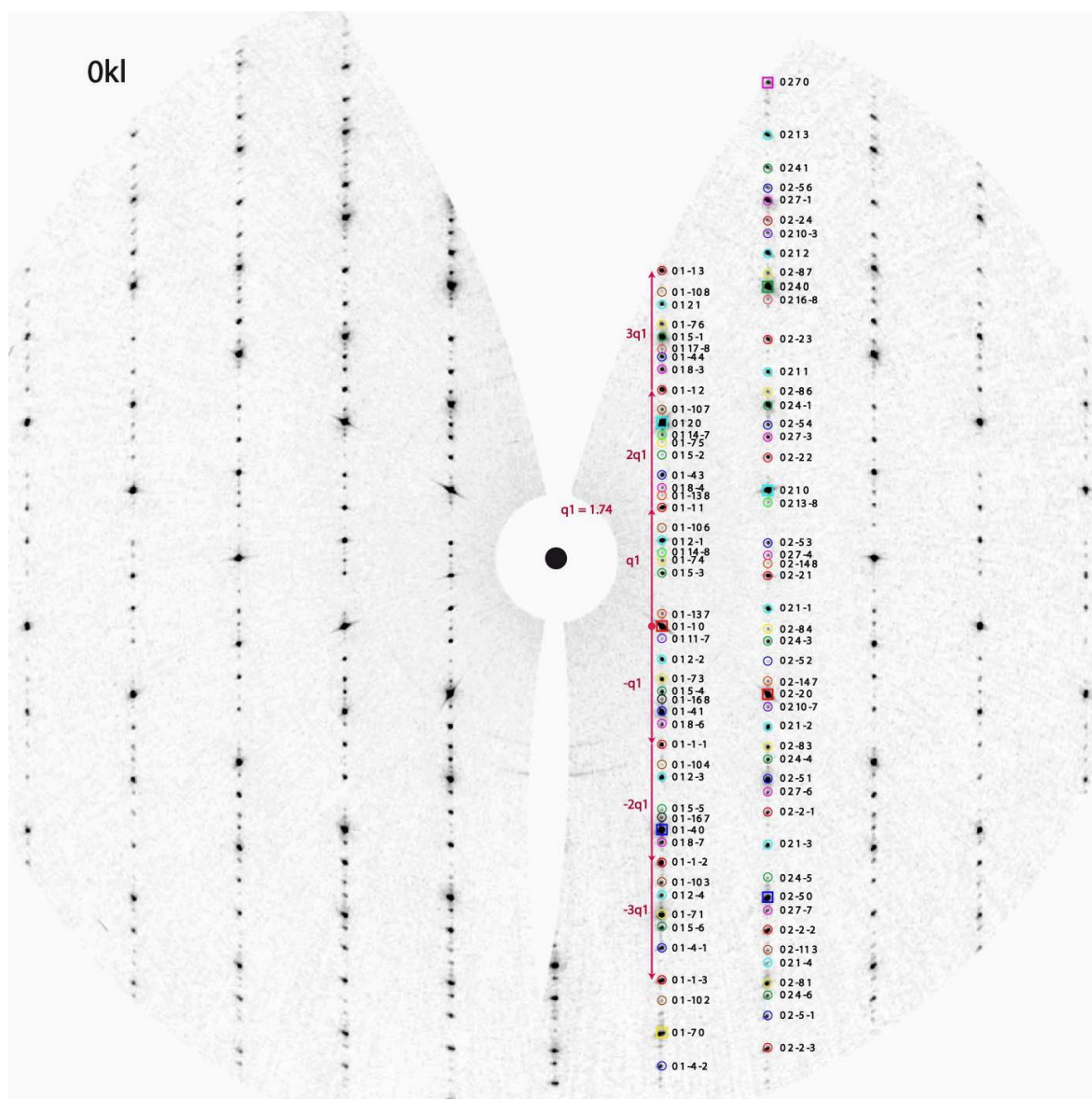


Figure A3. Reciprocal lattice section $0kl$ with the q -vector of 1.74 (red arrows) and identified reflections up to 8th order “satellites”. The satellite reflections are highlighted in the same color as the corresponding main reflections.

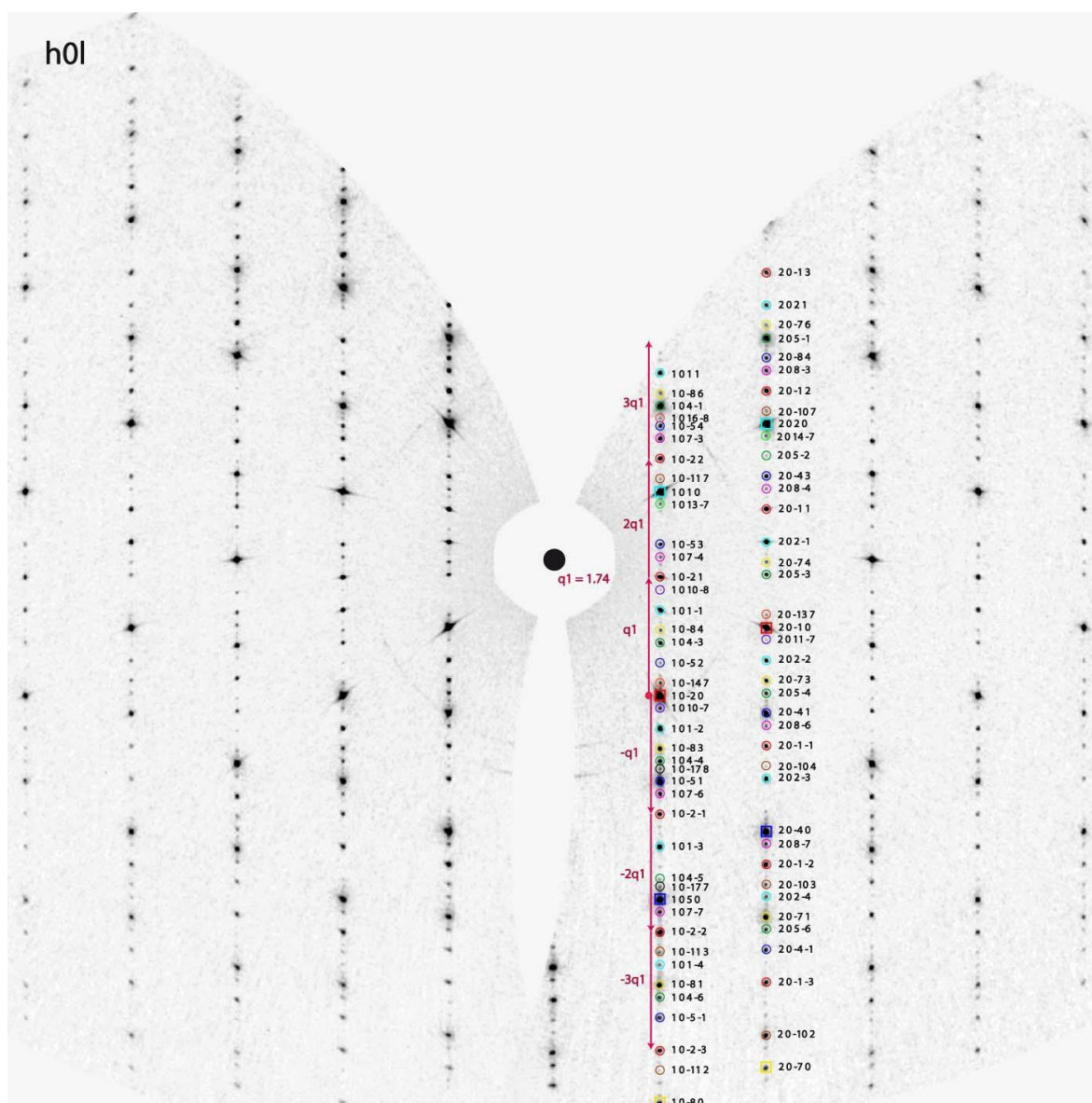


Figure A4. Reciprocal lattice section $h0l$ with the q -vector of 1.74 (red arrows) and identified reflections up to 8th order “satellites”. The satellite reflections are highlighted in the same color as the corresponding main reflections.

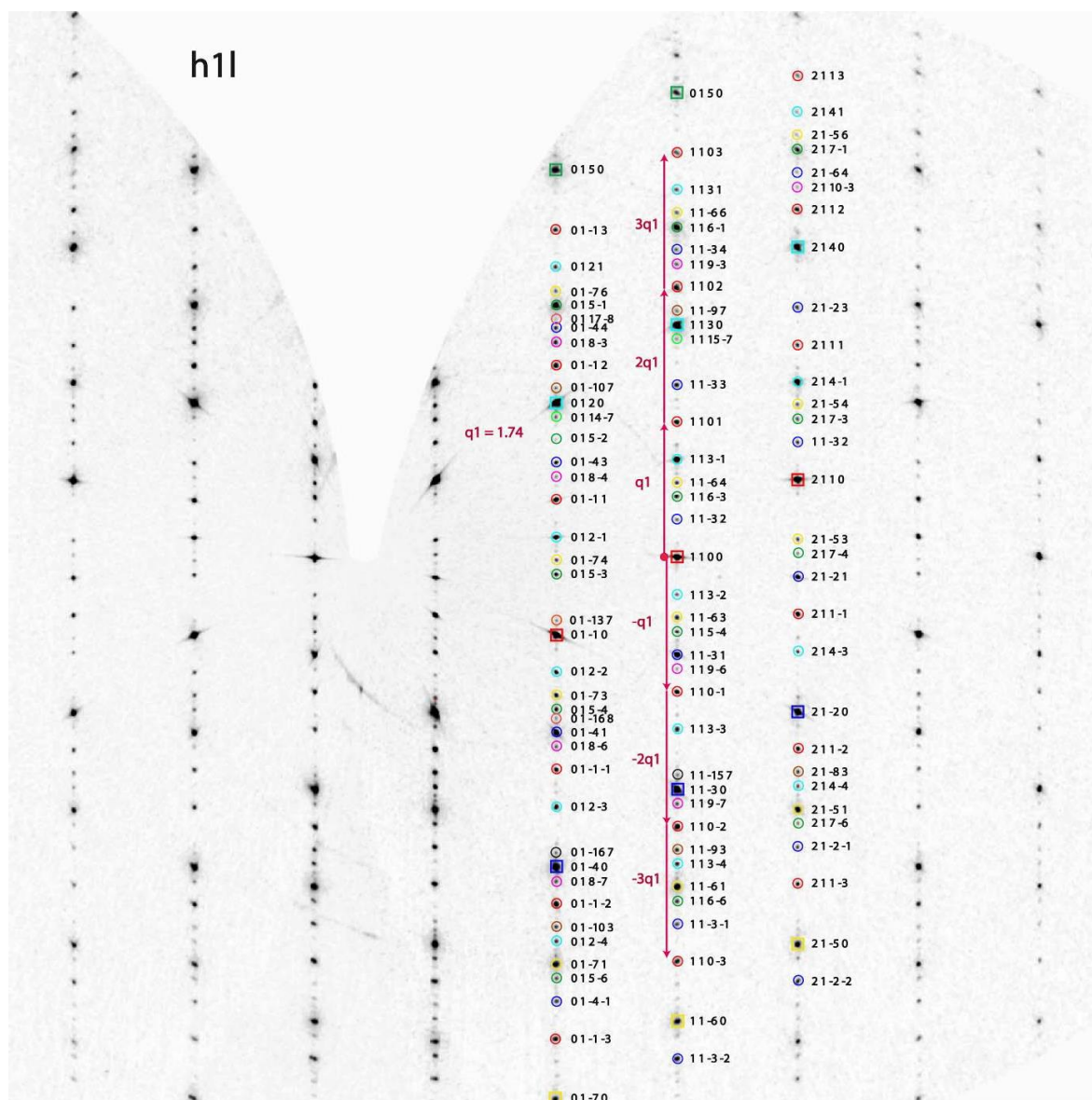


Figure A5. Reciprocal lattice section $h1l$ with the q -vector of 1.74 (red arrows) and identified reflections up to 8th order “satellites”. The satellite reflections are highlighted in the same color as the corresponding main reflections.

Refinement details. As a starting model, one Bi (Bi1) and Se atom (Se1) were set on the single atom site at the origin (0,0,0), both with formal full occupancy ($ai[Bi1] = ai[Se1] = 0.08333$). Note that in contrast to 3D structure refinements, the additional dimension in (3+1)D descriptions can be used to modulate the occupancy using discontinuous functions, e.g. crenel- or sawtooth-shaped.^[14] Crenel functions are specified by the width (δ) and the centre (x_4) and describe the modulation of occupancy by defining an interval in the additional dimension x_4 where the corresponding atom exists. In the refinement for $Sn_{2.8(4)}Bi_{20.2(4)}Se_{27}$, crenel functions combined with Legendre polynomials were used for both atoms. The crenel function of Bi1 has its center at $x_4[Bi1] = 0$ and a refined width of $\delta[Bi1] = 0.4602(12)$; the function of Se1 atom has its center at $x_4[Se1] = 0.5$ and a refined width of $\delta[Se1] = 0.5398(2)$. The sum of the overall width was constrained to 1 to retain full occupancy in x_4 . As the resulting structure model corresponds to a commensurate modulation, there is a corresponding 3D structure model in space group $R\bar{3}m$ with lattice parameters $a = 4.1819(4)$ Å and $c = 282.64(6)$ Å. It contains 150 atom layers forming double ("2"), quintuple ("5") and septuple ("7") slabs, which results in a stacking sequence symbolized by 7525757525|7525757525|7525757525. After the refinement of anisotropic atom displacement parameters, additional positional modulation waves for each atom were included. Since the $x_1 (= x)$ and $x_2 (= y)$ contribution of the q -vector is zero, the modulation functions are restricted to the $x_3 (z)$ direction. The positional modulation waves for Se (red) and Bi/Sn (green) thus only show displacements along the x_3 direction, which is displayed in the F_{obs} Fourier maps (Fig. S6). As a next step, $hklm$ reflections of $m = 5-8$ were excluded from the refinement due to their high $R1$ values compared to the other satellite orders; $m = 1-3$: $R1(all) = 0.09-0.11$, $m = 4$: $R1(all) = 0.28$, $m = 5-8$: $R1(all) = 0.41-1.31$. At this stage, the width of the Bi1 wave function refined to $\delta[Bi1] = 0.4608(10)$. This value was fixed at $\delta[Bi1] = 0.46$ in order to provide integer numbers of atoms in the unit cell of the commensurate structure. Note that STEM micrographs clearly show the commensurate structure. Therefore, the q -vector of $q = 1.74 = 87 / 50$ can also be written as a fraction of an integer number (87) and the number of atoms in one stacking period 7525757525 (50) (cf. Tab. S9). Sn (Sn1) was introduced into the structure with identical coordinates, modulations and displacement parameters as Bi1, including $\delta[Sn1] = \delta[Bi1]$. The occupancies were modulated in a complementary way with site occupancy factors $ai[Sn1] = 0.083333 - ai[Bi1]$,

i.e. constrained to full total occupancy. The refined value of $a_i[\text{Sn1}] = 0.014(2)$ corresponds to a seemingly uniform distribution of 17% Sn and 83% Bi on all cation sites. An additional occupancy wave for Sn1 and Bi1 reveals a varying distribution of 4% (Bi-Bi double layer) up to 16% Sn (central position in septuple layer) on the cation sites. Note that this seemingly yields a chemical composition that is slightly different from the model that assumed uniform distribution, i.e. the uniform distribution is not an “average” of the modulated one; this difference, however, is not significant within standard deviations. Fig. S7 shows the occupancy of the atoms Se (red), Bi (green) and Sn (black) as a function of the t variable in superspace. This graph displays where the corresponding atoms exist in the additional x_4 dimension. Note that this occupancy wave can be (rather incorrectly) modelled assuming a modulation of the displacement parameters for a uniform distribution of Sn and Bi on the cation sites. Such a modulation of the displacement parameters is not significant after applying the occupational wave. This corroborates a varying cation distribution, and no modulation of the displacement parameters was applied in the final model. The structure refinement results are displayed in Table S4. Information on the modulation parameters are given in Table S5 and S6.

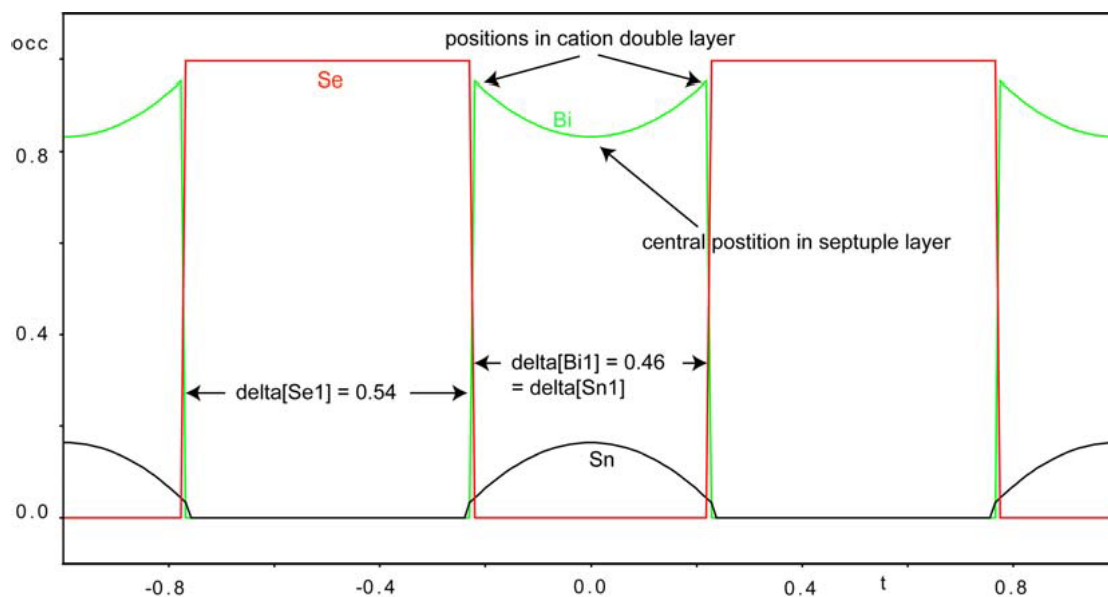


Figure A6. F_{obs} Fourier maps with the positional modulations waves for Se (red) and Bi/Sn (green), shown along x_1 (= x ; left) and x_3 (= z ; right) direction.

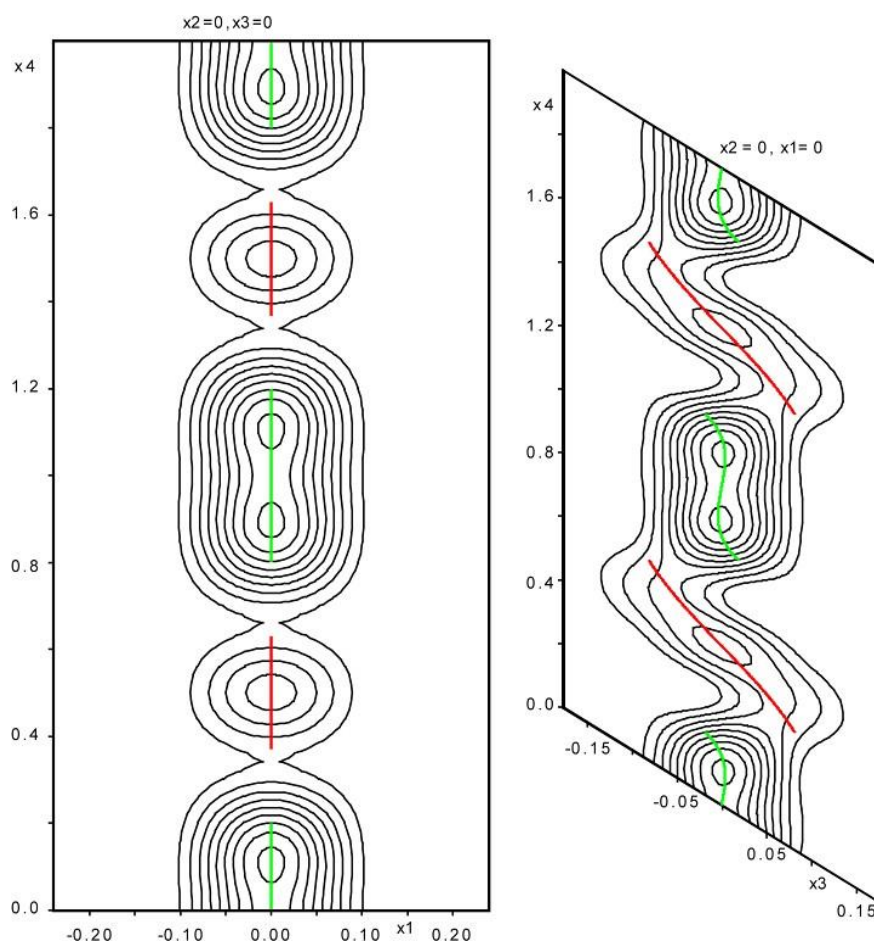


Figure A7. Graph showing the occupancy of the atoms Se (red), Bi (green) and Sn (black) as a function of the t variable in superspace. The Bi/Sn atom has its domain centered at $t = 0$ and the Se atom centered at $t = 0.5$.

Description of the structure model

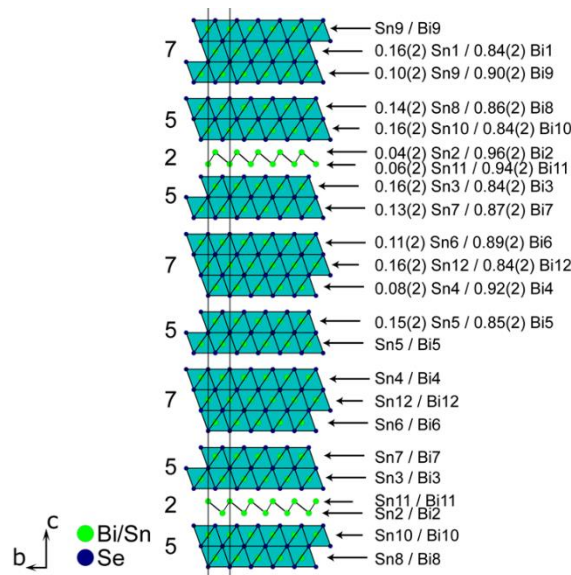


Figure A8. Characteristic part of the crystal structure of $\text{Sn}_{2.8(4)}\text{Bi}_{20.2(4)}\text{Se}_{27}$ with the stacking sequence 7525757525. The mixed occupancies of Sn and Bi are displayed for the different cation positions listed in Table S8. Site occupancies are given for the asymmetric unit, labelled atoms without s.o.f. values are symmetry-equivalent to the others.

Table A3. Bond lengths (in Å) derived from crystal structure analysis of $\text{Sn}_{2.8(4)}\text{Bi}_{20.2(4)}\text{Se}_{27}$ compared with (Sn)/Bi/Se compounds from literature.

Compound (and references)	Bi-Bi	Bi-Se (next to van der Waals gap)	Bi-Se (center)	Sn-Se (center)	Se-Se (at van der Waals gap)	Bi ₂ -Se [a]
Bi_2Se_3 [16]	-	2.85	3.08	-	3.52	-
BiSe [13]	3.05	2.91	3.03	-	3.51	3.27
Bi_8Se_9 [17]	3.06	2.94	2.95 - 3.07	-	3.45	3.26
Bi_8Se_7 [16] [b]	2.68 - 3.10	2.98 - 3.13	2.98 - 3.15	-	3.05	3.21 - 3.68
Bi_4Se_3 [18]	3.04	2.88	3.08	-	-	3.47
SnBi_2Se_4 [19]	-	2.80	3.17	2.95	3.72	-
$\text{Sn}_{0.57}\text{Bi}_{2.29}\text{Se}_4$ [20]	-	2.86	3.12	2.95	3.44	-
$\text{Sn}_{0.57}\text{Bi}_{2.29}\text{Se}_4$ [12]	-	2.85	3.11	2.96	3.48	-
$\text{Sn}_{2.8(4)}\text{Bi}_{20.2(4)}\text{Se}_{27}$	3.15	2.83 - 2.88	3.02 - 3.17	2.95 - 3.00	3.57	3.17

[a] bond length of Se atom to Bi atom (part of cation double layer)

[b] rather unreliable distances from imprecise coordinates derived from X-ray photographic film data, taking into account only 00ℓ reflections.

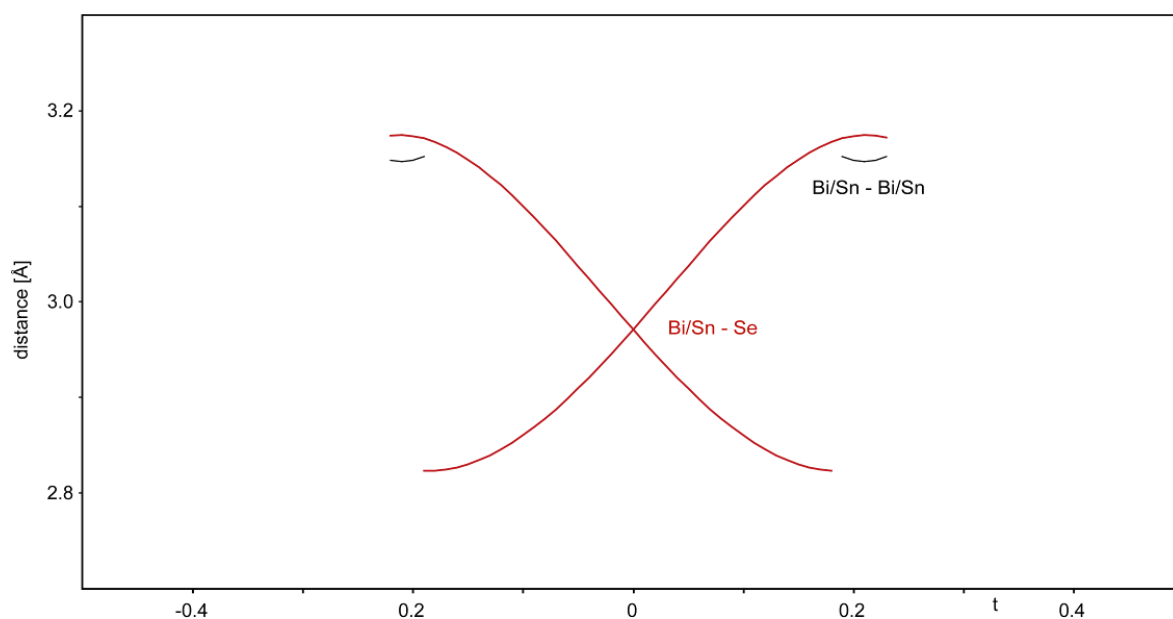


Figure A9. Graph of interatomic distances vs. the t variable of superspace. The Bi/Sn – Bi/Sn bonds in the double layers (corresponding to the structure of elemental Bi, cf. main manuscript) are displayed in black, the Bi/Sn – Se bonds within the quintuple and septuple layers are displayed in red.

Numerical refinement results

Table A4. Crystallographic data of the single-crystal structure refinement of $\text{Sn}_{2.8(4)}\text{Bi}_{20.2(4)}\text{Se}_{27}$ in $(3+1)\text{D}$ superspace.

Sum formula for basic unit cell	$\text{Sn}_{0.055(7)}\text{Bi}_{0.405(7)}\text{Se}_{0.54}$
Formula mass / $\text{g} \cdot \text{mol}^{-1}$	133.8
Superspace group	$R\bar{3}m(00\gamma)00$
Basic cell parameters / \AA	$a = 4.1819(4), c = 5.6528(5)$
$c_{\text{supercell}}$ (of commensurate 3D structure) / \AA	282.6(6)
q	$1.74 = 87/50$
X-ray density / $\text{g} \cdot \text{cm}^{-3}$	7.786
Temperature / K	295
Radiation	synchrotron, $\lambda = 0.29470 \text{ \AA}$
θ range / $^\circ$	2.32 – 17.42
μ / mm^{-1}	8.703
Reflections meas. / indep.	6375 / 411
$hklm$ range	$-6 \leq h \leq 6$ $-8 \leq k \leq 7$ $-11 \leq l \leq 11$ $-3 \leq m \leq 3$
Extinction method	type 1 Gaussian isotropic (JANA)
Extinction coefficient	530 (160)
Parameters	12
$R_{\text{int}}; R_{\sigma}$	0.0310; 0.0054
$R1$ [$I > 2\sigma(I)$] / $R1$ (all)	0.446 / 0.451
wR [$I > 2\sigma(I)$] / wR (all)	0.0678 / 0.0699
main reflections: $R1$ [$I > 2\sigma(I)$]	0.0481 / 0.0600
1 st order satellite reflections: $R1$ [$I > 2\sigma(I)$]	0.0384 / 0.494
2 nd order satellite: $R1$ [$I > 2\sigma(I)$]	0.0600 / 0.1086
3 rd order satellite: $R1$ [$I > 2\sigma(I)$]	0.0347 / 0.0504
Goof	1.62
$\Delta\rho$ (min./ max., $\text{e}\text{\AA}^{-3}$)	-2.56 / 6.10

Table A5. Atom sites, site occupancy factors (relative to general position),, resulting occupancies and modulation functions (details cf. Tab. S6) of the structure refinement in superspace.

Atoms	x	y	z	site occupancy factor (ai)	delta	Resulting occupancy	Occupational modulation	Positional modulation
Sn1 / Bi1	0	0	0	0.0733(13) / 0.0100(13)	0.46	0.055(7) / 0.405(7)	2 Legendre polynomials	2 Legendre polynomials
Se1	0	0	0	0.083333	0.54	0.54	1 Legendre polynomial	2 Legendre polynomials

Table A6. Anisotropic displacement parameters (in Å²) and modulation parameters of the structure refinement of Sn_{2.8(4)}Bi_{20.2(4)}Se₂₇ in (3+1)D superspace; $U_{eq} = 1/3[U_{11} + U_{22} + U_{33}]$.

Atoms	$U_{11} = U_{22} = 2 U_{12}$	U_{33}	U_{eq}	oort1	oort2	zort1	zort2	zort3	zort4
Bi1	0.0157(3)	0.0354(4)	0.0223(2)	0	0.0997(13)	-0.0051(2)	0	-0.0136(4)	0
Sn1	0.0157(3)	0.0354(4)	0.0223(2)	0	-0.7293(13)	-0.0051(2)	0	-0.0136(4)	0
Se1	0.0130(4)	0.0285(6)	0.0182(3)	-	-	-0.0855(5)	0	0.0046(7)	0

3D structure model. Sn_{2.8(4)}Bi_{20.2(4)}Se₂₇ can be described as a long-periodic 3D structure with a stacking sequence of 7525757525|7525757525|7525757525 built up from double (2), quintuple (5) and septuple (7) layers. The 3D structure can be derived from the commensurately modulated one. A tentative refinement in 3D has been performed by transforming the *hklm* file to a standard SHELX 3D *hkl* file by calculating ℓ_{3D} values: $\ell_{3D} = m \cdot (c_{supercell} / c_{basic\ cell}) + \ell_{4D} \cdot (c_{supercell} / c_{basic\ cell}) \cdot q$ with $c_{supercell} = c_{3D} = 50 \cdot c_{basic\ cell}$, i.e. the lattice parameter of the 3D model. The structure model derived from the commensurately modulated description was used as starting model. Site occupancies were fixed and the atom coordinates as well as isotropic displacement parameters were refined. The latter were set equal for all cations and all anions, respectively.

The sum formula Sn_{2.8(4)}Bi_{20.2(4)}Se₂₇ corresponds to 23 cations and 27 anions of a stacking sequence of 7525757525. Assuming Bi⁰ and Sn⁰ in the double layers (comparable to those in elemental Bi) and Sn²⁺, Bi³⁺ and Se²⁻ in the NaCl-type-like quintuple and septuple layers, the overall charge of the compound is neutral within standard deviations:

Sn_{2.8(4)}Bi_{20.2(4)}Se₂₇ = Bi_{3.8}Sn_{0.2} (two double layers) + Sn_{2.6(4)}Bi_{16.4(4)}Se₂₇ (five quintuple and three

septuple layers):

$$\rightarrow (3.8 \cdot 0 + 0.2 \cdot 0) + (2.6 \cdot 2 + 16.4 \cdot 3 - 27 \cdot 2) = 0.4 \text{ negative charges.}$$

Table A7. Crystallographic data of the structure refinement of $\text{Sn}_{2.8(4)}\text{Bi}_{20.2(4)}\text{Se}_{27}$ in 3D.Sum formula

Sum formula	$\text{Sn}_{2.8(4)}\text{Bi}_{20.2(4)}\text{Se}_{27}$
Formula mass / $\text{g} \cdot \text{mol}^{-1}$	6688.66
Space group	$R\bar{3}m$
Cell parameters / \AA	$a = 4.1819(4), c = 282.64(6)$
Cell volume / \AA^3	4280.7(12)
X-ray density / $\text{g} \cdot \text{cm}^{-3}$	7.784
Formula units per cell	3
$F(000)$	8207
Radiation	synchrotron, $\lambda = 0.29470 \text{ \AA}$
θ range / $^\circ$	3.32 – 14.18
Reflections meas. / indep.	896 / 131
$hklm$ range	$-6 \leq h \leq 6$ $-6 \leq k \leq 6$ $-437 \leq l \leq 400$
Parameters	28
$R_{\text{int}}; R_{\sigma}$	0.0251; 0.0081
$R1 [I > 2\sigma(I)] / R1 (\text{all})$	0.0410 / 0.0411
$wR [I > 2\sigma(I)] / wR (\text{all})$	0.1018 / 0.1018
Goof	1.248
$\Delta\rho$ (min./ max., $\text{e}\text{\AA}^{-3}$)	-2.06/ 1.40

Table A8. Wyckoff positions, atomic coordinates, site occupancies and isotropic displacement parameters (in Å²) for the commensurable 3D structure model of Sn_{2.8(4)}Bi_{20.2(4)}Se₂₇. The *z* positions and *U*_{iso} have been refined for each atom. Site occupancy factors were taken from the refinement in (3+1)D and not refined. The *z* coordinates of the starting model as derived from the refinement in superspace are given as a comparison.

Atom	Wyckoff position	<i>x</i>	<i>y</i>	<i>z</i>	<i>z</i> derived from (3+1)D model	s.o.f.	<i>U</i> _{iso}
Sn1/Bi1	3 <i>a</i>	0	0	0	0	0.16/0.84	0.0156(4)
Sn2/Bi2	3 <i>a</i>	0	0	0.0609(1)	0.0597	0.04/0.96	0.0156(4)
Sn3/Bi3	6 <i>c</i>	0	0	0.0808(1)	0.0800	0.016/0.84	0.0156(4)
Sn4/Bi4	6 <i>c</i>	0	0	0.1396(5)	0.1399	0.08/0.92	0.0156(4)
Sn5/Bi5	6 <i>c</i>	0	0	0.1593(2)	0.1599	0.15/0.85	0.0156(4)
Sn6/Bi6	6 <i>c</i>	0	0	0.2196(3)	0.2200	0.11/0.89	0.0156(4)
Sn7/Bi7	6 <i>c</i>	0	0	0.2395(3)	0.2399	0.13/0.87	0.0156(4)
Sn8/Bi8	6 <i>c</i>	0	0	0.3004(3)	0.3001	0.14/0.86	0.0156(4)
Sn9/Bi9	6 <i>c</i>	0	0	0.3204(4)	0.3200	0.10/0.90	0.0156(4)
Sn10/Bi10	6 <i>c</i>	0	0	0.3801(4)	0.3801	0.16/0.84	0.0156(4)
Sn11/Bi11	6 <i>c</i>	0	0	0.4005(4)	0.4002	0.06/0.94	0.0156(4)
Sn12/Bi12	6 <i>c</i>	0	0	0.4600(9)	0.4600	0.16/0.84	0.0156(4)
Se1	6 <i>c</i>	0	0	0.0197(8)	0.0185	1	0.0124(6)
Se2	6 <i>c</i>	0	0	0.0401(15)	0.0401	1	0.0124(6)
Se3	6 <i>c</i>	0	0	0.0986(7)	0.0987	1	0.0124(6)
Se4	6 <i>c</i>	0	0	0.1203(7)	0.1204	1	0.0124(6)
Se5	6 <i>c</i>	0	0	0.1792(9)	0.1790	1	0.0124(6)
Se6	6 <i>c</i>	0	0	0.2012(7)	0.2007	1	0.0124(6)
Se7	6 <i>c</i>	0	0	0.2588(10)	0.2592	1	0.0124(6)
Se8	6 <i>c</i>	0	0	0.2812(9)	0.2809	1	0.0124(6)
Se9	6 <i>c</i>	0	0	0.3406(1)	0.3395	1	0.0124(6)
Se10	6 <i>c</i>	0	0	0.3613(7)	0.3612	1	0.0124(6)
Se11	6 <i>c</i>	0	0	0.4198(8)	0.4197	1	0.0124(6)
Se12	6 <i>c</i>	0	0	0.4405(10)	0.4414	1	0.0124(6)
Se13	6 <i>c</i>	0	0	0.4778(2)	0.4784	1	0.0124(6)
Se14	6 <i>c</i>	0	0	1/2	1/2	1	0.0124(6)

Comparison with other compounds

Table A9. Comparison of $\text{Sn}_{2.8(4)}\text{Bi}_{20.2(4)}\text{Se}_{27}$ with other Bi-Se compounds that can be described by a (3+1)D superspace formalism, where the commensurate modulation vector determines the actual 3D structure and thus the stacking sequence;^[15] $q = 3 (N_{\text{Se}} + N_{\text{Bi/Sn-Bi/Sn}}) / N$ with N_{Se} = number of Se atom layers per unit cell, $N_{\text{Bi/Sn-Bi/Sn}}$ = number of Bi/Sn-Bi/Sn double layers (comparable to those in elemental Bi) per unit cell and N = total number of atom layers per unit cell.

Sum formula	Space group	$c / \text{\AA}$	q vector	Number of atom layers per unit cell	Slabs in the unit cell
Bi_2Se_3	$R\bar{3}m$	28.6	$27/15 = 9/5 = 1.800$	15	3x Se-Bi-Se-Bi-Se (5)
Bi_8Se_9	$R\bar{3}m$	97.1	$90/51 = 30/17 = 1.765$	51	9x Se-Bi-Se-Bi-Se (5) 3x Bi-Bi (2)
BiSe	$P\bar{3}m1$	22.9	$21/12 = 7/4 = 1.750$	12	2x Se-Bi-Se-Bi-Se (5) Bi-Bi (2)
$\text{Sn}_{2.8(4)}\text{Bi}_{20.2(4)}\text{Se}_{27}$	$R\bar{3}m$	282.6	$261/150 = 87/50 = 1.740$	150	15x Se-Bi/Sn-Se-Bi/Sn-Se (5) 9x Se-Bi/Sn-Se-Bi/Sn-Se-Bi/Sn-Se (7) 6x Bi/Sn-Bi/Sn (2)
Bi_8Se_7	$P\bar{3}m1$	85.7	$78/45 = 26/15 = 1.733$	45	7x Se-Bi-Se-Bi-Se (5) 5x Bi-Bi (2)
Bi_4Se_3	$R\bar{3}m$	40	$36/21 = 12/7 = 1.714$	21	3x Se-Bi-Se-Bi-Se (5) 3x Bi-Bi (2)

Additional electron diffraction data, STEM images and image of STEM sample

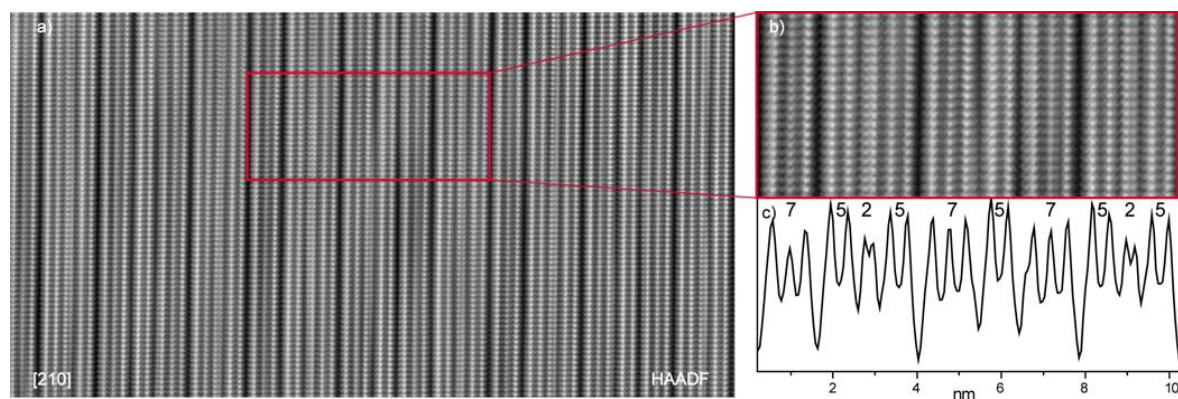


Figure A10. a, b) Fourier-filtered STEM-HAADF image along zone axis [210] (Fourier filtered); c) 2D plot of the projected intensity observed in the red box of the left image. The peaks show the stacking sequence 75257525, which had also been revealed by single-crystal data.

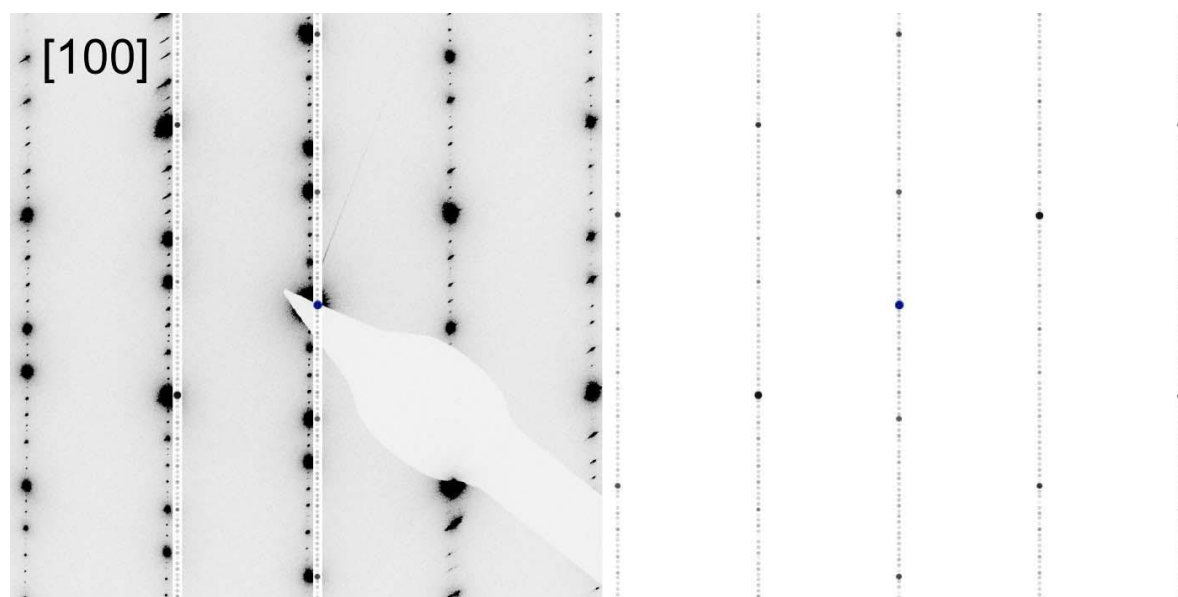


Figure A11. Comparison of an experimental SAED pattern (left) along the [100] zone axis with simulated SAED pattern (middle); the model for simulation was taken from the commensurate structure model in $R\bar{3}m$ with the atom coordinates resulting from the refinement in (3+1)D superspace.

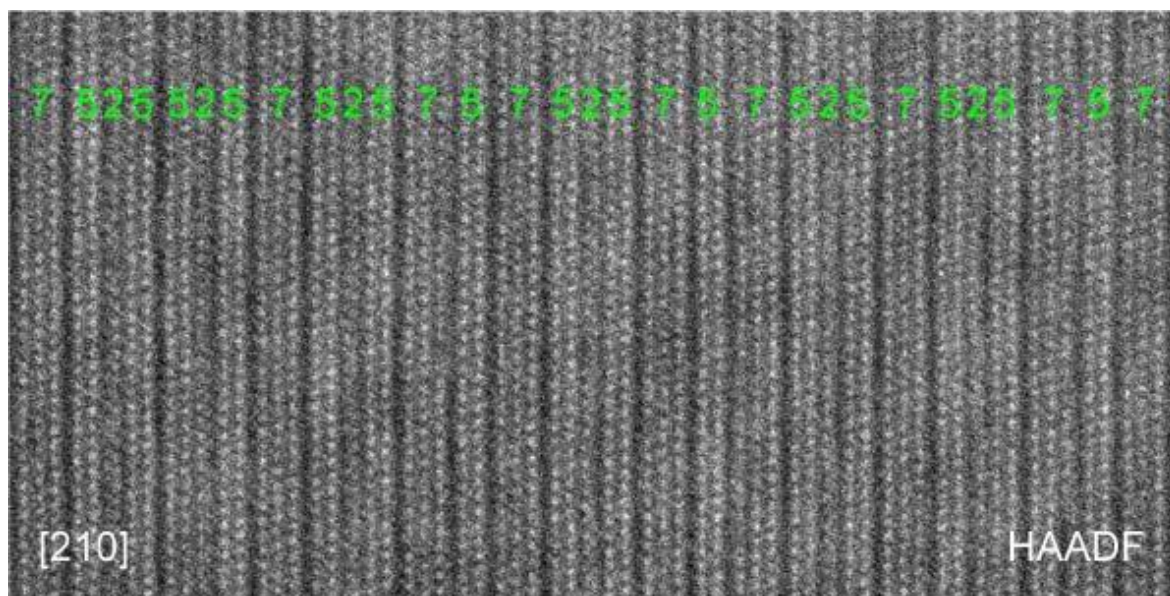


Figure A12. Unfiltered STEM-HAADF image along zone axis [210] showing stacking faults.

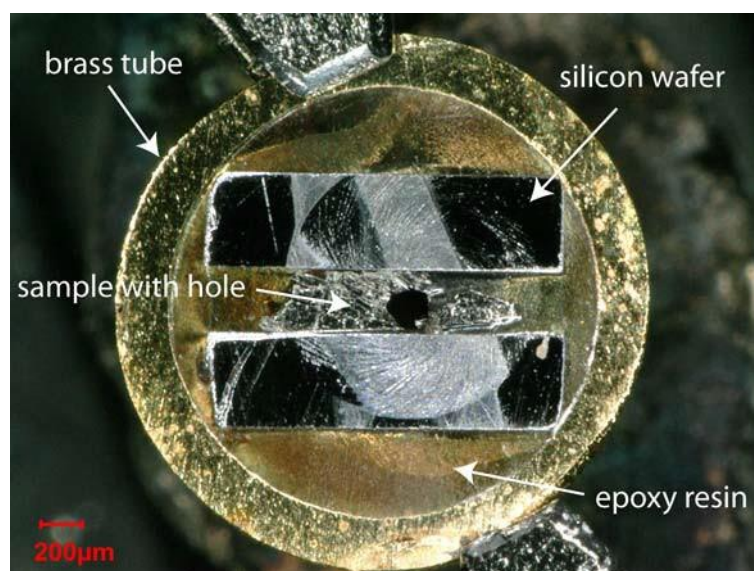


Figure A13. Picture of the prepared sample (cf. experimental section) used for STEM studies.

References

- [1] F. Heinke, P. Urban, A. Werwein, C. Fraunhofer, T. Rosenthal, S. Schwarzmüller, D. Souchay, F. Fahrnbauer, V. Dyadkin, G. Wagner, O. Oeckler, *Inorg. Chem.* **2018**, *57*, 4427-4440.
- [2] *Genesis*, v 6.1, EDAX, Mahwah, USA, **2010**.
- [3] *analySIS*, v 2.1, Olympus Soft Imaging Solutions, Münster, Germany, **1996**.
- [4] a) P. A. Stadelmann, *jEMS*, v 4.4631 U2016, CIME-EPFL, Lausanne, Switzerland, **2016**;
b) P.A. Stadelmann, *Ultramicroscopy* **1987**, *21*, 131-145.
- [5] Gatan Software Team, Digital Micrograph, v. 3.6.5, **1999**.
- [6] J. L. Lábár, *Ultramicroscopy* **2005**, *103*, 237-249.
- [7] J.-C. Labiche, O. Mathon, S. Pascarelli, M. A. Newton, G. G. Ferre, C. Curfs, G. Vaughan, A. Homs, D. F. Carreiras, *Rev. Sci. Instrum.* **2007**, *78*, 091301.
- [8] *CrysAlis Pro*, Agilent Technologies, Yarnton, Oxfordshire, England, **2015**.
- [9] G. Wu, B. L. Rodrigues, P. Coppens, *J. Appl. Crystallogr.* **2002**, *35*, 356-359.
- [10] V. Petríček, M. Dušek, L. Palatinus, *Z. Kristallogr.* **2014**, *229*, 345-352.
- [11] G. M. Sheldrick, *Acta Crystallogr. Sect. C* **2015**, *71*, 3-8.
- [12] K. Brandenburg, *Diamond*; Crystal Impact GbR, Bonn, Germany, **2014**.
- [13] M. M. Stasova, *J. Struct. Chem.* **1967**, *8*, 584-589.
- [14] a) M Dušek, V Petříček, L Palatinus, *J. Phys. Conf. Ser.* **2010**. 226, 012014; b) G. Oszlányi, A. Süto, *Acta Crystallogr. Sect. A* **2004**. *60*, 134-141.
- [15] H. Lind, S. Lidin, *Solid State Sci.* **2003**, *5*, 47-57.
- [16] S. Nakajima, *J. Phys. Chem. Solids* **1963**, *24*, 479-485.
- [17] R. M. Imamov, S. A. Semiletov, *Sov. Phys. Crystallogr.* **1971**, *15*, 845-850.
- [18] M. M. Stasova, *Inorg. Mater.* **1968**, *4*, 21-23.

- [19] A. A. Sher, I. N. Odin, A. V. Novoselova, *Inorg. Mater.* **1978**, *14*, 993-998.
- [20] C. Pérez Vicente, J. L. Tirado, K. Adouby, J. C. Jumas, A. Abba Touré, G. Kra, *Inorg. Chem.* **1999**, *38*, 2131-2135.

B Supporting Information for Chapter 3

Experimental Procedures

Preparation of starting materials

P_3N_5 was prepared following a procedure by Stock et al. by heating P_4S_{10} (Sigma-Aldrich, 99,99%) in a constant flow of ammonia gas (5.0, Air Liquide). After drying a fused silica tube and a fused silica boat in a tube furnace (at 1273 K) under dynamic vacuum ($<10^{-3}$ mbar) the boat was loaded with P_4S_{10} in a constant flow of Ar. The apparatus was saturated with ammonia for 4 h and the temperature was increased to 1123 K and maintained for four additional hours. Then, the furnace was cooled to room temperature afterward and heating/cooling ramps were set at 5 K/min each. The product was obtained as an orange powder and purity was confirmed by PXRD as well as CHNS analysis (C 0%, H 0%, N 42.69%, S 0%).^[6]

The azides $AE(N_3)_2$ ($AE = \text{Sr, Ba}$) were prepared by reaction of the respective alkaline earth carbonates (SrCO_3 : Sigma Aldrich, 99.995 %; BaCO_3 : Grüssing, 99.8 %) with in situ generated HN_3 .^[7] An aqueous solution of NaN_3 (Acros Organics, 99 %) was passed through a cation exchanger (Amberlyst 15). Formed HN_3 dropped into a suspension of the alkaline earth carbonate in water until it became clear and the pH of the eluate was neutral. Residual carbonate was filtered off and the water was removed with a rotary evaporator (50 mbar, 40°C). The products were obtained as colorless powders, recrystallized from acetone, and dried under vacuum. The purity of the alkaline earth azides was confirmed by PXRD.

Amorphous Si_3N_4 (UBE, SNA-00) and NH_4F (Sigma Aldrich, $\geq 98\%$) were used as purchased.

High-pressure high-temperature synthesis

The nitridosilicatephosphates $AE\text{SiP}_3\text{N}_7$ ($AE = \text{Sr, Ba}$) were obtained by high-pressure high-temperature synthesis using a 1000 t press with a modified Walker-type multianvil apparatus.^[8–12] All products were synthesized from stoichiometric amounts of P_3N_5 , Si_3N_4 , the respective alkaline earth azide, and 5 wt% NH_4F (Table S1). Owing to the air and moisture sensitivity of the azides, the starting materials were handled in an Ar-filled glovebox (Unilab, MBraun, Garching, $\text{O}_2 < 1$ ppm, $\text{H}_2\text{O} < 0.1$ ppm) and ground thoroughly in an agate mortar. The

mixture was transferred into a cylindrical crucible made from hexagonal boron nitride (HeBoSint® S100, Henze, Kempten, Germany) and sealed with a boron nitride cap. The crucible was then placed in a specially prepared octahedron (MgO, doped with Cr₂O₃ (5 %), edge length 18 mm, Ceramic Substrates & Components, Isle of Wight, UK), which was drilled through and loaded with different components. First, a ZrO₂ sleeve (Cesima Ceramics, Wust-Fischbeck, Germany) was fixed in the borehole and closed on one side by a Mo plate. Then, a long graphite tube (Schunk Kohlenstofftechnik GmbH, Gießen, Germany), a MgO spacer (Cesima Ceramics, Wust-Fischbeck, Germany), and a short graphite tube were put into the octahedron. While ZrO₂ served as a thermal insulator, the two graphite tubes were used as electrical resistance furnace; the combination of two single tubes is necessary to decrease the temperature gradient. After inserting the crucible with the sample, the assembly was completed by adding a second MgO spacer and a further Mo plate to ensure a symmetric setup. In order to generate approximately hydrostatic conditions, the uniaxial force of the hydraulic press was converted by a Walker-type module with inserted steel wedges, forming a cubic cavity. This cavity was filled with eight Co-doped (7 %) WC cubes (Hawedia, Marklkofen, Germany). In order to enclose the sample octahedron, the edges of the WC cubes were truncated (11 mm edge length). Furthermore, four of the cubes were equipped with a PTFE film (Vitaflon Technische Produkte GmbH, Bad Kreuznach, Germany) for electrical insulation. The remaining cubes were prepared with pyrophyllite gaskets (Ceramic Substrates & Components, Isle of Wight, UK) to prevent the outflow of the MgO octahedron. Bristol board (369 g m⁻²) was used to fix the gaskets.^[13-15] Different pressure and temperature settings were used (SrSiP₃N₇: 8 GPa, ~1700 °C; BaSiP₃N₇: 8 GPa, ~1400 °C).

Powder X-ray diffraction

Powder X-ray diffraction was carried out on StadiP diffractometers (STOE & Cie, Darmstadt, Germany) equipped with a MYTHEN 1K detector (Dectris, Baden, Switzerland; angular range $\Delta 2\theta = 12.5^\circ$), either a Mo- or Cu-source and a Ge(111) monochromator for Mo-K α_1 or Cu-K α_1 radiation. Samples were filled into glass capillaries with 0.3 mm diameter and 0.01 mm wall thickness (Hilgenberg GmbH, Malsfeld, Germany). Data were recorded in the angular range between $2\theta = 5-76^\circ$ (BaSiP₃N₇) and $2\theta = 5-120^\circ$ (SrSiP₃N₇) with a step width of 0.015°/step. Diffraction data were analyzed with the TOPAS-Academic V6 software. Structure models

were refined with the Rietveld method. Estimated standard deviations were calculated by TOPAS-Academic using the matrix inversion method.

Scanning electron microscopy and energy-dispersive X-ray spectroscopy (EDX)

Samples were placed on conducting carbon foil and coated with carbon. EDX spectra were collected using a FEI Helios Nanolab G3 Dual Beam UC (FEI, Hillsboro, OR, USA) with an attached X-Max 80 SDD detector (Oxford Instruments, Abingdon, UK).

(Scanning) transmission electron microscopy

Samples were ground in absolute ethanol and a drop of the resulting suspension was cast on a TEM grid with holey carbon film (Plano GmbH, Wetzlar, Germany). The grid was mounted on a double-tilt holder and transferred into a Cs DCOR probe-corrected Titan Themis 300 (FEI, USA) TEM equipped with X-FEG, post-column filter (Enfinium ER-799), US1000XP/FT camera system (Gatan, Germany), and a windowless, 4-quadrant Super-X EDX detector. TEM images were recorded using a $4k \times 4k$ FEI Ceta CMOS camera. The microscope was operated at 300 kV accelerating voltage for SAED and STEM-HAADF and -EDX (convergence angle of 16.6 mrad, 50 μm aperture, detector inner half angle 33 mrad for 245 mm camera length). For evaluation of the TEM data, the following software was used: Digital Micrograph (Fourier filtering of STEM images), ProcessDiffraction7 (geometric calculations for SAED), JEMS (SAED simulations), Velox v2.8 (Thermo Fisher Scientific, USA).

Solid-state MAS NMR spectroscopy

Solid-state NMR measurements were performed on an Avance III 500 spectrometer (Bruker, Karlsruhe) equipped with an 11.7 T magnet operating at 500.25 MHz ^1H frequency and a commercial double-resonance MAS probe. The sample was ground and loaded in a ZrO_2 rotor with an outer diameter of 2.5 mm. NMR spectra were collected at 20 kHz spinning frequency.

Single-crystal X-ray diffraction

Single-crystal X-ray diffraction data were collected on a Bruker D8 Venture TXS diffractometer (rotating anode, Mo- $\text{K}\alpha$ radiation, $\lambda = 0.71073 \text{ \AA}$, multilayer monochromator) by combined φ - and ω -scans. Indexing, integration, semi-empiric absorption correction

(based on equivalent reflections), were performed by the APEX3 software package. Employing SHELX-2018, the structure was solved by direct methods and refined against F^2 by the full-matrix least-squares method.^[16]

Bond-valence sum (BVS) Calculations

BVS calculations were performed using the software VaList v4.0.7.^[17,18] The structure models of $AE\text{SiP}_3\text{N}_7$ ($AE = \text{Sr}, \text{Ba}$) were taken into account with either all tetrahedra centers occupied by P, occupied by Si, or a mixed occupation of $\text{P}_{0.5}\text{Si}_{0.5}$ where it was indicated by BVS values.

FTIR spectroscopy

FTIR spectra of the title compounds were collected on a Spectrum BX II spectrometer (PerkinElmer, Waltham, MA, USA) between 600 and 4400 cm^{-1} with DuraSampler attenuated total reflectance unit (ATR).

Polyhedra volumes

Comparisons of the different tetrahedra volumes were performed using the software VESTA v3.4.0.^[19]

Luminescence measurements

Luminescence spectra of Eu^{2+} -doped samples were examined on a HORIBA Fluoromax4 spectrofluorimeter system with an Olympus BX51 microscope. Emission spectra were collected at room temperature with $\lambda_{\text{exc}} = 400$, in a range from 400 to 800 nm (step width: 2 nm).

Results and Discussion

Synthesis

Table B1 Weighed portions of starting materials for the syntheses of $AE\text{SiP}_3\text{N}_7$ ($AE = \text{Sr}, \text{Ba}$).

Title compounds		Starting material / mg		
SrSiP_3N_7	$\text{Sr}(\text{N}_3)_2$	P_3N_5	Si_3N_4	NH_4F
	16.79	15.94	4.57	2
BaSiP_3N_7	$\text{Ba}(\text{N}_3)_2$	P_3N_5	Si_3N_4	NH_4F
	19.36	19.00	8.18	2

Structure determination

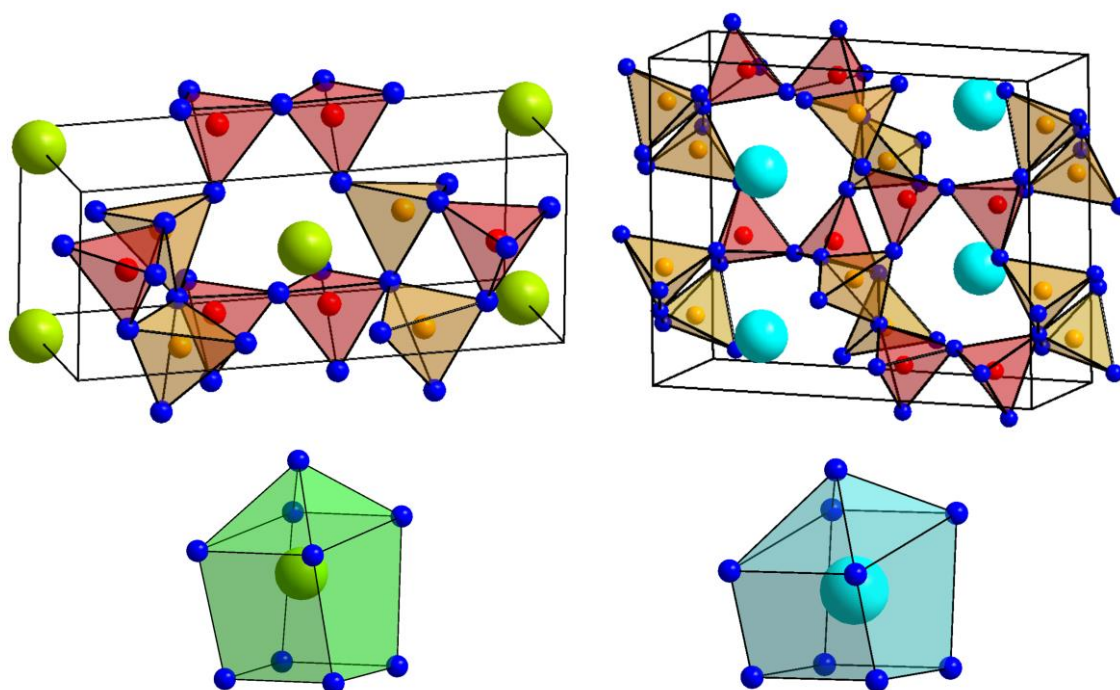


Figure B1. Structure representations of SrSiP_3N_7 (top left) and BaSiP_3N_7 (top right) and corresponding $AE\text{N}_9$ polyhedra (bottom) (Sr green, Ba light blue, P red, $\text{Si}_{0.5}\text{P}_{0.5}$ orange and N blue).

B Supporting Information for Chapter 3

Table B2 Atomic coordinates, isotropic displacement parameters/ \AA^2 , and occupancy of SrSiP_3N_7 .

Atom	Wyckoff	x	y	z	U_{eq}	$s.o.f.$
Sr1	$2a$	0	0.70251(11)	0.00052(11)	0.01702(15)	1
P1	$4b$	0.11859(5)	0.17613(14)	0.5034(3)	0.00453(14)	1
P2 Si2	$4b$	0.24912(6)	0.31942(15)	0.0235(2)	0.00528(15)	0.5 0.5
N1	$4b$	0.3615(2)	0.1391(6)	0.0785(7)	0.0085(5)	1
N2	$4b$	0.2811(2)	0.6332(6)	0.1667(6)	0.0062(4)	1
N3	$4b$	0.1305(2)	0.2367(7)	0.1673(7)	0.0083(5)	1
N4	$2a$	0	0.2788(9)	0.6213(10)	0.0083(7)	1

Table B3 Anisotropic displacement parameters for SrSiP_3N_7 with standard deviations in parentheses.

Atom	U_{11}	U_{22}	U_{33}	U_{23}	U_{13}	U_{12}
Sr1	0.0160(2)	0.0231(2)	0.0119(2)	0.0004(3)	0	0
P1	0.0046(3)	0.0045(3)	0.0045(3)	0.0000(4)	0.0005(3)	0.00006(18)
P2 Si2	0.0059(3)	0.0055(3)	0.0045(3)	0.0004(3)	0.0002(3)	0.0004(2)
N1	0.0088(10)	0.0051(10)	0.0116(12)	-0.0014(8)	-0.0020(8)	0.0001(9)
N2	0.0061(9)	0.0071(10)	0.0053(10)	-0.0002(9)	0.0002(8)	-0.0011(8)
N3	0.0071(10)	0.0136(12)	0.0043(10)	0.0016(9)	-0.0004(8)	-0.0015(9)
N4	0.0028(13)	0.0134(17)	0.0087(17)	-0.0010(13)	0	0

Table B4 Atomic coordinates, isotropic displacement parameters/ \AA^2 , and occupancy of BaSiP_3N_7 .

Atom	Wyckoff	x	y	z	U_{eq}	$s.o.f.$
Ba1	$4c$	0.14950(3)	0.25	0.76102(6)	0.01189(8)	1
P1	$8d$	0.40923(7)	0.13039(6)	0.29058(14)	0.00225(13)	1
P2 Si2	$8d$	0.15603(8)	0.00047(6)	0.28611(15)	0.00256(14)	0.5 0.5
N1	$8d$	0.0612(3)	0.1098(2)	0.3097(6)	0.0065(4)	1
N2	$4c$	0.3567(4)	0.25	0.2000(8)	0.0068(6)	1
N3	$8d$	0.3045(3)	0.0401(2)	0.1254(5)	0.0039(4)	1
N4	$8d$	0.1108(3)	0.6112(2)	0.1231(5)	0.0058(4)	1

B Supporting Information for Chapter 3

Table B5 Anisotropic displacement parameters for BaSiP₃N₇ with standard deviations in parentheses.

Atom	U_{11}	U_{22}	U_{33}	U_{23}	U_{13}	U_{12}
Ba1	0.01304(13)	0.01160(12)	0.01103(12)	0	0.00102(10)	0
P1	0.0018(3)	0.0028(3)	0.0021(3)	-0.0003(2)	-0.0002(2)	-0.0003(2)
P2 Si2	0.0028(3)	0.0033(3)	0.0016(3)	0.0000(2)	0.0001(3)	0.0000(2)
N1	0.0036(10)	0.0063(10)	0.0097(11)	-0.0013(8)	-0.0017(9)	0.0004(9)
N2	0.0091(15)	0.0030(13)	0.0083(15)	0	-0.0022(13)	0
N3	0.0036(10)	0.0038(10)	0.0043(9)	-0.0007(8)	-0.0001(8)	-0.0016(9)
N4	0.0074(11)	0.0058(11)	0.0042(9)	0.0005(8)	0.0005(8)	0.0023(9)

Table B6 Interatomic distances (Å) and bond angles (°) in the structure of BaSiP₃N₇.

Ba1	N1	2x	2.872(3)	N1	-P1-	N4	112.68(14)
	N2	1x	2.921(4)	N1		N2	111.60(17)
	N4	2x	2.987(3)	N1		N3	109.65(13)
	N4	2x	3.132(3)	N4		N2	110.76(17)
P1	N1	2x	3.230(3)	N4	-P2 Si2-	N3	106.33(13)
	N1	1x	1.598(3)	N2		N3	105.43(16)
	N4	1x	1.604(3)	N4		N1	123.79(14)
	N2	1x	1.6062(18)	N4		N3	105.02(13)
P2 Si2	N3	1x	1.703(3)	N4		N3	105.35(13)
	N4	1x	1.627(3)	N1		N3	107.47(13)
	N1	1x	1.635(3)	N1		N3	106.97(13)
	N3	1x	1.724(3)	N3		N3	107.32(9)
	N3	1x	1.726(3)				

B Supporting Information for Chapter 3

Table B7 Interatomic distances (Å) and bond angles (°) in the structure of SrSiP₃N₇.

Sr1	N1	2x	2.696(3)	N4	-P1-	N3	111.0(2)
	N4	1x	2.735(4)	N4		N1	110.99(19)
	N3	2x	2.876(3)	N4		N2	107.28(18)
	N3	2x	3.149(3)	N3		N1	112.31(18)
	N1	2x	3.270(3)	N3		N2	106.02(15)
P1	N4	1x	1.605(2)	N1		N2	109.01(16)
	N3	1x	1.609(4)	N3	-P2 Si2-	N1	121.41(16)
	N1	1x	1.604(3)	N3		N2	104.84(16)
	N2	1x	1.704(3)	N3		N2	104.59(15)
P2 Si2	N3	1x	1.624(3)	N1		N2	113.53(16)
	N1	1x	1.631(3)	N1		N2	103.82(14)
	N2	1x	1.722(3)	N2		N2	107.70(11)
	N2	1x	1.727(3)				

EDX measurements

Table B8. EDX measurements (several point analyses) for AESiP₃N₇ (AE = Sr, Ba) compared to values derived from sum formulas.

atom %	Sr	Si	P	N	O
	8.3	9.5	25.4	56.8	0
	9.2	7.1	24.4	53.4	5.9
	8.2	9.4	25.1	53.7	3.5
	7.3	7.1	21.6	57.2	6.9
	5.9	6.1	19.8	64.9	3.2
	6.1	6.2	20.3	61.0	6.2
	7.3	7.1	21.6	57.2	6.9
	6.0	6.1	20.1	61.4	6.3
calc.	8.3	8.3	25	58.3	0
	Ba	Si	P	N	O
	9.2	8.4	26.6	51.5	4.3
	8.9	7.3	25.9	50.2	7.7
	8.2	7.9	24.8	54.8	4.3
	8.3	7.5	27.4	48.1	8.7
	6.3	5.7	21.4	56.8	9.9
calc.	8.3	8.3	25	58.3	0

Rietveld refinements

Table B9. Crystallographic data from the Rietveld refinements for $AE\text{SiP}_3\text{N}_7$ ($AE = \text{Sr}, \text{Ba}$), standard deviations are given in parentheses. For BaSiP_3N_7 , both polytypes were taken into account.

	SrSiP ₃ N ₇	BaSiP ₃ N ₇	
phase fraction	92.2(9)*)	96.3(1)	3.7(1)
crystal system	orthorhombic	orthorhombic	orthorhombic
space group	<i>Pmn</i> 2 ₁ (no. 31)	<i>Pnma</i> (no. 62)	<i>Pmn</i> 2 ₁ (no. 31)
formula units/ unit cell	2	4	2
lattice parameters / Å	<i>a</i> = 11.9975(2)	<i>a</i> = 9.90917(5)	<i>a</i> = 11.9975(2)
	<i>b</i> = 4.9236(1)	<i>b</i> = 12.19036(8)	<i>b</i> = 4.9236(1)
	<i>c</i> = 4.70029(9)	<i>c</i> = 4.73862(3)	<i>c</i> = 4.70029(9)
radiation λ / Å	1.54056 (Cu-K _{α1})	0.70930(Mo-K _{α1})	
cell volume / Å ³	277.65(1)	572.409(6)	283.28(6)
2θ– range/°	5 <2θ< 120	5 <2θ< 76.35	
refined parameters	29	32	
(incl. side phases)			
background function	Shifted Chebyshev (12 parameters)		
<i>R</i> -values	<i>R</i> _p = 0.0609	<i>R</i> _p = 0.0296,	
	<i>wR</i> _p = 0.0929	<i>wR</i> _p = 0.0396	
	<i>R</i> _{Bragg} = 0.0353	<i>R</i> _{Bragg} = 0.0165	<i>R</i> _{Bragg} = 0.0191

*) Si_3N_4 as a side phase

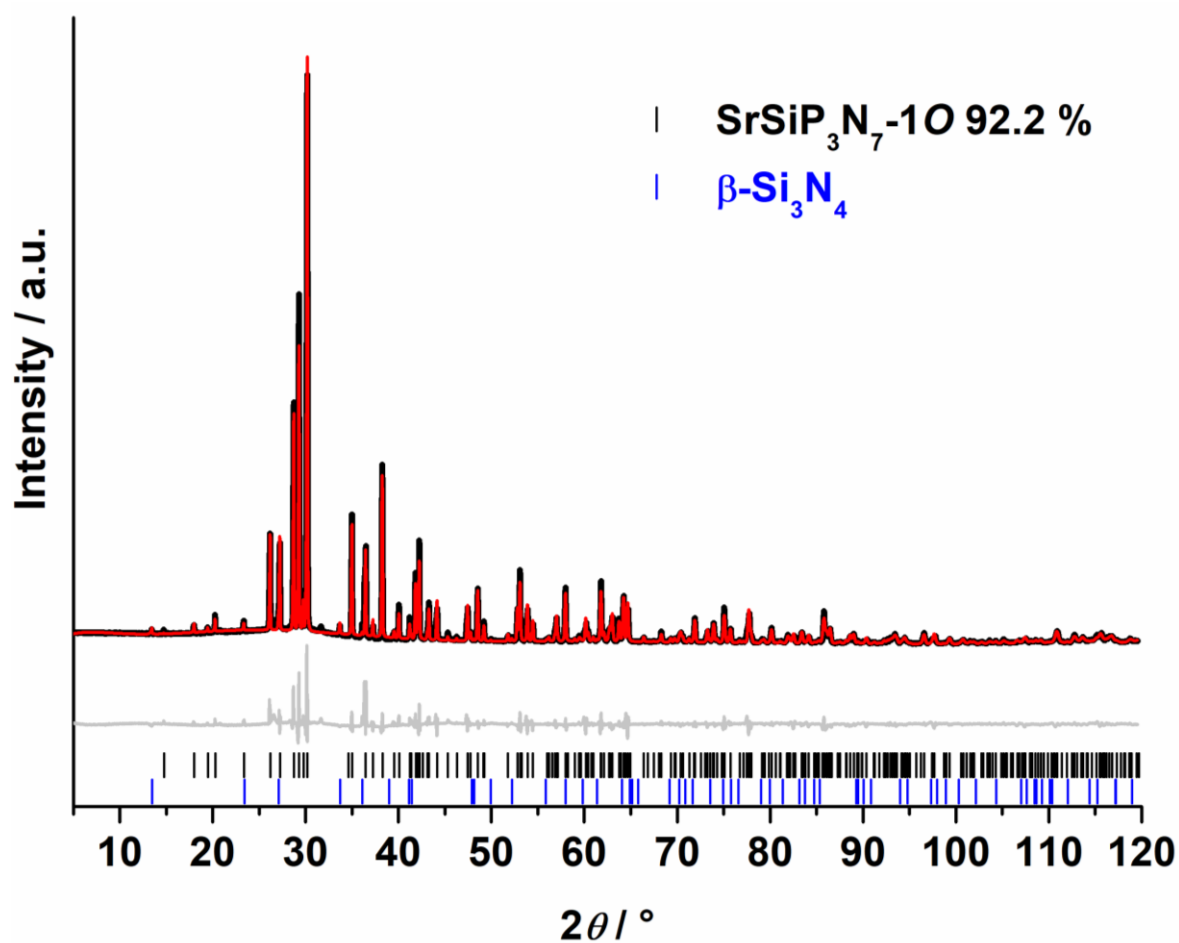


Figure B2. Rietveld refinement for $\text{SrSiP}_3\text{N}_7\text{-10}$; observed (black line) and calculated (red line) X-ray powder diffraction patterns, positions of Bragg reflections of $\text{SrSiP}_3\text{N}_7\text{-10}$ (vertical black bars), $\beta\text{-Si}_3\text{N}_4$ (vertical blue bars), and difference profile (gray line).

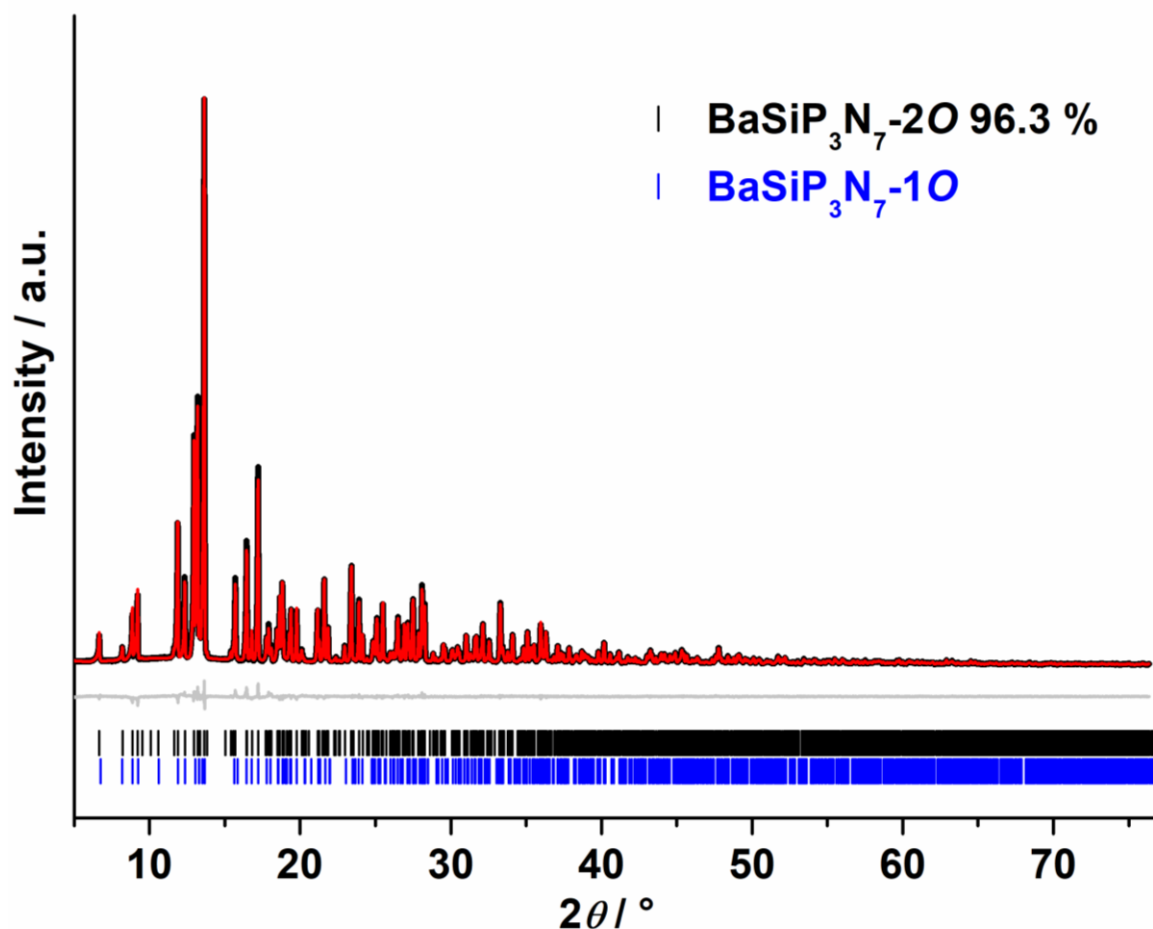


Figure B3. Rietveld refinement for BaSiP₃N₇-2O; observed (black line) and calculated (red line) X-ray powder diffraction patterns, positions of Bragg reflections of BaSiP₃N₇-2O (vertical black bars), BaSiP₃N₇-1O (vertical blue bars), and difference profile (gray line).

Polyhedra volumes

Table B10 Tetrahedra volumes of several known nitridosilicates and nitridophosphates.

TN ₄ volumes in Å ³			
	SiN ₄		PN ₄
Sr ₂ Si ₅ N ₈ ^[20]	2.5450, 2.7127	BaP ₂ N ₄ ^[21]	2.2816
La ₃ Si ₆ N ₁₁ ^[22]	2.6125, 2.6964	BaP ₈ N ₁₄ ^[23]	2.1911, 2.2289
Ce ₅ Si ₃ N ₉ ^[24]	2.5182, 2.7600, 2.5840	Ce ₂ P ₃ N ₇ ^[25]	2.2511, 2.2805
SrSi ₇ N ₁₀ ^[26]	2.6844, 2.6067, 2.6183	Cs ₃ P ₆ N ₁₁ ^[27]	2.2299
CeSi ₃ N ₅ ^[28]	2.6041, 2.6677, 2.6199	LiPN ₂ ^[29]	2.2687
LiSi ₂ N ₃ ^[30]	2.6870	BP ₃ N ₆ ^[31]	2.2223, 2.1882, 2.1313
LaSi ₃ N ₅ ^[28]	2.6907, 2.6425, 2.6265	NaP ₄ N ₇ ^[32]	2.2465, 2.2310
∅	2.6398		2.2292

Table B11. Tetrahedra volumes for SrSiP₃N₇ in space groups Pnm2₁, P2₁, Pn, and Pm. Red values indicate deviations from expected volumes for PN₄ tetrahedra ($V \sim 2.2 \text{ \AA}^3$).

Tetrahedra volumes/ \AA^3	<i>Pnm2₁</i>	<i>P2₁</i>	<i>Pn</i>	<i>Pm</i>
1	2.2423	2.2177	2.2225	2.2212
2	2.4024	2.2183	2.2162	2.2124
3	-	2.3779	2.3758	2.3703
4	-	2.3753	2.3754	2.3860

Table B12. Tetrahedra volumes for BaSiP₃N₇ in space groups Pnma, Pna2₁, P2₁/c, and P2₁ma. Red values indicate deviations from expected volumes for PN₄ tetrahedra ($V \sim 2.2 \text{ \AA}^3$).

Tetrahedra volumes/ \AA^3	<i>Pnma</i>	<i>Pna2₁</i>	<i>P2₁/c</i>	<i>P2₁ma</i>
1	2.2105	2.2076	2.2128	2.1965
2	2.3839	2.3915	2.2084	2.4043
3	-	2.2118	2.3825	2.3639
4	-	2.3718	2.3850	2.2300

BVS calculations

Table B13. BVS for SrSiP₃N₇ in space group Pnm2₁ and subgroups P2₁, Pn, and Pm. The structures were refined against SCXRD with all tetrahedra center positions occupied by P. Red values indicate mixed occupancy of P/Si (BVS P_{0.5}Si_{0.5} = 4.5).

Atom	<i>Pnm2₁</i>	<i>P2₁</i>	<i>Pn</i>	<i>Pm</i>
Sr1	1.63	1.67	1.67	1.67
Sr2	-	-	-	1.67
P1	4.92	5.00	4.99	4.99
P2	4.40	4.99	5.01	5.02
P3	-	4.47	4.47	4.49
P4	-	4.48	4.47	4.45

Table B14. BVS for SrSiP₃N₇ in space group Pnm2₁ and subgroups **P2₁**, **Pn**, and **Pm**. The structures were refined against SCXRD with all tetrahedra center positions occupied by Si. Red values indicate mixed occupancy of P/Si (BVS P_{0.5}Si_{0.5} = 4.5).

Atom	<i>Pnm2₁</i>	<i>P2₁</i>	<i>Pn</i>	<i>Pm</i>
Sr1	1.63	1.68	1.67	1.67
Sr2	-	-	-	1.68
Si1	5.22	5.31	5.32	5.30
Si2	4.62	5.31	5.32	5.33
Si3	-	4.69	4.70	4.70
Si4	-	4.70	4.69	4.67

Table B15. BVS for SrSiP₃N₇ in space group Pnm2₁ and subgroups **P2₁**, **Pn**, and **Pm**. The structure models were refined against SCXRD with tetrahedra center positions occupied by P (positions with a BVS value of ~5) and tetrahedra center positions occupied by P_{0.5}Si_{0.5} (positions with a BVS value of ~4.5). Red values show a mixed occupancy of P/Si with their respective occupation factor indicated by BVS.

Atom	<i>Pnm2₁</i>	<i>P2₁</i>	<i>P1n1</i>	<i>Pm</i>
Sr1	1.63	1.68	1.68	1.68
Sr2	-	-	-	1.68
Si1/P1	4.91	5.00	4.99	4.99
Si2/P2	4.65/4.40 48/52	4.99	5.01	5.01
Si3/P3	-	4.71/4.46 43/57	4.71/4.47 43/57	4.74/4.49 41/59
Si4/P4	-	4.72/4.47 42/58	4.71/4.46 43/57	4.69/4.44 45/55

Table B16. BVS for BaSiP₃N₇ in space group Pnma and subgroups **Pna2₁**, **P2₁ma**, and **P2₁/c**. The structure models were refined against SCXRD with all tetrahedra center positions occupied by P. Red values indicate mixed occupancy of P/Si (BVS P_{0.5}Si_{0.5} = 4.5).

Atom	<i>Pnma</i>	<i>Pna2₁</i>	<i>P2₁/c</i>	<i>P2₁ma</i>
Ba1	2.46	2.47	2.46	2.43
Ba2	-	-	-	2.54
P1	5.01	5.01	5.01	5.06
P2	4.42	4.44	5.02	4.38
P3	-	5.03	4.44	4.45
P4	-	4.43	4.43	4.93

Table B17. BVS for BaSiP₃N₇ in space group Pnma and subgroups Pna2₁, P2₁ma, and P2₁/c. The structure models were refined against SCXRD with all tetrahedra center positions occupied by Si. Red values indicate mixed occupancy of P/Si (BVS P_{0.5}Si_{0.5} = 4.5).

Atom	<i>Pnma</i>	<i>Pn2₁a</i>	<i>P2₁/c</i>	<i>P2₁ma</i>
Ba1	2.46	2.46	2.46	2.43
Ba2	-	-	-	2.53
Si1	5.30	5.27	5.30	5.30
Si2	4.68	4.70	5.30	4.59
Si3	-	5.35	4.68	4.73
Si4	-	4.66	4.67	5.25

Table B18. BVS for BaSiP₃N₇ in space group Pnma and subgroups Pna2₁, P2₁ma, and P2₁/c. The structure models were refined against SCXRD with tetrahedra center positions occupied by P (positions with a BVS value of ~5) and tetrahedra center positions occupied by P_{0.5}Si_{0.5} (positions with a BVS value of ~4.5). Red values show a mixed occupancy of P/Si with their respective occupation factor indicated by BVS.

Atom	<i>Pnma</i>	<i>Pn2₁a</i>	<i>P2₁/c</i>	<i>P2₁ma</i>
Ba1	2.46	2.47	2.46	2.57
Ba2	-	-	-	2.40
Si1/P1	5.01	4.99	5.01	4.94
Si2/P2	4.68/4.43	4.69/4.44	5.02	4.69/4.45
	46/54	45/55		44/66
Si3/P3	-	5.04	4.68/4.44	4.63/4.39
			45/55	49/51
Si4/P4	-	4.68/4.43	4.67/4.43	5.05
		45/55	46/54	

Solid-state NMR spectra

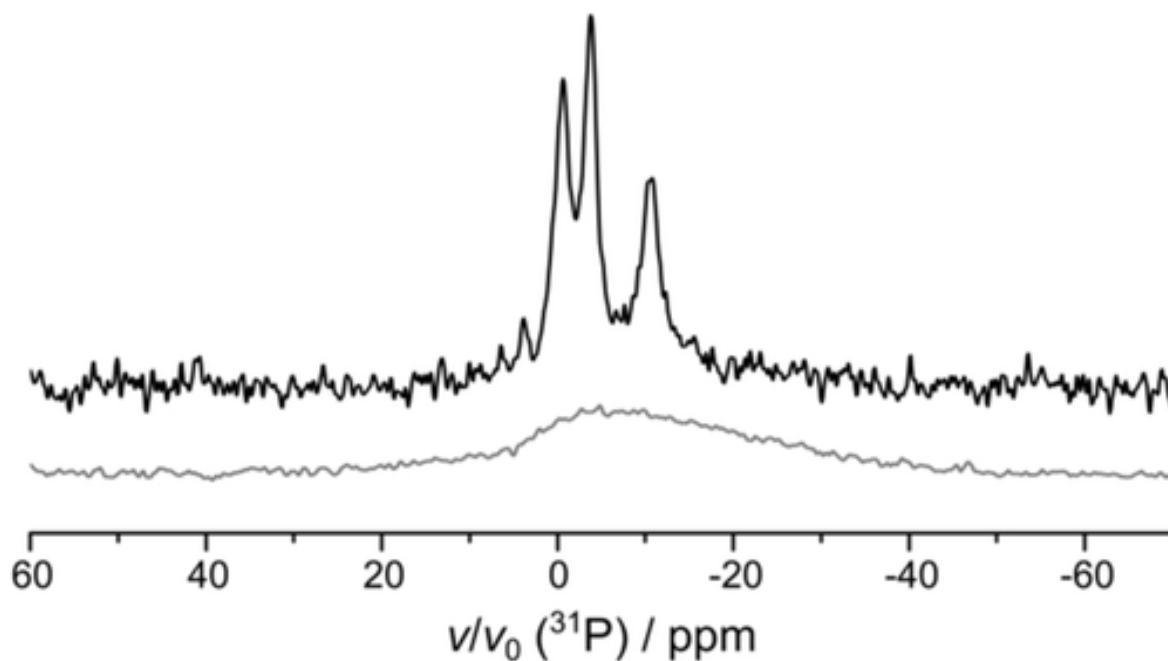


Figure B4. ³¹P solid-state NMR spectrum (MAS) of BP₃N₆ showing three narrow signals (fwhm < 5 ppm).^[31]

(Scanning) transmission electron microscopy

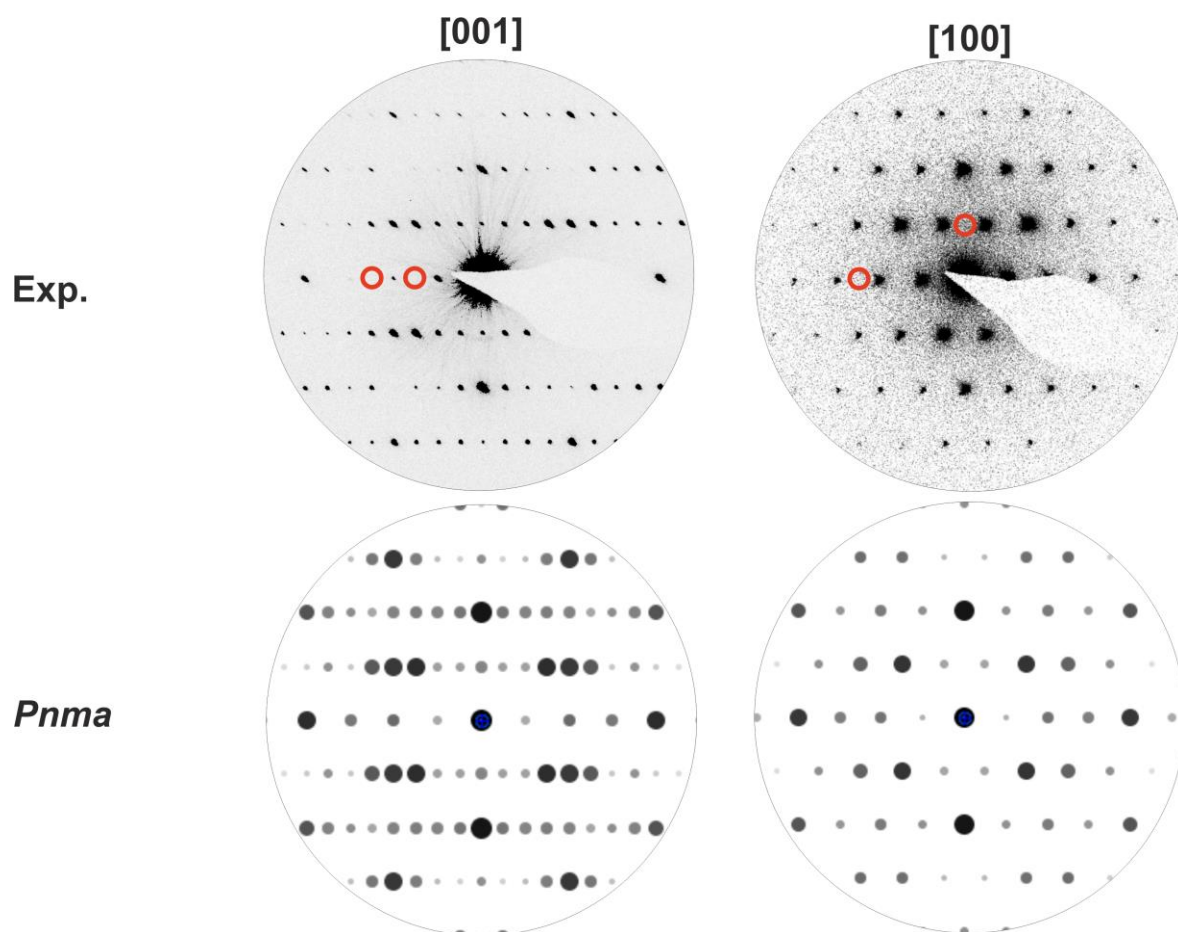


Figure B5. Experimental electron diffraction patterns of BaSiP₃N₇ (top) and simulations for the final structure model in *Pnma*. Reflections, affected by systematic absences, are marked by a red circle.

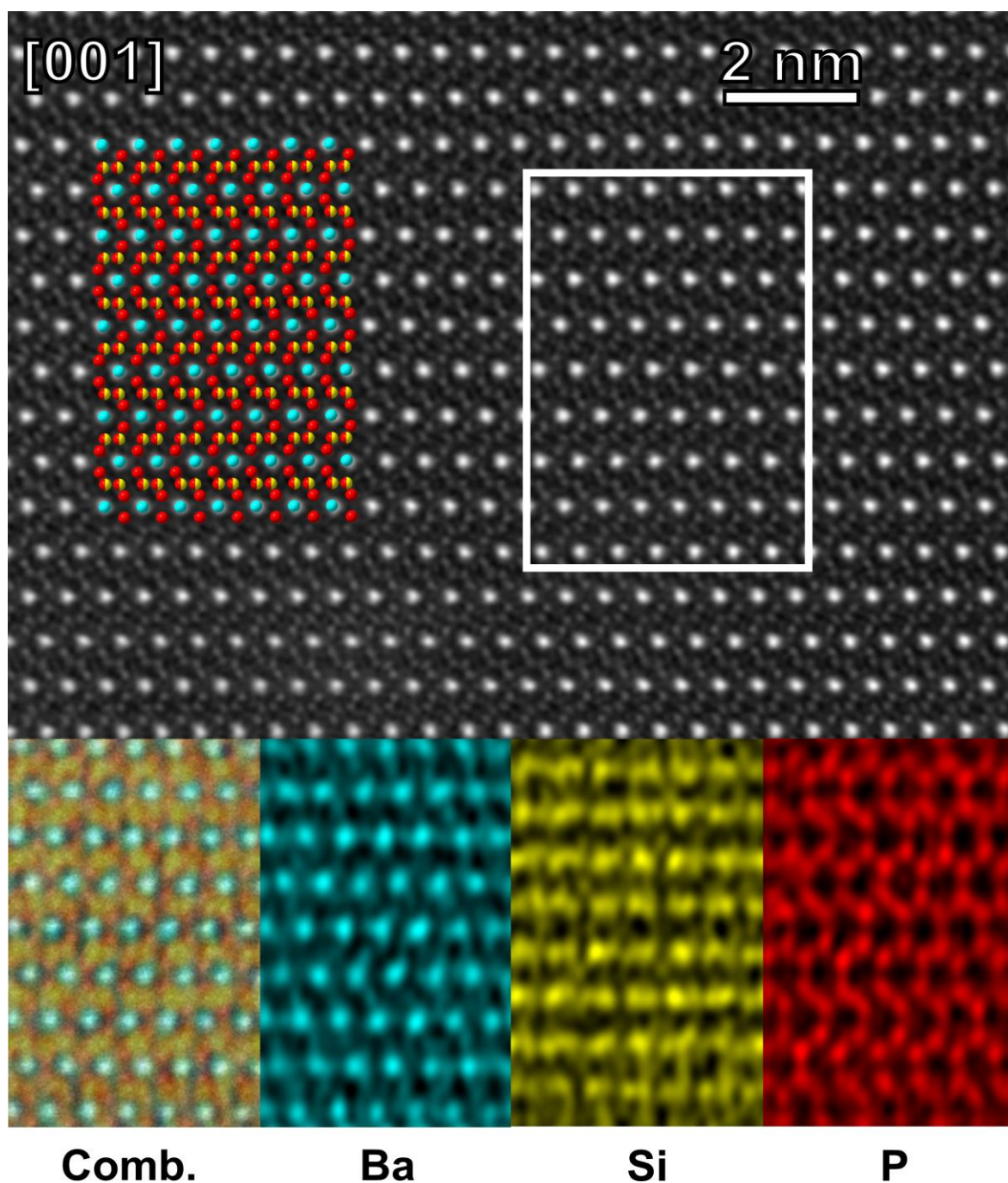


Figure B6. STEM and EDX mapping of BaSiP₃N₇ along [001]. STEM HAADF image (top) with structure overlay (Ba cyan, P red, Si yellow). The inset shows the corresponding area for EDX maps (bottom, atomic resolution) with a combined color map, Ba map (light blue), Si map (yellow), and P map (red).

FTIR spectra

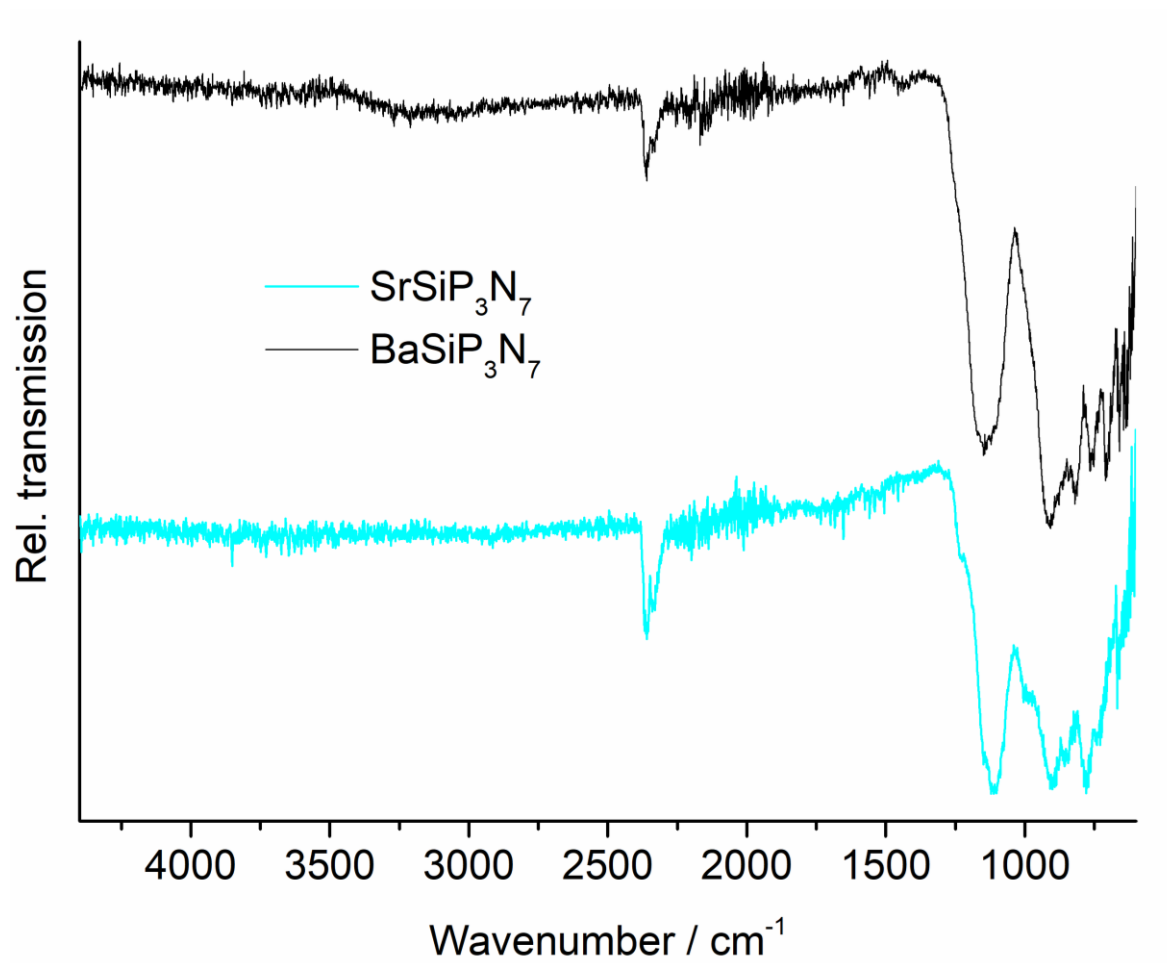


Figure B7. FTIR spectra for SrSiP₃N₇ (blue) and BaSiP₃N₇ (black).

References

- [1] A. Stock, H. Grüneberg, *Ber. Dtsch. Chem. Ges.* **1907**, *40*, 2573–2578.
- [2] R. Suhrmann, K. Clusius, *Z. Anorg. Allg. Chem.* **1926**, *152*, 52–58.
- [3] H. Huppertz, *Z. Kristallogr.* **2004**, *219*, 330–338.
- [4] N. Kawai, S. Endo, *Rev. Sci. Instrum.* **1970**, *41*, 1178–1181.
- [5] D. C. Rubie, *Phase Transitions* **1999**, *68*, 431–451.
- [6] D. Walker, M. A. Carpenter, C. M. Hitch, *Am. Mineral.* **1990**, *75*, 1020–1028.
- [7] W. David, *Am. Mineral.* **1991**, *76*, 1092–1100.
- [8] A. Marchuk, L. Neudert, O. Oeckler, W. Schnick, *Eur. J. Inorg. Chem.* **2014**, *2014*, 3427–3434.
- [9] M. Mallmann, S. Wendl, P. Strobel, P. J. Schmidt, W. Schnick, *Chem. Eur. J.* **2020**, *26*, 6257–6263.
- [10] E. Bertschler, R. Niklaus, W. Schnick, *Chem. Eur. J.* **2017**, *23*, 9592–9599.
- [11] G. M. Sheldrick, *Acta Crystallogr. Sect. C* **2015**, *71*, 3–8.
- [12] N. E. Brese, M. O’Keeffe, *Acta Crystallogr. Sect. B* **1991**, *47*, 192–197.
- [13] A. S. Wills, *Valist*, Program available from www.ccp14.ac.uk
- [14] K. Momma, F. Izumi, *J. Appl. Crystallogr.* **2011**, *44*, 1272–1276.
- [15] T. Schlieper, W. Milius, W. Schnick, *Z. Anorg. Allg. Chem.* **1995**, *621*, 1380–1384.
- [16] F. W. Karau, W. Schnick, *J. Solid State Chem.* **2005**, *178*, 135–141.
- [17] H. Yamane, T. Nagura, T. Miyazaki, *Acta Crystallogr. Sect. E* **2014**, *70*, i23–i24.
- [18] S. Wendl, L. Eisenburger, P. Strobel, D. Günther, J. P. Wright, P. J. Schmidt, O. Oeckler, W. Schnick, *Chem. Eur. J.* **2020**, *26*, 7292–7298.
- [19] C. Schmolke, D. Bichler, D. Johrendt, W. Schnick, *Solid State Sci.* **2009**, *11*, 389–394.

- [20] S. D. Kloß, N. Weidmann, R. Niklaus, W. Schnick, *Inorg. Chem.* **2016**, *55*, 9400–9409.
- [21] G. Pilet, H. A. Höppe, W. Schnick, S. Esmaeilzadeh, *Solid State Sci.* **2005**, *7*, 391–396.
- [22] K. Landskron, W. Schnick, *J. Solid State Chem.* **2001**, *156*, 390–393.
- [23] M. Woike, W. Jeitschko, *Inorg. Chem.* **1995**, *34*, 5105–5108.
- [24] R. Marchand, P. L'Haridon, Y. Laurent, *J. Solid State Chem.* **1982**, *43*, 126–130.
- [25] J. David, Y. Laurent, J.-P. Charlot, J. Lang, *Bull. Soc. Fr. Mineral. Cristallogr.* **1973**, *96*, 21–24.
- [26] S. Vogel, A. T. Buda, W. Schnick, *Angew. Chem. Int. Ed.* **2018**, *57*, 13202–13205; *Angew. Chem.* 2018, *130*, 13386–13389.
- [27] K. Landskron, E. Irran, W. Schnick, *Chem. Eur. J.* **1999**, *5*, 2548–2553.

C Supporting Information for Chapter 4

Experimental Procedures

Preparation of starting materials

P_3N_5 was prepared following a procedure by Stock et al.^[6] The product was obtained as an orange powder. Purity was confirmed by PXRD as well as CHNS analysis (C 0%, H 0%, N 42.69%, S 0% expected C 0%, H 0%, N 42.98%, S 0%).

The amides $AE(NH_2)_2$ ($AE = Sr, Ba$) were prepared by reaction of the respective alkaline earth metal and supercritical ammonia according to the literature.^[33,34]

Amorphous Si_3N_4 (UBE, SNA-00) and NH_4F (Sigma Aldrich, $\geq 98\%$) were used as purchased.

High-pressure high-temperature synthesis

The silicon imidonitridophosphates $AE Si_3 P_4 N_{10} (NH)_2$ ($AE = Mg, Mg_{0.94}Ca_{0.06}, Ca, Sr$) were obtained by high-pressure high-temperature synthesis using a 1000 t press with a modified Walker-type multianvil apparatus.^[8–10,35,36] All products were synthesized from stoichiometric amounts of P_3N_5 , Si_3N_4 , the respective alkaline earth amide, and 5 wt% NH_4F (Table S1). Owing to the air and moisture sensitivity of the amides, starting materials were handled in an Ar-filled glovebox (Unilab, MBraun, Garching, $O_2 < 1$ ppm, $H_2O < 0.1$ ppm) and ground thoroughly in an agate mortar. Details on the preparation and handling of the 1000 t Walker-type multianvil press are described in the literature.^[14,15,37] All reactions were carried out at 8 GPa and 1400°C.

Powder X-ray diffraction

Powder X-ray diffraction was carried out on a StadiP diffractometer (STOE & Cie, Darmstadt, Germany) equipped with an MYTHEN 1K detector (Dectris, Baden, Switzerland; angular range $\Delta 2\theta = 12.5^\circ$), a Cu source and a Ge(111) monochromator for Cu- $K\alpha_1$ radiation. Samples were filled into glass capillaries with 0.3 mm diameter and 0.01 mm wall thickness (Hilgenberg GmbH, Malsfeld, Germany). Data were recorded in the angular range $5^\circ < 2\theta < 120^\circ$. Diffraction data were analyzed with the TOPAS-Academic V6 software, where phase

compositions were analyzed with the Rietveld method. Rietveld refinements were performed with atomic and lattice parameters from $\text{CaSi}_3\text{P}_4\text{N}_{10}(\text{NH})_2$ as starting values. H positions and isotropic displacement parameters were not refined.

Unit cell volumes of $\text{AESi}_3\text{P}_4\text{N}_{10}(\text{NH})_2$ ($AE = \text{Mg}, \text{Mg}_{0.94}\text{Ca}_{0.06}, \text{Ca}$) were extracted from Pawley Fits with Si ($a = 5.43054 \text{ \AA}$) as an internal standard. The Ca content of $\text{Mg}_{0.94}\text{Ca}_{0.06}\text{Si}_3\text{P}_4\text{N}_{10}(\text{NH})_2$ was determined from the unit cell volume of $\text{Mg}_{0.94}\text{Ca}_{0.06}\text{Si}_3\text{P}_4\text{N}_{10}(\text{NH})_2$ in relation to the end members $\text{MgSi}_3\text{P}_4\text{N}_{10}(\text{NH})_2$ and $\text{CaSi}_3\text{P}_4\text{N}_{10}(\text{NH})_2$.

High-temperature PXRD patterns were recorded on a StadiP diffractometer (STOE & Cie, Darmstadt, Germany) in the range $2^\circ < 2\theta < 75^\circ$ and Mo- $K\alpha_1$ radiation ($\lambda = 0.709300 \text{ \AA}$). An image-plate position-sensitive detector was used for X-ray detection. Diffraction patterns were collected in 50°C steps up to 950°C . Samples were filled into silica capillaries with 0.4 mm diameter and 0.01 mm wall thickness (Hilgenberg GmbH, Malsfeld, Germany). Lattice parameters were extracted from Pawley-Fits.

Scanning electron microscopy and energy-dispersive X-ray spectroscopy (EDX)

Samples were placed on conducting carbon foil and coated with carbon. EDX spectra were collected using an FEI Helios Nanolab G3 Dual Beam UC (FEI, Hillsboro, OR, USA) with an attached X-Max 80 SDD detector (Oxford Instruments, Abingdon, UK).

(Scanning) transmission electron microscopy

Samples were ground in absolute ethanol and a drop of the resulting suspension was cast on a TEM grid with lacey carbon film (Plano GmbH, Wetzlar, Germany). The grid was mounted on a double-tilt low background holder and transferred into a Cs DCOR probe-corrected Titan Themis 300 (FEI, USA) TEM equipped with X-FEG, post-column filter (Enfinium ER-799), US1000XP/FT camera system (Gatan, Germany), and a windowless, 4-quadrant Super-X EDX detector (FEI, USA) TEM images were recorded using a $4\text{k} \times 4\text{k}$ FEI Ceta CMOS camera. The microscope was operated at 300 kV accelerating voltage for SAED, STEM-HAADF and EDX (semiconvergence angle 16.6 mrad , $50 \text{ }\mu\text{m}$ aperture, HAADF detector inner half angle 33 mrad for 245 mm camera length). The element maps were filtered using a radial Wiener filter (highest frequency 20.0 software-specific units and edge smoothing 30.0 units).

Samples for data collection with microfocused synchrotron radiation were prepared as described above but TEM finder grids were used. Suitable crystallites were identified by EDX and electron diffraction. Their positions on the grid were mapped using bright-field images at different magnifications. This allowed the correct positioning of the grid in the synchrotron beam. For evaluation of the TEM data, the following software was used: Digital Micrograph (Fourier filtering of STEM images), ProcessDiffraction7 (geometric calculations for SAED), JEMS (SAED simulations), Velox v2.8 (Thermo Fisher Scientific, USA for EDX mappings).

Solid-state MAS NMR spectroscopy

Solid-state NMR measurements were performed on an Avance III 500 spectrometer (Bruker, Karlsruhe) equipped with an 11.7 T magnet operating at 500.25 MHz ^1H frequency and a commercial double-resonance MAS probe. The sample was ground and loaded in a ZrO_2 rotor with an outer diameter of 2.5 mm. NMR spectra were collected at 20 kHz spinning frequency and a relaxation delay of 12 s.

Single-crystal X-ray diffraction

The crystallites on TEM finder grids were optically centered in the synchrotron beam with a high magnification telescope at ESRF beamline ID11. Centering was precisely optimized by fluorescence and diffraction scans utilizing a hexapod setup (Symétrie Hexapods Nanopos and PI-MARS P563 piezo stage).^[38–40] The datasets of two crystallites were evaluated and combined for the sake of better completeness using CrysalisPro (Agilent Technologies). Absorption correction was performed using SADABS.^[41] Employing SHELX-2018, the structure was solved by direct methods and refined against F^2 by the full-matrix least-squares method.^[16] Raw diffraction data are archived at the ESRF.^[42]

Bond-valence sum (BVS) Calculations

BVS calculations were performed using the software Valist v4.0.7.^[17,18]

Luminescence measurements

Luminescence spectra of Eu^{2+} -doped samples were examined on a HORIBA Fluoromax4 spectrofluorimeter system with an Olympus BX51 microscope. Emission spectra were collected at room temperature with $\lambda_{\text{exc}} = 400$, in a range from 400 to 800 nm (step width:

2 nm). Cryo spectra between 6 K and 300 K were recorded in an evacuated, He-cooled sample chamber with an Ocean Optics HR2000 + ES spectrometer (2.048 pixels, grating UA (200-1.100 nm) slit 50).

IR spectroscopy

FTIR spectra of the title compounds were collected on a Spectrum BX II spectrometer (PerkinElmer, Waltham, MA, USA) between 600 and 4400 cm^{-1} with DuraSampler attenuated total reflectance unit (ATR).

UV-Vis spectroscopy

A V-650 UV-Vis spectrophotometer (JASCO, Gross-Umstadt, Germany) equipped with a photomultiplier tube detector and a single monochromator with 1200 lines/mm was used for recording UV-Vis spectra in the range of 240 to 800 nm. A deuterium (240–330 nm) and a halogen lamp (330–880 nm) were used with a 2 nm resolution and a scan speed of 400 nm/min controlled by the Spectra Manager II software. Samples were fixed between a fused silica glass slide and a BaSO_4 -coated stamp. Pseudo-absorption spectra were calculated by the Kubelka-Munk function $F(R) = (1-R)^2/2R$ where R is reflectance. In the Tauc plots, $h\nu$ was plotted against $[F(R)h\nu]^{1/n}$ with $n = 1/2$ for direct bandgaps.^[43]

Results and Discussion

Synthesis

Table C1 Weighed portions of starting materials for the syntheses of $AE\text{Si}_3\text{P}_4\text{N}_{10}(\text{NH})_2$ ($AE = \text{Mg}_{0.94}\text{Ca}_{0.06}$, Mg, Ca, Sr).

Compound	Starting material			
$\text{Mg}_{0.94}\text{Ca}_{0.06}\text{Si}_3\text{P}_4\text{N}_{10}(\text{NH})_2$	$\text{Mg}(\text{NH}_2)_2$	P_3N_5	Si_3N_4	NH_4F
	14.9 mg,	64.1 mg,	41.4 mg,	6 mg
	0.27 mmol	0.39 mmol	0.30 mmol	
	$\text{Ca}(\text{NH}_2)_2$			
	2.1 mg, 0.03 mmol			
$\text{MgSi}_3\text{P}_4\text{N}_{10}(\text{NH})_2$	$\text{Mg}(\text{NH}_2)_2$	P_3N_5	Si_3N_4	NH_4F
	5.6 mg,	21.59 mg,	13.94 mg,	2 mg
	0.10 mmol	0.13 mmol	0.10 mmol	
$\text{CaSi}_3\text{P}_4\text{N}_{10}(\text{NH})_2$	$\text{Ca}(\text{NH}_2)_2$	P_3N_5	Si_3N_4	NH_4F
	6.93 mg,	20.88 mg,	13.48 mg,	2 mg
	0.10 mmol	0.13 mmol	0.10 mmol	
$\text{SrSi}_3\text{P}_4\text{N}_{10}(\text{NH})_2$	$\text{Sr}(\text{NH}_2)_2$	P_3N_5	Si_3N_4	NH_4F
	10.27,	18.66,	12.04,	2 mg
	0.09 mmol	0.11 mmol	0.09 mmol	

Structure determination

As diffraction data of both crystallites showed threefold twinning, reflection files of each crystallite were first transformed to SHELX HKLF 5 files taking into account the hkl transformation matrix shown below.^[44] The two crystallites showed slightly different twin volume fractions of the threefold twinning, which was taken into account by refinements with six BASF where BASF 1–3 represent the first crystal and BASF 4–6 represent the second crystal. This allowed merging of the two datasets and refinement of the structure model with increased data completeness.

$$\begin{pmatrix} \frac{1}{2} & -\frac{1}{2} & 0 \\ -\frac{3}{2} & -\frac{1}{2} & 0 \\ -\frac{1}{2} & \frac{1}{6} & -1 \end{pmatrix}$$

Table C2 Crystallographic data of the single-crystal structure refinements of $\text{CaSi}_3\text{P}_4\text{N}_{10}(\text{NH})_2$.
Standard deviations are given in parentheses.

formula	$\text{CaSi}_3\text{P}_4\text{N}_{10}(\text{NH})_2$
molar mass / $\text{g}\cdot\text{mol}^{-1}$	418.37
crystal system	monoclinic
space group	$C2/m$ (no. 12)
lattice parameters / $\text{\AA}, ^\circ$	$a = 4.91790(10)$
	$b = 8.5159(2)$
	$c = 9.8267(2)$
	$\beta = 99.476(3)^\circ$
cell volume / \AA^3	405.930(15)
formula units/ unit cell	2
density / $\text{g}\cdot\text{cm}^3$	3.423
μ / mm^{-1}	0.247
temperature / K	293(2)
absorption correction	semiempirical
radiation	synchrotron, ESRF ID11 ($\lambda = 0.3252 \text{ \AA}$)
F(000)	416
θ range / $^\circ$	$2.2 \leq \theta \leq 21.9$
total no. of reflections	16003
Independent reflections [$I \geq 2\sigma(I)$ / all]	4198/ 4895
R_σ	0.0383
refined parameters / restraints	61 / 1
Goodness of fit	1.087
R -values [$I \geq 2\sigma(I)$]	$R_1 = 0.0805$; $wR_2 = 0.2262$
R -values (all data)	$R_1 = 0.0862$; $wR_2 = 0.2398$
$\Delta\rho_{\text{max}}, \Delta\rho_{\text{min}}$ / $\text{e}\cdot\text{\AA}^{-3}$	1.563, -1.558

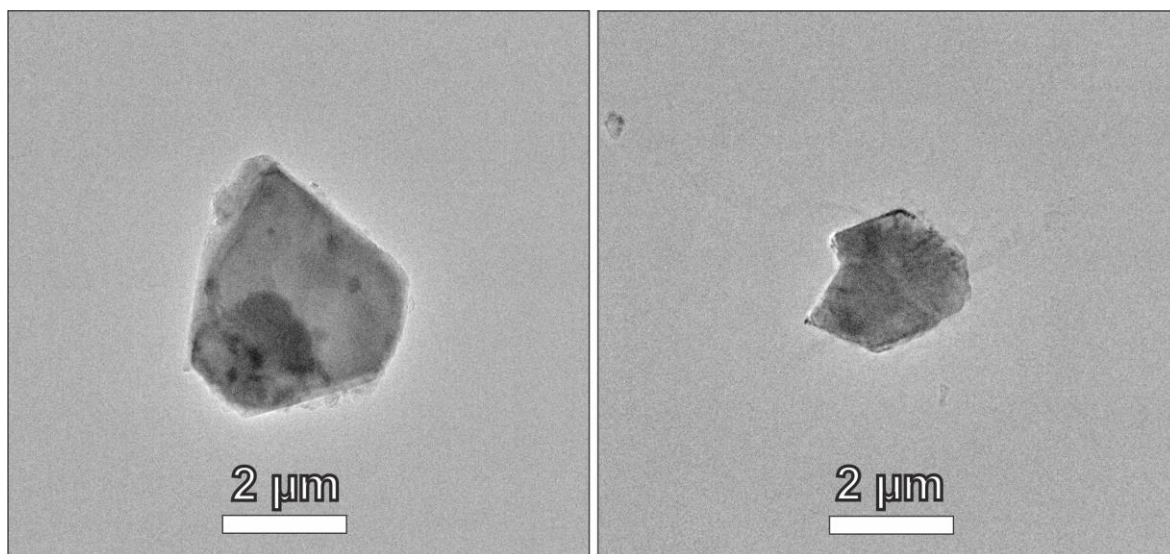


Figure C1. TEM bright-field images of the crystallites used for data collection with microfocused synchrotron radiation.

Table C3 Atomic coordinates, isotropic displacement parameters (\AA^2), and site occupancies of $\text{CaSi}_3\text{P}_4\text{N}_{10}(\text{NH})_2$.

Atom	Wyckoff position	<i>x</i>	<i>y</i>	<i>z</i>	U_{eq}	<i>occ.</i>
Ca1	2 <i>a</i>	0	0	0	0.0124(5)	1
P1	8 <i>j</i>	0.0738(3)	0.33298(16)	0.22228(16)	0.0126(4)	1
Si1	4 <i>h</i>	0	0.1643(2)	1/2	0.0132(6)	1
Si2	2 <i>d</i>	0	1/2	1/2	0.0127(7)	1
N1	4 <i>i</i>	0.1419(17)	0	0.4097(7)	0.0109(11)	1
N2	8 <i>j</i>	0.1313(15)	0.3318(5)	0.3978(5)	0.0122(8)	1
N3	4 <i>i</i>	0.6701(12)	0	0.1680(8)	0.0129(14)	1
N4	8 <i>j</i>	0.2496(10)	0.1927(6)	0.1663(6)	0.0131(9)	1
H1	4 <i>i</i>	0.12(3)	0	0.319(5)	0.04(4)	1

Table C4 Anisotropic displacement parameters (U_{ij} in \AA^2) for $\text{CaSi}_3\text{P}_4\text{N}_{10}(\text{NH})_2$ with standard deviations in parentheses. The anisotropic displacement factor is expressed as $\exp[-2\pi^2 (U_{11}h^2a^{*2} + U_{22}k^2b^{*2} + U_{33}l^2c^{*2} + U_{12}hka^*b^* + U_{13}hla^*c^* + U_{23}klb^*c^*)]$.

Atom	U_{11}	U_{22}	U_{33}	U_{23}	U_{13}	U_{12}
Ca1	0.0100(8)	0.0132(10)	0.0156(11)	0	0.0064(7)	0
P1	0.0089(7)	0.0121(8)	0.0184(9)	0.0000(5)	0.0074(7)	0.0000(3)
Si1	0.0089(12)	0.0145(16)	0.0187(12)	0	0.0096(13)	0
Si2	0.0084(14)	0.0145(18)	0.0173(17)	0	0.0085(14)	0
N1	0.009(3)	U_{11}	0.016(3)	0	0.005(3)	0
N2	0.011(2)	0.014(3)	U_{22}	-0.0006(16)	0.008(2)	0.0003(12)
N3	0.012(3)	0.010(3)	0.019(4)	0	0.008(2)	0
N4	0.0095(19)	0.0117(18)	0.020(3)	-0.0015(18)	0.0072(17)	0.0009(14)

Table C5 Interatomic distances (\AA) and bond angles ($^\circ$) in the structure of $\text{CaSi}_3\text{P}_4\text{N}_{10}(\text{NH})_2$.

Ca1	N4	4x	2.492(5)	N4	P1	N3	109.5(3)
Ca1	N3	2x	2.498(6)	N4	P1	N4	109.7(3)
P1	N4	1x	1.614(6)	N3	P1	N4	109.5(3)
P1	N3	1x	1.617(4)	N4	P1	N2	109.5(3)
P1	N4	1x	1.622(6)	N3	P1	N2	109.3(3)
P1	N2	1x	1.702(5)	N4	P1	N2	109.3(3)
Si1	N1	1x	1.854(5)	N1	Si1	N1	82.0(4)
Si1	N2	1x	1.916(5)	N1	Si1	N2	176.8(3)
Si1	N2	1x	1.923(7)	N1	Si1	N2	97.2(3)
Si2	N1	2x	1.837(8)	N2	Si1	N2	83.8(3)
Si2	N2	4x	1.921(5)	N1	Si1	N2	82.3(3)
N1	H1	1x	0.88(5)	N1	Si1	N2	99.2(3)
				N2	Si1	N2	94.8(2)
				N2	Si1	N2	178.0(3)
				N1	Si2	N1	180
				N1	Si2	N2	82.8(2)
				N1	Si2	N2	97.2(2)
				N2	Si2	N2	180
				N2	Si2	N2	96.4(3)
				N2	Si2	N2	83.6(3)
				N1	Si2	N2	82.8(2)
				Si2	N1	H1	117(9)
				Si1	N1	H1	119(4)

EDX measurements**Table C6.** EDX measurements (several point analyses) for $AE\text{Si}_3\text{P}_4\text{N}_{10}(\text{NH})_2$ ($AE = \text{Mg, Ca, Sr}$) compared to values derived from sum formulas.

EDX point / atom %	Mg	Si	P	N
1	7.0	17.1	19.1	56.7
2	7.0	17.0	20.3	55.5
3	7.5	18.4	20.2	53.7
4	8.1	16.9	22.0	52.9
average	7.4(4)	17.4(6)	20(1)	54(1)
	Ca	Si	P	N
1	4.8	13.8	18.9	62.4
2	5.0	15.6	20.7	58.6
3	5.1	15.4	20.9	58.5
4	4.1	15.6	20.2	60.1
average	4.8(4)	15.1(7)	20.2(8)	60(2)
	Sr	Si	P	N
1	5.3	15.4	21.4	57.8
2	5.6	16.5	20.6	57.3
3	5.6	16.5	22.6	55.3
4	5.6	15.8	19.8	58.8
average	5.5(1)	16.0(5)	21(1)	57(1)
Calc.	5	15	20	60

Rietveld refinements

Table C7. Crystallographic data from the Rietveld refinements for $AE\text{Si}_3\text{P}_4\text{N}_{10}(\text{NH})_2$ ($AE = \text{Mg}, \text{Ca}, \text{Sr}, \text{Mg}_{0.94}\text{Ca}_{0.06}$) standard deviations are given in parentheses.

	$\text{MgSi}_3\text{P}_4\text{N}_{10}(\text{NH})_2$	$\text{CaSi}_3\text{P}_4\text{N}_{10}(\text{NH})_2$	$\text{SrSi}_3\text{P}_4\text{N}_{10}(\text{NH})_2$	$\text{Mg}_{0.94}\text{Ca}_{0.06}\text{Si}_3\text{P}_4\text{N}_{10}(\text{NH})_2$
crystal system	monoclinic			
space group	$C2/m$ (no. 12)			
lattice	$a = 4.86919(6)$	$a = 4.9184(2)$	$a = 4.93846(8)$	$a = 4.8716(1)$
parameters /	$b = 8.4260(1)$	$b = 8.5137(3)$	$b = 8.5496(1)$	$b = 8.4339(2)$
$\text{\AA},^\circ$	$c = 9.36667(9)$	$c = 9.8294(3)$	$c = 10.1206(1)$	$c = 9.3928(2)$
	$\beta = 99.901(1)$	$\beta = 99.447(1)$	$\beta = 99.197(1)$	$\beta = 99.873(3)$
radiation $\lambda / \text{\AA}$	1.54056 (Cu- $K_{\alpha 1}$)			
cell volume /	378.560(9)	406.02(3)	421.82(1)	380.02(2)
\AA^3				
2θ -range/ $^\circ$	5 < 2θ < 120			
refined	54	94	74	54
parameters (incl. side phases)				
thereof	12	24	24	18
background				
R -values	$R_p = 0.0520$	$R_p = 0.0480$	$R_p = 0.0727$	$R_p = 0.0560$
	$wR_p = 0.0702$	$wR_p = 0.0624$	$wR_p = 0.0983$	$wR_p = 0.0743$
	$R_{\text{Bragg}} = 0.0377$	$R_{\text{Bragg}} = 0.0230$	$R_{\text{Bragg}} = 0.0568$	$R_{\text{Bragg}} = 0.0337$

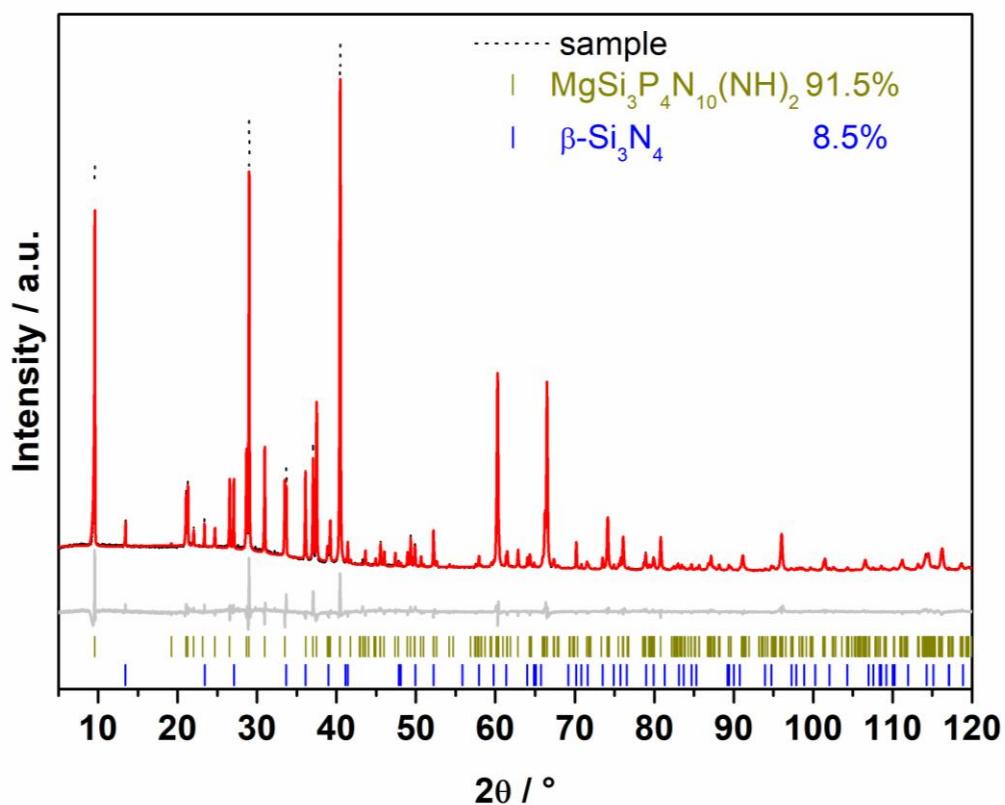


Figure C2. Rietveld refinement for $\text{MgSi}_3\text{P}_4\text{N}_{10}(\text{NH})_2$; observed (black line) and calculated (red line) X-ray powder diffraction patterns, positions of Bragg reflections of $\text{MgSi}_3\text{P}_4\text{N}_{10}(\text{NH})_2$ (vertical yellow bars), $\beta\text{-Si}_3\text{N}_4$ (vertical blue bars), and difference profile (gray line).

Table C8 Atomic coordinates, isotropic displacement parameters (\AA^2), and occupancy of $\text{MgSi}_3\text{P}_4\text{N}_{10}(\text{NH})_2$.

Atom	Wyckoff	<i>x</i>	<i>y</i>	<i>z</i>	U_{iso}	occ.
Mg1	2 <i>a</i>	0	0	0	0.021(1)	1
P1	8 <i>j</i>	0.0643(6)	0.3332(2)	0.2073(1)	0.0070(9)	1
Si1	4 <i>h</i>	0	0.1647(3)	1/2	0.0036(9)	1
Si2	2 <i>d</i>	0	1/2	1/2	0.0036(9)	1
N1	4 <i>i</i>	0.158(1)	0	0.4041(7)	0.002(1)	1
N2	8 <i>j</i>	0.137(1)	0.3304(7)	0.3908(5)	0.002(1)	1
N3	4 <i>i</i>	0.696(2)	0	0.1531(7)	0.002(1)	1
N4	8 <i>j</i>	0.228(1)	0.1812(6)	0.1523(4)	0.002(1)	1
H1	4 <i>i</i>	0.12	0	0.319	0.04	1

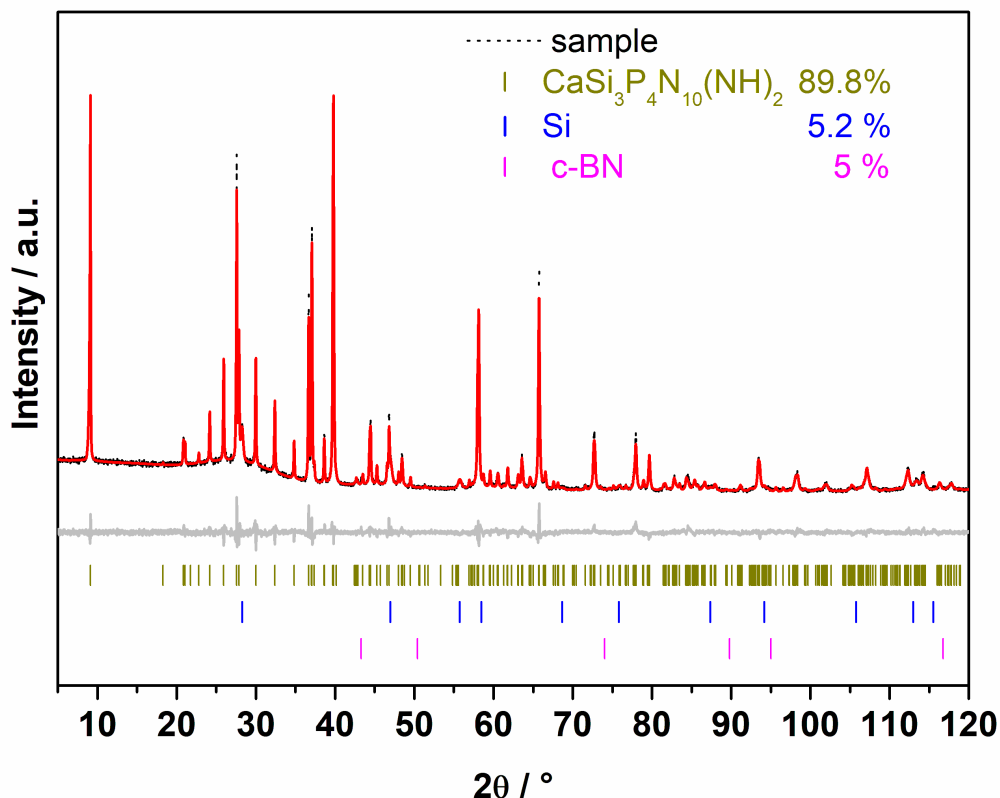


Figure C3. Rietveld refinement for $\text{CaSi}_3\text{P}_4\text{N}_{10}(\text{NH})_2$; observed (black line) and calculated (red line) X-ray powder diffraction patterns, positions of Bragg reflections of $\text{CaSi}_3\text{P}_4\text{N}_{10}(\text{NH})_2$ (vertical yellow bars), Si (vertical blue bars), c-BN (vertical violet bars) and difference profile (gray line).

Table C9 Atomic coordinates, isotropic displacement parameters/ \AA^2 , and occupancy of $\text{CaSi}_3\text{P}_4\text{N}_{10}(\text{NH})_2$.

Atom	Wyckoff	<i>x</i>	<i>y</i>	<i>z</i>	U_{iso}	occ.
Ca1	2 <i>a</i>	0	0	0	0.021(1)	1
P1	8 <i>j</i>	0.0680(6)	0.3322(3)	0.2206(2)	0.013(1)	1
Si1	4 <i>h</i>	0	0.1664(2)	1/2	0.009(1)	1
Si2	2 <i>d</i>	0	1/2	1/2	0.009(1)	1
N1	4 <i>i</i>	0.123(2)	0	0.4056(9)	0.010(1)	1
N2	8 <i>j</i>	0.116(1)	0.3312(7)	0.3982(5)	0.010(1)	1
N3	4 <i>i</i>	0.690(2)	0	0.169(1)	0.010(1)	1
N4	8 <i>j</i>	0.252(1)	0.1920(8)	0.1685(7)	0.010(1)	1
H1	4 <i>i</i>	0.12	0	0.319	0.04	1

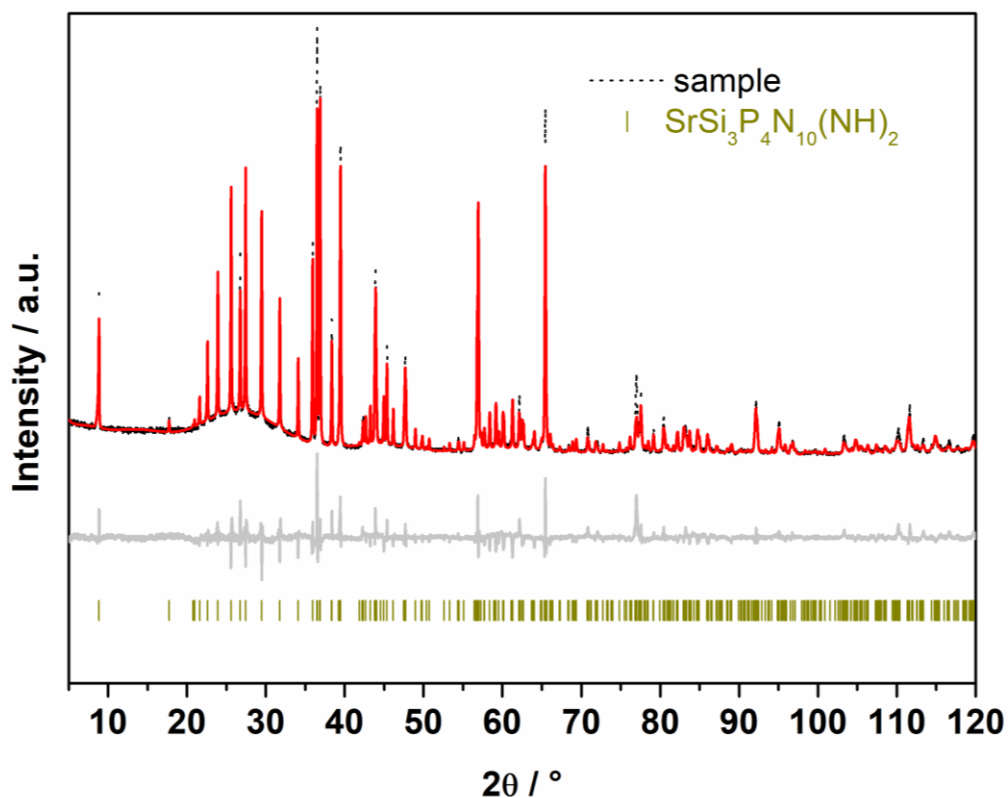


Figure C4. Rietveld refinement for $\text{SrSi}_3\text{P}_4\text{N}_{10}(\text{NH})_2$; observed (black line) and calculated (red line) X-ray powder diffraction patterns, positions of Bragg reflections of $\text{SrSi}_3\text{P}_4\text{N}_{10}(\text{NH})_2$ (vertical yellow bars) and difference profile (gray line).

Table C10 Atomic coordinates, isotropic displacement parameters/ \AA^2 , and occupancy of $\text{SrSi}_3\text{P}_4\text{N}_{10}(\text{NH})_2$.

Atom	Wyckoff	x	y	z	U_{iso}	occ.
Sr1	2a	0	0	0	0.030(1)	1
P1	8j	0.0758(7)	0.3328(4)	0.2309(1)	0.018(1)	1
Si1	4h	0	0.1659(5)	1/2	0.009(1)	1
Si2	2d	0	1/2	1/2	0.009(1)	1
N1	4i	0.130(3)	0	0.404(1)	0.015(1)	1
N2	8j	0.128(2)	0.333(1)	0.4035(7)	0.015(1)	1
N3	4i	0.676(2)	0	0.176(1)	0.015(1)	1
N4	8j	0.268(1)	0.186(1)	0.1779(7)	0.015(1)	1
H1	4i	0.12	0	0.319	0.04	1

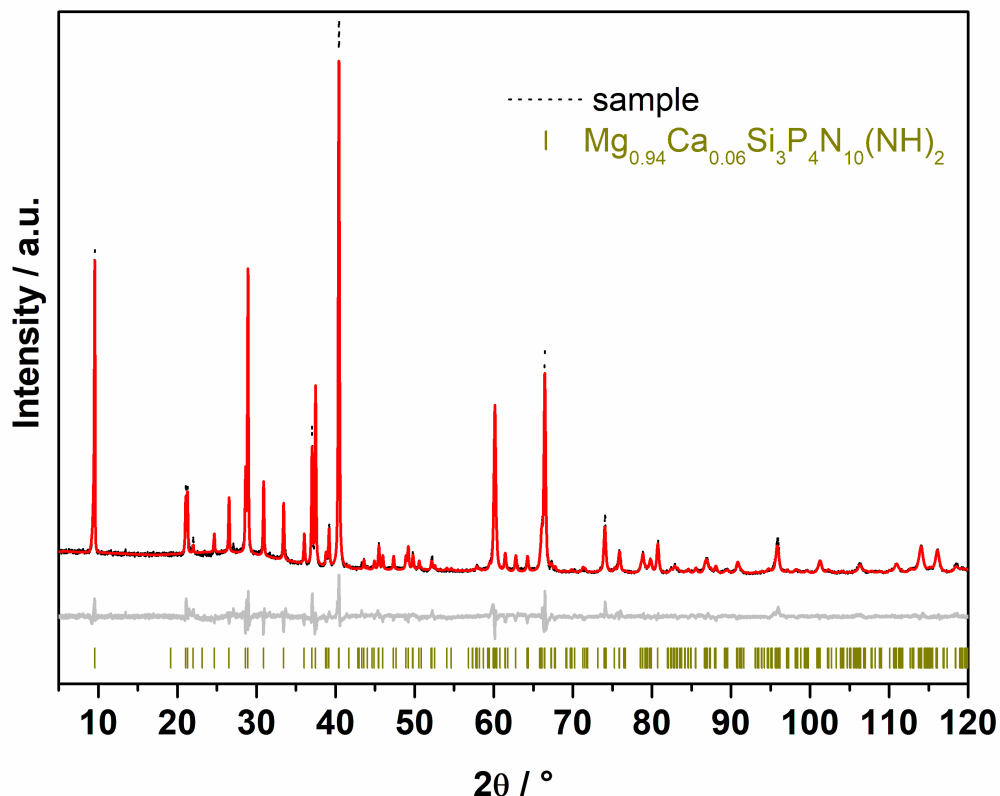


Figure C5. Rietveld refinement for $\text{Mg}_{0.94}\text{Ca}_{0.06}\text{Si}_3\text{P}_4\text{N}_{10}(\text{NH})_2$; observed (black line) and calculated (red line) X-ray powder diffraction patterns, positions of Bragg reflections of $\text{Mg}_{0.94}\text{Ca}_{0.06}\text{Si}_3\text{P}_4\text{N}_{10}(\text{NH})_2$ (vertical yellow bars) and difference profile (gray line).

Table C11 Atomic coordinates, isotropic displacement parameters/ \AA^2 , and occupancy of $\text{Mg}_{0.94}\text{Ca}_{0.06}\text{Si}_3\text{P}_4\text{N}_{10}(\text{NH})_2$.

Atom	Wyckoff	<i>x</i>	<i>y</i>	<i>z</i>	<i>U</i> _{iso}	occ.
Mg1	2 <i>a</i>	0	0	0	0.0264(2)	0.94
Ca1	2 <i>a</i>	0	0	0	0.0264(2)	0.06
P1	8 <i>j</i>	0.0631(7)	0.3330(2)	0.2084(1)	0.012(1)	1
Si1	4 <i>h</i>	0	0.1640(4)	1/2	0.012(1)	1
Si2	2 <i>d</i>	0	1/2	1/2	0.008(1)	1
N1	4 <i>i</i>	0.175(1)	0	0.4031(9)	0.003(1)	1
N2	8 <i>j</i>	0.147(1)	0.3300(8)	0.3931(6)	0.003(1)	1
N3	4 <i>i</i>	0.690(2)	0	0.1509(9)	0.003(1)	1
N4	8 <i>j</i>	0.224(1)	0.1826(7)	0.1543(6)	0.003(1)	1
H1	4 <i>i</i>	0.12	0	0.319	0.04	1

Table C12. Crystallographic data from the Pawley Fits for $AE\text{Si}_3\text{P}_4\text{N}_{10}(\text{NH})_2$ ($AE = \text{Mg}, \text{Ca}, \text{Mg}_{0.94}\text{Ca}_{0.06}$) standard deviations are given in parentheses.

	MgSi₃P₄N₁₀(NH)₂	CaSi₃P₄N₁₀(NH)₂	Mg_{0.94}Ca_{0.06}Si₃P₄N₁₀(NH)₂
crystal system	monoclinic		
space group	$C2/m$ (no. 12)		
lattice parameters / Å, °	$a = 4.8682(1)$	$a = 4.9167(2)$	$a = 4.8709(2)$
	$b = 8.4228(3)$	$b = 8.5136(3)$	$b = 8.4296(4)$
	$c = 9.3639(2)$	$c = 9.8198(2)$	$c = 9.3895(2)$
	$\beta = 99.927(3)$	$\beta = 99.429(3)$	$\beta = 99.872(4)$
radiation λ / Å	1.54056 (Cu-K α_1)		
cell volume / Å ³	378.21(2)	405.49(3)	379.83(3)
2θ – range/°	5 < 2θ < 120		
refined parameters	363	352	352
(incl. side phases)			
thereof	18	18	18
background			
R -values	$R_p = 0.0517$	$R_p = 0.0536$	$R_p = 0.0727$
	$wR_p = 0.0713$	$wR_p = 0.0751$	$wR_p = 0.0983$

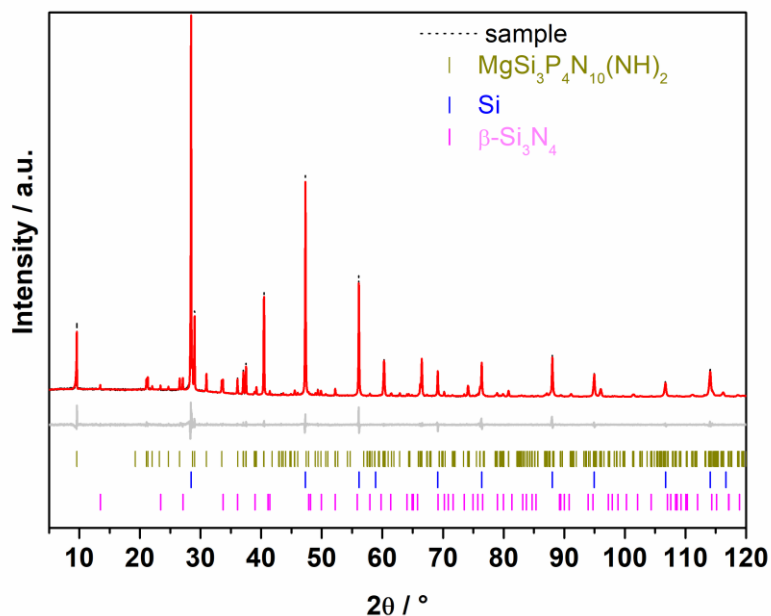


Figure C6. Pawley Fit for $\text{MgSi}_3\text{P}_4\text{N}_{10}(\text{NH})_2$; observed (black line) and calculated (red line) X-ray powder diffraction patterns, positions of Bragg reflections of $\text{MgSi}_3\text{P}_4\text{N}_{10}(\text{NH})_2$ (vertical yellow bars), Si (vertical blue bars), $\beta\text{-Si}_3\text{N}_4$ (vertical magenta bars) and difference profile (gray line).

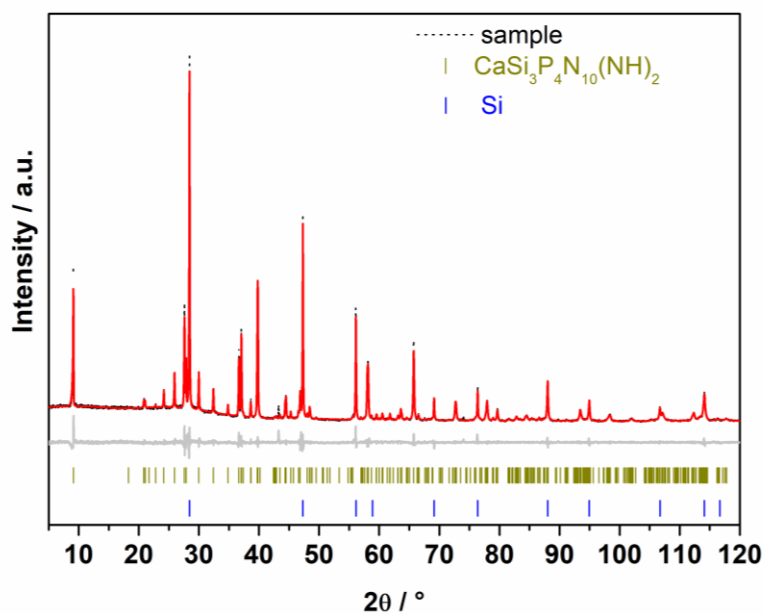


Figure C7. Pawley Fit for $\text{CaSi}_3\text{P}_4\text{N}_{10}(\text{NH})_2$; observed (black line) and calculated (red line) X-ray powder diffraction patterns, positions of Bragg reflections of $\text{CaSi}_3\text{P}_4\text{N}_{10}(\text{NH})_2$ (vertical yellow bars), Si (vertical blue bars) and difference profile (gray line).

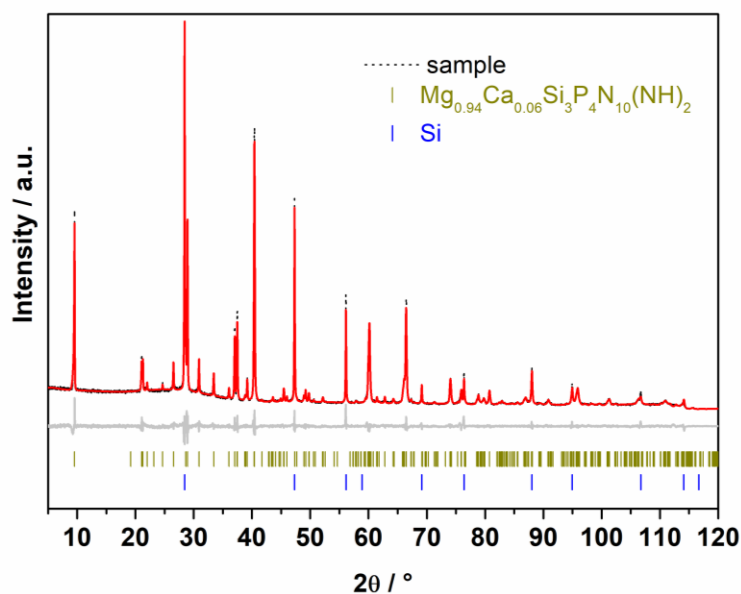


Figure C8. Pawley Fit for $\text{Mg}_{0.94}\text{Ca}_{0.06}\text{Si}_3\text{P}_4\text{N}_{10}(\text{NH})_2$; observed (black line) and calculated (red line) X-ray powder diffraction patterns, positions of Bragg reflections of $\text{Mg}_{0.94}\text{Ca}_{0.06}\text{Si}_3\text{P}_4\text{N}_{10}(\text{NH})_2$ (vertical yellow bars), Si (vertical blue bars) and difference profile (gray line).

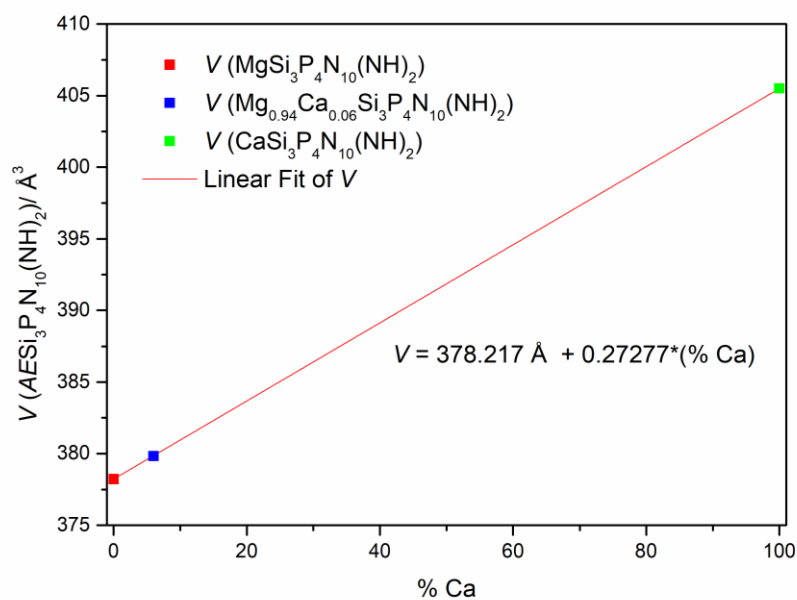


Figure C9. Linear Fit of the unit cell volumes of $\text{MgSi}_3\text{P}_4\text{N}_{10}(\text{NH})_2$ (red square), $\text{Mg}_{0.94}\text{Ca}_{0.06}\text{Si}_3\text{P}_4\text{N}_{10}(\text{NH})_2$ (blue square) and $\text{CaSi}_3\text{P}_4\text{N}_{10}(\text{NH})_2$ (green square) used for Ca-content estimation of $\text{Mg}_{0.94}\text{Ca}_{0.06}\text{Si}_3\text{P}_4\text{N}_{10}(\text{NH})_2$.

High-temperature PXRD

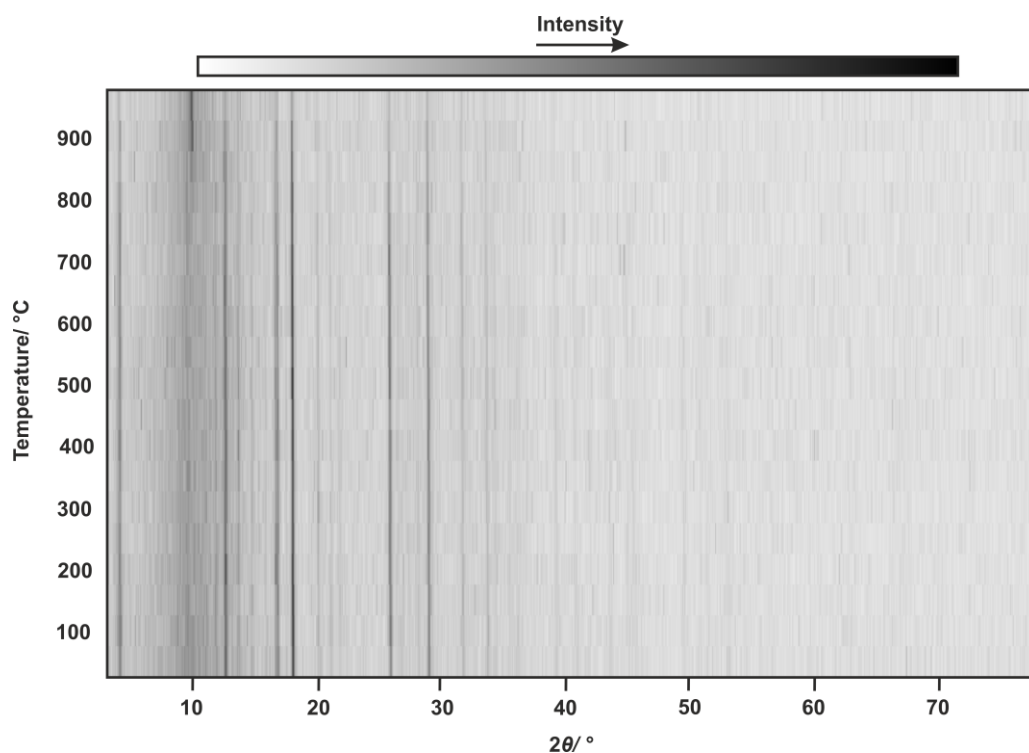


Figure C10. Temperature-dependent powder X-ray diffraction patterns (Mo- $K_{\alpha 1}$ radiation, $\lambda = 0.71073$ Å) of $\text{CaSi}_3\text{P}_4\text{N}_{10}(\text{NH})_2$ measured under Ar atmosphere showing a minor expansion of lattice parameters with increasing temperature, and decomposition above 900 °C.

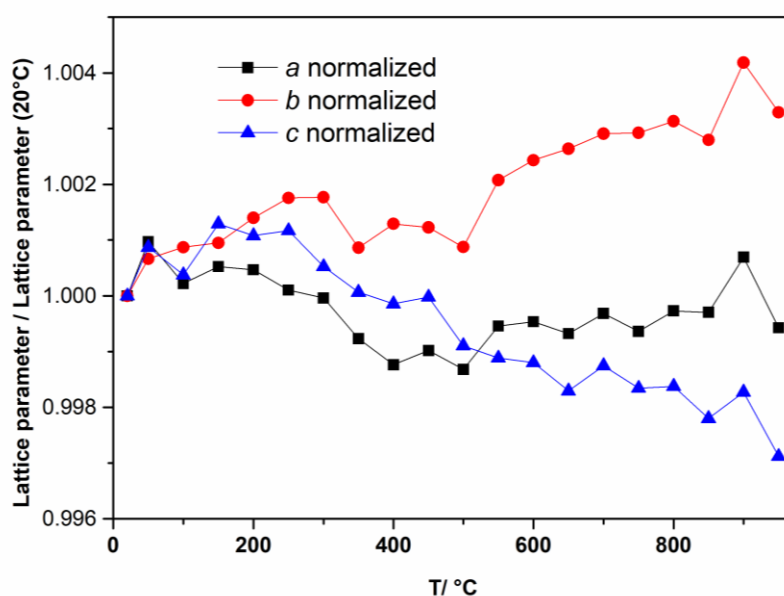


Figure C11. Change of lattice parameters of $\text{CaSi}_3\text{P}_4\text{N}_{10}(\text{NH})_2$ during heating. Lattice parameters were normalized with respect to their values at 20 °C.

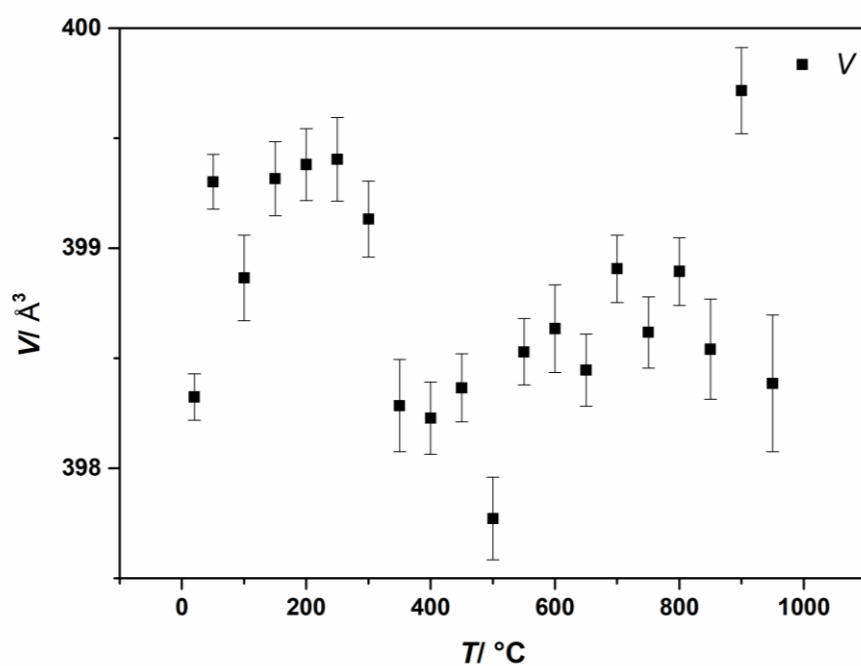


Figure C12. Change of unit cell volume of $\text{CaSi}_3\text{P}_4\text{N}_{10}(\text{NH})_2$ during heating with error bars.

Solid-state NMR spectra

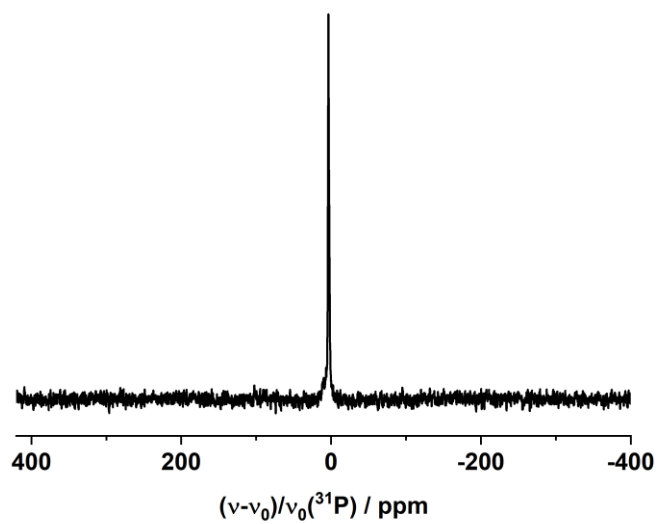


Figure C13. ^{31}P solid-state MAS NMR spectrum of $\text{CaSi}_3\text{P}_4\text{N}_{10}(\text{NH})_2$.

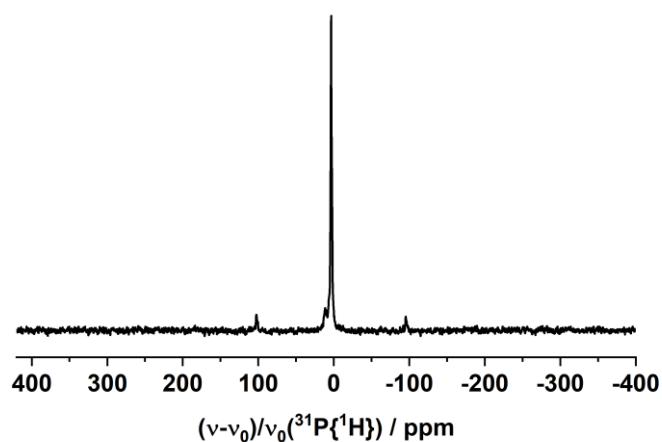


Figure C14. $^{31}\text{P}\{^1\text{H}\}$ solid-state MAS NMR spectrum of $\text{CaSi}_3\text{P}_4\text{N}_{10}(\text{NH})_2$. Spinning sidebands are marked with asterisks.

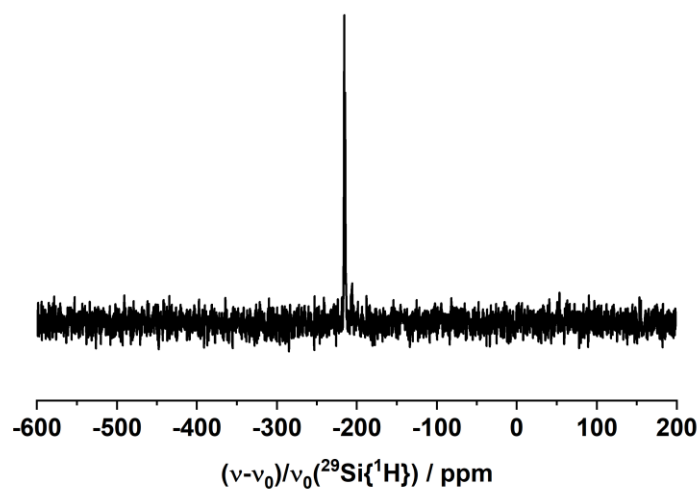


Figure C15. $^{29}\text{Si}\{^1\text{H}\}$ solid-state MAS NMR spectrum of $\text{CaSi}_3\text{P}_4\text{N}_{10}(\text{NH})_2$.

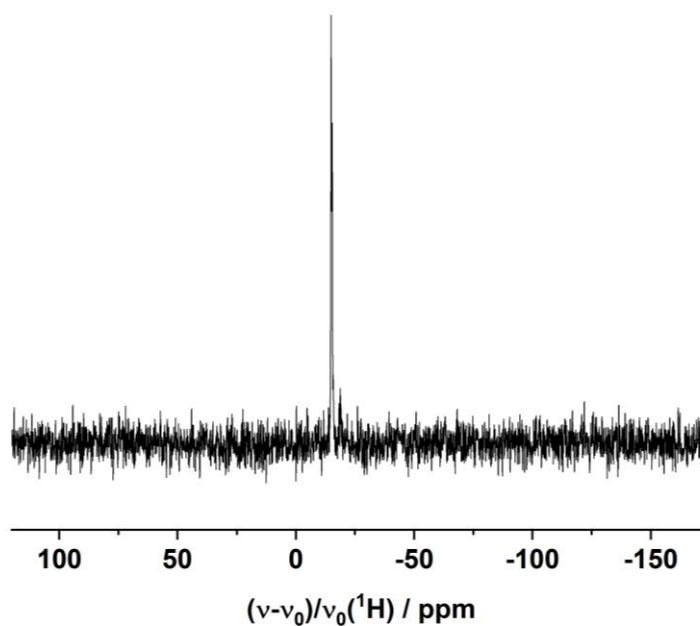


Figure C16. ^1H solid-state MAS NMR spectrum of $\text{CaSi}_3\text{P}_4\text{N}_{10}(\text{NH})_2$.

Table C13 Distances (\AA) of Si and H in $\text{CaSi}_3\text{P}_4\text{N}_{10}(\text{NH})_2$ from SCXRD Data and the arithmetic mean (\AA)

Atoms	Wyckoff position	distance/ \AA	mean value/ \AA
Si1-H1	$4h$	2.4114	3.06
Si1-H1		2.4114	
Si1-H1		3.7060	
Si1-H1		3.7060	
Si2-H1	$2d$	2.3583	3.07
Si2-H1		2.3583	
Si2-H1		3.7744	
Si2-H1		3.7744	

Bond-valence sum (BVS) Calculations

Table C14 Calculated bond valence sums and expected charges for the atom sites in the crystal structure of $\text{CaSi}_3\text{P}_4\text{N}_{10}(\text{NH})_2$.

site	bond-valence sum	expected charge
Ca1	2.50	+2
P1	4.89	+5
Si1	3.86	+4
Si2	3.92	+4
H1	1.57	+1
N1	3.53	-3
N2	2.88	-3
N3	3.01	-3
N4	3.01	-3

FTIR spectra

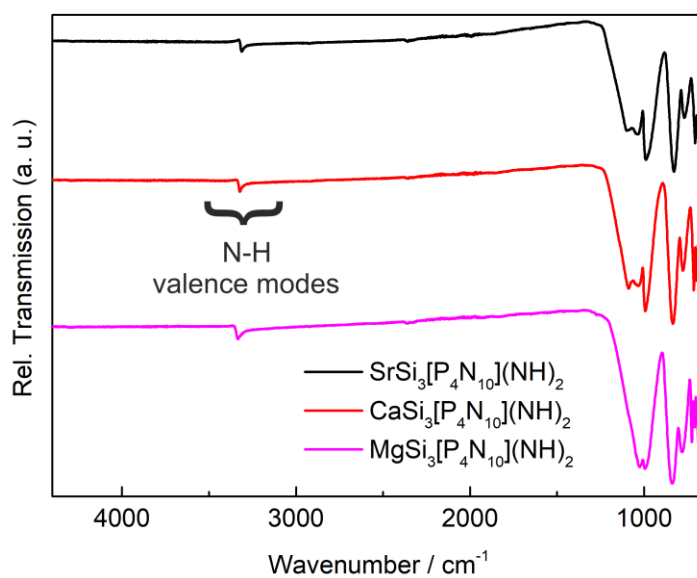
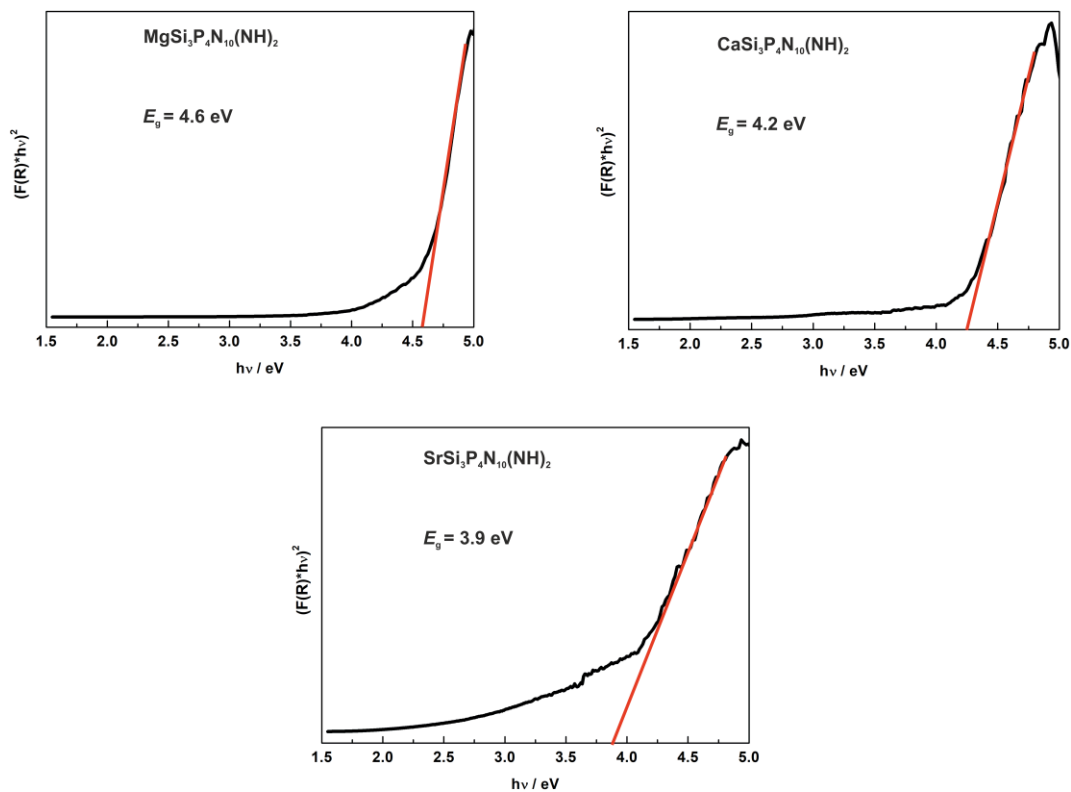


Figure C17. FTIR spectra of $\text{MgSi}_3\text{P}_4\text{N}_{10}(\text{NH})_2$ (violet), $\text{CaSi}_3\text{P}_4\text{N}_{10}(\text{NH})_2$ (red) and $\text{SrSi}_3\text{P}_4\text{N}_{10}(\text{NH})_2$ (black).

UV-Vis spectra

Figure C18: Tauc plots (for UV-Vis spectra of $\text{MgSi}_3\text{P}_4\text{N}_{10}(\text{NH})_2$ (top left), $\text{CaSi}_3\text{P}_4\text{N}_{10}(\text{NH})_2$ (top right)

and $\text{SrSi}_3\text{P}_4\text{N}_{10}(\text{NH})_2$ (bottom). Red lines represent linear regressions from the steep regions to estimate the direct optical band gaps from the inflection points with the abscissa. Data between 4.6 and 4.9 eV ($\text{MgSi}_3\text{P}_4\text{N}_{10}(\text{NH})_2$), 4.3 to 4.8 eV ($\text{CaSi}_3\text{P}_4\text{N}_{10}(\text{NH})_2$) and 4.15 to 4.85 eV ($\text{SrSi}_3\text{P}_4\text{N}_{10}(\text{NH})_2$) were used for linear regressions.

Low-temperature luminescence spectroscopy

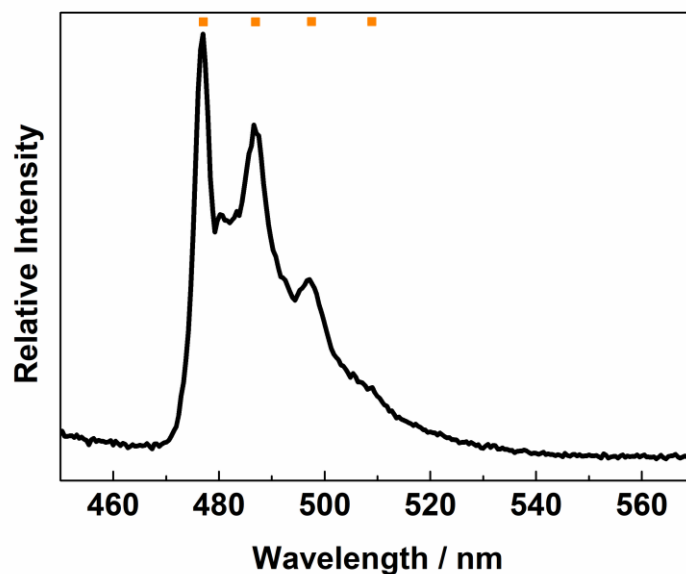


Figure C19: Low-temperature emission spectrum of $\text{CaSi}_3\text{P}_4\text{N}_{10}(\text{NH})_2$, obtained at 6 K (blue line). Red squares indicate the energetic distance of the main phonon mode. The zero-phonon-line is found at ca. 20970 cm^{-1} . The Stokes shift was estimated to a value of approx. 258 cm^{-1} following the equation $E_{\text{Stokes}} = (2S-1)\hbar\omega$ with Huang-Rhys-factor $S \sim 0.8$ and $\hbar\omega \sim 430 \text{ cm}^{-1}$.

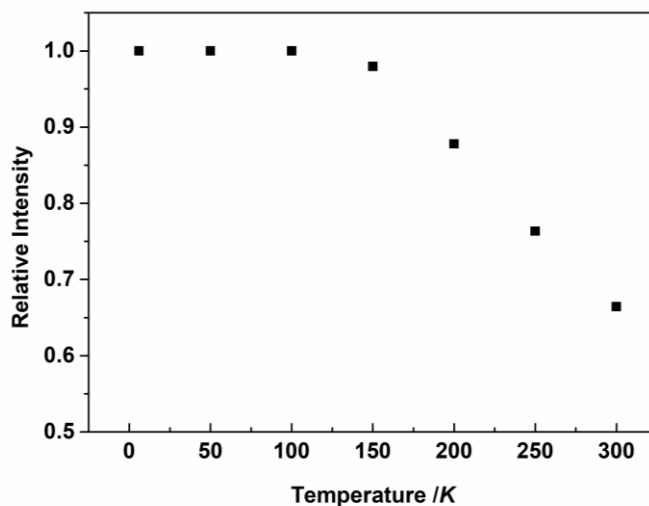


Figure C20: Thermal quenching behavior of $\text{CaSi}_3\text{P}_4\text{N}_{10}(\text{NH})_2$.

References

- [1] A. Stock, H. Grüneberg, *Ber. Dtsch. Chem. Ges.* **1907**, *40*, 2573–2578.
- [2] M. Zeuner, F. Hintze, W. Schnick, *Chem. Mater.* **2009**, *21*, 336–342.
- [3] J. Senker, H. Jacobs, M. Müller, W. Press, P. Müller, H. M. Mayer, R. M. Ibberson, *J. Phys. Chem. B* **1998**, *102*, 931–940.
- [4] H. Huppertz, *Z. Kristallogr.* **2004**, *219*, 330–338.
- [5] N. Kawai, S. Endo, *Rev. Sci. Instrum.* **1970**, *41*, 1178–1181.
- [6] D. C. Rubie, *Phase Transitions* **1999**, *68*, 431–451.
- [7] D. Walker, M. A. Carpenter, C. M. Hitch, *Am. Mineral.* **1990**, *75*, 1020–1028.
- [8] D. Walker, *Am. Mineral.* **1991**, *76*, 1092–1100.
- [9] A. Marchuk, L. Neudert, O. Oeckler, W. Schnick, *Eur. J. Inorg. Chem.* **2014**, *2014*, 3427–3434.
- [10] M. Mallmann, S. Wendl, P. Strobel, P. J. Schmidt, W. Schnick, *Chem. Eur. J.* **2020**, *26*, 6257–6263.
- [11] E. Bertschler, R. Niklaus, W. Schnick, *Chem. Eur. J.* **2017**, *23*, 9592–9599.
- [12] F. Fahrenbauer, T. Rosenthal, T. Schmutzler, G. Wagner, G. B. M. Vaughan, J. P. Wright, O. Oeckler, *Angew. Chem. Int. Ed.* **2015**, *54*, 10020–10023; *Angew. Chem.* **2015**, *127*, 10158–10161.
- [13] P. Bielec, R. Nelson, R. P. Stoffel, L. Eisenburger, D. Günther, A. K. Henß, J. P. Wright, O. Oeckler, R. Dronskowski, W. Schnick, *Angew. Chem. Int. Ed.* **2019**, *58*, 1432–1436; *Angew. Chem.* **2019**, *131*, 1446–1450.
- [14] J. Wright, C. Giacobbe, M. Majkut, *Curr. Opin. Solid State Mater. Sci.* **2020**, *24*, 100818.
- [15] G. M. Sheldrick, *SADABS, v.2: Multi-Scan Absorption Correction*; Bruker-AXS, Billerica, MA, **2012**.
- [16] G. M. Sheldrick, *Acta Crystallogr. Sect. A* **2015**, *71*, 3–8.

- [17] L. Eisenburger, P. Strobel, J. Wright, E. Lawrence Bright, C. Giacobbe, O. Oeckler, W. Schnick (2021). Nitridic Analogs of Micas $AE\text{Si}_3\text{P}_4\text{N}_{10}(\text{NH})_2$ ($AE = \text{Mg}, \text{Mg}_{0.94}\text{Ca}_{0.06}, \text{Ca}, \text{Sr}$). European Synchrotron Radiation Facility (ESRF) doi:10.15151/ESRF-DC-543252921.
- [18] N. E. Brese, M. O’Keeffe, *Acta Crystallogr. Sect. B* **1991**, 47, 192–197.
- [19] A. S. Wills, *VaList*, Program available from www.ccp14.ac.uk.
- [20] J. Tauc, R. Grigorovici, A. Vancu, *Phys. Status Solidi* **1966**, 15, 627–637.
- [21] H. Kalo, W. Milius, M. Bräu, J. Breu, *J. Solid State Chem.* **2013**, 198, 57–64.

D Supporting Information for Chapter 5

Experimental Procedures

Preparation of starting materials

P_3N_5 was prepared following a procedure by Stock et al. by heating P_4S_{10} (Sigma-Aldrich, 99,99%) in a constant flow of ammonia gas (5.0, Air Liquide). After drying a fused silica tube and a fused silica boat in a tube furnace (at 1273 K) under dynamic vacuum ($<10^{-3}$ mbar) the boat was loaded with P_4S_{10} in a constant flow of Ar. The apparatus was saturated with ammonia for 4 h and the temperature was increased to 1123 K and maintained for four additional hours. Then, the furnace was cooled to room temperature afterwards and heating/cooling ramps were set at 5 K/min each. The product was obtained as an orange powder and purity was confirmed by PXRD as well as CHNS analysis (C 0%, H 0%, N 42.69%, S 0%, expected C 0%, H 0%, N 42.98%, S 0% .^[6] Cristoballite-type PON was synthesized according to the literature and phase purity was confirmed by PXRD.^[45] ScN was prepared by nitridation of Sc in flowing N_2 utilizing a radio-frequency furnace according to the literature.^[46] TiN (Alfa Aesar, 99.7%), TiO_2 (Alfa Aesar, anatase, 99.9%) and NH_4F (Sigma Aldrich, $\geq 98\%$) were used as purchased.

High-pressure high-temperature synthesis

The oxonitridophosphates $TM_5P_{12}N_{26-x}O_x$ ($TM = Sc, Ti$ $x = 2, 3$) were obtained by high-pressure high-temperature synthesis using a 1000 t press with a modified Walker-type multianvil apparatus. $Sc_5P_{12}N_{23}O_3$ was synthesized from stoichiometric amounts of P_3N_5 , ScN, and PON. $Ti_5P_{12}N_{24}O_2$ was synthesized from 0.8 equiv. TiO_2 and stoichiometric amounts of TiN and P_3N_5 . 8 wt% NH_4F were added to the starting mixtures as a mineralizing agent (Table S1). The starting materials were handled in an Ar-filled glovebox (Unilab, MBraun, Garching, $O_2 < 1$ ppm, $H_2O < 0.1$ ppm) and ground thoroughly in an agate mortar to minimize external oxygen contamination. The mixture was transferred into a cylindrical crucible made from hexagonal boron nitride (HeBoSint® S100, Henze, Kempten, Germany) closed with a boron nitride cap. The crucible was then placed in an octahedron (MgO with 5 % Cr_2O_3 , edge length 18 mm, Ceramic Substrates & Components, Isle of Wight, UK), which was drilled through and

loaded with different components. First, a ZrO_2 cylinder (Cesima Ceramics, Wust-Fischbeck, Germany) was fixed in the borehole and closed on one side by a Mo plate. Then, a graphite tube (Schunk Kohlenstofftechnik GmbH, Gießen, Germany), a MgO spacer (Cesima Ceramics, Wust-Fischbeck, Germany), and a shorter graphite tube were put into the octahedron. While ZrO_2 served as a thermal insulator, the two graphite tubes were used as electrical resistance furnaces; the combination of two single tubes is necessary to decrease the temperature gradient. After inserting the crucible with the sample, the assembly was completed by adding a second MgO spacer and a further Mo plate to ensure a symmetric setup. To generate approximately hydrostatic conditions, the uniaxial force of the hydraulic press was converted by a Walker-type module with inserted steel wedges, forming a cubic cavity. This cavity was filled with eight Co-doped (7 %) WC cubes (Hawedia, Marklkofen, Germany). To enclose the sample octahedron, the edges of the WC cubes were truncated (11 mm edge length). Furthermore, four of the cubes were equipped with a PTFE film (Vitaflon Technische Produkte GmbH, Bad Kreuznach, Germany) for electrical insulation. The remaining cubes were prepared with pyrophyllite gaskets (Ceramic Substrates & Components, Isle of Wight, UK) to prevent the outflow of the MgO octahedron. Bristol board (369 g m^{-2}) was used to fix the gaskets. The reactions were carried out under 8 GPa of pressure and 1400°C .^[8,11,12,23]

Powder X-ray diffraction

Powder X-ray diffraction was carried out on a StadiP diffractometer (STOE & Cie, Darmstadt, Germany) equipped with a MYTHEN 1K detector (Dectris, Baden, Switzerland; angular range $\Delta 2\theta = 12.5^\circ$), a Cu source and a Ge(111) monochromator for Cu- $K\alpha_1$ radiation. Samples were filled into glass capillaries with 0.3 mm diameter and 0.01 mm wall thickness (Hilgenberg GmbH, Malsfeld, Germany). Data were recorded in the angular range between $2\theta = 5\text{--}120^\circ$ with a step width of $0.015^\circ/\text{step}$. Diffraction data were analyzed with the TOPAS-Academic V6 software. Structure models were refined with the Rietveld method.

Scanning electron microscopy and energy-dispersive X-ray spectroscopy (EDX)

Samples were placed on conducting carbon foil and coated with carbon. EDX spectra were collected using a FEI Helios Nanolab G3 Dual Beam UC (FEI, Hillsboro, OR, USA) with an attached X-Max 80 SDD detector (Oxford Instruments, Abingdon, UK).

(Scanning) transmission electron microscopy

Samples were ground in absolute ethanol and a drop of the resulting suspension was cast on a TEM grid with holey carbon film (Plano GmbH, Wetzlar, Germany). The grid was mounted on a double-tilt holder and transferred into a Cs DCOR probe-corrected Titan Themis 300 (FEI, USA) TEM equipped with X-FEG, post-column filter (Enfinium ER-799), US1000XP/FT camera system (Gatan, Germany), and a windowless, 4-quadrant Super-X EDX detector. TEM images were recorded using a $4k \times 4k$ FEI Ceta CMOS camera. The microscope was operated at 300 kV accelerating voltage for SAED and STEM-HAADF and -EDX (convergence angle of 16.6 mrad, 50 μm aperture, detector inner half angle 33 mrad for 245 mm camera length). For evaluation of the TEM data, the following software was used: Digital Micrograph (Fourier filtering of STEM images), ProcessDiffraction7 (geometric calculations for SAED), JEMS (SAED simulations), Velox v2.8 (Thermo Fisher Scientific, USA).

Single-crystal X-ray diffraction

Single-crystal X-ray diffraction data were collected on a Bruker D8 Venture TXS diffractometer (rotating anode, Mo-K α radiation, $\lambda = 0.71073 \text{ \AA}$, multilayer monochromator) by combined φ - and ω -scans. Indexing, integration, semi-empirical absorption correction (based on equivalent reflections), were performed by the APEX3 software package. Employing SHELX-2018, the structure was solved by direct methods and refined against F^2 by the full-matrix least-squares method. ^[16]

Bond-valence sum (BVS) Calculations

BVS calculations were performed using the software ValList v4.0.7.^[18] The structure models of $TM_5P_{12}N_{26-x}O_x$ ($TM = \text{Sc, Ti}$ $x = 2, 3$) were taken into account with either all anion positions occupied by N or O to determine mixed occupied sites where it was indicated by BVS values. BVS values of cations were determined for the final structure models by taking mixed occupied anionic sites into account.^[17]

FTIR spectroscopy

FTIR spectra of the title compounds were collected on a Spectrum BX II spectrometer (PerkinElmer, Waltham, MA, USA) between 600 and 4400 cm⁻¹ with DuraSampler attenuated total reflectance unit (ATR).

Magnetization Measurements

Magnetization isotherms and susceptibility measurements of a powdered sample was performed with a Quantum Design Inc. Physical Property Measurements System (PPMS) equipped with a vibrating sample magnetometer (VSM) option. Data were collected at temperatures of 2-300 K with field strengths of ± 50 kOe with the PPMS MultiVu software package.^[11] Inverse molar susceptibility data were fitted with a modified Curie-Weiss equation:

$$\frac{1}{\chi_m(T)} = \frac{1}{\chi_0 + \frac{n \cdot (N_A \cdot \frac{\mu_B^2}{3k_B}) \cdot \mu_{eff}}{T - \theta}} = \frac{1}{\chi_0 + \frac{n \cdot 0.12503776 \cdot \mu_{eff}}{T - \theta}}$$

UV-Vis spectroscopy

A V-650 UV-Vis spectrophotometer (JASCO, Gross-Umstadt, Germany) equipped with a photomultiplier tube detector and a single monochromator with 1200 lines/mm was used for recording UV-Vis spectra in the range of 240 to 800 nm. A deuterium (240–330 nm) and a halogen lamp (330–880 nm) was used with a 2 nm resolution and a scan speed of 400 nm/min controlled by the Spectra Manager II software. Samples were affixed between a fused silica glass slide and a BaSO₄-coated stamp.

Results and Discussion

Synthesis

Table D1 Weighed portions of starting materials for the syntheses of $\text{Sc}_5\text{P}_{12}\text{N}_{23}\text{O}_3$ and $\text{Ti}_5\text{P}_{12}\text{N}_{24}\text{O}_2$.

Title compounds	Starting material / mg				
$\text{Sc}_5\text{P}_{12}\text{N}_{23}\text{O}_3$	ScN	P_3N_5	PON	NH_4F	
	22.87	37.93	14.19	6	
$\text{Ti}_5\text{P}_{12}\text{N}_{24}\text{O}_2$	TiN	P_3N_5	TiO_2	NH_4F	
	20.43	53.79	5.27	5	

Structure determination

Table D2 Atomic coordinates, isotropic displacement parameters/ \AA^2 , and occupancy of $\text{Sc}_5\text{P}_{12}\text{N}_{23}\text{O}_3$.

Atom	Wyckoff	<i>x</i>	<i>y</i>	<i>z</i>	U_{eq}	<i>Occ.</i>
Sc1	$32g$	0.35363(2)	0.06101(2)	0.04356(2)	0.00594(5)	1
Sc2	$8b$	0	1/4	1/8	0.02492(13)	1
P1	$32g$	0.26625(2)	0.14843(2)	0.16907(2)	0.00410(6)	1
P2	$32g$	0.25578(2)	0.30895(2)	0.08368(2)	0.00340(5)	1
P3	$32g$	0.06818(2)	0.34112(2)	0.25058(2)	0.00323(5)	1
N1	$32g$	0.34971(7)	0.07463(7)	0.13246(4)	0.00485(14)	1
N2	$32g$	0.02045(7)	0.05360(7)	0.12108(4)	0.00525(14)	1
N3	$32g$	0.00848(8)	0.08744(7)	0.29230(4)	0.00497(14)	1
N4	$32g$	0	1/4	0.03295(5)	0.00475(19)	1
N5/O5	$32g$	0.17606(7)	0.05919(7)	0.04477(4)	0.00651(14)	0.25/0.75
N6	$16b$	0.16331(7)	0.37506(8)	0.04840(4)	0.00554(15)	1
N7	$32g$	0.16249(7)	0.28013(7)	0.28644(4)	0.00552(15)	1

Table D3 Anisotropic displacement parameters for $\text{Sc}_5\text{P}_{12}\text{N}_{23}\text{O}_3$ with standard deviations in parentheses.

Atom	U_{11}	U_{22}	U_{33}	U_{23}	U_{13}	U_{12}
Sc1	0.00665(8)	0.00607(8)	0.00512(8)	-0.00010(6)	-0.00009(6)	-0.00129(6)
Sc2	0.0351(2)	U_{11}	0.00456(18)	0	0	0.0213(3)
P1	0.00476(11)	0.00383(11)	0.00371(11)	-0.00010(8)	-0.00038(8)	0.00029(8)
P2	0.00357(11)	0.00353(11)	0.00309(10)	0.00018(8)	0.00012(8)	-0.00029(8)
P3	0.00342(10)	0.00306(10)	0.00322(10)	-0.00003(8)	-0.00001(8)	-0.00027(8)
N1	0.0054(3)	0.0052(3)	0.0040(3)	0.0000(3)	0.0000(3)	0.0017(3)
N2	0.0053(3)	U_{11}	0.0051(3)	0.0007(3)	0.0020(3)	0.0005(3)
N3	0.0043(3)	0.0050(3)	0.0056(3)	0.0018(3)	-0.0003(3)	-0.0002(3)
N4	0.0044(5)	0.0057(5)	0.0042(4)	0	0	-0.0019(4)
N5/O5	0.0059(3)	0.0073(3)	0.0062(3)	0.0012(3)	0.0001(3)	-0.0006(3)
N6	0.0052(3)	0.0056(4)	0.0058(4)	-0.0011(3)	-0.0021(3)	0.0008(3)
N7	0.0057(4)	0.0044(3)	0.0065(4)	-0.0006(3)	-0.0020(3)	0.0004(3)

Table D4 Atomic coordinates, isotropic displacement parameters/ \AA^2 , and occupancy of $\text{Ti}_5\text{P}_{12}\text{N}_{24}\text{O}_2$.

Atom	Wyckoff	x	y	z	U_{eq}	$Occ.$
Ti1	$32g$	0.33980(2)	0.07346(2)	0.04256(2)	0.00686(8)	1
Ti2	$8b$	0	1/4	1/8	0.01103(11)	1
P1	$32g$	0.26168(3)	0.15620(3)	0.16788(2)	0.00303(8)	1
P2	$32g$	0.25231(3)	0.31833(3)	0.08339(2)	0.00280(8)	1
P3	$32g$	0.07509(3)	0.33688(3)	0.25077(2)	0.00279(8)	1
N1	$32g$	0.34379(10)	0.07642(9)	0.13085(5)	0.00412(19)	1
N2/O2	$32g$	0.01550(9)	0.06164(9)	0.12382(4)	0.00480(19)	0.85/0.15
N3	$32g$	0.00218(10)	0.08563(9)	0.29203(4)	0.00405(19)	1
N4	$16d$	0	1/4	0.03403(7)	0.0041(3)	1
N5/O5	$32g$	0.17064(9)	0.06275(9)	0.04280(5)	0.00465(19)	0.8/0.2
N6/O6	$32g$	0.16239(9)	0.38895(9)	0.04614(5)	0.00509(19)	0.85/0.15
N7	$32g$	0.16260(9)	0.26818(9)	0.28992(4)	0.00400(18)	1

Table D5 Anisotropic displacement parameters for $\text{Ti}_5\text{P}_{12}\text{N}_{24}\text{O}_2$ with standard deviations in parentheses.

Atom	U_{11}	U_{22}	U_{33}	U_{23}	U_{13}	U_{12}
Ti1	0.00887(12)	0.00499(12)	0.00673(12)	-0.00132(7)	0.00305(8)	-0.00158(8)
Ti2	0.01242(16)	U_{11}	0.0082(2)	0	0	-0.00250(18)
P1	0.00336(14)	0.00297(14)	0.00276(14)	0.00027(10)	-0.00014(10)	0.00033(10)
P2	0.00259(14)	0.00308(15)	0.00274(14)	0.00044(10)	-0.00004(10)	-0.00005(10)
P3	0.00292(14)	0.00275(14)	0.00270(14)	-0.00001(10)	-0.00004(10)	-0.00030(10)
N1	0.0047(4)	0.0044(4)	0.0033(4)	-0.0003(3)	-0.0001(3)	0.0012(3)
N2/O2	0.0050(4)	0.0044(4)	0.0050(4)	-0.0001(3)	0.0010(3)	0.0004(3)
N3	0.0040(4)	0.0043(4)	0.0038(4)	0.0013(3)	-0.0002(3)	-0.0002(3)
N4	0.0050(6)	0.0049(6)	0.0025(6)	0	0	-0.0023(5)
N5/O5	0.0048(4)	0.0046(5)	0.0045(4)	0.0004(3)	-0.0002(3)	-0.0003(3)
N6/O6	0.0057(4)	0.0045(4)	0.0050(4)	0.0000(3)	-0.0014(3)	0.0002(3)
N7	0.0053(4)	0.0034(4)	0.0033(4)	-0.0001(3)	-0.0017(3)	0.0000(3)

Table D6 Interatomic distances (Å) and bond angles (°) in the structure of $\text{Sc}_5\text{P}_{12}\text{N}_{23}\text{O}_3$.

Sc1	N1	1x	2.1421(9)	N5/O5	-P1-	N1	110.18(5)
	N5/O5	1x	2.1526(9)	N5/O5		N2	111.79(5)
	N5/O5	1x	2.1950(9)	N1		N2	110.97(5)
	N7	1x	2.2125(9)	N5/O5		N7	105.87(5)
	N3	1x	2.2402(10)	N1		N7	108.16(5)
	N6	1x	2.3108(10)	N2		N7	109.68(5)
Sc2	N4	2x	2.2106(13)	N1	-P2-	N2	108.53(5)
	N2	4x	2.4424(9)	N1		N6	106.04(5)
P1	N5/O5	1x	1.5722(9)	N2		N6	109.20(5)
	N1	1x	1.6338(9)	N1		N3	109.40(5)
	N2	1x	1.6372(9)	N2		N3	111.87(5)
	N7	1x	1.6423(9)	N6		N3	111.60(5)
P2	N1	1x	1.6310(9)	N4	-P3-	N7	108.20(4)
	N2	1x	1.6378(9)	N4		N6	104.20(5)
	N6	1x	1.6407(9)	N7		N6	108.92(5)
	N3	1x	1.6434(9)	N4		N3	112.19(4)
P3	N4	1x	1.6207(7)	N7		N3	109.82(5)
	N7	1x	1.6336(10)	N6		N3	113.24(5)
	N6	1x	1.6351(10)				
	N3	1x	1.6376(9)				

Table D7 Interatomic distances (Å) and bond angles (°) in the structure of $\text{Ti}_5\text{P}_{12}\text{N}_{24}\text{O}_2$.

Ti1	N5/O5	1x	2.0435(11)	N5/O5	-P1-	N2/O2	112.79(6)
	N5/O5	1x	2.0546(11)	N5/O5		N7	106.31(6)
	N1	1x	2.1064(11)	N2/O2		N7	110.62(6)
	N3	1x	2.1141(13)	N5/O5		N1	108.27(6)
	N7	1x	2.1697(11)	N2/O2		N1	110.09(6)
	N6/O6	1x	2.2384(11)	N7		N1	108.60(6)
Ti2	N4	1x	2.1691(16)	N1	-P2-	N2/O2	109.88(6)
	N4	1x	2.1692(16)	N1		N6/O6	107.86(6)
	N2/O2	4x	2.2911(11)	N2/O2		N6/O6	110.24(6)
P1	N5/O5	1x	1.6002(12)	N1		N3	108.25(6)
	N2/O2	1x	1.6368(11)	N2/O2		N3	109.95(6)
	N7	1x	1.6418(11)	N6/O6		N3	110.61(6)
	N1	1x	1.6447(12)	N4	-P3-	N6/O6	106.18(6)
P2	N1	1x	1.6336(12)	N4		N7	108.96(5)
	N1	1x	1.6354(11)	N6/O6		N7	111.50(6)
	N2/O2	1x	1.6462(12)	N4		N3	110.86(5)
	N6/O6	1x	1.6502(12)	N6/O6		N3	110.90(6)
P3	N4	1x	1.6206(9)	N7		N3	108.44(6)
	N6/O6	1x	1.6395(12)				
	N7	1x	1.6402(12)				
	N3	1x	1.6516(12)				

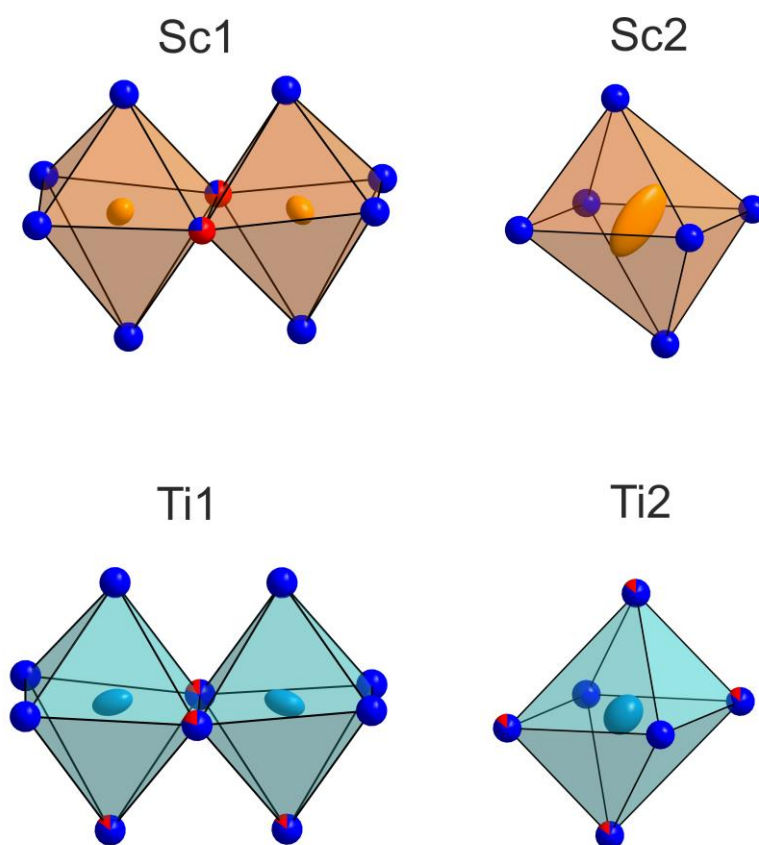


Figure D1. Thermal displacement ellipsoids for the *TM* sites of $\text{Sc}_5\text{P}_{12}\text{N}_{23}\text{O}_3$ (top) and $\text{Ti}_5\text{P}_{12}\text{N}_{24}\text{O}_2$ (bottom). Ellipsoids are displayed at a probability level of 99% (Sc orange, Ti light blue, N dark blue and mixed O/N sites in red/blue).

EDX measurements**Table D8.** EDX measurements (several point analyses) for $TM_5P_{12}N_{26-x}O_x$ ($TM = Sc, Ti$ $x = 2, 3$) compared to values derived from sum formulas.

atom % Crystal no.	Sc	P	N	O
1	11.2	26.3	52.1	10.2
2	12.5	29.0	50.3	8.01
3	11.3	26.4	51.7	10.5
4	11.3	26.5	43.5	18.6
5	12.8	28.3	42.6	16.2
6	9.6	22.9	53.7	13.7
7	11.5	26.9	52.0	9.4
calc.	11.6	27.9	53.5	6.9
	Ti	P	N	O
1	11.7	33.1	48.8	6.5
2	11.1	31.4	51.5	6.0
3	11.9	31.3	46.3	8.3
4	9.9	26.9	56.7	6.5
5	11.4	30.3	52.2	6.2
Calc.	11.6	27.9	55.8	4.7

Rietveld refinements**Table D9.** Crystallographic data from the Rietveld refinements for $TM_5P_{12}N_{26-x}O_x$ ($TM = Sc, Ti$ $x = 2, 3$), standard deviations are given in parentheses.

	$Sc_5P_{12}N_{23}O_3^*$	$Ti_5P_{12}N_{24}O_2^{**}$
phase fraction	79(1)	94.9(3)
crystal system	tetragonal	
space group	$I4_1/acd$ (no. 142)	
formula units/ unit cell	8	
lattice parameters / Å	$a = 12.36955(7)$ $c = 24.0304(1)$	$a = 12.1133(1)$ $c = 23.8656(4)$
radiation λ / Å	1.54056 (Cu- $K_{\alpha 1}$)	
cell volume / Å ³	3676.80(5)	3501.8(1)
2θ - range/°	5 < 2θ < 120	
refined parameters (incl. side phases)	29	26
background function	Shifted Chebyshev (12 parameters)	
R -values	$R_p = 0.0440$ $wR_p = 0.0612$ $R_{Bragg} = 0.0273$	$R_p = 0.0465$ $wR_p = 0.0662$ $R_{Bragg} = 0.0294$

*) BN from crucible as side phases

**) TiN (starting material) as side phase

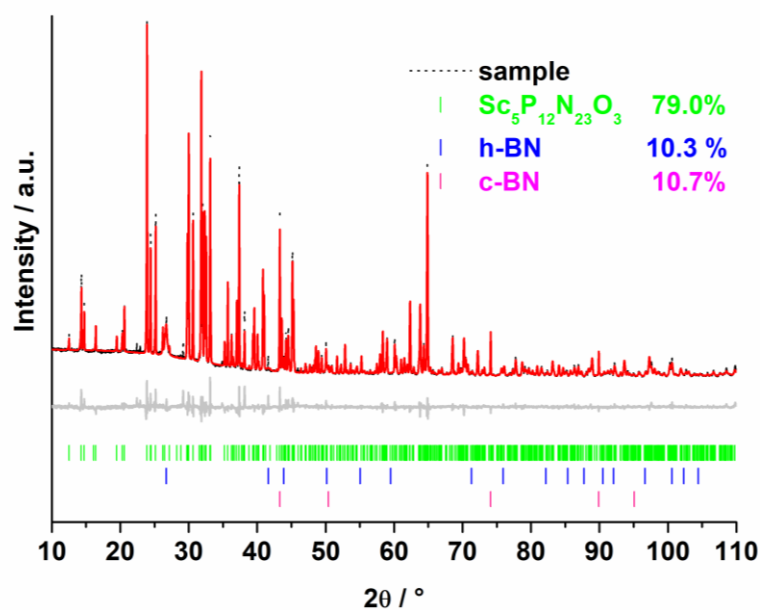


Figure D2 Rietveld refinement for $\text{Sc}_5\text{P}_{12}\text{N}_{23}\text{O}_3$; observed (black line) and calculated (red line) X-ray powder diffraction patterns, positions of Bragg reflections of $\text{Sc}_5\text{P}_{12}\text{N}_{23}\text{O}_3$ (vertical green bars), h-BN (vertical blue bars), c-BN (vertical violet bars), and difference profile (gray line).

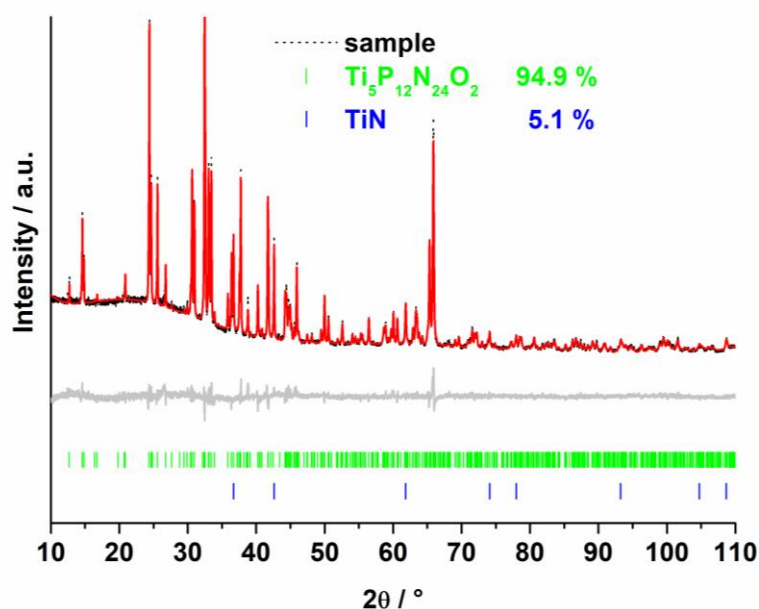


Figure D3. Rietveld refinement for $\text{Ti}_5\text{P}_{12}\text{N}_{24}\text{O}_2$ observed (black line) and calculated (red line) X-ray powder diffraction patterns, positions of Bragg reflections of $\text{Ti}_5\text{P}_{12}\text{N}_{24}\text{O}_2$ (vertical green bars), TiN (vertical blue bars), and difference profile (gray line).

BVS calculations

Table D10. Anion BVS for $\text{Sc}_5\text{P}_{12}\text{N}_{23}\text{O}_3$. Assumed mixed occupied sites are highlighted in green.

N1	N2	N3	N4	N5	N6	N7
3.14	2.77	2.93	3.09	2.68	2.90	3.03
O1	O2	O3	O4	O5	O6	O7
2.42	2.15	2.27	2.40	2.01	2.25	2.34

Table D11. Cation BVS for $\text{Sc}_5\text{P}_{12}\text{N}_{23}\text{O}_3$. Assumed mixed occupied anion sites were considered for calculations.

	Sc1	Sc2	P1	P2	P3
calc.	3.17	2.42	4.89	4.89	4.96
expected	3	3	5	5	5

Table D12. Anion BVS for $\text{Ti}_5\text{P}_{12}\text{N}_{24}\text{O}_2$. Assumed mixed occupied sites are highlighted in green.

N1	N2	N3	N4	N5	N6	N7
3.05	2.86	2.99	3.09	2.85	2.89	2.98
O1	O2	O3	O4	O5	O6	O7
2.39	2.20	2.33	2.39	2.16	2.25	2.32

Table D13. Cation BVS for in $\text{Ti}_5\text{P}_{12}\text{N}_{24}\text{O}_2$. Assumed mixed occupied anion sites were considered for calculations.

	Ti1	Ti2	P1	P2	P3
calc.	3.65	2.64	4.91	4.79	4.87
expected	3	4	5	5	5

FTIR spectra

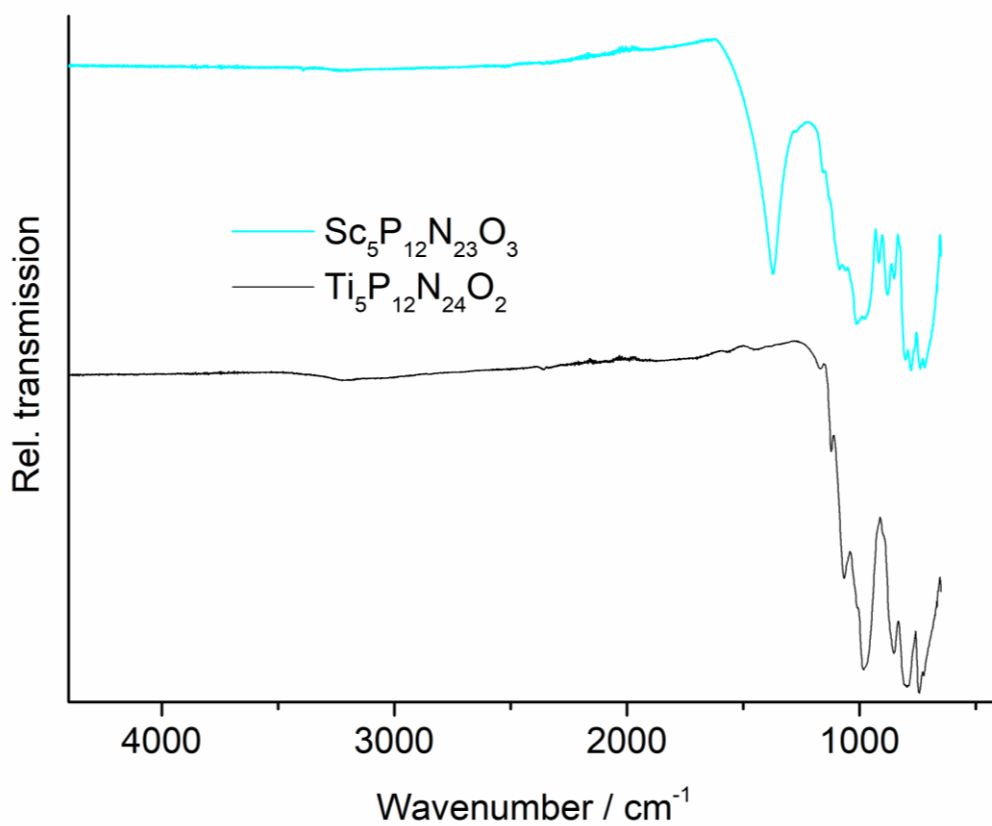
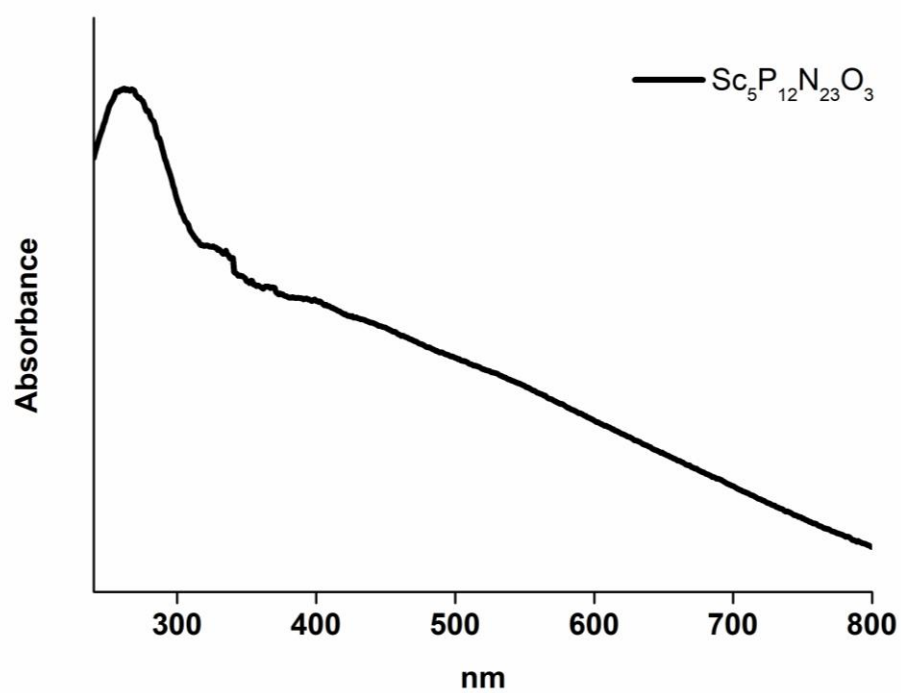
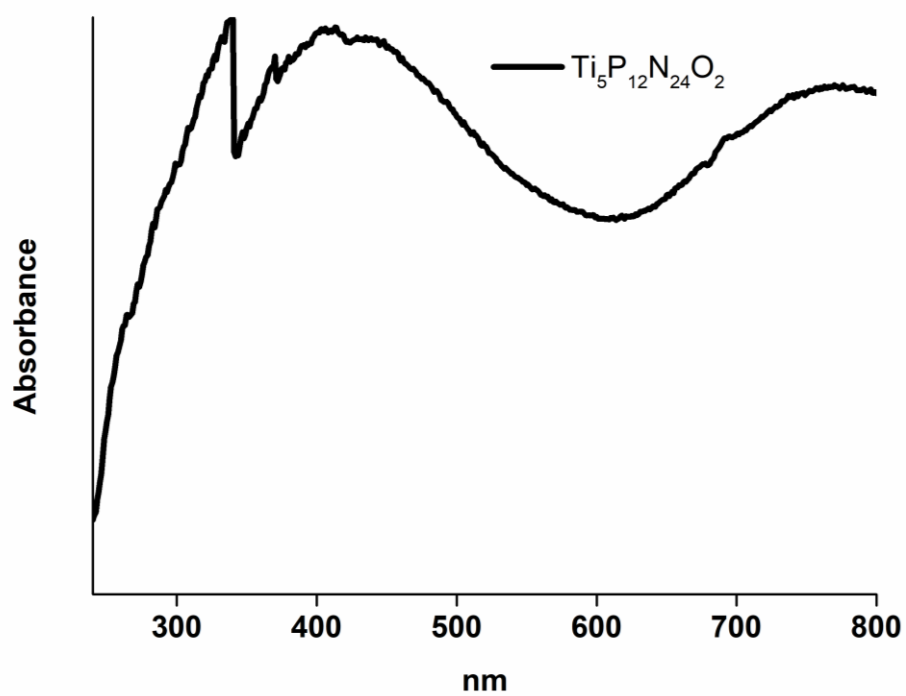


Figure D4. FTIR spectra of Sc₅P₁₂N₂₃O₃ (blue) and Ti₅P₁₂N₂₄O₂ (black).

UV-Vis spectra

Figure D5: UV-Vis spectrum of $\text{Sc}_5\text{P}_{12}\text{N}_{23}\text{O}_3$.Figure D6: UV-Vis spectrum of $\text{Ti}_5\text{P}_{12}\text{N}_{24}\text{O}_2$.

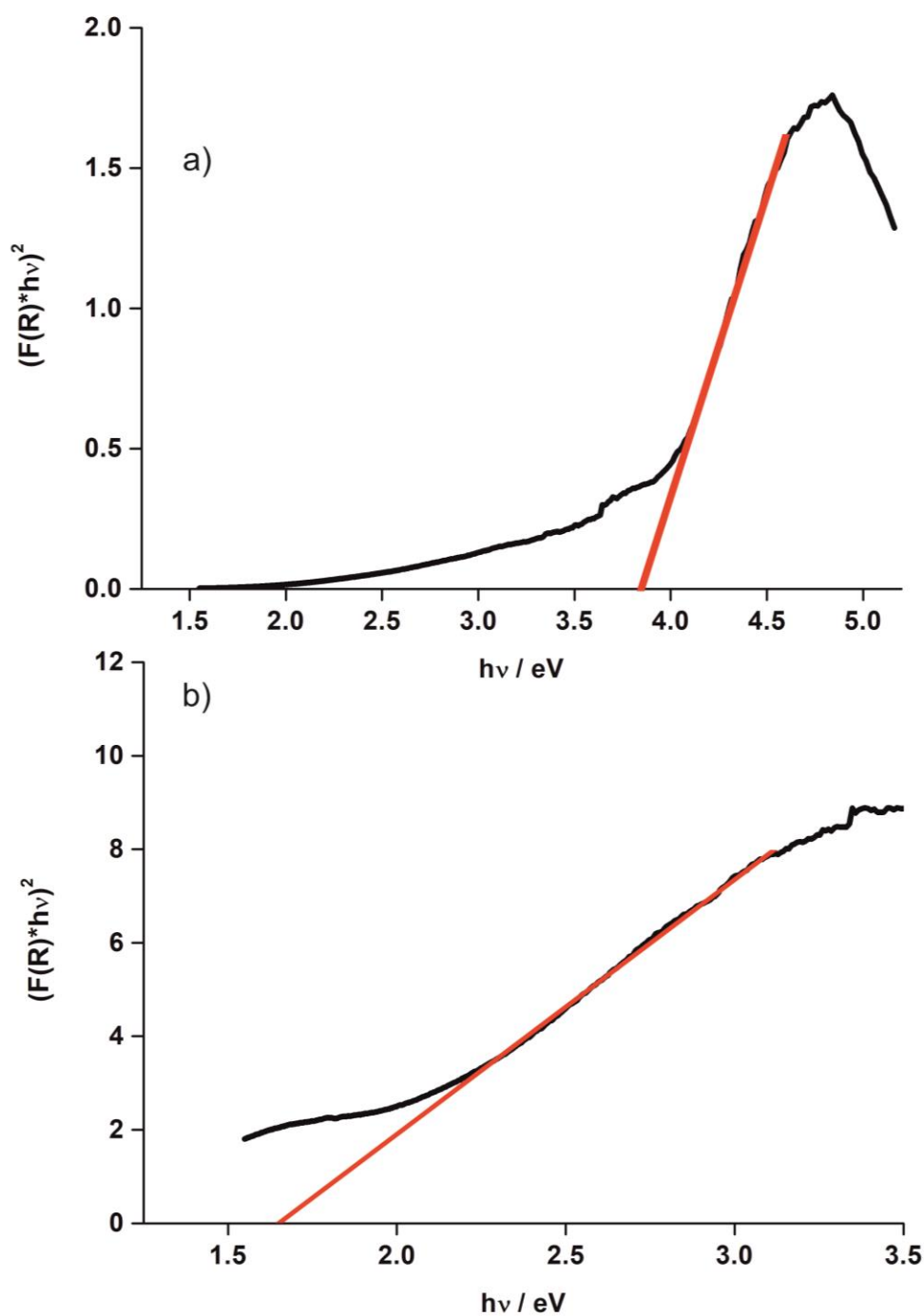


Figure D7: Tauc plots for $\text{Sc}_5\text{P}_{12}\text{N}_{23}\text{O}_3$ (top) and $\text{Ti}_5\text{P}_{12}\text{N}_{24}\text{O}_2$ (bottom). Red lines represent linear regressions from the steep regions to estimate the optical band gaps from the inflection points with the abscissa. Data between 2.1 and 3.1 eV ($\text{Ti}_5\text{P}_{12}\text{N}_{24}\text{O}_2$) and 4.0 to 4.5 eV ($\text{Sc}_5\text{P}_{12}\text{N}_{23}\text{O}_3$) were used for linear regressions.

References

- [1] A. Stock, H. Grüneberg, *Ber. Dtsch. Chem. Ges.* **1907**, *40*, 2573–2578.
- [2] S. Vogel, D. Baumann, R. Niklaus, E. Bykova, M. Bykov, N. Dubrovinskaia, L. Dubrovinsky, W. Schnick, *Angew. Chem. Int. Ed.* **2018**, *57*, 6691–6695; *Angew. Chem.* **2018**, *130*, 6801–6805.
- [3] R. Niewa, D. A. Zharebtsov, M. Kirchner, M. Schmidt, W. Schnelle, *Chem. Mater.* **2004**, *16*, 5445–5451.
- [4] W. David, *Am. Mineral.* **1991**, *76*, 1092–1100.
- [5] D. Walker, M. A. Carpenter, C. M. Hitch, *Am. Mineral.* **1990**, *75*, 1020–1028.
- [6] H. Huppertz, *Z. Kristallogr.* **2004**, *219*, 330–338.
- [7] S. Wendl, L. Eisenburger, P. Strobel, D. Günther, J. P. Wright, P. J. Schmidt, O. Oeckler, W. Schnick, *Chem. Eur. J.* **2020**, *26*, 7292–7298.
- [8] G. M. Sheldrick, *Acta Crystallogr. Sect. C* **2015**, *71*, 3–8.
- [9] A. S. Wills, *Valist*, Program available from www.ccp14.ac.uk.
- [10] N. E. Brese, M. O’Keeffe, *Acta Crystallogr. Sect. B* **1991**, *47*, 192–197.
- [11] Version 1.5.11 ed., Quantum Design Inc., San Diego, USA, **2013**.

E Supporting Information for Chapter 6

Experimental Procedures

Preparation of starting materials

P_3N_5 was prepared following a procedure by Stock et al.^[1] The product was obtained as an orange powder. Purity was confirmed by PXRD as well as CHNS analysis (C 0%, H 0%, N 42.69%, S 0% expected C 0%, H 0%, N 42.98%, S 0%). The azide NH_4N_3 was prepared according to literature.^[2] TiN (Alfa Aesar, 99.7%) and NH_4F (Sigma Aldrich, $\geq 98\%$) were used as purchased.

High-pressure high-temperature synthesis

The nitridophosphate β - TiP_4N_8 was obtained by high-pressure high-temperature synthesis using a 1000 t press with a modified Walker-type multianvil apparatus.^[3–7] All products were synthesized from stoichiometric amounts of P_3N_5 , TiN, NH_4N_3 , and additional 10 wt% NH_4F (Table E1). To prevent oxygen contamination, starting materials were handled in an Ar-filled glovebox (Unilab, MBraun, Garching, $O_2 < 1$ ppm, $H_2O < 0.1$ ppm) and ground thoroughly in an agate mortar. Details on the preparation and handling of the 1000 t Walker-type multianvil press are described in the literature.^[8–10] The reaction was carried out at 8 GPa and 1400°C.

Annealing of TiP_4N_8

β - TiP_4N_8 was annealed in sealed silica ampoules in a tube furnace at 850 °C for 20 h with heating and cooling rates of 5 °C/ min to obtain bulk α - TiP_4N_8 .

Powder X-ray diffraction

Powder X-ray diffraction was carried out on a StadiP diffractometer (STOE & Cie, Darmstadt, Germany) equipped with an MYTHEN 1K detector (Dectris, Baden, Switzerland; angular range $\Delta 2\theta = 12.5^\circ$), a Cu source and a Ge(111) monochromator for Cu- $K\alpha_1$ radiation. Samples were filled into glass capillaries with 0.3 mm diameter and 0.01 mm wall thickness (Hilgenberg GmbH, Malsfeld, Germany). Data were recorded in the angular range $5^\circ < 2\theta <$

120°. Diffraction patterns were analyzed with the TOPAS-Academic V6 software, where phase fractions were approximately quantified with the Rietveld method.

Temperature-dependent PXRD patterns were recorded on a StadiP diffractometer (STOE & Cie, Darmstadt, Germany) in the range $2^\circ < 2\theta < 75^\circ$ and Mo-K α_1 radiation ($\lambda = 0.709300 \text{ \AA}$). An image-plate position-sensitive detector was used for X-ray detection. Diffraction patterns were collected in steps of 50°C up to 700 °C for two cycles. Samples were filled into silica capillaries with 0.4 mm diameter and 0.01 mm wall thickness (Hilgenberg GmbH, Malsfeld, Germany). Lattice parameters were extracted by means of Pawley fits.

Scanning electron microscopy and energy-dispersive X-ray spectroscopy (EDX)

Samples were placed on conducting carbon foil and coated with carbon. EDX spectra were collected using an FEI Helios Nanolab G3 Dual Beam UC (FEI, Hillsboro, OR, USA) with an attached X-Max 80 SDD detector (Oxford Instruments, Abingdon, UK).

(Scanning) transmission electron microscopy (TEM, STEM)

Samples were ground in absolute ethanol and a drop of the resulting suspension was cast on a TEM grid with lacey carbon film (Plano GmbH, Wetzlar, Germany). The grid was mounted on a double-tilt low background holder and transferred into a Cs DCOR probe-corrected Titan Themis 300 (FEI, USA) TEM equipped with X-FEG, post-column filter (Enfinium ER-799), US1000XP/FT camera system (Gatan, Germany), and a windowless, 4-quadrant Super-X EDX detector (FEI, USA) TEM images were recorded using a 4k × 4k FEI Ceta CMOS camera. The microscope was operated at 300 kV accelerating voltage for SAED, STEM-HAADF and EDX (semiconvergence angle 16.6 mrad, 50 μm aperture, HAADF detector inner half angle 33 mrad for 245 mm camera length). For evaluation of the TEM data, the following software was used: Digital Micrograph (Fourier filtering of STEM images), ProcessDiffraction7 (geometric calculations for SAED), JEMS (SAED simulations).

Single-crystal X-ray diffraction

Single-crystal X-ray diffraction data at ambient conditions were collected on a Bruker D8 Venture TXS diffractometer (rotating anode, Mo-K α radiation, $\lambda = 0.71073 \text{ \AA}$, multilayer

monochromator) by combined φ - and ω -scans. Indexing, integration, semi-empirical absorption correction (based on equivalent reflections), were performed by the APEX3 software package. Employing SHELX-2018, the structure was solved by direct methods and refined against F^2 by the full-matrix least-squares method.^[11]

Temperature-dependent high-intensity synchrotron diffraction data of a TiP_4N_8 single crystal were obtained at beamline P24, DESY, Hamburg, ($\lambda = 0.49920 \text{ \AA}$) with a Pilatus 1M CdTe. Single crystals of disordered β - TiP_4N_8 were mounted and sealed inside silica glass capillaries and held in place with silica glass fibers. Integration was done with CrysAlis Pro and semiempirical absorption correction with SADABS.^[12,13] Solution and refinement of the average structure were done with SHELX-2018.

In some cases, separate scale factors for reflections with $h = 3n$ and $h \neq 3n$ were used (HKL F 5 format).

Bond-valence sum (BVS) Calculations

BVS calculations were performed using the software ValList v4.0.7.^[14,15]

IR spectroscopy

FTIR spectra of the title compounds were collected on a Spectrum BX II spectrometer (PerkinElmer, Waltham, MA, USA) between 600 and 4400 cm^{-1} with DuraSampler attenuated total reflectance unit (ATR).

UV-Vis spectroscopy

A V-650 UV-Vis spectrophotometer (JASCO, Gross-Umstadt, Germany) equipped with a photomultiplier tube detector and a single monochromator with 1200 lines/mm was used for recording UV-Vis spectra in the range of 240 to 800 nm. A deuterium (240–330 nm) and a halogen lamp (330–880 nm) were used with a 2 nm resolution and a scan speed of 400 nm/min controlled by the Spectra Manager II software. Samples were fixed between a fused silica glass slide and a BaSO_4 -coated stamp. Pseudo-absorption spectra were calculated by the Kubelka-Munk function $F(R) = (1-R)^2/2R$ where R is reflectance. In the Tauc plots, $h\nu$ was plotted against $[F(R)h\nu]^{1/n}$ with $n = -1/2$ for indirect bandgaps.^[16]

DFT calculations

The Vienna ab initio simulation package (VASP) based on density functional theory (DFT) and plane wave basis sets^[17,18] was used for the electronic structure calculations. The projector-augmented waves (PAW)^[19] approach was applied, and contributions of correlation and exchange were treated in the generalized-gradient approximation (GGA)^[20] using PBE^[20] and SCAN^[21] potentials. Dispersion corrections with the Grimme D2-Method were applied.^[22] The Brillouin zones were sampled with either a 4x20x11 (β -TiP₄N₈) or 12x20x11 (α -TiP₄N₈) Γ -centered Monkhorst Pack k -point mesh and a 500 eV plane wave energy cutoff. Both structures were optimized until forces between atoms are below 5×10^{-5} eVÅ⁻¹ and total energy changes below 10^{-8} eV. For $E(V)$ calculations the cell volumes were varied $\pm 5\%$ around the equilibrium and the results evaluated with the universal Vinet equation of state (EOS). Band structures and electronic density of states are shown in Figure E12. Phonon dispersions and phonon density-of states (Figure E13) were calculated from forces acting on displaced atoms in 2x2x2 supercells using PHONOPY.^[23] Thermodynamic properties were obtained within the quasi-harmonic approximation (QHA)^[24] by calculating the phonon states at nine volumes ($\pm 5\%$ around the equilibrium volume) and finding the Gibbs free energy $G(T,p)$ at the minima of the function $[U(V) + F_{\text{phonon}}(V,T) + pV]$ at each temperature as shown exemplarily for zero pressure in Figure E14. The energy barrier between α -TiP₄N₈ and β -TiP₄N₈ was calculated using the climbing nudged elasting band (CI-NEB) method^[25] with 16 images between the initial and final states. Linear extrapolations between the initial and final structures were used as starting parameters, respectively.

Results and Discussion

Synthesis

Table E11 Weighed portions of starting materials for the syntheses of TiP_4N_8 .

Compound		Starting material		
TiP_4N_8	TiN	P_3N_5	NH_4N_3	NH_4F
	16.4 mg	57.4 mg	2.1 mg	6 mg
	0.26 mmol	0.35 mmol	0.03 mmol	0.16 mmol

Structure representations

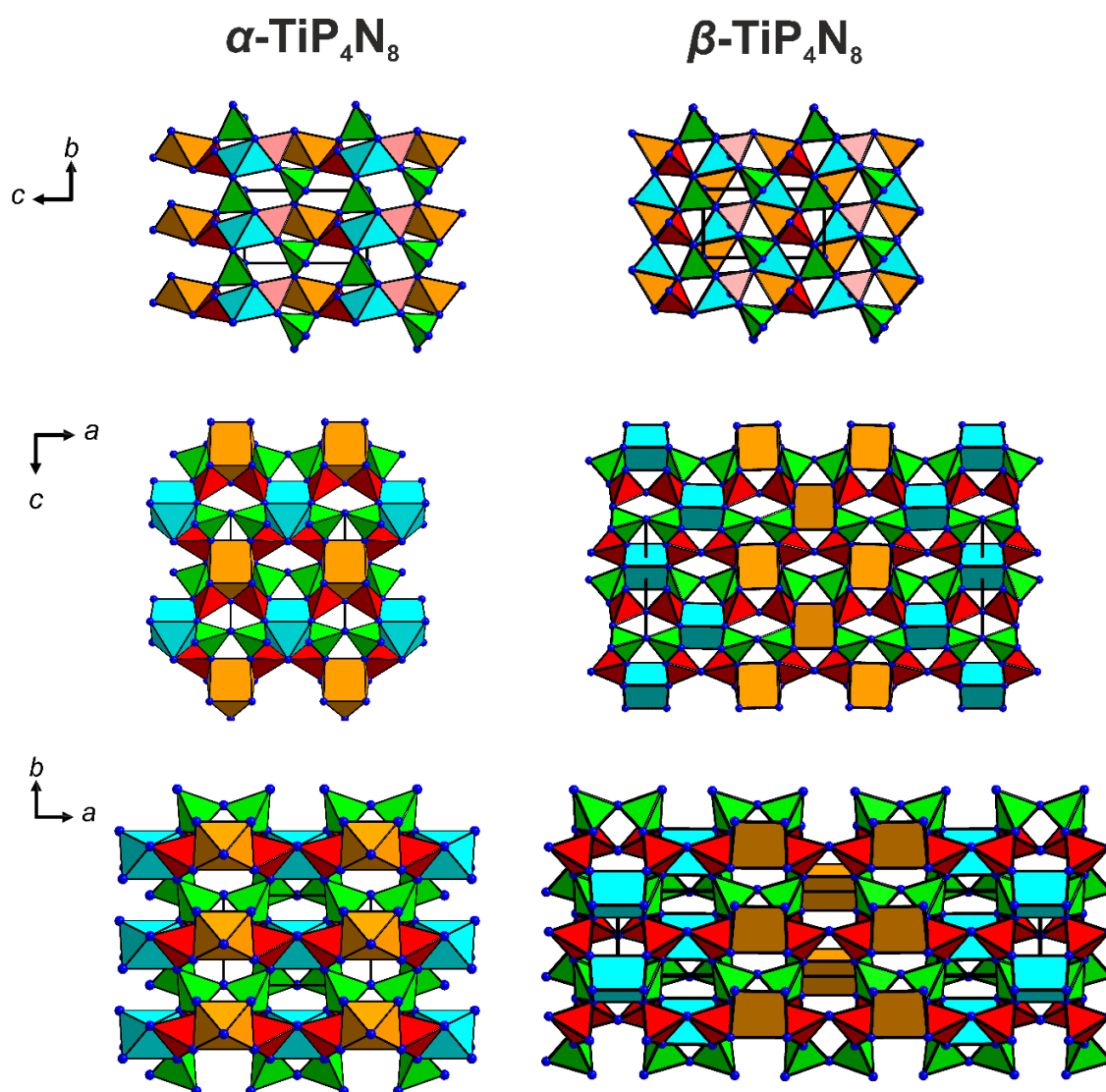


Figure E1. Structure projections of $\alpha\text{-TiP}_4\text{N}_8$ and $\beta\text{-TiP}_4\text{N}_8$ along [100], [010] and [001]

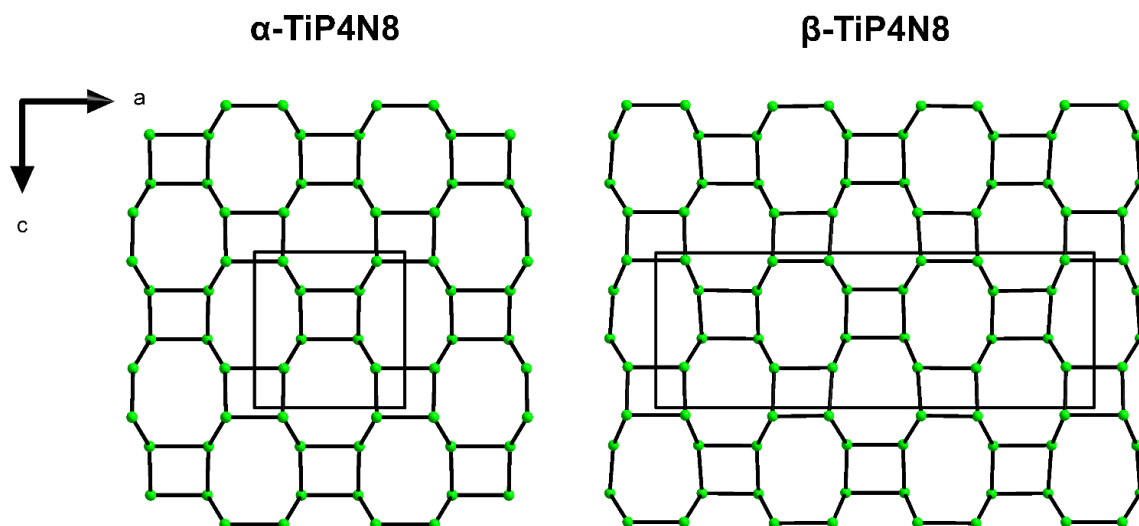


Figure E2. Nodal representations of α -TiP₄N₈ and β -TiP₄N₈ along [010]

Structure determination

Table E2 Crystallographic data of the single-crystal structure refinements of TiP_4N_8 . Estimated standard deviations are given in parentheses.

compound	$\alpha\text{-TiP}_4\text{N}_8$	$\beta\text{-TiP}_4\text{N}_8$	disordered TiP_4N_8	HT- $\beta\text{-TiP}_4\text{N}_8$
temperature/ K	296(2)	298(2)	293	873
molar mass /g·mol ⁻¹	283.86			
crystal system	orthorhombic			
space group	$Pmn2_1$ (no. 31)			
lattice parameters / Å, °	$a = 7.6065(2)$	$a = 22.9196(5)$	$a = 22.907(5)$	$a = 22.962(5)$
	$b = 4.63320(10)$	$b = 4.58800(10)$	$b = 4.5827(9)$	$b = 4.6045(9)$
	$c = 7.8601(3)$	$c = 8.0970(2)$	$c = 8.0988(16)$	$c = 8.0982(16)$
cell volume / Å ³	277.009(14)	851.44(3)	850.2(3)	856.2(3)
formula units/ per unit cell	2	6	6	6
density / g·cm ³	3.403	3.322	3.327	3.303
μ / mm ⁻¹	2.640	2.577	0.939	0.939
temperature / K	296(2)	298(2)	293(3)	873(5)
absorption correction	semiempirical			
radiation	Mo- K_α ($\lambda = 0.71073$ Å)		synchrotron, DESY P24 ($\lambda = 0.4992$ Å)	
F(000)	276	828	828	828
θ range / °	$3.7 \leq \theta \leq 36.3$	$1.7 \leq \theta \leq 34.9$	$1.9 \leq \theta \leq 23.3$	$1.9 \leq \theta \leq 23.3$
$\sin \theta \cdot \lambda^{-1}$ / Å ⁻¹	0.83	0.80	0.79	0.79
total no. of reflections	7500	9236	11025	33096
Independent	1357/ 1416	6268/ 6574	3055/ 3136	23542/ 23542
reflections [$I \geq 2\sigma(I)$ / all]				
$R_\sigma / R_{\text{int}}$	0.0317 / 0.0428	0.0133/ -*	0.0217/ 0.0182	0.0342/ -*
refined parameters / restraints	65/ 1	179/ 1	193/ 2	184/ 1
Goodness of fit	1.091	1.126	1.102	1.081
R-values [$I \geq 2\sigma(I)$]	$R1 = 0.0255$; $wR2 = 0.0617$	$R1 = 0.0220$; $wR2 = 0.0684$	$R1 = 0.0244$ $wR2 = 0.0721$	$R1 = 0.0395$ $wR2 = 0.1217$
R-values (all data)	$R1 = 0.0277$; $wR2 = 0.0631$	$R1 = 0.0232$; $wR2 = 0.0692$	$R1 = 0.0247$ $wR2 = 0.0730$	$R1 = 0.0419$ $wR2 = 0.1256$
$\Delta\rho_{\text{max}}, \Delta\rho_{\text{min}}$ / e·Å ⁻³	0.494, -0.643	0.720, -0.467	0.706/ -1.482	1.725/ -1.075

*separate scale factors were used (HKLF 5 format)

Table E3 Atomic coordinates, isotropic displacement parameters (\AA^2), and site occupancies of α - TiP_4N_8 .

Atom	Wyckoff position	x	y	z	U_{eq}	occ.
Ti1	2a	0	0.61255(12)	0.42990(9)	0.00623(12)	1
P1	4b	0.30454(8)	0.41321(13)	0.24765(9)	0.00409(12)	1
P2	4b	0.31171(8)	0.09790(13)	0.56012(8)	0.00397(12)	1
N1	4b	0.3147(3)	0.1809(5)	0.0931(3)	0.0059(4)	1
N2	4b	0.1736(3)	0.6911(5)	0.2278(3)	0.0050(3)	1
N3	4b	0.2060(3)	0.2858(4)	0.4157(3)	0.0058(3)	1
N4	2a	0	0.0007(7)	0.0000(4)	0.0075(5)	1
N5	2a	0	0.4548(7)	0.7394(5)	0.0092(5)	1

Table E4 Anisotropic displacement parameters (U_{ij} in \AA^2) for α - TiP_4N_8 with estimated standard deviations in parentheses. The anisotropic displacement factor is expressed as $\exp[-2\pi^2 (U_{11}h^2a^{*2} + U_{22}k^2b^{*2} + U_{33}l^2c^{*2} + U_{12}hka^*b^* + U_{13}hla^*c^* + U_{23}klb^*c^*)]$.

Atom	U_{11}	U_{22}	U_{33}	U_{23}	U_{13}	U_{12}
Ti1	0.0056(3)	0.0073(2)	0.0058(2)	0.0002(2)	0	0
P1	0.0036(2)	0.0045(2)	0.0041(2)	-0.0005(2)	0.0003(2)	0.00020(18)
P2	0.0041(3)	0.0038(2)	0.0040(2)	-0.0001(2)	0.00008(19)	- 0.00024(18)
N1	0.0047(9)	0.0065(8)	0.0065(9)	-0.0011(6)	0.0005(6)	-0.0015(7)
N2	0.0049(8)	0.0052(8)	0.0049(9)	0.0018(7)	0.0006(7)	0.0013(6)
N3	0.0065(8)	0.0061(8)	0.0048(8)	0.0012(7)	0.0009(7)	0.0007(6)
N4	0.0037(11)	0.0096(13)	0.0093(12)	0.0039(10)	0	0
N5	0.0055(12)	0.0054(11)	0.0167(14)	0.0024(11)	0	0

E Supporting Information for Chapter 6

Table E5 Interatomic distances (\AA) and bond angles ($^\circ$) in the structure of $\alpha\text{-TiP}_4\text{N}_8$.

Ti1	N2	2x	2.098(2)	N5	P1	N1	100.23(15)
Ti1	N1	2x	2.132(2)	N5	P1	N3	126.54(17)
Ti1	N3	2x	2.182(2)	N1	P1	N3	112.83(11)
T1	N5	1x	2.540(4)	N5	P1	N2	105.06(13)
P1	N5		1.6089(14)	N1	P1	N2	118.62(13)
P1	N1		1.625(2)	N3	P1	N2	94.74(11)
P1	N3		1.629(2)	N4	P2	N1	110.73(15)
P1	N2		1.636(2)	N4	P2	N3	113.05(15)
P2	N4		1.5758(15)	N1	P2	N3	103.95(11)
P2	N1		1.631(2)	N4	P2	N2	110.52(13)
P2	N3		1.641(2)	N1	P2	N2	112.56(13)
P2	N2		1.644(2)	N3	P2	N2	105.81(11)

Table E6 Atomic coordinates, isotropic displacement parameters (\AA^2), and site occupancies of $\beta\text{-TiP}_4\text{N}_8$.

Atom	Wyckoff position	<i>x</i>	<i>y</i>	<i>z</i>	<i>U_{eq}</i>	<i>occ.</i>
Ti1	2 <i>a</i>	0	0.88420(17)	0.39418(13)	0.0161(2)	1
Ti2	4 <i>b</i>	0.33332(3)	0.62120(15)	0.40469(12)	0.0206(2)	1
P1	4 <i>b</i>	0.43551(4)	0.39932(19)	0.23748(12)	0.0110(2)	1
P2	4 <i>b</i>	0.43389(4)	0.09922(19)	0.54809(13)	0.0116(2)	1
P3	4 <i>b</i>	0.09807(4)	0.40398(18)	0.24156(12)	0.0111(2)	1
P4	4 <i>b</i>	0.10473(4)	0.10293(19)	0.55210(12)	0.0119(2)	1
P5	4 <i>b</i>	0.22996(4)	0.40090(19)	0.24674(13)	0.0124(2)	1
P6	4 <i>b</i>	0.23394(4)	0.09939(19)	0.55727(13)	0.0126(2)	1
N1	4 <i>b</i>	0.43858(14)	0.1694(8)	0.0878(6)	0.0172(6)	1
N2	4 <i>b</i>	0.05888(14)	0.6935(7)	0.2108(5)	0.0148(6)	1
N3	4 <i>b</i>	0.10349(14)	0.1949(7)	0.0813(5)	0.0152(6)	1
N4	4 <i>b</i>	0.10919(14)	0.3320(7)	0.7053(5)	0.0152(6)	1
N5	4 <i>b</i>	0.22510(14)	0.1803(7)	0.0925(6)	0.0167(6)	1
N6	4 <i>b</i>	0.27091(14)	0.6830(7)	0.2172(5)	0.0153(6)	1
N7	4 <i>b</i>	0.33060(13)	0.0094(9)	0.0123(5)	0.0232(8)	1
N8	2 <i>a</i>	0	0.4769(9)	0.7734(6)	0.0164(8)	1
N9	4 <i>b</i>	0.16395(11)	0.5218(8)	0.2821(6)	0.0216(7)	1
N10	4 <i>b</i>	0.06771(12)	0.2294(7)	0.3937(4)	0.0144(6)	1
N11	4 <i>b</i>	0.40100(14)	0.2628(7)	0.3960(4)	0.0172(6)	1
N12	4 <i>b</i>	0.26554(13)	0.2686(8)	0.4033(4)	0.0179(6)	1
N13	2 <i>a</i>	0	0.0044(11)	0.0017(7)	0.0218(10)	1

Table E7 Anisotropic displacement parameters (U_{ij} in \AA^2) for β -TiP₄N₈ with estimated standard deviations in parentheses. The anisotropic displacement factor is expressed as $\exp[-2\pi^2 (U_{11}h^2a^{*2} + U_{22}k^2b^{*2} + U_{33}l^2c^{*2} + U_{12}hka^*b^* + U_{13}hla^*c^* + U_{23}klb^*c^*)]$.

Atom	U_{11}	U_{22}	U_{33}	U_{23}	U_{13}	U_{12}
Ti1	0.0150(4)	0.0217(4)	0.0116(4)	-0.0008(4)	0	0
Ti2	0.0136(3)	0.0264(4)	0.0217(4)	-0.0029(3)	-0.00007(16)	-0.00033(17)
P1	0.0107(4)	0.0105(4)	0.0119(4)	-0.0018(3)	0.0010(3)	0.0008(3)
P2	0.0132(4)	0.0106(4)	0.0111(5)	0.0013(3)	-0.0014(3)	0.0000(3)
P3	0.0095(3)	0.0099(4)	0.0138(4)	-0.0012(3)	-0.0004(4)	0.0008(3)
P4	0.0114(4)	0.0115(4)	0.0130(5)	0.0009(3)	0.0006(4)	-0.0002(3)
P5	0.0110(4)	0.0108(4)	0.0153(5)	-0.0013(3)	-0.0012(4)	-0.0006(3)
P6	0.0126(4)	0.0107(4)	0.0144(5)	0.0012(4)	0.0005(4)	0.0003(3)
N1	0.0127(11)	0.0178(13)	0.0210(16)	-0.0054(12)	0.0001(12)	-0.0060(10)
N2	0.0176(12)	0.0123(12)	0.0147(13)	0.0039(11)	0.0054(12)	0.0041(10)
N3	0.0136(10)	0.0143(12)	0.0177(13)	-0.0021(11)	-0.0012(12)	-0.0036(11)
N4	0.0167(13)	0.0143(11)	0.0147(13)	-0.0044(10)	-0.0056(12)	0.0025(11)
N5	0.0152(11)	0.0156(12)	0.0194(16)	-0.0044(11)	0.0005(12)	0.0053(11)
N6	0.0168(13)	0.0137(12)	0.0154(14)	0.0053(11)	-0.0056(12)	-0.0039(11)
N7	0.0115(12)	0.0233(17)	0.035(2)	0.0106(16)	-0.0005(13)	-0.0002(10)
N8	0.0096(15)	0.0162(17)	0.023(2)	0.0074(16)	0	0
N9	0.0103(12)	0.0164(14)	0.038(2)	-0.0095(15)	-0.0010(13)	0.0001(9)
N10	0.0142(13)	0.0149(11)	0.0141(12)	0.0047(16)	0.0035(10)	-0.0014(9)
N11	0.0146(12)	0.0207(13)	0.0163(13)	0.0012(17)	0.0058(10)	0.0018(9)
N12	0.0149(13)	0.0230(14)	0.0159(15)	0.0046(17)	-0.0060(10)	-0.0028(10)
N13	0.0111(17)	0.022(2)	0.032(3)	0.0103(19)	0	0

E Supporting Information for Chapter 6

Table E8 Interatomic distances (/Å) and bond angles (/°) in the structure of β -TiP₄N₈.

Ti1	N1	2x	2.105(3)	N8	P1	N1	109.75(14)
Ti1	N2	2x	2.216(3)	N8	P1	N4	110.37(15)
Ti1	N10	2x	2.219(2)	N1	P1	N4	113.19(16)
Ti2	N4	1x	2.086(3)	N8	P1	N11	115.55(17)
Ti2	N6	1x	2.108(3)	N1	P1	N11	111.69(12)
Ti2	N3	1x	2.200(3)	N4	P1	N11	95.75(13)
Ti2	N5	1x	2.201(3)	N11	P2	N2	112.40(12)
Ti2	N12	1x	2.229(2)	N11	P2	N3	106.08(13)
Ti2	N11	1x	2.241(2)	N2	P2	N3	114.16(17)
P1	N8	1x	1.5998(15)	N11	P2	N13	113.16(17)
P1	N1	1x	1.617(3)	N2	P2	N13	105.28(15)
P1	N4	1x	1.630(2)	N3	P2	N13	105.74(15)
P1	N11	1x	1.644(3)	N10	P3	N2	107.35(12)
P2	N11	1x	1.617(3)	N10	P3	N3	112.57(12)
P2	N2	1x	1.618(3)	N2	P3	N3	114.08(17)
P2	N3	1x	1.625(2)	N10	P3	N9	112.78(13)
P2	N13	1x	1.6608(16)	N2	P3	N9	104.78(12)
P3	N10	1x	1.622(2)	N3	P3	N9	105.13(12)
P3	N2	1x	1.623(2)	N7	P4	N1	110.98(13)
P3	N3	1x	1.625(3)	N7	P4	N4	109.01(12)
P3	N9	1x	1.650(2)	N1	P4	N4	113.24(17)
P4	N7	1x	1.603(2)	N7	P4	N10	115.92(13)
P4	N1	1x	1.623(2)	N1	P4	N10	95.29(12)
P4	N4	1x	1.624(3)	N4	P4	N10	111.95(12)
P4	N10	1x	1.642(2)	N5	P5	N6	116.33(14)
P5	N5	1x	1.617(3)	N5	P5	N12	116.08(12)
P5	N6	1x	1.623(2)	N6	P5	N12	97.20(12)
P5	N12	1x	1.629(3)	N5	P5	N9	105.03(12)
P5	N9	1x	1.651(2)	N6	P5	N9	106.24(12)
P6	N7	1x	1.608(2)	N12	P5	N9	115.90(13)
P6	N5	1x	1.630(2)	N7	P6	N5	109.81(13)
P6	N12	1x	1.634(3)	N7	P6	N12	113.08(13)
P6	N6	1x	1.634(3)	N5	P6	N12	104.35(12)
				N7	P6	N6	109.08(12)
				N5	P6	N6	111.55(13)
				N12	P6	N6	108.93(12)

Table E9 Atomic coordinates, isotropic displacement parameters (\AA^2), and site occupancies of disordered TiP_4N_8 .

Atom	Wyckoff position	<i>x</i>	<i>y</i>	<i>z</i>	U_{eq}	<i>occ.</i>
Ti1	2 <i>a</i>	0	0.88211(9)	0.39689(12)	0.00513(10)	1
Ti2	4 <i>b</i>	0.33322(2)	0.62344(7)	0.40121(10)	0.00587(9)	0.9077(14)
Ti2a	4 <i>b</i>	0.33324(13)	0.8723(8)	0.3901(6)	0.00587(9)	0.0923(14)
P1	4 <i>b</i>	0.43596(2)	0.40265(10)	0.23892(8)	0.00383(11)	1
P2	4 <i>b</i>	0.43308(2)	0.10273(10)	0.54869(8)	0.00416(13)	1
P3	4 <i>b</i>	0.09742(2)	0.39922(9)	0.24256(7)	0.00387(11)	1
P4	4 <i>b</i>	0.10499(2)	0.09899(10)	0.55237(7)	0.00424(12)	1
P5	4 <i>b</i>	0.23046(2)	0.39854(10)	0.24582(8)	0.00399(12)	1
P6	4 <i>b</i>	0.23377(2)	0.09840(10)	0.55549(8)	0.00440(12)	1
N1	4 <i>b</i>	0.43890(6)	0.1729(4)	0.0873(3)	0.0055(3)	1
N2	4 <i>b</i>	0.05901(7)	0.6923(4)	0.2099(3)	0.0058(3)	1
N3	4 <i>b</i>	0.10446(7)	0.1916(4)	0.0819(3)	0.0052(3)	1
N4	4 <i>b</i>	0.10868(6)	0.3269(4)	0.7051(3)	0.0061(3)	1
N5	4 <i>b</i>	0.22376(6)	0.1797(4)	0.0910(3)	0.0055(3)	1
N6	4 <i>b</i>	0.27019(7)	0.6859(4)	0.2152(3)	0.0062(3)	1
N7	4 <i>b</i>	0.33052(6)	0.0165(4)	0.0100(3)	0.0078(3)	1
N8	2 <i>a</i>	0	0.4786(5)	0.7778(3)	0.0066(4)	1
N9	4 <i>b</i>	0.16386(5)	0.5155(4)	0.2848(3)	0.0064(3)	1
N10	4 <i>b</i>	0.06739(5)	0.2302(3)	0.3972(4)	0.0052(3)	1
N11	4 <i>b</i>	0.40067(6)	0.2674(3)	0.3987(4)	0.0065(2)	1
N12	4 <i>b</i>	0.26601(6)	0.2692(3)	0.4040(3)	0.0065(3)	1
N13	2 <i>a</i>	0	0.0092(5)	0.0020(3)	0.0077(4)	1

Table E10 Anisotropic displacement parameters (U_{ij} in Å²) for disordered TiP₄N₈ with estimated standard deviations in parentheses. The anisotropic displacement factor is expressed as $\exp[-2\pi^2(U_{11}h^2a^{*2} + U_{22}k^2b^{*2} + U_{33}l^2c^{*2} + U_{12}hka^*b^* + U_{13}hla^*c^* + U_{23}klb^*c^*)]$.

Atom	U_{11}	U_{22}	U_{33}	U_{23}	U_{13}	U_{12}
Ti1	0.00450(16)	0.00693(16)	0.0040(2)	0.0002(2)	0	0
Ti2	0.00440(13)	0.00832(15)	0.00490(19)	-0.00061(18)	-0.00001(7)	-0.00008(7)
Ti2a	0.00440(13)	0.00832(15)	0.00490(19)	-0.00061(18)	-0.00001(7)	-0.00008(7)
P1	0.00414(18)	0.00435(18)	0.0030(3)	-0.0005(2)	0.00030(17)	0.00025(13)
P2	0.00463(18)	0.00417(19)	0.0037(3)	0.0004(2)	-0.00035(18)	-0.00012(13)
P3	0.00405(17)	0.00414(18)	0.0034(2)	-0.00040(19)	0.0000(2)	0.00003(13)
P4	0.00413(18)	0.00432(18)	0.0043(3)	0.0001(2)	0.0002(2)	-0.00013(13)
P5	0.00392(17)	0.00440(19)	0.0037(3)	-0.0004(2)	-0.00031(19)	-0.00025(13)
P6	0.00466(18)	0.00418(18)	0.0043(3)	0.0001(2)	-0.00006(18)	0.00031(13)
N1	0.0048(5)	0.0056(6)	0.0060(9)	-0.0015(6)	0.0007(5)	-0.0023(5)
N2	0.0068(5)	0.0058(6)	0.0048(8)	0.0012(6)	0.0014(6)	0.0013(5)
N3	0.0051(5)	0.0052(6)	0.0052(7)	-0.0014(6)	0.0005(6)	-0.0020(5)
N4	0.0064(6)	0.0068(6)	0.0050(9)	-0.0017(7)	-0.0018(6)	0.0010(5)
N5	0.0050(5)	0.0056(6)	0.0057(8)	-0.0020(6)	-0.0009(6)	0.0018(5)
N6	0.0065(6)	0.0068(6)	0.0053(8)	0.0018(6)	-0.0020(6)	-0.0009(5)
N7	0.0044(5)	0.0084(6)	0.0107(9)	0.0035(8)	0.0004(5)	0.0006(4)
N8	0.0040(7)	0.0067(8)	0.0090(11)	0.0028(9)	0	0
N9	0.0047(5)	0.0063(6)	0.0082(8)	-0.0025(8)	-0.0002(5)	-0.0006(4)
N10	0.0053(5)	0.0058(5)	0.0044(7)	0.0017(10)	0.0009(8)	-0.0005(4)
N11	0.0054(5)	0.0100(5)	0.0042(6)	0.0020(9)	0.0017(7)	0.0008(4)
N12	0.0051(5)	0.0104(6)	0.0041(7)	0.0014(9)	-0.0017(7)	-0.0009(4)
N13	0.0028(7)	0.0088(8)	0.0114(11)	0.0036(9)	0	0

E Supporting Information for Chapter 6

Table E11 Interatomic distances (/Å) and bond angles (/°) in the structure of disordered TiP_4N_8 .

Ti1	N1	2x	2.098(2)	N8	P1	N1	109.45(10)
Ti1	N2	2x	2.208(2)	N8	P1	N4	110.52(10)
Ti1	N10	2x	2.2196(14)	N1	P1	N4	113.15(13)
Ti2	Ti2a	1x	1.144(3)	N8	P1	N11	115.13(12)
Ti2	N4	1x	2.085(2)	N1	P1	N11	111.81(11)
Ti2	N6	1x	2.106(2)	N4	P1	N11	96.33(9)
Ti2	N5	1x	2.209(2)	N11	P2	N2	112.83(10)
Ti2	N3	1x	2.213(2)	N11	P2	N3	105.67(9)
Ti2	N12	1x	2.2374(15)	N2	P2	N3	114.08(14)
Ti2	N11	1x	2.2470(16)	N11	P2	N13	113.49(13)
Ti2a	N5	1x	2.099(5)	N2	P2	N13	105.05(10)
Ti2a	N3	1x	2.129(4)	N3	P2	N13	105.68(10)
Ti2a	N6	1x	2.196(4)	N3	P3	N10	112.41(11)
Ti2a	N4	1x	2.202(4)	N3	P3	N2	114.09(13)
Ti2a	N11	1x	2.381(4)	N10	P3	N2	106.83(9)
Ti2a	N12	1x	2.386(4)	N3	P3	N9	105.34(9)
P1	N8	1x	1.5959(10)	N10	P3	N9	112.65(10)
P1	N1	1x	1.619(2)	N2	P3	N9	105.43(9)
P1	N4	1x	1.6299(18)	N7	P4	N4	109.11(9)
P1	N11	1x	1.647(2)	N7	P4	N1	110.70(9)
P2	N11	1x	1.611(3)	N4	P4	N1	113.16(14)
P2	N2	1x	1.619(2)	N7	P4	N10	116.14(11)
P2	N3	1x	1.6221(19)	N4	P4	N10	112.10(10)
P2	N13	1x	1.6601(11)	N1	P4	N10	95.15(9)
P3	N3	1x	1.620(2)	N5	P5	N6	116.12(12)
P3	N10	1x	1.626(2)	N5	P5	N12	115.63(10)
P3	N2	1x	1.6273(19)	N6	P5	N12	97.76(9)
P3	N9	1x	1.6483(14)	N5	P5	N9	105.25(9)
P4	N7	1x	1.6064(15)	N6	P5	N9	106.56(9)
P4	N4	1x	1.621(2)	N12	P5	N9	115.50(11)
P4	N1	1x	1.6260(18)	N7	P6	N5	109.37(9)
P4	N10	1x	1.638(2)	N7	P6	N6	109.24(9)
P5	N5	1x	1.613(2)	N5	P6	N6	111.56(12)
P5	N6	1x	1.6200(18)	N7	P6	N12	113.55(11)
P5	N12	1x	1.630(2)	N5	P6	N12	103.75(9)
P5	N9	1x	1.6474(14)	N6	P6	N12	109.32(11)
P6	N7	1x	1.6069(15)				
P6	N5	1x	1.6288(18)				

E Supporting Information for Chapter 6

P6	N6	1x	1.631(2)
P6	N12	1x	1.632(2)

Table E12 Atomic coordinates, isotropic displacement parameters (\AA^2), and site occupancies of β - TiP_4N_8 at HT.

Atom	Wyckoff position	<i>x</i>	<i>y</i>	<i>z</i>	<i>U_{eq}</i>	<i>occ.</i>
Ti1	2 <i>a</i>	0	0.88420(17)	0.39418(13)	0.0161(2)	1
Ti2	4 <i>b</i>	0.33332(3)	0.62120(15)	0.40469(12)	0.0206(2)	1
P1	4 <i>b</i>	0.43551(4)	0.39932(19)	0.23748(12)	0.0110(2)	1
P2	4 <i>b</i>	0.43389(4)	0.09922(19)	0.54809(13)	0.0116(2)	1
P3	4 <i>b</i>	0.09807(4)	0.40398(18)	0.24156(12)	0.0111(2)	1
P4	4 <i>b</i>	0.10473(4)	0.10293(19)	0.55210(12)	0.0119(2)	1
P5	4 <i>b</i>	0.22996(4)	0.40090(19)	0.24674(13)	0.0124(2)	1
P6	4 <i>b</i>	0.23394(4)	0.09939(19)	0.55727(13)	0.0126(2)	1
N1	4 <i>b</i>	0.43858(14)	0.1694(8)	0.0878(6)	0.0172(6)	1
N2	4 <i>b</i>	0.05888(14)	0.6935(7)	0.2108(5)	0.0148(6)	1
N3	4 <i>b</i>	0.10349(14)	0.1949(7)	0.0813(5)	0.0152(6)	1
N4	4 <i>b</i>	0.10919(14)	0.3320(7)	0.7053(5)	0.0152(6)	1
N5	4 <i>b</i>	0.22510(14)	0.1803(7)	0.0925(6)	0.0167(6)	1
N6	4 <i>b</i>	0.27091(14)	0.6830(7)	0.2172(5)	0.0153(6)	1
N7	4 <i>b</i>	0.33060(13)	0.0094(9)	0.0123(5)	0.0232(8)	1
N8	2 <i>a</i>	0	0.4769(9)	0.7734(6)	0.0164(8)	1
N9	4 <i>b</i>	0.16395(11)	0.5218(8)	0.2821(6)	0.0216(7)	1
N10	4 <i>b</i>	0.06771(12)	0.2294(7)	0.3937(4)	0.0144(6)	1
N11	4 <i>b</i>	0.40100(14)	0.2628(7)	0.3960(4)	0.0172(6)	1
N12	4 <i>b</i>	0.26554(13)	0.2686(8)	0.4033(4)	0.0179(6)	1
N13	2 <i>a</i>	0	0.0044(11)	0.0017(7)	0.0218(10)	1

Table E13 Anisotropic displacement parameters (U_{ij} in Å²) for β -TiP₄N₈ at HT with estimated standard deviations in parentheses. The anisotropic displacement factor is expressed as $\exp[-2\pi^2 (U_{11}h^2a^{*2} + U_{22}k^2b^{*2} + U_{33}l^2c^{*2} + U_{12}hka^*b^* + U_{13}hla^*c^* + U_{23}klb^*c^*)]$.

Atom	U_{11}	U_{22}	U_{33}	U_{23}	U_{13}	U_{12}
Ti1	0.0150(4)	0.0217(4)	0.0116(4)	-0.0008(4)	0	0
Ti2	0.0136(3)	0.0264(4)	0.0217(4)	-0.0029(3)	-0.00007(16)	-0.00033(17)
P1	0.0107(4)	0.0105(4)	0.0119(4)	-0.0018(3)	0.0010(3)	0.0008(3)
P2	0.0132(4)	0.0106(4)	0.0111(5)	0.0013(3)	-0.0014(3)	0.0000(3)
P3	0.0095(3)	0.0099(4)	0.0138(4)	-0.0012(3)	-0.0004(4)	0.0008(3)
P4	0.0114(4)	0.0115(4)	0.0130(5)	0.0009(3)	0.0006(4)	-0.0002(3)
P5	0.0110(4)	0.0108(4)	0.0153(5)	-0.0013(3)	-0.0012(4)	-0.0006(3)
P6	0.0126(4)	0.0107(4)	0.0144(5)	0.0012(4)	0.0005(4)	0.0003(3)
N1	0.0127(11)	0.0178(13)	0.0210(16)	-0.0054(12)	0.0001(12)	-0.0060(10)
N2	0.0176(12)	0.0123(12)	0.0147(13)	0.0039(11)	0.0054(12)	0.0041(10)
N3	0.0136(10)	0.0143(12)	0.0177(13)	-0.0021(11)	-0.0012(12)	-0.0036(11)
N4	0.0167(13)	0.0143(11)	0.0147(13)	-0.0044(10)	-0.0056(12)	0.0025(11)
N5	0.0152(11)	0.0156(12)	0.0194(16)	-0.0044(11)	0.0005(12)	0.0053(11)
N6	0.0168(13)	0.0137(12)	0.0154(14)	0.0053(11)	-0.0056(12)	-0.0039(11)
N7	0.0115(12)	0.0233(17)	0.035(2)	0.0106(16)	-0.0005(13)	-0.0002(10)
N8	0.0096(15)	0.0162(17)	0.023(2)	0.0074(16)	0	0
N9	0.0103(12)	0.0164(14)	0.038(2)	-0.0095(15)	-0.0010(13)	0.0001(9)
N10	0.0142(13)	0.0149(11)	0.0141(12)	0.0047(16)	0.0035(10)	-0.0014(9)
N11	0.0146(12)	0.0207(13)	0.0163(13)	0.0012(17)	0.0058(10)	0.0018(9)
N12	0.0149(13)	0.0230(14)	0.0159(15)	0.0046(17)	-0.0060(10)	-0.0028(10)
N13	0.0111(17)	0.022(2)	0.032(3)	0.0103(19)	0	0

E Supporting Information for Chapter 6

Table E14 Interatomic distances (\AA) and bond angles ($^\circ$) in the structure of $\beta\text{-TiP}_4\text{N}_8$ at HT.

Ti1	N1	2x	2.123(4)	N1	P1	N8	109.1(2)
Ti1	N2	2x	2.192(4)	N1	P1	N4	114.0(3)
Ti1	N10	2x	2.224(3)	N8	P1	N4	109.8(2)
Ti2	N4	1x	2.097(4)	N1	P1	N11	111.1(2)
Ti2	N6	1x	2.107(4)	N8	P1	N11	116.1(2)
Ti2	N3	1x	2.206(4)	N4	P1	N11	96.46(18)
Ti2	N5	1x	2.225(4)	N3	P2	N11	105.39(18)
Ti2	N12	1x	2.249(3)	N3	P2	N13	106.6(2)
Ti2	N11	1x	2.268(3)	N11	P2	N13	113.0(2)
P1	N1	1x	1.611(4)	N3	P2	N2	114.0(2)
P1	N8	1x	1.613(2)	N11	P2	N2	112.74(18)
P1	N4	1x	1.628(3)	N13	P2	N2	105.1(2)
P1	N11	1x	1.634(4)	N3	P3	N2	114.0(2)
P2	N3	1x	1.626(3)	N3	P3	N10	110.2(2)
P2	N11	1x	1.629(4)	N2	P3	N10	106.47(17)
P2	N13	1x	1.635(2)	N3	P3	N9	106.63(19)
P2	N2	1x	1.635(4)	N2	P3	N9	105.65(19)
P3	N3	1x	1.621(4)	N10	P3	N9	114.0(2)
P3	N2	1x	1.628(3)	N7	P4	N1	110.7(2)
P3	N10	1x	1.628(3)	N7	P4	N4	107.65(18)
P3	N9	1x	1.640(3)	N1	P4	N4	113.7(3)
P4	N7	1x	1.605(3)	N7	P4	N10	115.8(2)
P4	N1	1x	1.626(3)	N1	P4	N10	95.49(18)
P4	N4	1x	1.632(4)	N4	P4	N10	113.34(18)
P4	N10	1x	1.645(3)	N5	P5	N6	115.5(2)
P5	N5	1x	1.614(4)	N5	P5	N12	113.7(2)
P5	N6	1x	1.621(3)	N6	P5	N12	97.11(18)
P5	N12	1x	1.627(3)	N5	P5	N9	106.6(2)
P5	N9	1x	1.640(3)	N6	P5	N9	106.85(19)
P6	N7	1x	1.606(3)	N12	P5	N9	117.1(2)
P6	N5	1x	1.620(3)	N7	P6	N5	109.1(2)
P6	N12	1x	1.639(4)	N7	P6	N12	112.6(2)
P6	N6	1x	1.641(4)	N5	P6	N12	104.76(18)
				N7	P6	N6	107.88(18)
				N5	P6	N6	112.7(2)
				N12	P6	N6	109.87(19)

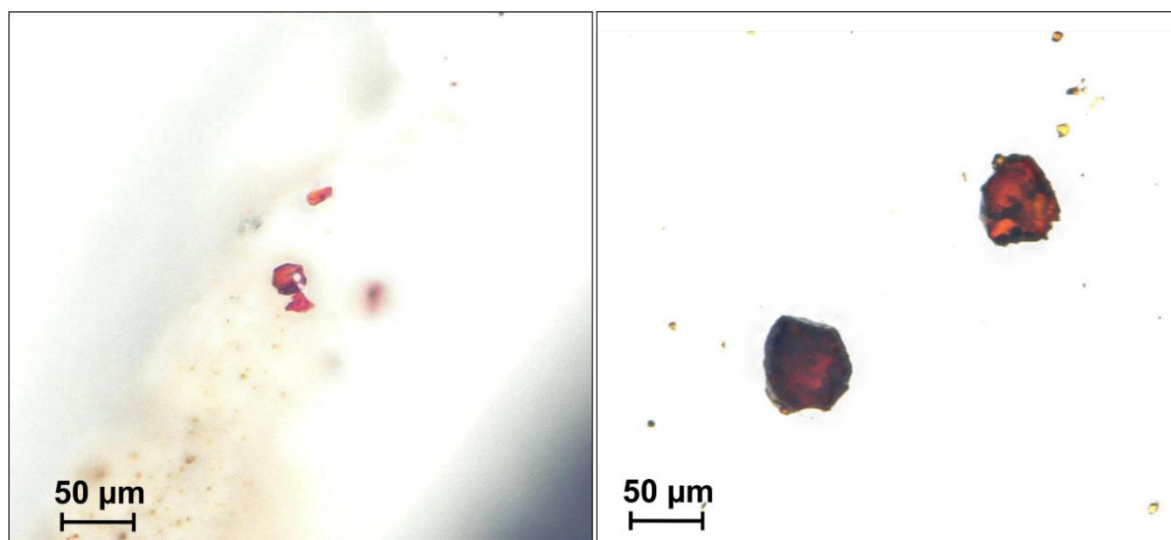


Figure E3. Photographs of representative crystals of α -TiP₄N₈ (left) and β -TiP₄N₈ (right).

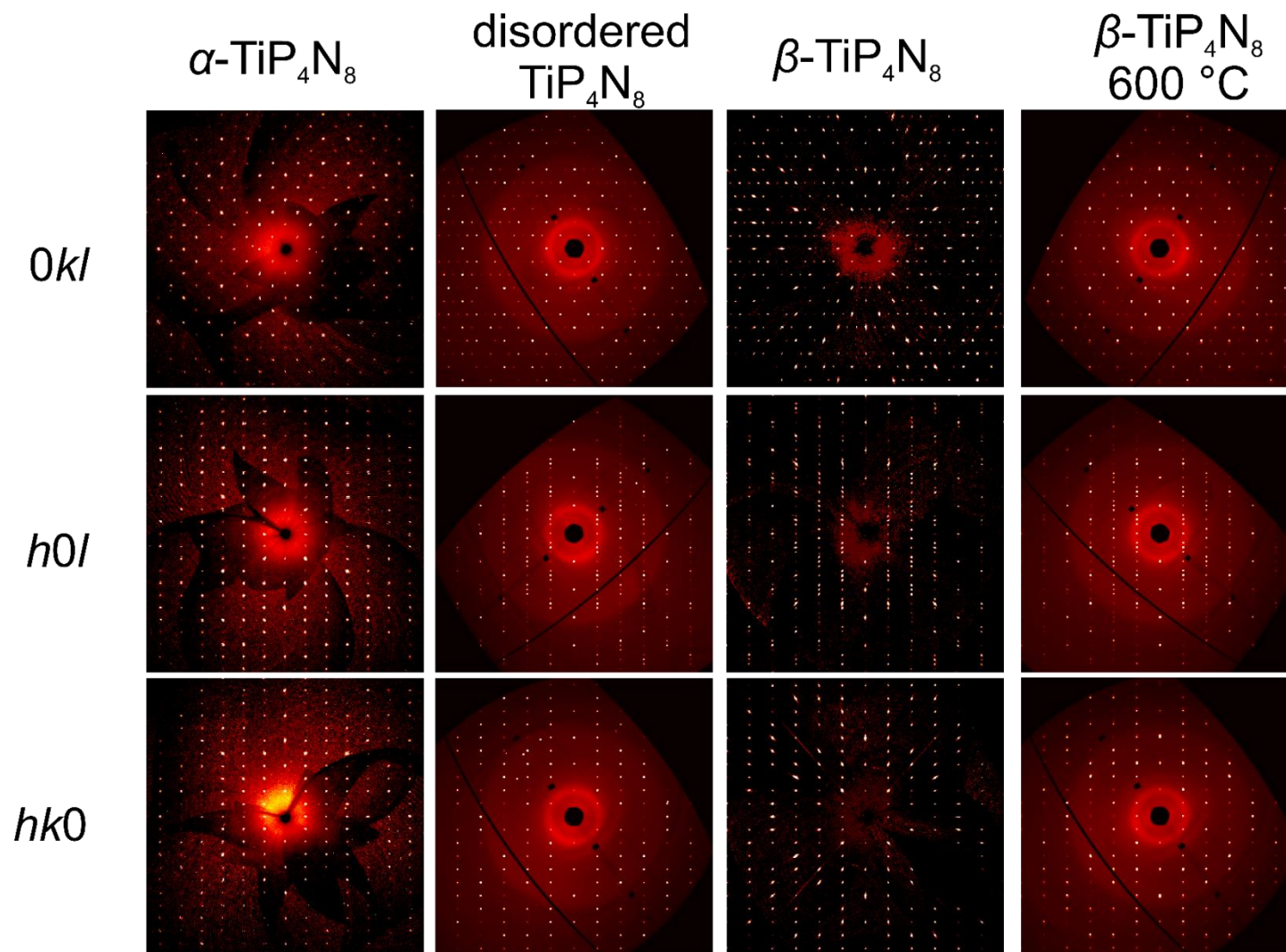


Figure E4. Reciprocal lattice sections of α -TiP₄N₈, disordered β -TiP₄N₈, β -TiP₄N₈ and HT β -TiP₄N₈.

EDX measurements**Table E15.** EDX measurements for TiP_4N_8 compared to values derived from sum formula.

EDX point / atom %	Ti	P	N
1	6.2	28.8	63.9
2	6.4	29.3	63.2
3	6.8	30.5	61.7
4	6.6	33.2	60.2
5	7.5	33.8	58.8
6	7.9	35.8	56.3
average	6.9(6)	32(2)	60(2)
calculated	7.7	30.8	61.5

Rietveld refinements**Table E16.** Crystallographic data from the Rietveld refinements for α - and β - TiP_4N_8 standard deviations are given in parentheses.

	α - TiP_4N_8	β - TiP_4N_8
crystal system	orthorhombic	
space group	$Pmn2_1$ (no. 31)	
lattice parameters / Å	$a = 7.6063(1)$ $b = 4.6354(1)$ $c = 7.8418(2)$	$a = 22.9196(5)$ $b = 4.58800(10)$ $c = 8.0970(2)$
radiation λ / Å	1.54056 (Cu- $K_{\alpha 1}$)	
cell volume / Å ³	276.49(1)	852.27(1)
2θ - range/°	5 < 2θ < 120	
refined parameters (incl. side phases)	53	119
thereof	18	12
background		
R -values	$R_p = 0.0625$ $wR_p = 0.0821$ $R_{\text{Bragg}} = 0.0334$	$R_p = 0.0880$ $wR_p = 0.1383$ $R_{\text{Bragg}} = 0.0400$

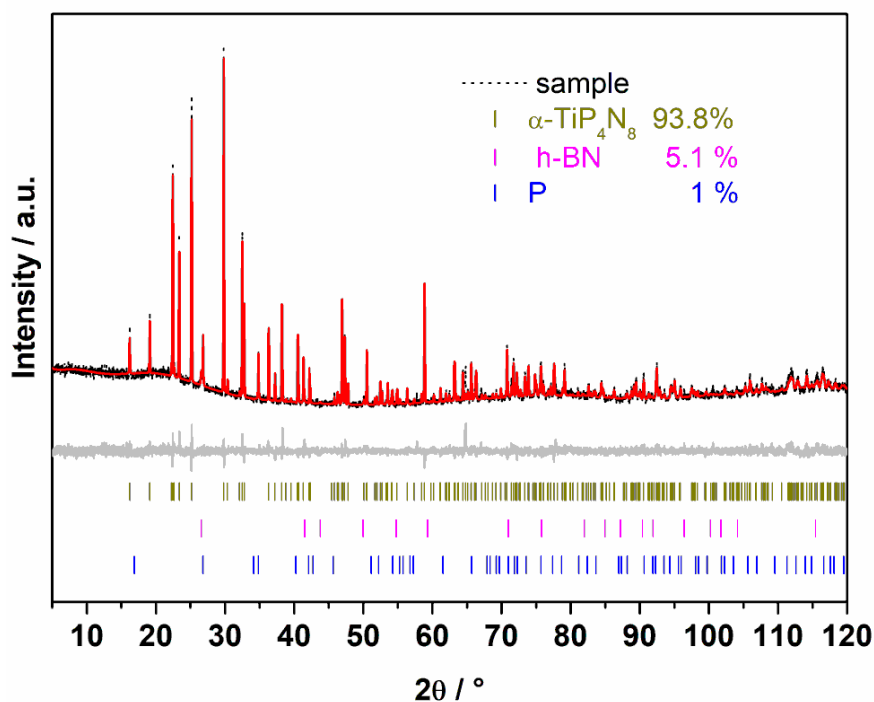


Figure E5. Rietveld refinement for $\alpha\text{-TiP}_4\text{N}_8$; observed (black line) and calculated (red line) X-ray powder diffraction patterns, positions of Bragg reflections of $\alpha\text{-TiP}_4\text{N}_8$ (vertical yellow bars), h-BN (vertical magenta bars), black P (vertical blue bars) and difference profile (gray line).

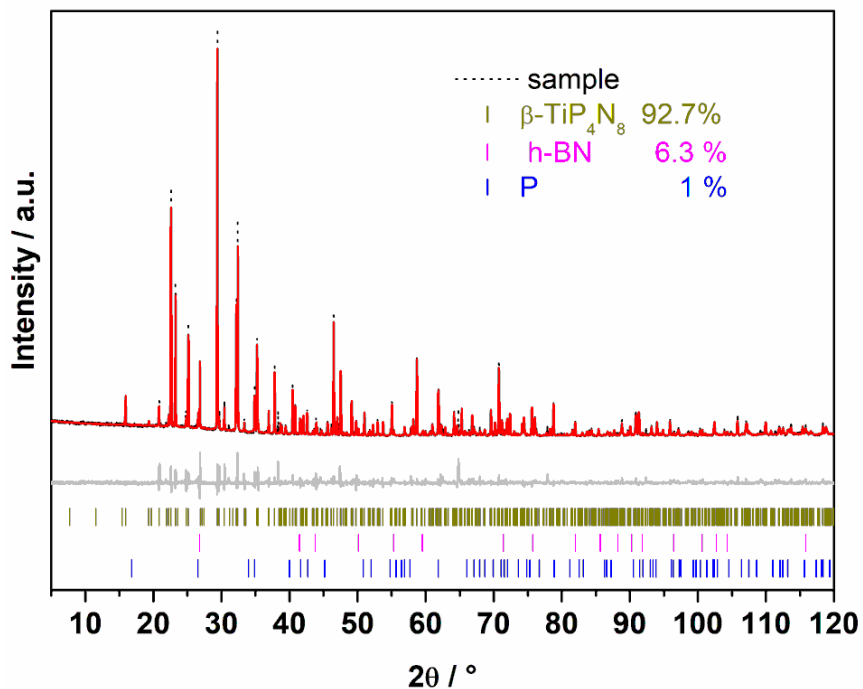


Figure E6. Rietveld refinement for $\beta\text{-TiP}_4\text{N}_8$; observed (black line) and calculated (red line) X-ray powder diffraction patterns, positions of Bragg reflections of $\beta\text{-TiP}_4\text{N}_8$ (vertical yellow bars), h-BN (vertical magenta bars), black P (vertical blue bars) and difference profile (gray line).

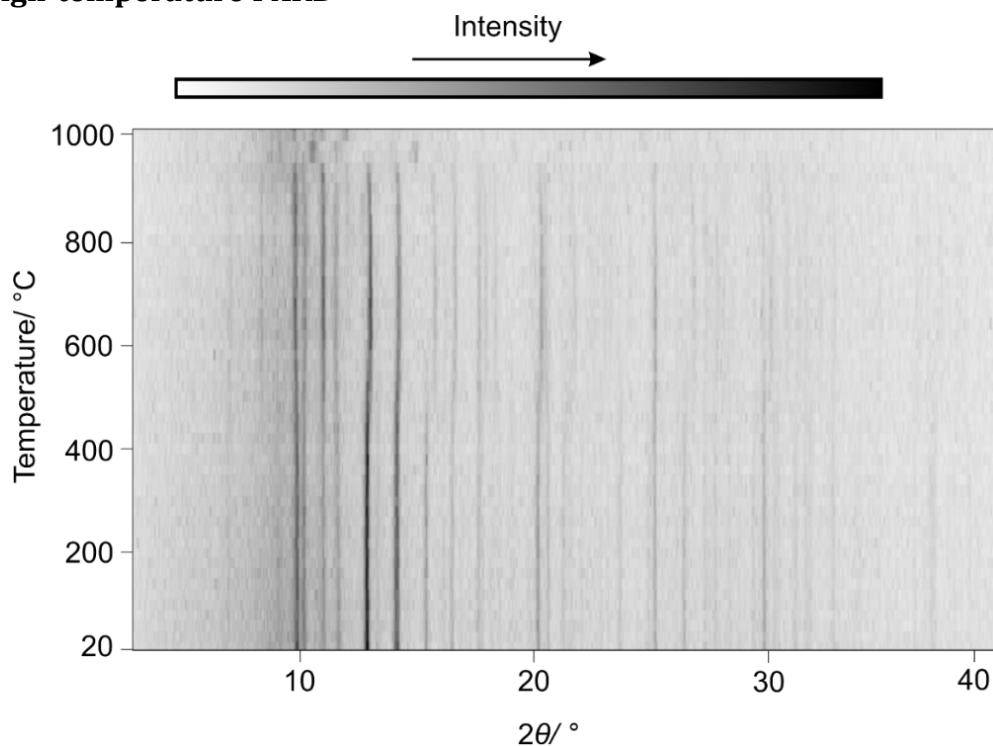
High-temperature PXRD

Figure E7. Temperature-dependent powder X-ray diffraction patterns ($\text{Mo-K}\alpha_1$ radiation, $\lambda = 0.71073$ Å) of TiP_4N_8 measured under Ar atmosphere showing thermal stability of TiP_4N_8 until 950 $^{\circ}\text{C}$.

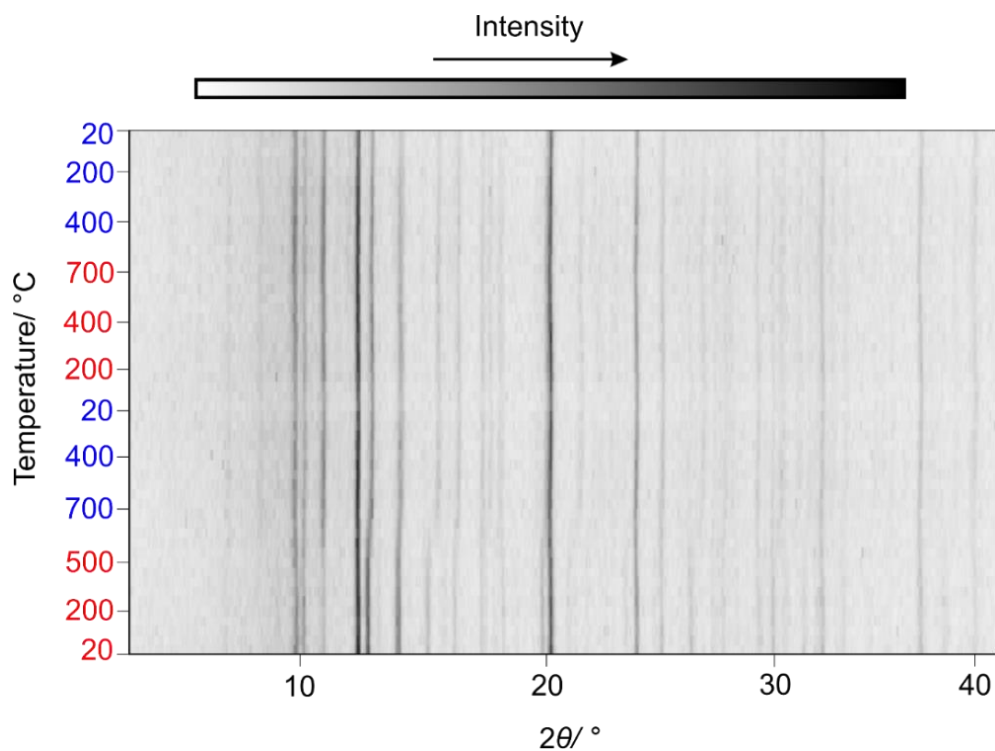


Figure E8. Temperature-dependent powder X-ray diffraction patterns ($\text{Mo-K}\alpha_1$ radiation, $\lambda = 0.71073$ Å) of TiP_4N_8 measured under Ar atmosphere showing a change of lattice parameters at 700 $^{\circ}\text{C}$ of the first heating ramp. Heating in red and cooling in blue.

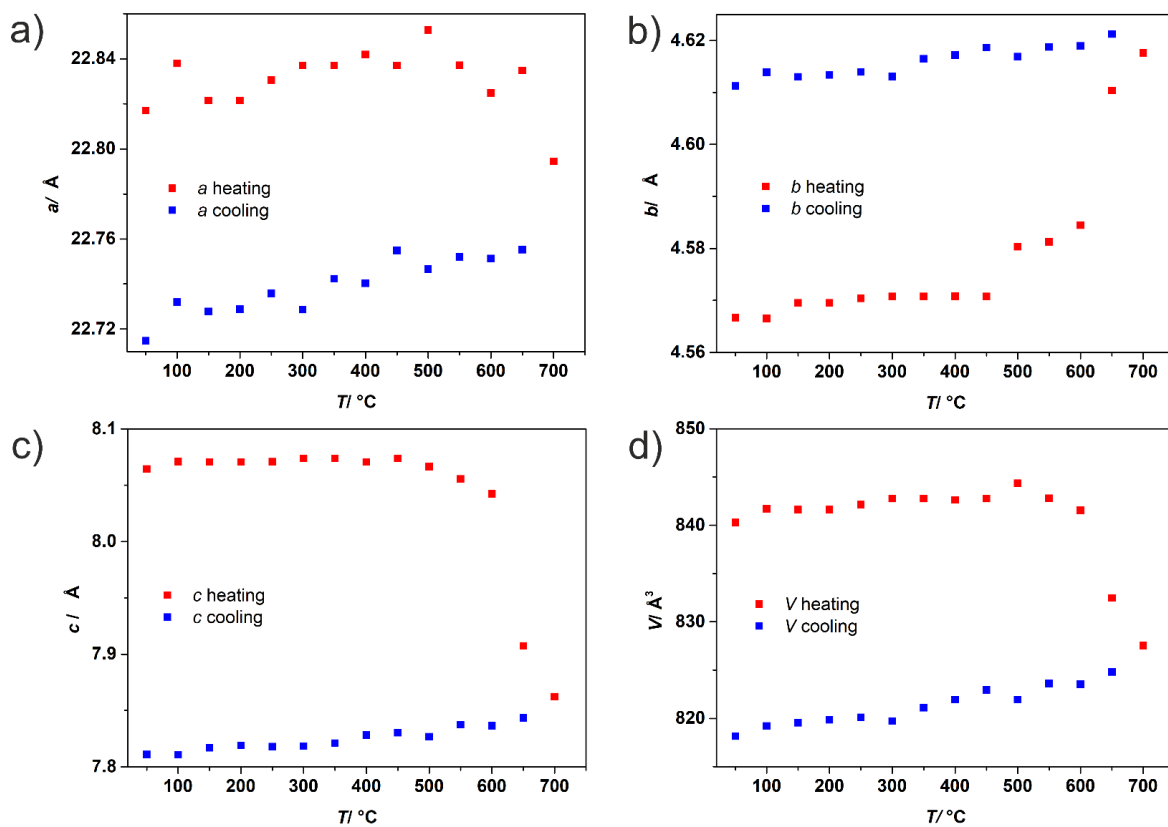


Figure E9. Change of lattice parameters and unit cell volume of TiP_4N_8 from the first HTPXRD cycle.

Heating curves in red and cooling curves in blue.

Bond-valence sum (BVS) Calculations**Table E17** Bond valence sums and expected charges for the atom sites in the crystal structure of α - TiP_4N_8 .

site	bond-valence sum	expected charge
Ti1	3.69	+4
P1	5.06	+5
P2	5.06	+5
N1	3.07	-3
N2	3.07	-3
N3	2.98	-3
N4	2.89	-3
N5	2.82	-3

Table E18 Bond valence sums and expected charges for the atom sites in the crystal structure of β - TiP_4N_8 .

site	bond-valence sum	expected charge
Ti1	3.18	+4
Ti2	3.18	+4
P1	5.05	+5
P2	4.98	+5
P3	4.95	+5
P4	5.03	+5
P5	5.01	+5
P6	5.03	+5
N1	3.14	-3
N2	2.98	-3
N3	3.00	-3
N4	3.12	-3
N5	3.01	-3
N6	3.10	-3
N7	2.67	-3
N8	2.64	-3
N9	2.47	-3
N10	2.89	-3
N11	2.89	-3
N12	2.90	-3
N13	2.51	-3

IR spectroscopy

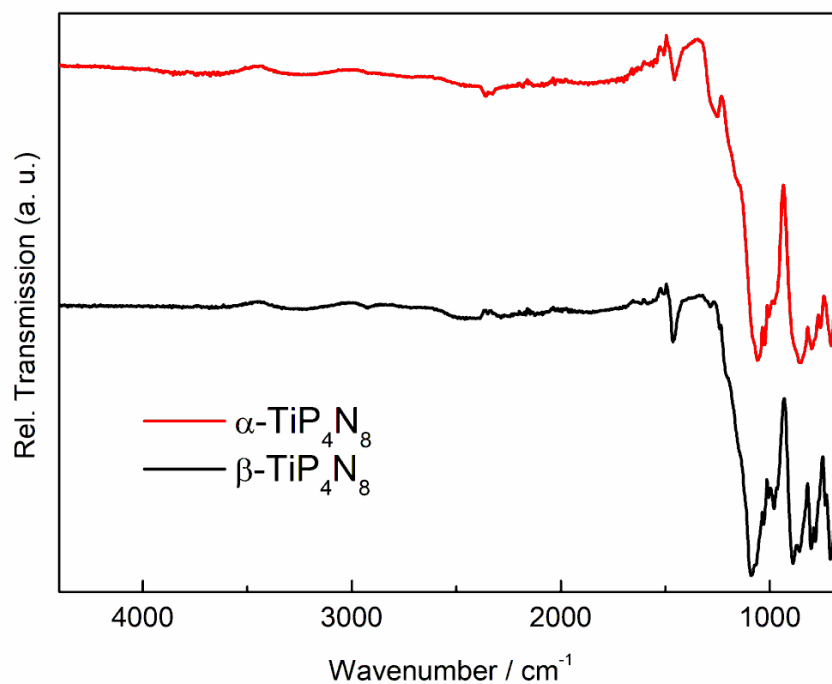


Figure E10. IR spectra of α -TiP₄N₈ (red) and β -TiP₄N₈ (black).

UV-Vis spectra

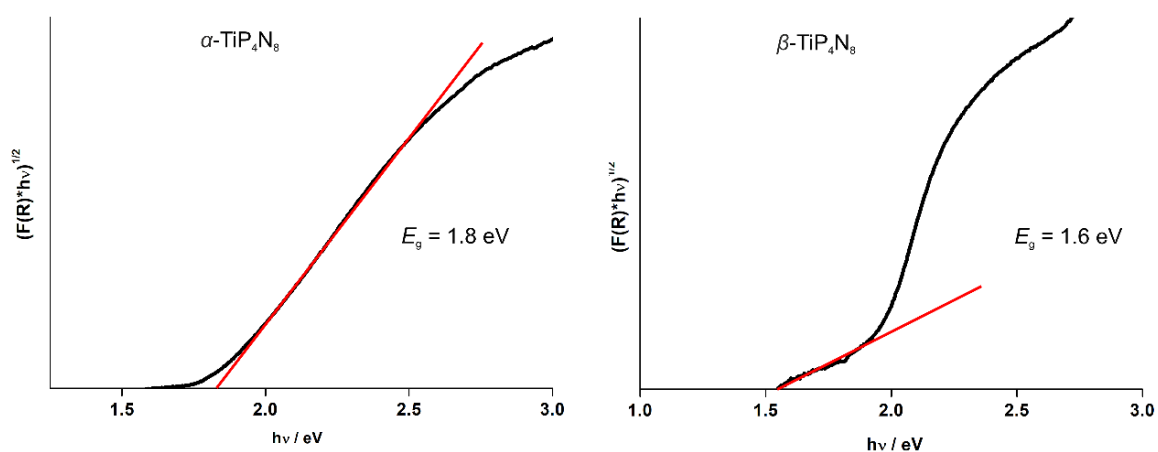


Figure E11: Tauc plots for UV-Vis spectra of α -TiP₄N₈ (left) and β -TiP₄N₈ (right). Red lines represent linear regressions from the steep regions to estimate the direct optical band gaps from the inflection points with the abscissa. Data between 1.7 and 2.4 eV (α -TiP₄N₈) and 1.5 to 1.9 eV (β -TiP₄N₈) were used for linear regressions.

DFT-calculations

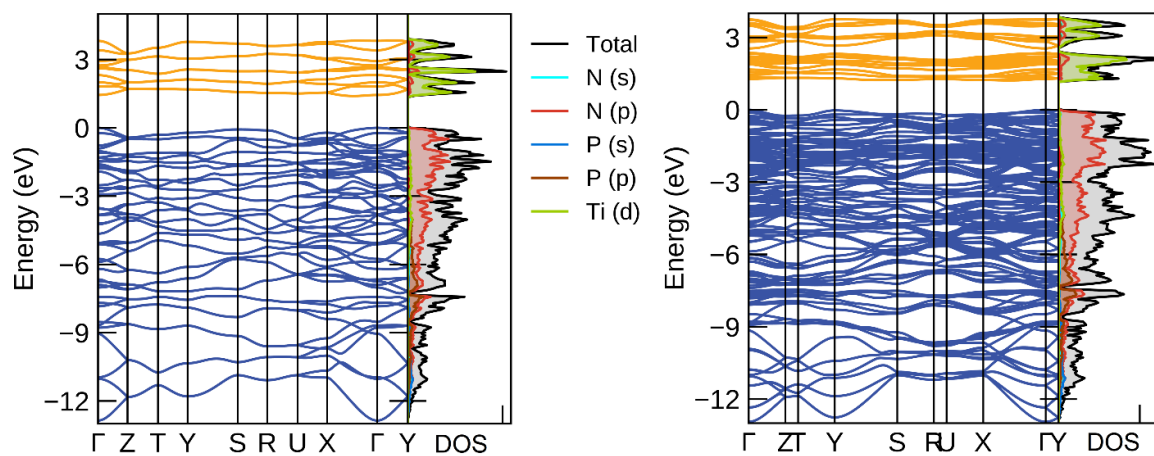


Figure E12: Electronic band structures and density-of-states (PBE) of α -TiP₄N₈ (left) and β -TiP₄N₈ (right). The energy zeros are taken at the Fermi levels.

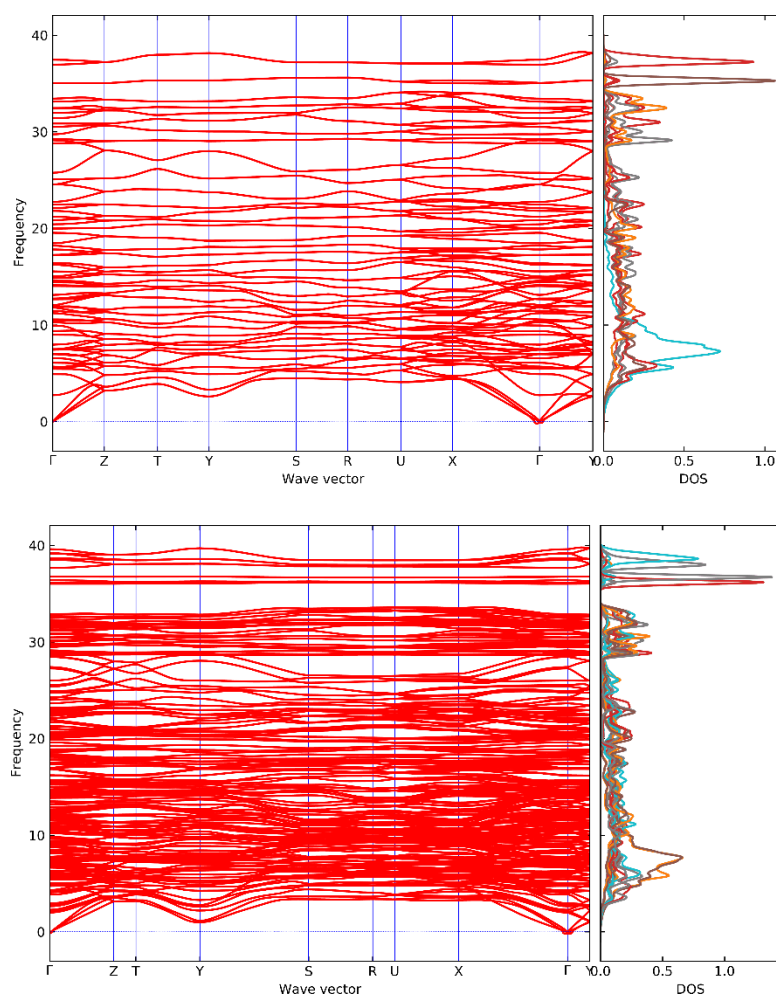


Figure E13: Phonon band structures and phonon density-of-states of α -TiP₄N₈ (top) and β -TiP₄N₈ (bottom).

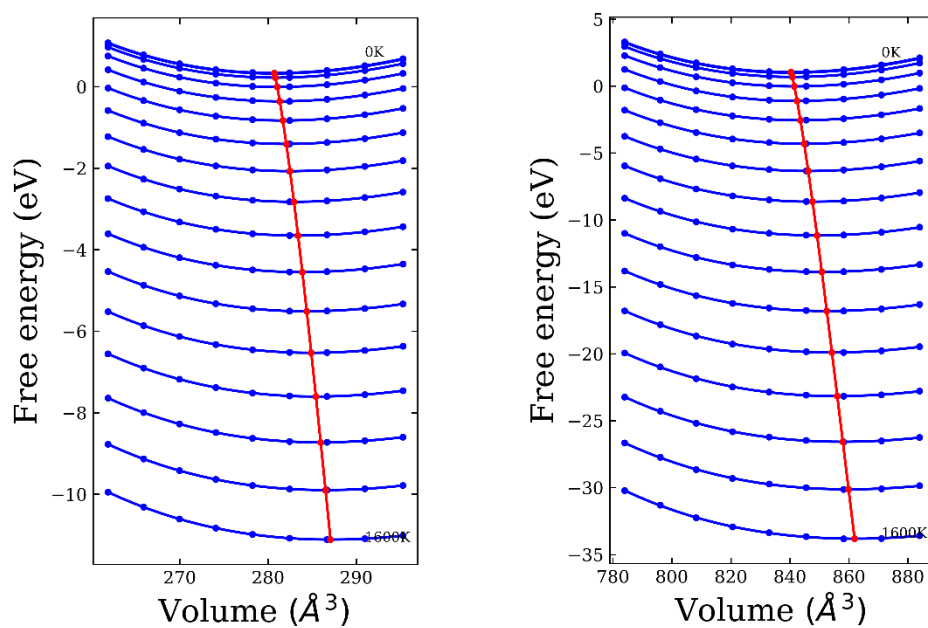


Figure E14: Volume dependent Helmholtz free energies at different temperatures for α -TiP₄N₈ (left) and β -TiP₄N₈ (right). The red lines mark the minima where the Gibbs free energy is obtained, respectively.

References

- [1] A. Stock, H. Grüneberg, *Ber. Dtsch. Chem. Ges.* **1907**, 40, 2573–2578.
- [2] W. J. Frierson, W. F. Filbert, in *Inorg. Synth.*, Wiley Blackwell, **2007**, pp. 136–138.
- [3] H. Huppertz, *Z. Kristallogr.* **2004**, 219, 330–338.
- [4] N. Kawai, S. Endo, *Rev. Sci. Instrum.* **1970**, 41, 1178–1181.
- [5] D. C. Rubie, *Phase Trans.* **1999**, 68, 431–451.
- [6] D. Walker, M. A. Carpenter, C. M. Hitch, *Am. Mineral.* **1990**, 75, 1020–1028.
- [7] D. Walker, *Am. Mineral.* **1991**, 76, 1092–1100.
- [8] A. Marchuk, L. Neudert, O. Oeckler, W. Schnick, *Eur. J. Inorg. Chem.* **2014**, 2014, 3427–3434.
- [9] M. Mallmann, S. Wendl, P. Strobel, P. J. Schmidt, W. Schnick, *Chem. Eur. J.* **2020**, 26, 6257–6263.
- [10] E. Bertschler, R. Niklaus, W. Schnick, *Chem. Eur. J.* **2017**, 23, 9592–9599.
- [11] G. M. Sheldrick, *Acta Crystallogr. Sect. C Struct. Chem.* **2015**, 71, 3–8.
- [12] G. M. Sheldrick, *SADABS, v.2: Multi-Scan Absorption Correction*; Bruker-AXS, Billerica, MA, **2012**.
- [13] *CrysAlis Pro*, Agilent Technologies, Yarnton, Oxfordshire, England, **2015**.
- [14] N. E. Brese, M. O’Keeffe, *Acta Crystallogr. Sect. B* **1991**, 47, 192–197.
- [15] A. S. Wills, *Valist*, Program available from www.ccp14.ac.uk.
- [16] J. Tauc, R. Grigorovici, A. Vancu, *Phys. status solidi* **1966**, 15, 627–637.
- [17] G. Kresse, J. Hafner, *Phys. Rev. B* **1994**, 49, 14251–14269.
- [18] G. Kresse, J. Furthmüller, *Comput. Mater. Sci.* **1996**, 6, 15–50.
- [19] P. E. Blöchl, *Phys. Rev. B* **1994**, 50, 17953–17979.

- [20] J. P. Perdew, K. Burke, M. Ernzerhof, *Phys. Rev. Lett.* **1996**, 77, 3865–3868.
- [21] J. Sun, A. Ruzsinszky, J. Perdew, *Phys. Rev. Lett.* **2015**, 115, 036402.
- [22] S. Grimme, *J. Comput. Chem.* **2006**, 27, 1787–1799.
- [23] A. Togo, I. Tanaka, *Scr. Mater.* **2015**, 108, 1–5.
- [24] M. T. Dove, *Introduction to Lattice Dynamics*, Cambridge University Press, **1993**.
- [25] K. J. Caspersen, E. A. Carter, *Proc. Natl. Acad. Sci. U. S. A.* **2005**, 102, 6738–6743.

F Miscellaneous

F.1 List of Publications within this Thesis

1. A Layered Tin Bismuth Selenide with Three Different Building Blocks that Account for an Extremely Large Lattice Parameter of 283 Å

M. Nentwig, L. Eisenburger, F. Heinke, D. Souchay, O. Oeckler

published in: *Chem. Eur. J.* **2020**, 26, 10676–10681.

XRD analyses were performed by Markus Nentwig. Syntheses were performed by Frank Heinke. STEM analyses and cross section sample preparation were performed by Lucien Eisenburger. TEM characterization was performed by Daniel Souchay. Oliver Oeckler supervised the project. The manuscript was written by Markus Nentwig in a leading role with support of all co-authors. All authors revised the manuscript.

2. High-Pressure High-Temperature Synthesis of Mixed Nitridosilicatephosphates and Luminescence of $AE\text{SiP}_3\text{N}_7\text{:Eu}^{2+}$ ($AE = \text{Sr, Ba}$)

L. Eisenburger, O. Oeckler, W. Schnick

published in: *Chem. Eur. J.* **2021**, 27, 4461–4465.

Syntheses and analyses were performed by Lucien Eisenburger. Oliver Oeckler and Wolfgang Schnick supervised the project. The manuscript was written by Lucien Eisenburger in a leading role with support of all co-authors. All authors revised the manuscript.

3. Nitridic Analogs of Micas $AE\text{Si}_3\text{P}_4\text{N}_{10}(\text{NH})_2$ ($AE = \text{Mg, Mg}_{0.94}\text{Ca}_{0.06}, \text{Ca, Sr}$)

L. Eisenburger, P. Strobel, P. J. Schmidt, T. Bräuniger, J. Wright, E. L. Bright, C. Giacobbe, O. Oeckler, W. Schnick

published in: *Angew. Chem. Int. Ed.* **2022**, 61, e202114902.

Angew. Chemie **2022**, 134, e202114902.

Syntheses, XRD and STEM analyses were performed by Lucien Eisenburger. Philipp Strobel and Peter. J. Schmidt performed luminescence measurements and analyses thereof. Thomas Bräuniger performed NMR measurements and aided in interpretation of data. Jonathan Wright, Eleanor Lawrence Bright and Carlotta Giacobbe measured X-ray diffraction data at

ID11, ESRF, Grenoble. Oliver Oeckler and Wolfgang Schnick supervised the project. The manuscript was written by Lucien Eisenburger in a leading role with support of all co-authors. All authors revised the manuscript.

4. High-Pressure Synthesis of $\text{Sc}_5\text{P}_{12}\text{N}_{23}\text{O}_3$ and $\text{Ti}_5\text{P}_{12}\text{N}_{24}\text{O}_2$ by Activation of the Binary Nitrides ScN and TiN with NH_4F

L. Eisenburger, V. Weippert, O. Oeckler, W. Schnick

published in: *Chem. Eur. J.* **2021**, 27, 14184–14188.

Syntheses, XRD and STEM analyses were performed by Lucien Eisenburger. Conducting and analyzing magnetic measurements was done by Valentin Weippert. Oliver Oeckler and Wolfgang Schnick supervised the project. The manuscript was written by Lucien Eisenburger in a leading role with support of all co-authors. All authors revised the manuscript.

5. Discovery of Two Polymorphs of TiP_4N_8 Synthesized from Binary Nitrides

L. Eisenburger, V. Weippert, C. Paulmann, D. Johrendt, O. Oeckler, W. Schnick

published in: *Angew. Chem. Int. Ed.* **2022**, DOI 10.1002/anie.202202014.

Angew. Chemie **2022**, DOI 10.1002/ange.202202014.

Syntheses, XRD and STEM analyses were performed by Lucien Eisenburger. Conducting and analyzing DFT calculations was done by Valentin Weippert and Dirk Johrendt. Carsten Paulmann aided in SCXRD data collection at P24, DESY, Hamburg. Oliver Oeckler and Wolfgang Schnick supervised the project. The manuscript was written by Lucien Eisenburger in a leading role with support of all co-authors. All authors revised the manuscript.

F.2 Full List of Publications

1. Nucleophilicity of Alkyl Zirconocene and Titanocene Precatalysts, and Kinetics of Activation by Carbenium Ions and by $B(C_6F_5)_3$

G. Berionni, H. Kurouchi, L. Eisenburger, H. Mayr,
Chem. Eur. J. **2016**, 22, 11196–11200.

2. The Influence of Nanoscale Heterostructures on the Thermoelectric Properties of Bi-substituted Tl_5Te_3

F. Heinke, L. Eisenburger, R. Schlegel, S. Schwarzmüller, O. Oeckler,
Z. Anorg. Allg. Chem. **2017**, 643, 447–454.

3. The Crystal Structures of $Pb_5Sb_4S_{11}$ (Boulangerite) – A Phase Transition Explains Seemingly Contradictory Structure Models

P. Schultz, F. Nietschke, G. Wagner, C. Eikemeier, L. Eisenburger, O. Oeckler,
Z. Anorg. Allg. Chem. **2017**, 643, 1531–1542.

4. $RE_4Ba_2[Si_{12}O_2N_{16}C_3]:Eu^{2+}$ ($RE = Lu, Y$): Green-Yellow Emitting Oxonitridocarbidosilicates with a Highly Condensed Network Structure

C. Maak, L. Eisenburger, J. P. Wright, M. Nentwig, P. J. Schmidt, O. Oeckler, W. Schnick,
Inorg. Chem. **2018**, 57, 13840–13846.

5. Ammonothermal Synthesis and Crystal Structure of the Nitridoalumogermanate $Ca_{1-x}Li_xAl_{1-x}Ge_{1+x}N_3$ ($x \approx 0.2$)

J. Häusler, L. Eisenburger, O. Oeckler, W. Schnick,
Eur. J. Inorg. Chem. **2018**, 2018, 759–764.

6. Syntheses and physical properties of the MAX phase boride Nb_2SB and the solid solutions $Nb_2SB_xC_{1-x}$ ($x = 0-1$)

T. Rackl, L. Eisenburger, R. Niklaus, D. Johrendt
Phys. Rev. Mater. **2019**, 3, 054001.

7. Ammonothermal Synthesis of the Mixed-Valence Nitrogen-Rich Europium Tantalum Ruddlesden-Popper Phase $\text{Eu}^{\text{II}}\text{Eu}^{\text{III}}_2\text{Ta}_2\text{N}_4\text{O}_3$

N. Cordes, M. Nentwig, L. Eisenburger, O. Oeckler, W. Schnick

Eur. J. Inorg. Chem. **2019**, 2019, 2304–2311.

8. The Long-Periodic Loop-Branched Chain Structure of the Oxonitridophosphate $\text{La}_{21}\text{P}_{40}\text{O}_{46}\text{N}_{57}$, Elucidated by a Combination of TEM and Microfocused Synchrotron Radiation

M. Nentwig, S. D. Klotz, L. Neudert, L. Eisenburger, W. Schnick, O. Oeckler

Chem. Eur. J. **2019**, 25, 14382–14387.

9. Cationic Pb_2 Dumbbells Stabilized in the Highly Covalent Lead Nitridosilicate $\text{Pb}_2\text{Si}_5\text{N}_8$

P. Bielec, R. Nelson, R. P. Stoffel, L. Eisenburger, D. Günther, A. K. Henß, J. P. Wright, O. Oeckler, R. Dronskowski, W. Schnick

Angew. Chem. Int. Ed. **2019**, 58, 1432–1436.

Angew. Chem. **2019**, 131, 1446–1450.

10. Targeting Vacancies in Nitridosilicates: Aliovalent Substitution of M^{2+} ($M = \text{Ca}, \text{Sr}$) by Sc^{3+} and U^{3+}

P. Bielec, L. Eisenburger, H. L. Deubner, D. Günther, F. Kraus, O. Oeckler, W. Schnick

Angew. Chem. Int. Ed. **2019**, 58, 840–843.

Angew. Chem. **2019**, 131, 850–853.

11. $\text{BaP}_6\text{N}_{10}\text{NH}:\text{Eu}^{2+}$ as a Case Study—An Imidonitridophosphate Showing Luminescence

S. Wendl, L. Eisenburger, M. Zipkat, D. Günther, J. P. Wright, P. J. Schmidt, O. Oeckler, W. Schnick

Chem. Eur. J. **2020**, 26, 5010–5016.

12. Nitridophosphate-Based Ultra-Narrow-Band Blue-Emitters: Luminescence Properties of $\text{AEP}_8\text{N}_{14}:\text{Eu}^{2+}$ ($\text{AE} = \text{Ca}, \text{Sr}, \text{Ba}$)

S. Wendl, L. Eisenburger, P. Strobel, D. Günther, J. P. Wright, P. J. Schmidt, O. Oeckler, W. Schnick

Chem. Eur. J. **2020**, 26, 7292–7298.

13. A Layered Tin Bismuth Selenide with Three Different Building Blocks that Account for an Extremely Large Lattice Parameter of 283 Å

M. Nentwig, L. Eisenburger, F. Heinke, D. Souchay, O. Oeckler

Chem. Eur. J. **2020**, *26*, 10676–10681.

14. BaGe₈As₁₄: a semiconducting sodalite-type compound

V. Weippert, T. Chau, K. Witthaut, L. Eisenburger, D. Johrendt

Chem. Commun. **2021**, *57*, 1332–1335.

15. High Thermoelectric Properties in the Sodalite Compounds BaGe₈As₁₄ and AGe₇As₁₅ (A = Rb, Cs)

V. Weippert, K. Witthaut, M. Pointner, M. Sachs, L. Eisenburger, F. Kraus, D. Johrendt

Chem. Mater. **2021**, *33*, 8248–8258.

16. High-Pressure High-Temperature Synthesis of Mixed Nitridosilicatephosphates and Luminescence of AEsP₃N₇:Eu²⁺ (AE = Sr, Ba)

L. Eisenburger, O. Oeckler, W. Schnick

Chem. Eur. J. **2021**, *27*, 4461–4465.

17. High-Pressure Synthesis of Sc₅P₁₂N₂₃O₃ and Ti₅P₁₂N₂₄O₂ by Activation of the Binary Nitrides ScN and TiN with NH₄F

L. Eisenburger, V. Weippert, O. Oeckler, W. Schnick

Chem. Eur. J. **2021**, *27*, 14184–14188.

18. Nitridic Analogs of Micas AEsP₃N₁₀(NH)₂ (AE = Mg, Mg_{0.94}Ca_{0.06}, Ca, Sr)

L. Eisenburger, P. Strobel, P. J. Schmidt, T. Bräuniger, J. Wright, E. L. Bright, C. Giacobbe, O. Oeckler, W. Schnick

Angew. Chem. Int. Ed. **2022**, *61*, e202114902.

Angew. Chem. **2022**, *134*, e202114902.

19. Discovery of Two Polymorphs of TiP₄N₈ Synthesized from Binary Nitrides

L. Eisenburger, V. Weippert, C. Paulmann, D. Johrendt, O. Oeckler, W. Schnick

Angew. Chem. Int. Ed. **2022**, DOI 10.1002/anie.202202014.

Angew. Chem. **2022**, DOI 10.1002/ange.202202014.

F.3 Conference Contributions

Heterostructured multinary thallium tellurides

Frank Heinke, Lucien Eisenburger, Stefan Schwarzmüller, Frederik Nietschke and Oliver Oeckler

Talk, Hirschegg-Seminar für Festkörperchemie, **2016**, Hirschegg, Austria

Cation disorder in $\text{Ca}_{1-x}\text{Li}_x\text{Al}_{1-x}\text{Ge}_{1+x}\text{N}_3$ ($x \approx 0.2$) by STEM-HAADF

Lucien Eisenburger, Jonas Häusler, Wolfgang Schnick, Oliver Oeckler

Talk, 26th Annual Meeting of the German Crystallographic Society (DGK), **2018**, Essen, Germany

Kationen- und Anionen-Ausordnung in der Ruddlesden-Popper-Phase $\text{Eu}^{2+}\text{Eu}^{3+}_2\text{Ta}_2\text{N}_4\text{O}_3$

Lucien Eisenburger, Niklas Cordes, Markus Nentwig, Juliane Stahl, Theresa Block, Rainer Pöttgen, Dirk Johrendt, Wolfgang Schnick, Oliver Oeckler

Talk, Mitteldeutsches Anorganisches Nachwuchs Symposium, **2018**, Jena, Germany

Influence of dopant concentration on dopant distribution in $\text{Ca}_{2-x}\text{Eu}_x\text{Si}_5\text{N}_8$ ($x = 0.02, 0.1, 0.15$) by STEM-HAADF

Lucien Eisenburger, Monika Pointner, Oliver Oeckler and Wolfgang Schnick

Poster, The 17th European Conference on Solid State Chemistry, **2019**, Lille, France

Crystal structure determination of microcrystalline compounds by the combination of TEM and microfocused synchrotron radiation

Daniel Günther, Johnathan P. Wright, Gavin B. M. Vaughan, Sebastian Wendl, Lucien Eisenburger, Wolfgang Schnick and Oliver Oeckler,

Talk, Microscopy Conference, **2019**, Berlin, Germany

Structural characterization of barium (imido-)nitridophosphate networks

Daniel Günther, Sebastian Wendl, Lucien Eisenburger, Wolfgang Schnick and Oliver Oeckler

Poster, 27th Annual Meeting of the German Crystallographic Society (DGK), **2019**, Leipzig, Germany

Nitridoberyllosilicates – Promising Host Materials for Solid-State Lighting

Tobias Giftthaler, Philipp Strobel, Lucien Eisenburger, Oliver Oeckler and Wolfgang Schnick
Poster, 10th International Symposium on Nitrides, **2019**, Barcelona, Spain

Nitridosilicatephosphates by high-pressure / high-temperature synthesis

Lucien Eisenburger, Oliver Oeckler and Wolfgang Schnick
Talk, Joint Polish-German Crystallographic Meeting, **2020**, Wrocław, Poland

NH₄F-Assisted Multi-Anvil Syntheses of Novel Nitrides

Lucien Eisenburger, Oliver Oeckler and Wolfgang Schnick
Talk, International Workshop on "Development of multianvil technology and its applications to Earth and material sciences", **2021**, virtual venue

Disorder in layered tellurides $Tt_1Pn_2Te_4$ ($Tt = \text{Ge, Sn, Pb}$; $Pn = \text{As, Sb, Bi}$)

Lennart Staab, Lucien Eisenburger, Sebastian. Geisler and Oliver Oeckler
Talk, 29th Annual Meeting of the German Crystallographic Society (DGK), **2021**, Hamburg, Germany/online

F.4 Deposited Crystal Structures

Table F.1: Compounds discussed within this thesis and their respective depository numbers.

Compound	CSD
SrSiP ₃ N ₇	2050660
BaSiP ₃ N ₇	2050661
Sc ₅ P ₁₂ N ₂₃ O ₃	2084626
Ti ₅ P ₁₂ N ₂₄ O ₂	2084627
CaSi ₃ P ₄ N ₁₀ (NH) ₂	2096670
α -TiP ₄ N ₈	2121162
β -TiP ₄ N ₈	2121163
disordered β -TiP ₄ N ₈	2121164
HT β -TiP ₄ N ₈	2121161

G Curriculum Vitae

Personal Details

Name	Lucien André Eisenburger
Date of Birth	11.06.1991
Place of Birth	Düsseldorf, Germany
Nationality	German

- | | |
|-------------------|---|
| 01/2018 - 09/2022 | Research assistant in the groups of Prof. Dr. Wolfgang Schnick (Department of Chemistry, Ludwig-Maximilians-Universität München) and of Prof. Dr. Oliver Oeckler (Institute for Material Science and Crystallography, Leipzig University, Leipzig)
Doctoral thesis: <i>"NH₄F-Assisted High-Pressure Synthesis of Novel Nitrides and Atomic-Resolution Chemical Mapping by STEM"</i> |
| 09/2017-02/2018 | Research assistant in the group of Prof. Dr. Oliver Oeckler (Institute for Material Science and Crystallography, Leipzig University, Leipzig) |
| 02/2017-08/2017 | Master thesis (Inorganic Chemistry)
Title: <i>"Transmissionselektronenmikroskopie an nitridischen Festkörpern"</i> |
| 07/2016-02/2017 | Managing Director
Fußorthopädie Eisenburger GmbH, 56457 Westerbург |
| 02/2016-05/2016 | Research internship (Inorganic Chemistry)
Universität Leipzig
Prof. Dr Oliver Oeckler |

04/2015-02/2017	Master of Science (Chemistry) Ludwig-Maximilians-Universität München
09/2014-01/2015	Bachelor Thesis (Inorganic Chemistry) Ludwig-Maximilians-Universität München, Prof. Dr. Wolfgang Schnick Title: „Beiträge zur Strukturaufklärung nitridischer Verbindungen durch Elektronenbeugung“
09/2011-09/2014	Bachelor of Science (Chemistry and Biochemistry) Ludwig-Maximilians-Universität München, Germany
04/2010-06/2011	Military Service FüUstgBtl 7./281 54568 Gerolstein
02/2010	Allgemeine Hochschulreife Advanced courses Biology, Chemistry and Latin
06/2001-02/2010	Secondary School Konrad-Adenauer-Gymnasium 56457 Westerburg